

Interlocking modular microfluidic cooling substrates for future high energy physics experiments

Présentée le 27 janvier 2023

Faculté des sciences et techniques de l'ingénieur
Laboratoire de microsystemes 4
Programme doctoral en microsystemes et microélectronique

pour l'obtention du grade de Docteur ès Sciences

par

Massimo ANGELETTI

Acceptée sur proposition du jury

Prof. H. Shea, président du jury
Prof. Ph. Renaud, directeur de thèse
Dr D. Alvarez Feito, rapporteur
Dr N. Pacifico, rapporteur
Prof. Y. Bellouard, rapporteur

Acknowledgements

I am deeply indebted to my CERN supervisor, Corrado Gargiulo, my thesis director at EPFL, Professor Philippe Renaud, and all the jury committee that took part in this journey, Professor Herbert Shea, Professor Bellouard Yves, Dr Nicola Pacifico and Dr Diego Alvarez Feito.

I would like to extend my sincere thanks to my CERN colleagues, particularly to Fabio Pellegrino, l'oracolo di Nio, Pascal Jean Secouet, Pieter Ijzermans, Vadim Eduardovich Kakichev, Jacob Bastiaan Van Beelen, Miranda Van Stenis, Phillippe Bouvier, Cedric Ducret, Gregory Lahu, Elisa Laudi, *...too many people, I hope I did not forget anyone!...*, Lee Mcalpine, Shawaiz Liaqat, Maria Soledad Molina Gonzalez, Mark Lenders, Gael Ledey, Quentin Piazza, Gilles Grandvaux, Jérôme Bendotti, Neil Dixon, Valery Akhnazarov, Francisco Perez Gomez, Jérôme Noël and Jérôme Daguin. You all supported me during this research and made me grow as an engineer. I would like to acknowledge also Eddy Kunnen for your help and interest in the project.

I would be remiss in not mentioning Alessandro Mapelli for introducing me to the immeasurable world of microfabrication. I had the pleasure of collaborating with a great person and friend, Timothee Frei. I am also thankful to the CMi team, in particular to Patrick Alain Madlinger, Giovanni Monteduro, Rémy Juttin, Julien Dorsaz and Adrien Toros. You all have been available and patient with me.

I would like to mention my family, especially my parents, Eleonora and my friends. Your encouragement has been of fundamental help during this work.

Finally, I thank future readers for their interest and patience in reading this manuscript
...until the end.

Geneva, 4 November 2022

M. Angeletti.

Acknowledgements

Abstract

In high energy physics, semiconductor-based sensors are widely used in particle tracking applications. These sensors are typically glued on low-mass cooling substrates, which guarantee the correct thermal management and, at the same time, minimise their interaction with the particles being detected. For future experiments, the coverage of larger surfaces with silicon trackers faces challenges related to the large number of sensors to be positioned, cooled and interconnected. A modular cooling substrate design must be adopted to access industrialised series production. Replacement of faulty sensors represents an additional design requirement. In present detectors, the sensing modules are in thermal contact with the cooling line through a thermal interface material that allows for sensor replacement. This solution has a negative effect on thermal performance and sensor resolution.

A different approach was followed in this research. A microfluidic cooling substrate is permanently glued at the back of the sensor, providing an integrated module that can be thoroughly tested, electrically and thermally, before the final detector integration. This solution minimises the material in front of the sensor by reducing the number of thermal interfaces. On the flip side, the challenge becomes the design of a re-workable and reliable hydraulic interconnection between the modules. The design of the "*interlocking Modular microfluidic Cooling Substrate*" (i-M μ CS) is based on embedded mini/microchannels produced by either silicon femtosecond laser engraving or polymer and ceramic additive manufacturing. The research presented here looked deeper into 3D-printed ceramic substrates as new attractive material and technology for high energy physics applications.

The proposed interconnection of the microfluidic module relies on mechanical and hydraulic interlocking fixations. The mechanical interface is based on a LEGO[®]-like concept, while an in-plane hydraulic connection across microfluidic modules provides the sealing through a micro O-ring. Design alternatives to the baseline interconnection were also explored. Production processes and materials play a key role with respect to achievable tolerances which affect the interconnection. The ability to guarantee correct modules dis/mounting, positioning capability, and sealing was investigated for polymer and ceramic samples. In addition, fundamental aspects of ceramic microfluidic substrates, such as substrate flatness, gluing interface with the sensors and their hydraulic and thermal performances, were investigated. Finally, a real detector layout was taken as a reference to evaluate the implementation of the newly developed modular microfluidic solutions.

Keywords: Microfluidic interconnection, microfabrication, femtosecond laser engraving, ceramic additive manufacturing, HEP thermal management.

Abstract

Sintesi

Negli esperimenti di fisica delle alte energie, i sensori semiconduttori sono ampiamente utilizzati nel tracciamento delle particelle. Questi sensori sono tipicamente incollati su leggeri substrati di raffreddamento; i quali, pur garantendo una corretta gestione termica, devono anche minimizzare la loro interazione con le particelle rilevate. Nei futuri esperimenti, la copertura di grandi superfici implicherà il posizionamento di un gran numero di sensori, la loro interconnessione e raffreddamento. Sarà quindi necessario adottare un disegno modulare del substrato di raffreddamento che ne permetta una industrializzazione seriale. In aggiunta, la sostituzione di sensori difettosi rappresenterà un ulteriore requisito di progettazione. Negli attuali rivelatori, i sensori sono in contatto termico con la linea di raffreddamento attraverso un materiale di interfaccia che ne consente la sostituzione; questa soluzione ha un effetto negativo sulle prestazioni termiche.

In questo lavoro è stato sviluppato un approccio diverso. Un substrato microfluidico di raffreddamento è incollato in modo permanente al sensore, realizzando un modulo indipendente che può essere testato, elettricamente e termicamente, prima dell'integrazione finale nel rivelatore. Questa soluzione riduce al minimo il materiale davanti al sensore, minimizzando il numero di interfacce termiche, e sposta il nodo della progettazione al disegno di un'interconnessione idraulica tra i moduli affidabile ma al tempo stesso smontabile. Il disegno di un *"interlocking Modular microfluidic Cooling Substrate"* (i-M μ CS) si basa su mini/microcanali integrati nel substrato. Diverse opzioni per la realizzazione del substrato sono state valutate e variano dall'incisione dei canali su un substrato in silicio mediante laser (femtosecond) alla stampa 3D di materiali polimerici o ceramici. I substrati ceramici stampati in 3D sono stati esaminati in dettaglio viste le loro caratteristiche meccaniche e termiche che meglio rispondono alle esigenze dei rivelatori di fisica delle particelle.

L'interconnessione tra i moduli è sia di tipo meccanico che idraulico. L'interfaccia meccanica si basa su un concetto LEGO[®], mentre la tenuta idraulica è realizzata attraverso una connessione che si sviluppa nel piano dei microcanali ed è garantita da un micro O-ring all'interfaccia. Alcune varianti a questo disegno sono state esplorate in una fase successiva. Il processo produttivo e il materiale del substrato giocano un ruolo fondamentale rispetto alle tolleranze ottenibili che hanno un impatto diretto sulle interconnessioni. Per questo motivo, è stata studiata, al variare del materiale e processo di produzione, l'abilità delle interconnessioni a garantire il corretto smontaggio/montaggio dei moduli, la capacità di posizionamento e la tenuta idraulica. In aggiunta, sono stati studiati alcuni aspetti fondamentali dei substrati microfluidici in ceramica come la planarità del substrato, l'interfaccia di incollaggio con i

Abstract

sensori e le loro prestazioni idrauliche e termiche. Infine, è stata valutata l'implementazione delle nuove soluzioni microfluidiche in un layout di un vero rivelatore.

Parole chiave: Interconnessioni microfluidiche, microfabbricazione, incisione a femtosecond laser, additive manufacturing in ceramica, gestione del raffreddamento termico per la fisica ad alte energie.

Résumé

Dans les détecteurs de trajectoire au silicium pour la physique des hautes énergies, les capteurs à base de semi-conducteurs au silicium sont collés sur des substrats de refroidissement de faible masse. Tout en garantissant une bonne gestion thermique des capteurs, la conception d'un substrat vise à minimiser l'interaction avec les particules détectées. Pour les futures expériences de physique des hautes énergies, la couverture de surfaces plus vastes avec des trackers en silicium est remise en question par le grand nombre de capteurs à positionner, refroidir et interconnecter. Une conception de substrat de refroidissement modulaire évolutive doit être adoptée pour accéder à la production en série industrialisée. Le remplacement des capteurs défectueux représente une exigence de conception supplémentaire. Dans les détecteurs actuels, les capteurs sont en contact thermique avec un substrat commun en carbone à haute conductivité thermique par l'intermédiaire d'un matériau d'interface thermique qui permet également le remplacement du capteur. Cette interface a un effet non négligeable sur la résolution de détection et les performances thermiques des capteurs.

Une approche différente a été suivie dans cette recherche. Le substrat de refroidissement est collé en permanence à l'arrière du capteur, fournissant un module intégré qui peut être entièrement testé, électriquement et thermiquement, avant l'assemblage final. Cette solution minimise le matériau devant le capteur en évitant l'utilisation du matériau d'interface thermique et le défi est devenu de concevoir une interconnexion hydraulique fiable entre les modules. À partir d'une analyse critique de la solution de refroidissement actuelle, basée sur des micros canaux de silicium, un nouveau substrat de refroidissement nommé "*Interlocking Modular Microfluidic Cooling Substrate*" (i-M μ CS) a été développé. Sa conception est basée sur des mini micros canaux intégrés dans un substrat et produits soit par gravure laser femtoseconde silicium, soit par fabrication additive polymère et céramique. La recherche a examiné de plus près les substrats céramiques imprimés en 3D en tant que nouveaux matériaux et technologies attrayants pour les expériences de physique des hautes énergies en raison de leur coefficient de dilatation thermique correspondant au capteur en silicium, de leur bonne conductivité thermique et de leur dureté de rayonnement élevée.

Cette nouvelle conception de module microfluidique repose sur une fixation par emboîtement mécanique et hydraulique. Alors que l'interface mécanique est basée sur un concept de type LEGO[®], l'étanchéité des modules microfluidiques est garantie par des micro-joints toriques. Le processus de production et le matériau jouent un rôle clé en ce qui concerne la tolérance réalisable. Des alternatives de conception à l'interconnexion de base ont également été explorées. La faisabilité de l'interconnexion pour garantir le montage /démontage correct des

Abstract

modules, la capacité de positionnement et l'étanchéité a été étudiée pour des échantillons de polymères et de céramiques. Certains aspects fondamentaux de l'utilisation de substrats microfluidiques en céramique imprimés en 3D, tels que la planéité du substrat, l'interface de collage avec les capteurs et leurs performances hydrauliques et thermiques, ont été étudiés. Enfin, la mise en œuvre des solutions micro fluidiques modulaires nouvellement développées dans une configuration de détecteur réelle a été évaluée.

Mots clefs: Interconnexions microfluidiques, micro-fabrication, gravure avec femtosecond laser, fabrication additive céramique, gestion thermique pour la physique des hautes énergies.

Contents

Acknowledgements	i
Abstract (English/Italian/French)	iii
List of figures	xiii
List of tables	xix
Acronyms	xxi
1 Introduction	1
1.1 Research approach	2
1.2 Structure of the thesis	3
2 State of the art	5
2.1 Principle of a silicon tracking detector in HEP	5
2.1.1 Silicon semiconductor-based sensor	5
2.1.2 Layouts of a silicon tracking detector	7
2.1.3 Radiation	10
2.1.4 Material budget	13
2.2 Mechanics and thermal management	14
2.2.1 Cooling systems	14
2.2.2 Cooling substrates and their support structures	18
2.3 Review of microchannel cooling substrate solutions	23
2.3.1 Silicon μ CS in present HEP experiments	23
2.3.2 R&Ds on μ CS for HEP experiments	24
2.3.3 Hydraulic connections	30
2.4 Cooling strategies comparison	34
3 Requirements for future Si tracking detectors	37
3.1 Mechanics and cooling challenges	37
3.1.1 Si tracking system for future hadron collider	38
3.1.2 Si tracking system for future lepton collider	40
3.2 Modular implementation	41
3.2.1 Limits of the re-workable thermal interfaces	42

Contents

3.3	The proposed concept	43
3.4	Challenges of the modular microfluidic implementation	44
4	Silicon microfluidic channels by femtosecond laser engraving	47
4.1	Purpose of the research	47
4.2	Methodology	48
4.3	DOE	49
4.4	Anodic bonding test	51
4.5	Pressure test	55
4.6	Metrology	56
4.7	Adhesive-based bonding procedure	57
4.8	Outcomes	59
5	Interlocking microfluidic interconnection	61
5.1	Guidelines for the interconnection development	61
5.2	The baseline interlocking microfluidic interconnection	62
5.2.1	Experimental methodology of the optimisation	63
5.2.2	Design optimisation	64
5.2.3	Validation and tests results	67
5.2.4	Outcomes	73
5.3	Guidelines for the development of alternative interconnections	74
5.4	Alternative hydraulic interface	75
5.4.1	Face seal limits	75
5.4.2	Radial seal	78
5.4.3	Outcomes	80
5.5	Alternative mechanical interfaces	82
5.5.1	Clip-based solution	82
5.5.2	Spring-based solution	84
5.5.3	Rail-based solution	87
5.5.4	Outcomes	88
6	Ceramic i-MμCS	89
6.1	Advantages of a 3D printed ceramic cooling substrate	89
6.2	Method and materials	90
6.2.1	Methodology	90
6.2.2	Selected AM technologies	91
6.2.3	Samples	94
6.3	Ceramics sample characterisation	95
6.3.1	Substrate inspection	95
6.3.2	Microchannel inspection	100
6.3.3	Outcomes	101
6.4	Interconnection validation	103
6.4.1	Substrate plug-and-play	105

6.4.2	Substrate interchangeability	106
6.4.3	Substrate sealing	108
6.4.4	Outcomes	111
7	i-MμCS implementation in silicon tracking systems	113
7.1	Guidelines of the research	113
7.2	Materials and manufacturing processes	114
7.2.1	Ceramics	115
7.2.2	Polymeric	117
7.2.3	Silicon	118
7.2.4	CFRP	119
7.3	Detector layout implemented with i-M μ CS	120
7.4	i-M μ CS in ceramic AM	123
7.4.1	Flatness dependence on substrate dimension	123
7.4.2	Gluing interface with the sensing module	126
7.4.3	Hydraulic and thermal assessment	130
7.5	Outcomes	143
8	Conclusions	145
8.1	Summary	145
8.2	Future work	147
	Bibliography	151
A	Introduction to High Energy Physics experiments	171
B	Flow distribution optimisation on silicon frame μCS	177
C	Experimental set-ups	197
D	Additional parts on the i-MμCS implementation	203
E	CAD drawing	207
	Curriculum Vitae	215

Contents

List of Figures

2.1	Micro-strip and pixel silicon sensors.	6
2.2	Hybrid and monolithic active pixel sensors	7
2.3	ALICE Inner tracking system 2 during installation	8
2.4	Tracking system layout of the CMS experiment	9
2.5	Air cooling system of the STAR silicon pixel detector	15
2.6	Air cooling system concept for the ALICE ITS3 prototypes	15
2.7	Example of HEP low-mass cooling substrates	18
2.8	Vascular CCS used for the first layer of the present ATLAS vertex detector	20
2.9	Vascular CCS used for the present ALICE vertex detector	20
2.10	Vascular CCS used for the present ALICE tracker	20
2.11	Schematic view of the re-workable CCS solution	21
2.12	Re-workable CCS solution for the future CMS tracker	22
2.13	Re-workable CCS solution for the future ATLAS tracker	22
2.14	The NA62 GTK station	24
2.15	The LHCb VeLo module	24
2.16	Alternative μ CS solutions proposed for the present VeLo detector	25
2.17	Prototype of the polyimide μ CS solution proposed for ALICE ITS2	25
2.18	The silicon μ CS solution proposed for the ALICE ITS2	26
2.19	Prototype with integrated μ CS of Belle II pixel detector ladder	27
2.20	Buried channel prototypes	28
2.21	Silicon microchannel oscillating heat pipes	29
2.22	Example of a commercially available connector	31
2.23	Direct soldering of stainless steel capillaries	31
2.24	Kovar connectors of the NA62 GTK detector	32
2.25	Invar connector of the LHCb VELO vertex detector	32
2.26	In plane 3D printed connector for BELLE II vertex detector	32
2.27	Interconnections for LOC devices in literature	33
2.28	Interconnections for cooling applications	34
3.1	The reference experiment of the FCC-hh	39
3.2	Longitudinal cross-section of the FCC-hh reference experiment	39
3.3	Tracking system layouts of the FCC-hh reference experiment	39
3.4	The FCC-ee reference experiment	40

List of Figures

3.5	Concepts of modular implementation	43
3.6	Schematic layout of microfluidic circuits	45
3.7	Schematic layout of a modular Si μ CS concept with auxiliary substrates	46
4.1	The outcomes of the DOE	50
4.2	Laser pattern for anodic bonding test	51
4.3	Silicon wafer (CMi 1 10 7236) with SiO ₂ hard mask after DI rinse	52
4.4	Silicon wafer (CMi 1 10 7236) after SiO ₂ hard mask removing	52
4.5	SEM pictures of the silicon wafer (CMi 1 10 7630) after DI rinse	53
4.6	Silicon wafer (CMi 1 10 7630) after CMP polishing	53
4.7	Anodic bonding of the silicon wafer (CMI 1 1 10 7630)	54
4.8	Anodic bonding of the silicon wafer (CMI 1 1 10 7260)	54
4.9	Burst pressure test sample	55
4.10	Burst pressure results	55
4.11	Failures of the burst pressure samples	56
4.12	Examples of the profilometer inspection (CMI 1 1 10 7630)	56
4.13	Cross section of a diced wafer (CMI 1 1 10 7630)	57
4.14	Si microchannels closed by a carbon fleece layer	57
4.15	Si dice bonded to a 3D printed connector by a carbon fleece layer	58
4.16	Burst failure of a Si sample closed by a carbon fleece layer	59
4.17	FS laser patterning of pillars on a silicon surface	59
5.1	Interlocking modular concept	62
5.2	Detail of the first prototype	63
5.3	Optimised design of the interconnection	65
5.4	Module assembly	66
5.5	Breadboard model of the optimised interlocking configuration	67
5.6	Pin-slot interference dependence on accuracy	67
5.7	FEA Analysis of the pin-slot interference	68
5.8	Pull force due to the pin and slot interference	69
5.9	Measurement of the sample positioning	70
5.10	X-Y measurements of the samples	71
5.11	Repeatability and Interchangeability	71
5.12	Pressure test results	72
5.13	Set-up for the pressure test of the hydraulic interfaces	76
5.14	Failure pressure of the face seal as a function of the O-ring compression	77
5.15	Failure pressure of the face seal as a function of the force	77
5.16	The radial seal solution	78
5.17	Seal fitting of the radial seal solution	79
5.18	Test results of the radial seal solution	80
5.19	Design of the clip-based solution	82
5.20	FEM of the clip-based solution	83
5.21	Assembly of the clip-based solution	83

5.22 Array of samples with the clip-based solution	84
5.23 Design of the spring-based solution	84
5.24 Design of the spring	85
5.25 FEM of the PMMA spring	85
5.26 Assembly of the spring-based solution	86
5.27 Array of samples with the spring-based solution	86
5.28 Design of the rail-based solution	87
5.29 Samples array of the rail-based solution	87
6.1 Lithoz CeraFab 7500 manufacturing system	93
6.2 Samples for the ceramics characterisation	94
6.3 Details of the X-ray computed tomography	95
6.4 X-ray computed tomography of the samples	97
6.5 3D scan measurement of a sample bottom surface	98
6.6 3D scans for the measurement of the samples flatness	99
6.7 Measurement of the channel roughness	100
6.8 Samples for the helium leak test	101
6.9 Design modifications for the ceramic samples	103
6.10 Details of the hydraulic interconnection of the alumina samples	104
6.11 Pull force results of the alumina samples	105
6.12 Interchangeability results for the alumina samples	106
6.13 X-Y position measurements of the alumina NPJ (S2) samples	107
6.14 X-Y position measurements of the alumina LCM (S4) samples	107
6.15 Burst pressure results for the LCM (S3) samples with face seal	108
6.16 Micro O-ring squeezed between the alumina LCM (S3) samples	109
6.17 Burst pressure test for the LCM (S4) samples with radial seal	110
6.18 Example of a deteriorated micro O-ring	110
7.1 Ceramic i-M μ CS with plate design	115
7.2 Ceramic i-M μ CS with frame and reduced thickness designs	116
7.3 2D thermal analysis of a polymeric cooling substrate	117
7.4 Si μ CS integrated on a modular concept	118
7.5 CFRP cold plates integrated on a modular concept	119
7.6 ALICE 3 detector concept	120
7.7 The barrel and disk layouts implemented with i-M μ CS	121
7.8 Prototypes of i-M μ CS with their support structures	122
7.9 Flatness of the alumina substrates	124
7.10 Flatness of the alumina substrates with and without surface grinding	125
7.11 HIC of the ALICE ITS2 tracker	126
7.12 Glue deposition on alumina substrate	127
7.13 Procedure of the HIC alignment used for the ALICE ITS2 outer tracker	128
7.14 Manual alignment of the HIC onto the alumina substrate	128
7.15 Assembled ceramic i-M μ CS	129

List of Figures

7.16 Flatness of the ceramic i-M μ CS used for the gluing of the HIC	129
7.17 Ceramic i-M μ CS for hydraulic and thermal tests	131
7.18 The module array connected to the hydraulic and thermal test set-up	132
7.19 Set-up configuration for the hydraulic and thermal tests	132
7.20 Cross-section of the investigated channel circuit inside the alumina module.	133
7.21 Modular SS samples for the pressure drop interconnection characterisation	134
7.22 Results of the pressure drops for the stainless steel samples	135
7.23 Results of the pressure drops for the alumina samples	136
7.24 Analytical estimate of the local heat transfer coefficient	137
7.25 Temperature increase along the channel circuit length	138
7.26 Interconnection effect for the configuration "1 Direction"	139
7.27 Interconnection effect for the configuration "2 Directions"	140
7.28 Thermal analysis of the alumina cooling substrate	141
7.29 Experimental evaluation of the TFM for the alumina samples	142
A.1 The CERN accelerator complex	173
A.2 Slice of the CMS experiment	174
A.3 A cutaway view of the CMS experiment	174
A.4 The coordinate system with the CMS cylindrical detector	175
A.5 Upgrade plans of the LHC and its experiments	175
B.1 Layout of the two interconnected microfluidic sub-circuits	178
B.2 The fluid domain of the CFD simulation	180
B.3 CFD results of the baseline geometry	181
B.4 Design of the new manifold according to the 23021 NACA profile	182
B.5 CFD results of the optimised geometry	182
B.6 Pressure losses in the inlet manifolds	183
B.7 CAD design of the sample for the test	184
B.8 Main steps of the process-flow for the production of the samples	185
B.9 Silicon wafer with embedded the microchannel circuits	185
B.10 Details of the samples with the two circuit geometries	186
B.11 Nomenclature of the circuit elements	186
B.12 Interface between the connector and the Si frame sample	187
B.13 Assembly details of the 3D printed connector and the Si sample	187
B.14 Set-up for the flow distribution inspection	188
B.15 Inspection of the flow distribution inside the manifolds	188
B.16 Details of the connector assembled with the dummy frame	189
B.17 Results of the pressure drop test for the connectors	189
B.18 Circuit sample assembled with the connector	190
B.19 Results of the pressure drop test for the two different circuits	190
B.20 Pressure drop estimation of the different circuit elements	193
B.21 Estimation of the pressure drop in the manifolds	193
B.22 Comparison between the CFD analysis and the test campaign	194

C.1	Set-up for the pressure test	197
C.2	CERN EP-DT set-up for the burst pressure test of silicon device	198
C.3	Set-up for the flow distribution inspection	198
C.4	Set-up for the He leak rate test	199
C.5	Set-up for the hydraulic and thermal tests	200
C.6	Schematic representation of the hydraulic set-up	200
E.1	Drawing of the polymeric pin-based samples	208
E.2	Drawing of the seal fitting	209
E.3	Drawing of the pin-based ceramic sample type 4	210
E.4	Drawing of the 30x60 mm ² pin-based ceramic module	211
E.5	Drawing of the 30x60 mm ² pin-based ceramic module	212
E.6	Drawing of the auxiliary PEEK substrate for the CFRP i-M μ CS solution	213

List of Figures

List of Tables

2.1	Material budget comparision	13
2.2	Thermal figure of merits in silicon tracking detectors	36
2.3	Expected cooling arrangement of the four LHC experiments after LS3	36
3.1	Operating parameters of two present silicon tracking systems	38
3.2	Operating parameters of future silicon tracking systems	38
4.1	Summary of Si wafer labelling.	49
4.2	FS laser parameters for DOE	49
5.1	Design parameters of the hydraulic interface	72
5.2	Types of micro O-ring	75
6.1	Comparison of the ceramics with the silicon material	90
6.2	Summary of the ceramic samples	94
6.3	Summary of surface 3D scan feature measurement	99
6.4	Summary of the roughness and flatness measurements	99
6.5	Summary of the channel roughness measurements	100
6.6	Summary of the helium leak test	101
7.1	Estimate of the thermal figure of merit with different materials	142
B.1	Parameters to estimate the pressure drops of the circuit elements	192
C.1	Error uncertainties of the instruments and TFM propagation	201
D.1	Summary of large ceramic substrate flatness	205

List of Tables

Acronyms

- 2-PACL** Two-Phase Accumulator Controlled Loop. [2.2](#)
- ALARA** As Low As Reasonably Achievable. [2.1](#)
- ALICE** A Large Ion Collider Experiment. [2.0–2.3](#), [7.1–7.4](#), [A.3](#), [B.2](#), [C.5](#), [D.1](#)
- ALICE 3** A Large Ion Collider Experiment 3. [7.1](#), [7.5](#)
- AlN** Aluminium Nitride. [2.3](#), [6.2](#)
- ALPIDE** ALice PxlEL DEtector. [2.1](#), [7.1](#), [7.2](#), [7.4](#), [7.5](#)
- AM** Additive Manufacturing. [1.0](#), [1.2](#), [5.1](#), [5.2](#), [6.3](#), [7.1](#), [7.2](#)
- AMS-02** Alpha Magnetic Spectrometer. [2.2](#)
- ATLAS** A Toroidal LHC ApparatuS. [2.0–2.2](#), [7.3](#), [A.3](#)
- BHF** Buffered Hydrofluoric Acid. [4.4](#)
- BMC** Bulk Moulding Compound. [7.2](#)
- CCS** Carbon Cooling Substrate. [2.2](#), [2.3](#), [7.2](#), [7.4](#)
- CERN** European Organization for Nuclear Research. [1.0](#), [2.0](#)
- CFD** Computational Fluid Dynamics. [3.4](#), [B.3–B.5](#), [B.7](#), [B.9](#)
- CFRP** Carbon Fiber Reinforced Polymer. [2.2](#), [2.3](#), [7.1–7.3](#), [7.5](#)
- CIM** Ceramic Injection Moulding. [7.2](#)
- CMi** Center of Micro-Nanofabrication. [2.3](#), [4.2](#), [4.4](#)
- CMM** Coordinate Measuring Machine. [5.2](#)
- CMOS** Complementary Metal-Oxide Semiconductor. [2.1](#), [2.3](#)
- CMP** Chemical Mechanical Polishing. [4.4](#)
- CMS** Compact Muon Solenoid. [2.0–2.2](#), [7.3](#), [A.3](#)
- CNC** Computerized Numerical Control. [5.4](#), [6.4](#), [7.1](#), [7.4](#)
- CS** Cross-section diameter. [5.2](#)
- CTE** Coefficient Of Thermal Expansion. [1.1](#), [2.3](#), [3.2](#), [5.2](#), [6.1](#), [6.2](#), [7.2](#), [7.4](#)
- DAQ** Data AcQuisition system. [7.4](#), [C.5](#)
- DLP** Digital Light Processing. [6.2](#)
- DOE** Design Of Experiments. [4.2](#), [4.3](#)
- DRIE** Deep Reactive-ion Etching. [4.1](#), [4.2](#), [4.5](#), [4.8](#), [B.6](#)
- ECFA** European Committee for Future Accelerators. [1.0](#), [3.1](#)
- EP** Experimental Physics department. [1.0](#), [3.1](#)
- EPFL** École polytechnique fédérale de Lausanne. [2.3](#), [4.2](#), [B.5](#)
- FCs** Fluorocarbons. [2.2](#)
- FEA** Finite Element Analysis. [5.2](#), [5.5](#)
- FEM** Finite Element Model. [5.5](#)
- FPC** Flexible Printed Circuit. [7.2](#), [7.4](#)
- FS** Full Scale. [4.1](#), [4.2](#), [4.6](#), [4.8](#), [7.5](#), [B.8](#), [C.1](#), [C.5](#)
- GTK** GigaTracKer. [2.2](#), [2.3](#)
- GWP** Global Warming potentials. [2.2](#)
- HAZ** Heat Affected Zone. [4.1](#)
- HEP** High Energy Physics. [1.0–1.2](#), [2.1–2.3](#), [3.0](#), [4.0](#), [4.8](#), [5.1](#), [5.2](#), [6.0–6.3](#), [7.1](#), [7.2](#), [7.4](#), [8.0](#)
- HFT** Heavy Flavor Tracker. [2.1](#)
- HIC** Hybrid Integrated Circuit. [7.2–7.4](#)

Acronyms

HNBR Hydrogenated Nitrile. 5.4	OHP Oscillating heat pipe. 2.3
i-MμCS interlocking Modular microfluidic Cooling Substrate. 1.0 , 3.3 , 5.2 , 7.0–7.5 , 8.0 , 8.2 , D.1	PDMS Polydimethylsiloxane. 2.3
IBL Insertable B-layer. 2.2	PEEK Polyetheretherketone. 0.0 , 5.4 , 5.5 , 7.2 , E.0
ID Inner Diameter. 5.2	PI Polyimide. 2.3
IP Interaction Point. 2.1	PVD Physical Vapour deposition. 4.4
IPA Isopropyl Alcohol. 2.3	PXL PiXeL detector. 2.1
ISS International Space Station. 2.2	QVP Mitutoyo Quick Vision Probe. 7.4
ITS2 Inner Tracking System 2. 2.1–2.3 , 7.1–7.4 , B.2 , D.1	RHIC Relativistic Heavy Ion Collider. 2.1
ITS3 Inner Tracking System 3. D.1	RIE Reactive-ion Etching. 4.6
LCM Lithography-based Ceramic Manufacturing. 6.2–6.4 , 7.2 , 7.4 , D.2	SEE Single Event Effect. 2.1
LHC Large Hadron Collider. 1.0 , 2.0–2.2 , 7.3 , A.3	SEM Scanning Electron Microscope. 4.4
LHCb Large Hadron Collider beauty. 2.0–2.3 , A.3	SLA Stereolithography Apparatus. 4.7 , B.6
LIPSS Laser Induced Periodic Surface Structures. 4.3	SOI Silicon On Insulator. 2.3
LOC Lab-on-a-chip. 2.3	SPD Silicon Pixel Detector. 2.2
LS3 Long Shutdown 3. 2.1 , 2.2	SS Stainless Steel. 7.4
MAPS Monolithic Active Pixel Sensors. 2.1 , 7.1	TFM Thermal Figure of Merit. 7.4 , C.5
MB Material Budget. 2.1 , 2.2 , 3.1 , 7.2	TID Total Ionising Dose. 2.1 , 3.1 , 3.2
NBR Nitrile Butadiene Rubber. 5.3 , 5.4	TIM Thermal Interface Material. 2.2 , 3.2 , 7.3 , 7.5
NI National Instruments corp. 7.4 , C.5	TTV Total Thickness Variation. 4.2
NIEL Non-ionising Energy Loss. 2.1 , 3.1 , 3.2	VeLo Vertex Locator. 2.2 , 2.3
NPJ Nanoparticle Jetting technology TM . 6.2–6.4 , 7.2 , D.2	μCS Microchannel Cooling Substrate. 2.2 , 2.3 , 3.4 , 4.1 , 4.8 , 5.2 , 7.2 , B.9

1 Introduction

This thesis aims to lay the foundation for a category of novel cooling substrates denoted hereafter as *interlocking Modular microfluidic Cooling Substrate* (i-M μ CS) and exploiting the use of ceramic Additive Manufacturing (AM) as a new material and technology for High Energy Physics (HEP) applications.

A silicon tracking detector reveals the paths of electrically charged particles as they pass through and interact with its silicon-based semiconductor sensors. In HEP experiments, silicon sensors are the core components of the experimental apparatus and are typically arranged into several coaxial cylindrical layers placed around the interaction point of the colliding beam or placed in planar layers crossing the colliding beam.

The thermal management of silicon sensors and the requirement for a lightweight mechanics represent major challenges, where the reduction of the material in the detection area is of particular importance for improving the overall detector resolution. Indeed, ultra-thin silicon sensors (50-100 μ m thick) are kept in position and cooled by minimum-material (low-mass) cooling substrates.

The Experimental Physics (EP) department at the European Organization for Nuclear Research (CERN) and the European Committee for Future Accelerators (ECFA) have drawn a roadmap for the R&D on future detector experimental technologies [1–4]. Future Si tracking detectors for HEP experiments in hadron particle accelerators will have to operate in a high radiation level environment, up to ≈ 300 MGy, over an expected lifetime of ~ 10 years, with detection layer areas that can reach tens of m^2 . High radiation levels will require efficient active cooling to extend the lifetime of the sensors. Future lepton colliders will produce considerably lower levels of radiation, therefore relaxing the design requirements for the cooling substrate.

In both cases, a scalable modular concept is required to cover large detection areas, which would allow access to industrialised series production. This is one of the most important parameters guiding the development of new cooling solutions.

In the framework of the recent upgrade programs (2019-2021) for the Large Hadron Collider

(LHC)[5] at CERN, two main categories of low-mass cooling substrates emerged, the carbon cooling substrate and the silicon microchannel cooling substrate. While the first allows the gluing of several sensors (O[100]) on a single substrate, the second one permits the cooling of smaller sensor arrays. The drawback of the first solution is the impossibility of reworking or replacing a single sensor. In contrast, the second approach is challenged by connectivity complexity among substrates, required to cover a large detection area.

Today, modularity at the sensor level is only achieved in silicon detectors that do not require extremely low-mass cooling substrates. In these cases, the sensors and their readout electronics are glued to a high thermal carbon plate that is then mounted in thermal contact with a large cooling plate where long metal pipelines guarantee the coolant flow along the detector. A thermal interface material, to guarantee a minimum thermal contact resistance, is placed in-between the sensor substrate and the cooling plate, when re-workability is required. However, thermal interfaces translate to a high thermal gradient (often greater than 20 °C) between the heat sink (the coolant) and the heat source (the sensors and their electronics). In addition, some sensor modules often manifest higher thermal resistance due to improper thermal interface application or deterioration.

An alternative approach is proposed in this thesis. A module is constituted by the sensor and its readout electronics glued directly on a cooling substrate with a dedicated integrated cooling circuit, whose dimensions are limited to the defined sensor module size. The challenge is therefore moved from the thermal re-workable interface between modules and the large-size cold plate, with its unique long cooling line, to the mechanical and hydraulic interconnection between modules equipped with its integrated small-size cold plate. In this way, thermal interfaces are minimised as well as materials near the sensors, while efficient and reliable mechanical and hydraulic interfaces become the key design features for the new modular microfluidic cooling substrate solution.

1.1 Research approach

The research started with looking into the microfluidic cooling substrates today implemented in HEP experiments, which are mainly based on microchannel etched into a silicon wafer, closed by a bonded silicon top cover. Limits for this technology were identified in dimensional constraints, defined by commercial wafer sizes, in the delicate process involved in the production and its high cost, and in the complexity of the interconnection across different modules, when large surface coverage is required. In order to address the process complexity and the high cost of the standard photolithography and etching steps, an alternative production process, based on femtosecond laser engraving, was then investigated.

Once the study of silicon microfluidic cooling substrates was considered to have reached a satisfying level, the research moved to design the re-workable interlocking microfluidic interconnections with different manufacturing technology and material. A baseline interlocking interconnection and possible alternatives were tested and validated with polymer AM

samples.

Taking into account the broad range of possibilities opened up by 3D printing a cooling substrate, ceramics additive manufacturing was then considered as a possible solution for the novel modular microfluidic cooling substrates.

Ceramic materials have always attracted HEP experiments because of their Coefficient of Thermal Expansion (CTE) matching with silicon sensor one (2-6 ppm/K), high thermal conductivity (10-200 W/mK) and radiation hardness (up to 100 MGy). As new material and production process for HEP experiments, a deep analysis on the 3D printed ceramic microfluidic cooling substrates was performed, and the ceramic interlocking interconnection was validated.

Finally, some aspects of the implementation of modular microfluidic cooling substrates in silicon tracking detectors were explored.

1.2 Structure of the thesis

The structure of the thesis is the following:

Chapter 2 introduces the silicon tracking detector now used in HEP applications. It reviews their mechanics and thermal management with a subsequent review on the microfluidic cooling solutions applied and explored in HEP as of today.

Chapter 3 presents the future silicon detector requirements, explaining the further need to implement a modular concept. It introduces the proposed interlocking modular microfluidic concept and its advantages compared to the modular solutions applied in present detectors. Finally, it identifies the limits to overcome for implementing microfluidic modularity in current silicon microchannel cooling substrates and, in general, in microfluidic cooling solutions.

Chapter 4 covers the research performed on silicon microchannel cooling solutions. A novel production technique for Si microchannels, based on femtosecond laser engraving, is investigated and compared to the typical photolithography and etching processes, followed by a novel adhesive-based bonding technique to close the microchannels and connect them to the feed-line connectors.

Chapter 5 introduces the novel in-plane interlocking solution. Design optimisation and qualification of the mechanical and hydraulic interfaces are presented for polymer-based AM microfluidic samples. After that, alternative designs of the interlocking interconnection are investigated.

Chapter 6 introduces the interest and the main objective of producing ceramic AM cooling substrates for HEP applications. Subsequently, the selection criteria and the chosen 3D printing processes and materials are described. The produced ceramic samples, their metrology and inspection are then presented, followed by the validation of the ceramic interconnections.

Chapter 1. Introduction

Chapter 7 starts introducing how the interlocking interconnections can be implemented on different cooling substrates materials. While focusing on the 3D printed modular ceramic cooling substrates, some fundamental aspects of the modular microfluidic implementation into silicon tracking systems are investigated.

Chapter 8 concludes the thesis with a summary of the achieved results with an outlook on potential future developments.

2 State of the art

In this chapter, the state-of-the-art of mechanics and cooling of silicon tracking detectors is introduced with a focus on the Si tracking systems of the four main large experiments (ALICE [6], ATLAS [7], CMS [8] and LHCb [9]) present in the (LHC) at CERN. An introduction to High Energy Physics experiments is in Appendix A.

2.1 Principle of a silicon tracking detector in HEP

2.1.1 Silicon semiconductor-based sensor

In silicon semiconductor-based sensors, a reverse-biased p-n type junction is used as a sensing element. Particle interacting with the sensor volume ionises the silicon crystalline structure generating holes/electron pairs. These charges are then collected into the cathode and anode. In the sensor depleted volume, the collection is by the drift; in the un-depleted volume, the collection is by diffusion. The charge signal is then processed by local analogue and digital circuits.

In general, a silicon semiconductor-based detector allows for a readout speed of one order of magnitude higher than many other particles tracking detector technologies, such as cloud chambers or wire chambers. The silicon semiconductor-based structure can be arranged in a variety of ways, resulting in different sensor architectures with different position resolutions, energy ranges, readout frequencies, and other detector properties.

Micro-strip and pixel sensors

Silicon semiconductor-based sensors are classified based on the sensing element patterns into micro-strip and pixel sensors [10, 11].

Silicon micro-strip sensors consist of a sensing element with a 1-dimensional stripe pattern. Experiments achieve a two-dimensional resolution by using two single-sided sensors or

double-sided sensors with orthogonal strips or tilted, strips (Figure 2.1.a and b). Micro-strip sensors provide simple fabrication procedures for huge surface sensors. For a $N \times N$ resolution grid, the number of readout channels is limited to $2N$. Micro-strip sensors exhibit ghost hits in case of multiple particles hit at the same time.

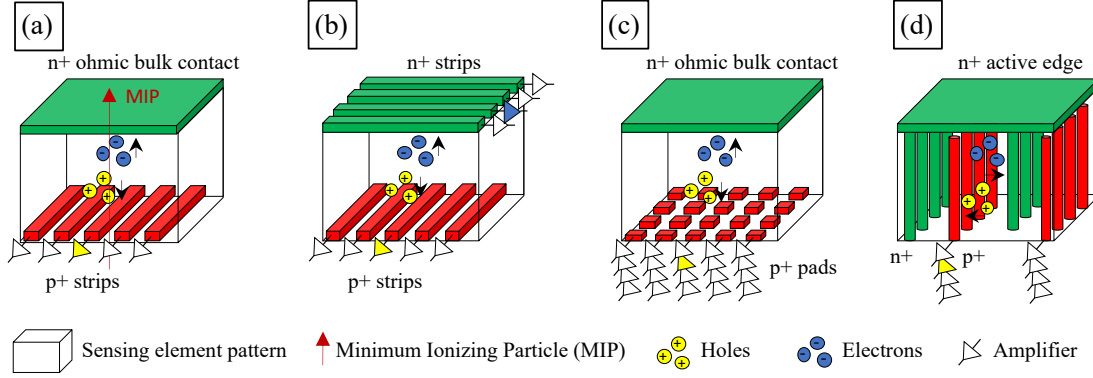


Figure 2.1: Micro-strip and pixel silicon sensors. Sketches of (a) single-sided micro-strip, (b) double-sided micro-strip, (c) planar and (c) 3D pixel silicon semiconductor-based sensors.

Pixel sensors combine the latest microfabrication processes with the extensive experience of commercial application makers. The sensing elements are arranged in densely packed two-dimensional arrays, hence the name pixel (Figure 2.1.c). Pixels are compact, high-precision single-sided detectors with no ghost effect. For a $N \times N$ resolution grid, the number of readout channels is N^2 . An alternative to the standard planar layout is a 3D-electrode structure where electrode columns extend perpendicularly through the substrate (Figure 2.1.d). The signal charge is independent of the electrode geometry; therefore, the 3D structure, reducing drift distance and charge collection time, provides higher radiation hardness.

Hybrid and monolithic pixel sensors

Depending on the sensor and readout circuit integration, silicon sensors can be either hybrid or monolithic.

In hybrid pixel sensors, a dedicated sensor grade silicon material is used to produce the sensor part. The readout chip, manufactured using standard Complementary Metal-Oxide Semiconductor (CMOS) processes, is separated and typically connected to the pixel sensor by flip-chip bump-bonding technology (Figure 2.2.a). This kind of sensor processing enables specific material and procedure optimization. On the other side, the chip bonding process and the production of the needed bumps raise the price of hybrid pixel sensors dramatically. Moreover, the hybrid configuration puts additional material into the detecting volume, lowering the position resolution.

Monolithic pixel sensors combine the sensor and CMOS readout circuits in a single silicon wafer (Figure 2.2.b). They are attractive candidates due to the possibility of achieving large

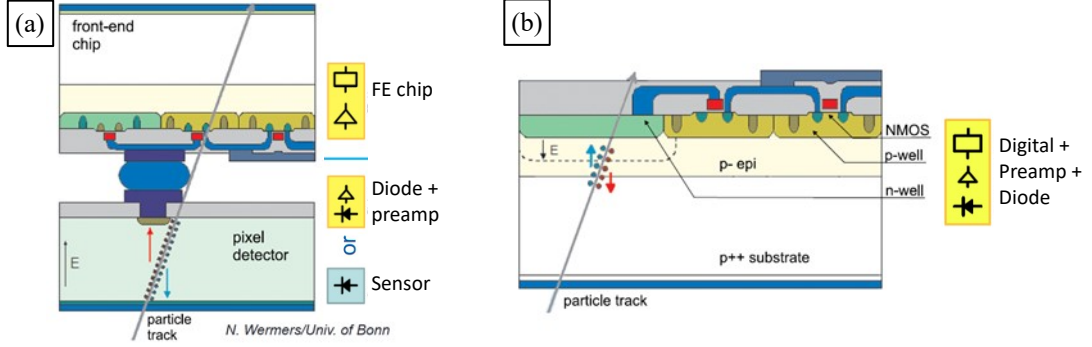


Figure 2.2: Hybrid and monolithic active pixel sensors. Sketches of (a) a hybrid pixel sensor cross-section and (b) a MAPS sensor cross-section. Picture adapted from [12]

signal-to-noise ratios, integrating advanced in-pixel signal processing circuitry and the availability of cost-efficient large-scale production [13–15]. A matrix of sensing elements and the related readout circuitry make up monolithic pixel detectors. Monolithic sensors, unlike hybrid pixel detectors, incorporate these elements on a single substrate (Figure 2.2.b). This avoids the costly bump-bonding step and decreases noise, resulting in a more reliable sensor. Among all possible flavours of monolithic pixel sensors used in Si tracking systems, the Monolithic Active Pixel Sensors (MAPSs) are able to fully integrate complex CMOS circuitry on a high resistivity Si epitaxial layer. Despite significant advancements in terms of radiation hardness, however, hybrid pixel sensors still provide better performances in harsh radiation environments.

The PiXeL detector (PXL) for the Heavy Flavor Tracker (HFT) of the STAR experiment at the Relativistic Heavy Ion Collider (RHIC) was the first tracking system that adopted a MAPS sensor, called ULTIMATE sensor [16–18]. Concerning the LHC experiments, the ALICE detector, which operates in a moderate radiation environment, has recently installed ALICE Pixel DEtector (ALPIDE [19]) MAPS sensor in its novel tracking system, named ALICE Inner Tracking System 2 (ITS2). This represents the first large-scale application based on MAPS sensors. On the contrary, hybrid silicon sensors have been selected for the recent upgrades of the ATLAS, CMS and LHCb, which operate at higher radiation doses [20–22].

2.1.2 Layouts of a silicon tracking detector

In medium-large silicon tracking detectors for collision experiments, thousands of "*sensing modules*", made of one or more silicon sensors and their readout circuitry, are installed around the interaction point (IP) of the two colliding beams. Several layout configurations are possible, and each experiment employs different naming conventions for the parts constituting the detector, depending on the position ("*inner*", "*outer*"), shape ("*barrel*", "*end-cap*", "*disk*", "*ring*") and type of sensors ("*strip*", "*pixel*"). However, it is possible to group them into the subcategories here below described.

According to the proximity of the silicon sensor layers to the IP, silicon tracking detectors can be divided into two main categories, "*trackers*" and "*vertex detectors*". Tracking the incident charged particles to measure particle momenta in the magnetic field of the experiment and reconstructing the decay vertices are, respectively, their essential scope in the overall experiment data analysis chain. It is to be noted that vertex and tracking nomenclatures correspond to the classical detector classification, where the vertex detector was constituted by silicon semiconductor-based sensors, while the tracker was typically a cloud chamber or a wire chamber detector. As of today, silicon sensors are gradually replacing other tracking systems in medium-large experiments.

The vertex detector is the innermost element of an experiment and constitutes its core (Figure 2.3). Typically, hybrid or monolithic pixel silicon sensors are preferred because of their high spatial resolution [23], and they are positioned as close as possible to the IP. The tracker typically encloses the vertex detector and its requirements, in terms of detector resolution, noise and radiation hardness, are typically less stringent compared to the vertex detector. Vertex detectors and trackers are typically made of a "*barrel*" and two "*end-caps*", one at each side.

The barrel arrangement consists of placing the sensors forming concentric "*cylindrical layers*" around the IP. While for the end-cap, the sensors are placed on "*planar layers*" crossed by the colliding beams. Cylindrical layers can be longitudinally segmented into sub-elements, typically called "*staves*". While a planar layer of an end-cap can be a single disk or split into concentric rings. Furthermore, the sensors inside a layer can be oriented to be normal to the particle trajectory or "*tilted*" at a given angle, to improve the resolution through the so-called "*Lorentz angle*" and allow for staggering of neighbouring elements, improving the hermeticity of the layer.

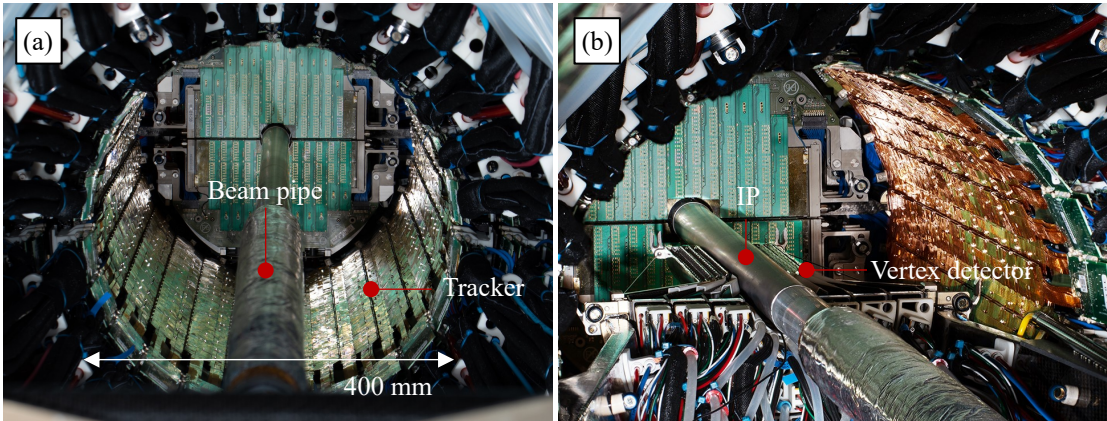


Figure 2.3: ALICE Inner tracking system 2 during installation. Picture (a) shows the tracker part of the new ALICE Inner Tracking System, while picture (b) shows the bottom part of the vertex tracker close to the beam pipe. The accelerated particles, close to the speed of light, collide in the Interaction Point (IP) inside the beam pipe. This detector was recently installed (May 2021).

2.1 Principle of a silicon tracking detector in HEP

In Figure 2.4, the tracking system layout of the CMS experiment [20] is shown as an example of possible different Si sensor arrangements. This is the new Si tracking system layout of CMS foreseen to be installed during the 2026-2028 upgrade, the Long Shut-Down 3 (LS3). In this case, the four barrels (green and yellow colours in Figure 2.4.a and .b) at 200 mm of distance from the IP, at (0,0) coordinate, can be considered as the vertex detector of the future CMS experiment.

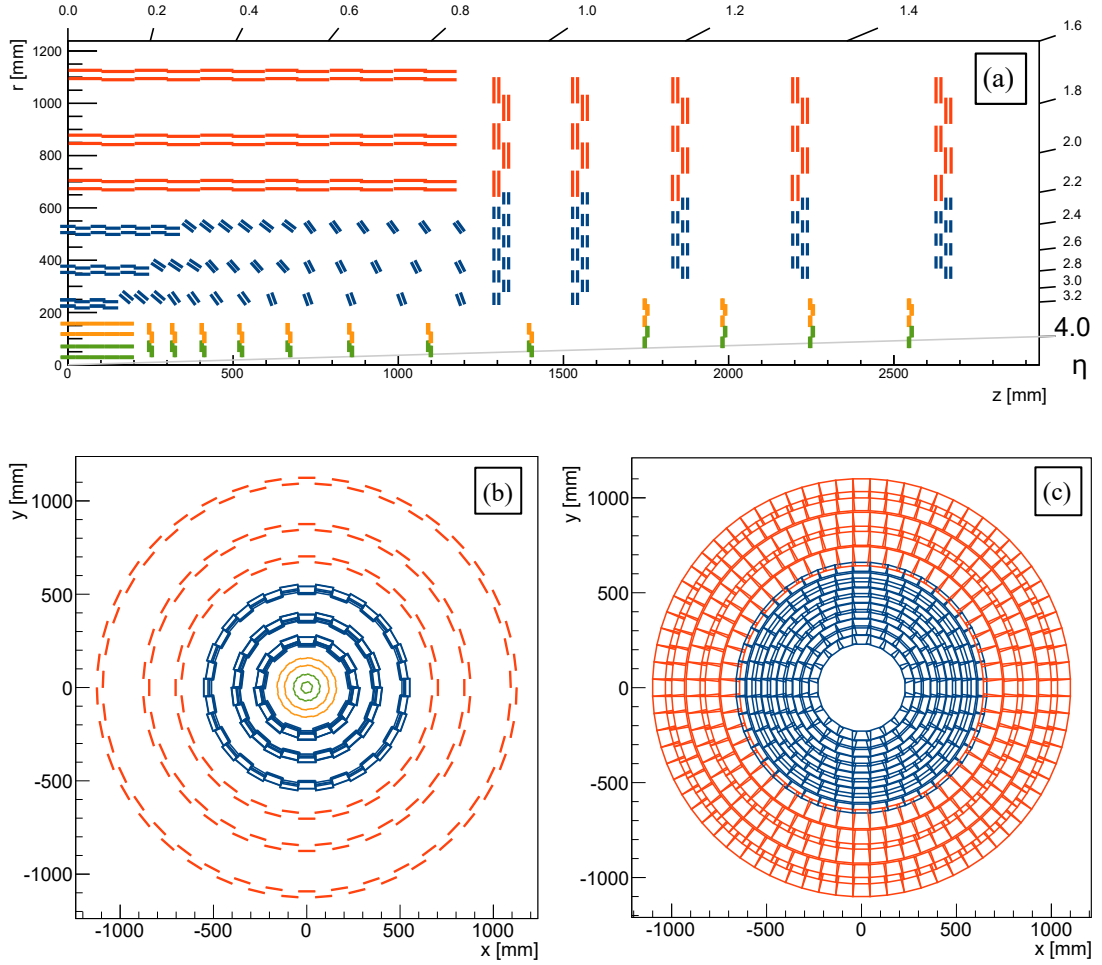


Figure 2.4: Tracking system layout of the CMS experiment. Picture (a) shows the r - z view of the tracking system, picture (b) represents the x - y section of the barrel layer for both vertex and tracker, while picture (c) is the projection of the tracker end-cap only. Information on the LHC coordinate system is in Appendix A. Pictures adapted from [24].

2.1.3 Radiation

Radiation damage

Radiation can induce damage in materials through two different mechanisms [25, 26]:

- The ionising radiation damage is due to particles having sufficient energy to ionize atoms. This is the case of high-energy charged particles or high-energy photons (gamma rays, X-rays). Such particles break molecular and crystalline bonds, which then can return to stable chemical configurations which are often different from the original ones. In silicon sensors, ionizing radiation is mainly responsible for the creation of localized defects than can contribute to the build-up of oxide charges. Such space-charge can especially affect gated devices, like MOS transistors.
- Non-ionising radiation damage is due to a displacement of crystal atoms by the interaction of hadrons (neutrons, protons, He nucleus, ions) with the nuclei of the lattice atoms. The recoil energy transferred by the incident particle is often sufficient to induce clustered damage to the lattice. Within the so-formed clusters, defects can interact with each other forming complex defects that can have multiple charge states and act as trapping sites, thus affecting both the extent of depletion areas and carrier lifetime.

Radiation effect on silicon sensors

The radiation effects on silicon sensors can be divided into Single Event Effects (SEEs) and cumulative effects [27, 28].

The SEEs are temporary effects mainly due to ionisation on the readout electronics. The most common SEEs are:

- Single Event Upset where the ionisation creates memory flip. A Triple Modular Redundancy in the memory is introduced to avoid data corruption.
- Single Event Transient, where an analogue transient pulse is formed. In this case, the readout is protected by design.
- Single Event Latch-Up, where unexpectedly high current locks a cell in a state. Also in this case, the readout electronics can be protected by layout (e.g. introducing isolation rings). Such event can be resolved by performing a readout power cycle.

The cumulative effects caused by the two types of radiation damage are quantified through the Total Ionising Dose (TID) for the ionizing radiation and Non-ionising Energy Loss (NIEL) for the non-ionising radiation. The Gray ($1 \text{ Gy} = 1 \text{ J/kg}$) is the SI unit of the TID, while NIEL is typically indicated in 1 MeV neutron equivalent fluence over the detector lifetime (or per year).

It is expressed in $\text{MeVn}_{\text{eq}}/\text{cm}^2(/yr)$. At the silicon diode level, three main NIEL cumulative effects can be identified:

- "*Leakage current increase*": The increase in leakage current causes an increase in noise in the amplifiers as well as an increase in dissipated power. Because the leakage current varies dramatically with temperature, cooling is a very effective way to limit the negative impacts.
- "*Effective space charge*": The effective space charge in undamaged sensors is made up of bulk doping (e.g., phosphorus or boron). Changes in the effective space charge caused by radiation cause a shift in the electric field distribution within the device, shifting the depletion voltage to lower or higher values. In the latter instance, larger voltages may be required to produce an electric field throughout the entire sensor volume in order to avoid under-depletion and, therefore, signal loss.
- "*Trapping*": Defect levels have the ability to capture (trap) charge carriers. If the charge carriers release (detrapping) time is longer than the system's collection time, or if the concentration of defects is very high, the overall signal of the sensor is reduced. For high fluence applications, trapping becomes a limiting factor. This issue can be mitigated by making device adjustments that result in faster collection times (i.e., device engineering). Due to the increased mobility of electrons and the ability of leveraging charge multiplication by impact ionization at lower fields and without device breakdown, the collection of electrons rather than holes at the detecting electrodes in segmented sensors can be advantageous.

While also ionizing particles can transfer enough energy to the material to induce the displacement of atoms, the amount of transferred energy is usually insufficient to produce localized defect clusters. Therefore, TID is generally overlooked in HEP experiments for what concerns silicon bulk material damage effect.

As of today, hybrid sensing modules can sustain higher radiation levels (10^{16} $1 \text{ MeV n}_{\text{eq}}/\text{cm}^2$ for Hybrid 3D pixel sensors [29]) than monolithic sensors. Hybrid pixel sensors have been selected for the recent upgrades of the innermost vertex layer of ATLAS, CMS and LHCb experiments which will be exposed to fluences greater than 10^{15} $1 \text{ MeV n}_{\text{eq}}/\text{cm}^2$ throughout their lifetime. Nevertheless, MAPS sensors demonstrated to correctly operate at high NIEL levels ($2 \cdot 10^{15}$ $1 \text{ MeV n}_{\text{eq}}/\text{cm}^2$ for the MALTA monolithic pixel sensor [30, 31]) and R&D is ongoing to improve their radiation hardness.

Radiation effect on mechanics and cooling

Radiation not only damages the sensors but also interacts with services and structural components. All the detector components must withstand the expected radiation level over the

lifetime detector without experiencing composition changes, chemical reactions, or physical damage:

- Radiation doses may alter the material's physical properties. For example, some polymers exhibit increased thermal conductivity after exposure to radiation [32]. While resins used for Carbon Fibre Reinforced Plastic (CFRP) experienced accelerated ageing degradation induced by radiation [33].
- The material's morphology, i.e. surface and crystallinity, can be altered. The yield and tensile strengths, abrasion resistance, and hardness can decrease, and porosity appears in the materials [34].
- High ionising radiation can cleavage one or several chemical bonds and, therefore, dissociate molecules (radiolysis). Compounds of radiolysis are very reactive and dangerous for the detector, infrastructures and personnel. Some refrigerants possess high hydrogen content with weak hydrogen chemical bonds. If the refrigerants are exposed to a high radiation level, highly explosive gasses can be created. Also, some formed compounds may recombine, forming acids corrosive to the channels that can bring piping leaks or cooling system obstruction. Usually, deionisation of the high-radiation resistance refrigerants is considered in the cooling system. These aspects are evaluated to qualify refrigerants, and cooling systems for HEP detectors [35].
- Substances derived from radiation damage can be deposited in the channels altering their thermal resistance.

High radiation hardness materials are preferred. Several technical reports on radiation damage and radiation compatibility were done on numerous engineering fluids and materials (cable insulating materials [36, 37], thermosetting and thermoplastic resins [38], composites [39] and adhesives [34]) used in HEP experiments[40]. At the same time, studies on new materials at higher radiation levels are continuously conducted in several facilities where beam tests are used to simulate radiation conditions (ionising and non-ionising radiations) present in the HEP experiment. Also, CERN provides safety instructions and regulations on using plastics and other non-metallic materials for fire safety and radiation resistance [41].

To conclude, during maintenance, the radiation to the personnel member is minimised following the safety principle of As Low As Reasonably Achievable (ALARA). The residual risk must be reduced as far as reasonably practicable. In virtue of minimising radiation to the personnel, three essential radiation protective measures are possible:

- Minimise the time of exposure
- Maximise the distance from the radioactive source
- Use shielding between the personnel and the radiation source.

2.1.4 Material budget

Any material introduced in the detection-sensitive zone interacts with the particles coming from the IP, causing multiple particles scattering that affects the detector's resolution. The material budget (MB) quantifies this effect, and it is so important that it drives the conceptual design of HEP particle detectors. Equation 2.1 quantifies the material budget:

$$MB = \frac{x}{X_0} 100[\%] \quad (2.1)$$

With x is the characteristic dimension of the considered material, i.e. the thickness particles traverse, and X_0 the material radiation length [42].

$$X_0 = \frac{716.4 A_n}{Z(Z+1) \ln \frac{287}{\sqrt{Z}}} \frac{1}{\rho} [cm]; \quad (2.2)$$

The radiation length of a material is the mean length (in cm) to reduce the energy of an electron by the factor $1/e$. The radiation length is also conventionally expressed in $[g\text{ cm}^{-2}]$. In this case, the density parameter is removed from Equation 2.2. X_0 Can be approximated by Equation 2.2. It depends on the atomic (Z) and mass (A_n) numbers as well as on the material volumetric mass density (ρ).

Close to the interaction point, where the maximum sensor resolution is the main target, lightweight materials having high X_0 and minimum thicknesses are adopted. Also, particular attention is paid to the type of refrigerant that can be activated by radiation and contributes to the MB. It is to be noted that two-phase and gas flows have a smaller MB contribution than liquid flows because of the low density of the gas/vapour (Table 2.1). In comparing different mechanics and cooling solutions, the total material budget for each detection layer is calculated by the contribution of each component (material) surrounding the layer, regardless of whether the material is on the front or backside of the sensor.

Table 2.1: Material budget comparison. The values of radiation length are taken from [43] and calculated from [42].

Material	$\rho [g\text{ cm}^{-3}]$	$X_0 [g\text{ cm}^{-2}]$	$X_0 [cm]$
Silicon	2.3	21.8	9.4
Aluminum (pure)	2.7	24	8.9
Copper (pure)	9	12.9	1.4
Polyimide (Kapton®)	1.4	40.6	28.6
Common carbon laminate	1.4 - 1.8	N.A.	25 - 30
Water (liquid, 20 °C, 1 atm)	1	36.1	36.1
CO ₂ ($T_{sat} = -25\text{ °C}$, liquid)	0.672	36.2	53.9
CO ₂ ($T_{sat} = -25\text{ °C}$, vapour)	0.0013	36.2	27846
CO ₂ ($T_{sat} = -25\text{ °C}$, vapour quality = 0.3)	0.0043	36.2	8419

2.2 Mechanics and thermal management

Materials selection in HEP particle detectors is driven not only by mechanical and thermal requirements but also by radiation resistance, material budget, and compliance with safety regulations. Due to the material budget requirements, the mechanical structures and cooling systems in HEP applications privilege the use of light mechanics structures based on Carbon Fiber Reinforced Polymer (CFRP) composite materials and non-standard cooling solutions.

An adequate thermal management strategy is required to operate silicon sensors over an extended period of time in radiation harsh environments. The increase of the depletion voltage and leakage current in sensors (along with the dissipated power), can eventually lead to thermal runaway, i.e. the non-linear self-heating of silicon sensors, which can render them inoperable. Leakage currents can be greatly reduced, and detector longevity can be increased by cooling the sensors to low temperatures below 0°C. The selected cooling strategy must guarantee the removal of the heat expected to be dissipated at the end of life of the sensor.

The cooling systems implemented in silicon tracking detectors are described below, followed by a review of the present cooling substrates and their mechanical support.

2.2.1 Cooling systems

The selection of the cooling system depends on the operating temperature range and dissipated heat flux which are strongly dependent on the sensor technology and expected particle rates.

Sensing modules, whether monolithic or hybrid, present a non-uniform power dissipation distribution mainly associated with different heat generated by the analogue and digital components of the readout electronics. For hybrid sensing modules operating at high readout frequency (>1 MHz) and in high radiation environments (>1 MGy integrated TID), heat fluxes at the readout circuitry can locally achieve $> 3 \text{ Wcm}^{-2}$, with an average power dissipation on the module that can reach $\sim 1 \text{ Wcm}^{-2}$.

The cooling systems maintain a fixed coolant temperature ranging from -40°C, for detectors operating in high radiation environments (TID ~ 10 MGy), to 30°C, for detectors operating in moderate radiation environments (TID ~ 0.01 MGy). The temperature gradient in a silicon sensor is typically kept within 10 °C or less, and the temperature difference in the overall detector (support structures and modules) must be minimised to reduce thermo-elastic deformations and stresses induced by the CTE mismatching of the different materials, that would impact the sensor positioning over time and, ultimately, could lead to detector failure.

A brief current status on gas, liquid and two-phase cooling systems in particle detectors is given below, followed by a review of the present cooling substrates and their mechanical support.

Gas cooling systems

Gas cooling systems are more transparent to radiation than all the other cooling systems. Gases, such as nitrogen, helium or air, have low mass, atomic number and, therefore, low radiation length. They are promising solutions for detectors operating at room temperature. Air cooling is indeed the chosen cooling system of the PiXeL sub-detector STAR detector [44, 45] that operates at 23 °C and must evacuate a moderate detector heat flux of 0.1 Wcm^{-2} (Figure 2.5).

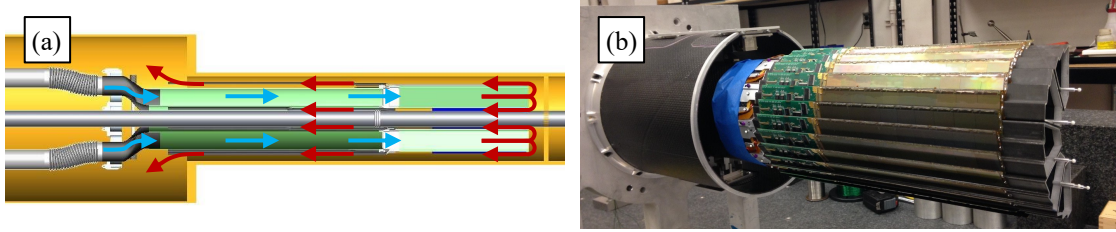


Figure 2.5: Air cooling system of the STAR silicon pixel detector. (a) Representation of the air-flow in the detector and (b) half PiXeL detector. Pictures adapted from [46].

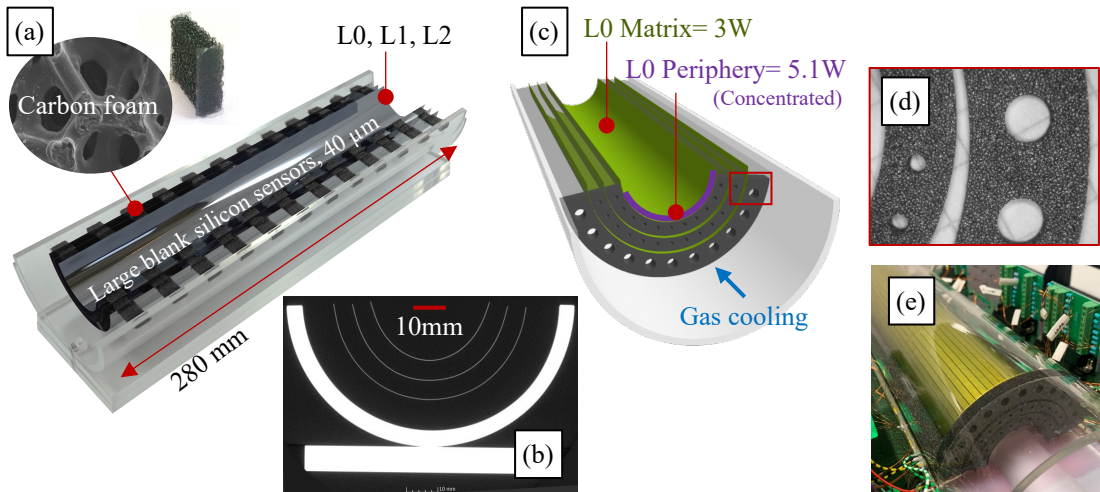


Figure 2.6: Air cooling system concept for the ALICE ITS3 prototypes.: (a) Half detector prototype with prime silicon sensors, (b) x-ray computed tomography of the three silicon half layers, (c) baseline design of the ITS3 prototypes with implemented half-ring radiators, (d) detail of the carbon foam radiators and (e) prototype with implemented heaters and half ring cooling radiators [3].

In addition, the ALICE experiment is developing a gas cooling strategy for the novel vertex detector (Inner Tracking System 3 [47]) consisting of curved wafer-scale ultra-thin MAPS silicon sensors (down to $50\text{-}30 \mu\text{m}$ thin) arranged in perfectly cylindrical layers, featuring an unprecedented low material budget of $0.05 \%X_0$ per layer. In this case, one single bent sensor (dimension up to $95 \times 280 \text{ mm}^2$) will cover an entire half-cylindrical layer. All the layers are going to be cooled by air (or nitrogen gas) flow at $15\text{-}20 \text{ }^\circ\text{C}$ (or $5 \text{ }^\circ\text{C}$). The average heat dissipation of these large sensors will be less than 50 mW/cm^2 , and the sensors should be kept

at 30-40 °C. This vertex detector is intended to be installed in the 2026-2028 upgrade phase.

However, the gas cooling system layout drives the detector's conceptual design; dynamic instability induced by cooling airflow can be propagated, affecting the sensors' position and, therefore, their resolution. Special care must be then taken for the flow distribution and the mechanics' integration.

It is to be noted that all the experiments at LHC integrate air ventilation in the underground cavern. For detectors operating at low temperatures (< 10 °C), air humidity tends to condense, leading to potential material corrosion and short circuits in the electronics. For this reason, nitrogen is continuously flushed at a low speed (less than 2 m/s) across some inner detectors.

Liquid cooling systems

Many detectors implement liquid cooling solutions. The main advantages of liquid cooling systems are the simplicity of realizing a reliable system and coping with particle detectors' low power dissipation. On the contrary, as seen in Section 2.1.4, liquid refrigerants usually bring to a higher average material budget contribution than gas or two-phase refrigerants. Among all the possible liquid refrigerants, demineralized/deionized water and fluorocarbons (FCs) are now implemented in the present detectors.

Demineralized/deionized water is now used in the new ALICE Inner Tracking System 2 (ITS2) for its vertex detector and tracker installed in May 2021 [48]. Radiation continuously ionizes water and any impurities present. As the ionized water is electrically conductive, it can destroy electronics and circuits in case of a leak. For this reason, purifiers and deionizing systems are implemented in the cooling system. In addition, demineralized/deionized water cooling systems are typically designed to cool the electronics in leak-less mode, i.e. maintaining the water pressure consistently lower than atmospheric pressure in the detector region. In this way, if a leak event appears, the water will not leak out, but instead, the air coming from the environment will be sucked into the circuit loop. Radiolysis of water must also be controlled to limit the production of O_2 and H_2 . Indeed, an alcohol-water mixture solution was considered for cooling the ATLAS inner detector [21] at a low temperature (-35°C), but the solution was not adopted because of the explosion risk of the H_2 produced by radiolysis.

Fluorocarbons (FCs), with C_xF_y as the general chemical formula, have good dielectric properties and high radiation resistances. The NA62 GigaTracKer (GTK) [49] and the tracker of CMS are now cooled with single-phase C_6F_{14} . However, fluorocarbons have high Global Warming potentials (GWPs), are expensive, and possess lower thermodynamic properties than water.

The concerns regarding GWPs and potential availability problems of fluorocarbons in the future, have motivated to consider other refrigerants like 3M Novec®-649 fluid [50]. This refrigerant has a much lower GWP and, at the same time, it is thermodynamically very similar to C_6F_{14} . Its characterisation in a high radiation environment is ongoing.

Two-phase cooling systems

Two-phase cooling usually yields higher heat transfer coefficients compared to single-phase systems. In addition, evaporative fluids maintain an (almost) constant temperature along the circuit that avoid an uneven temperature distribution of the silicon sensors when long distances must be covered by the cooling circuit.

Fluorocarbons' two-phase cooling systems are used in present detectors. Part of the present ATLAS vertex detector (ATLAS Inner Detector) uses evaporative C_3F_8 with a saturation temperature of -25°C [51], and the previous ALICE vertex detector (ALICE ITS Silicon Pixel Detector, SPD) used C_4F_{10} at ambient temperature [52].

However, as for the single-phase fluorocarbons, the high GWP concern is pushing the experiments to replace such refrigerants. In addition, the requirement of the sensor operating temperature is continuously going down and it raised more and more attention to evaporative CO_2 cooling systems [53, 54].

Compared to other two-phase refrigerants, the evaporative CO_2 has low density, low viscosity and high heat transfer capability that allow the use of small-diameter (down to 2-3 mm) and thin-walled pipes inside the detector region. The widely used two-phase CO_2 cooling system, based on a two-phase accumulator controlled loop (2-PACL) system [55], is now able to provide cooling at low temperatures in the range of -20°C and -45°C .

The 2-PACL system was firstly developed for the tracker of the Alpha Magnetic Spectrometer (AMS-02) at the International Space Station (ISS) [56] and for the LHCb Vertex Locator (VeLo) [9]. It is now adopted in the vertex detectors of the CMS (CMS Phase-1 Barrel Pixel Detector upgrade [57]) and the ATLAS (Insertable B-layer IBL [58]) experiments where the operative temperature of the evaporative CO_2 is set around -23°C and -35°C , respectively. Furthermore, two-phase CO_2 cooling systems are being implemented for the entirely new ATLAS [59–61] and CMS [20, 62, 63] silicon tracking detectors during the LS3 phase, as a demonstration of the effectiveness of such cooling solution for detectors operating at very low temperature.

A cooling circuit operating with the 2-PACL cooling system must be typically qualified up to 15 MPa. It corresponds to the maximum pressure (7 - 8 MPa) achieved by the circuit during the detector shut-off multiplied by a safety factor of ~ 2 . However, the maximum pressure during the detector operation does not achieve 2 MPa. In addition, the leak of CO_2 must be minimised. For this reason, each part of the cooling circuit is typically controlled by helium leak test, and the helium leak rate must be below 10^{-9} mbar l/s. Nevertheless, all the materials of the cooling circuit must be compatible with two-phase CO_2 .

The temperature limit of the current CO_2 2-PACL cooling system is -45°C . However, future detectors could require lower-temperature coolants. Among the candidates, the noble gas krypton (Kr) appears as an attractive alternative [64, 65]. Evaporative krypton can operate below -60°C and provide comparable thermal performance to evaporative CO_2 .

2.2.2 Cooling substrates and their support structures

A cooling substrate is required to fulfil operative requirements in HEP applications:

- It removes the heat dissipated by the sensing modules.
- It maintains the sensors at the correct temperature to minimize radiation damage.
- It keeps the sensors in position and stable over time.
- It has to minimise the impact on the detection resolution.

The sensing modules are thermally glued to the cooling substrates. Radiation hard glues, epoxy-based resin (e.g. Araldite 2011 [66]), are used. Radiation hard and thermal conductive epoxy-based glues are considered for more demanding applications. As example, the thermal conductive glue Loctite® Stycast 2850FT [67] is now selected for the new tracking system of the ATLAS experiment.

In the framework of the present upgrade programs for the LHC, several cooling substrates solutions have emerged that satisfy the specific requirements of material budget and cooling for each detector.

For tracking systems requiring extremely low passive material contribution ($MB < 1.5\% X_0$ for detection layer), two lightweight cooling substrate solutions were developed: the silicon Microchannels Cooling Substrate (Si μ CS) and the vascular Carbon Cooling Substrate (vascular CCS). They are both visible in Figure 2.7.

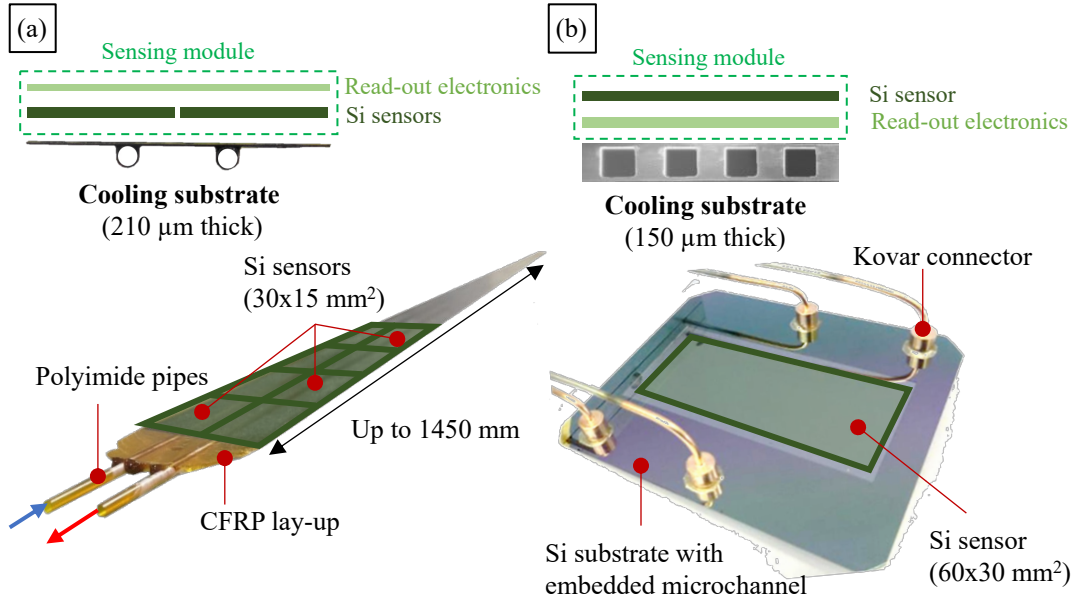


Figure 2.7: Example of HEP low-mass cooling substrates:(a) Vascular CCS solution of the ALICE ITS2 detector [68] and (b) Si μ CS solution chosen for NA62 GTK detector (prototype in the picture) [49].

The silicon μ CS is the most thermal efficient cooling substrate technology applied today in HEP detectors. It is now used in detectors that require the cooling of a limited number of silicon sensors (up to four). In this case, its limited size makes the substrate self-supporting. A review on μ CS is in the next Section 2.3.1.

A vascular CCS is based on a heat spreader made in Carbon Fibre Reinforced Plastic (CFRP) with embedded vascular cooling pipes. Thanks to the high thermal conductivity (k) of the carbon materials, the heat produced by the sensing modules is efficiently transferred to the refrigerant. Two different options have been developed and installed in LHC detectors:

- Cold plates made of CFRP laminates embedding polyimide capillaries [48, 69, 70].
- Cold plates made of high thermal conductivity CFRP and graphite-based material with metallic pipes for a high-pressure evaporative system [59, 62].

The CCS with polyimide capillaries (Figure 2.7.b) was developed for the ALICE tracking system and it will be implemented for the upgrade of several other detectors [71, 72]. It works with demineralised water at ambient temperature and in a leak-less mode (Section 2.2.1). R&D is ongoing to exploit the compatibility of such solution with more demanding refrigerants, i.e. evaporative CO₂. Instead, the CCS with metallic pipe option (titanium, stainless steel or copper-nickel) is well qualified to operate with evaporative CO₂, and it is being used for the upgrade of ATLAS and CMS vertex detectors.

The mechanical structures, supporting the sensing modules and their cooling substrates in position, are constituted by space frames or plates. In both cases, carbon materials are preferred for their stiffness-to-weight ratio; this minimises the material budget contribution. The space frame structures are made of carbon-roving filaments. While the plates are carbon laminates or sandwiches. A number of space frames or plates constitute a barrel or an end-cap detector (Section 2.1.2).

For the vertex detectors, the support structures are fully integrated with the cooling substrate and the sensing module forming a single element, typically referred to as the "*stave*". This is the case of the first layer of the present ATLAS vertex detector (ATLAS IBL, Figure 2.8) and the ALICE vertex detector (ALICE ITS2 inner barrel, Figure 2.9).

Similarly to the vertex detector, but on a larger scale, the vascular CCS solution is used in trackers that requires a minimum passive material contribution in the active detection area ($MB < 1.5\%X_0$ for detection layer). For the present ALICE tracker (ALICE ITS2 outer barrel, Figure 2.10), two vascular CCS, with embedded polyimide pipes, are glued on a single space frame structure. In this case, the stave (the sum of the two vascular CCSs, the space frame and several sensing modules), represents the main building block and the smallest replaceable component of the detector.

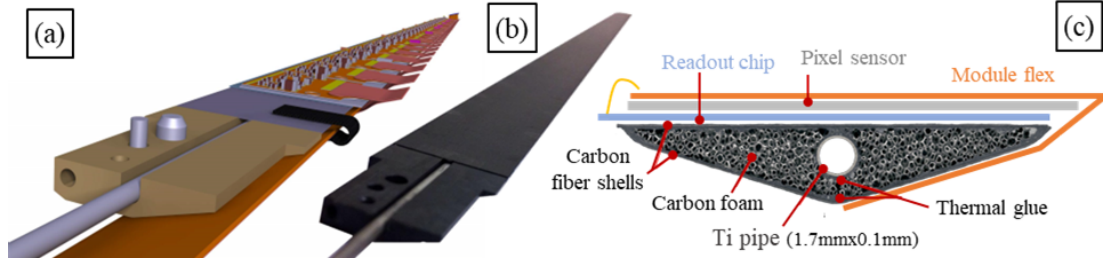


Figure 2.8: Vascular CCS used for the first layer of the present ATLAS vertex detector. (a) CAD model of the ATLAS IBL stave, (b) CVCS with embedded titanium pipe and (c) ATLAS IBL cross-section. The pictures are adapted from [58].

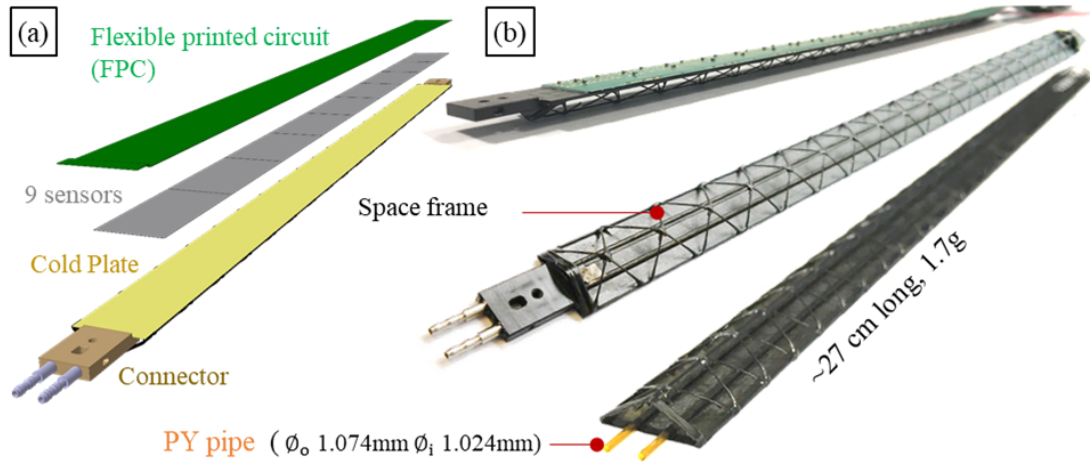


Figure 2.9: Vascular CCS used for the present vertex detector. (a) CAD exploded model of the ALICE ITS2 inner barrel stave and (b) space frame with the two glued CCS. The pictures are taken from [73].

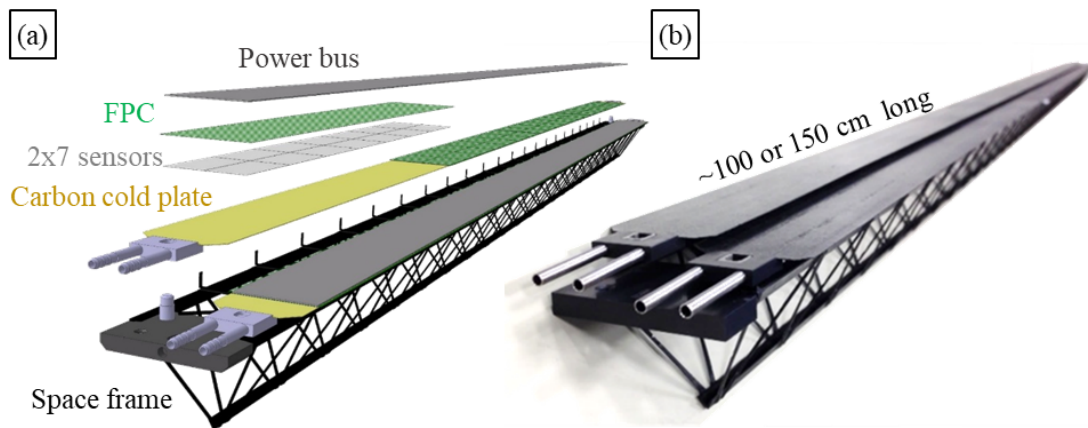


Figure 2.10: Vascular CCS used for the present ALICE tracker. (a) CAD exploded model of the ALICE ITS2 outer barrel stave and (b) space frame with the two glued CVCS. The pictures are taken from [73].

Instead, for tracking systems that do not have to satisfy a stringent material budget requirement ($MB > 2\%X_0$ for detection layer), a third cooling substrate category, where a single sensing module can be dismantled and replaced, was developed (Figure 2.11).

This category is denoted hereafter as re-workable Carbon Cooling Substrate (re-workable CCS). It represents the smallest modularity concept achieved as of today in silicon tracking systems and it is being used in the future ATLAS (Figure 2.13) and CMS trackers (Figure 2.12) foreseen for the LS3.

A re-workable CCS relies on cooling pipelines not integrated into the cooling substrate. In this case, the sensors and their readout electronics are glued to a high thermal conductive carbon plate that is then screwed and in thermal contact with a large cooling plate where a long titanium or stainless steel (SS) tube guarantees the coolant flow along the detector. To ensure a minimum thermal contact resistance, a Thermal Interface Material (TIM) is placed between the sensing module and the cooling plate, where re-workability is required.

At the moment, ATLAS and CMS are considering and qualifying different types of TIM:

- Thermal pastes: Arctic alumina TM [74], Ceramique TM 2 [75], Mx-4 thermal compound [76], MX-5 thermal compound [77].
- Thermal gap filler: Henkel Bergquist TGF 3500 LVO [78].
- Compressible pyrolytic graphite sheet (PGS): Panasonic graphiteTIM PGS [79].

If correctly applied, they can achieve a thermal contact resistance in the range $0.2\text{--}0.1\text{ }^{\circ}\text{K cm}^2/\text{W}$. The performance of the TIM depends on several factors (Section 3.2.1) and, like for the adhesives, TIMs are extensively tested to guarantee the proper working for the entire lifetime of the detector.

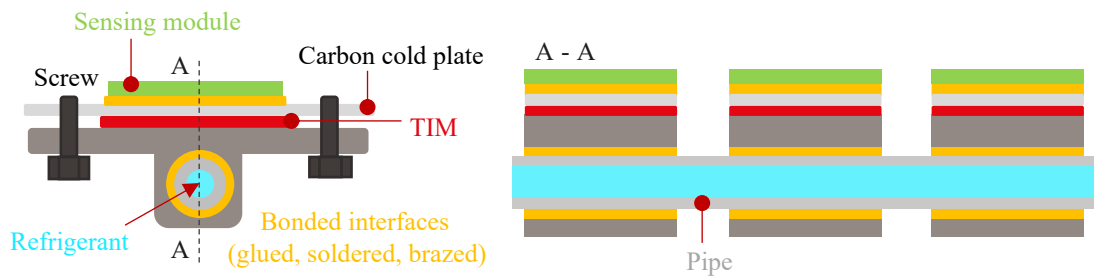


Figure 2.11: Schematic view of the re-workable CCS solution. Different bonded interfaces (dark yellow color) and the re-workable interface (red color), are posted between the cooling pipeline and the sensing module.

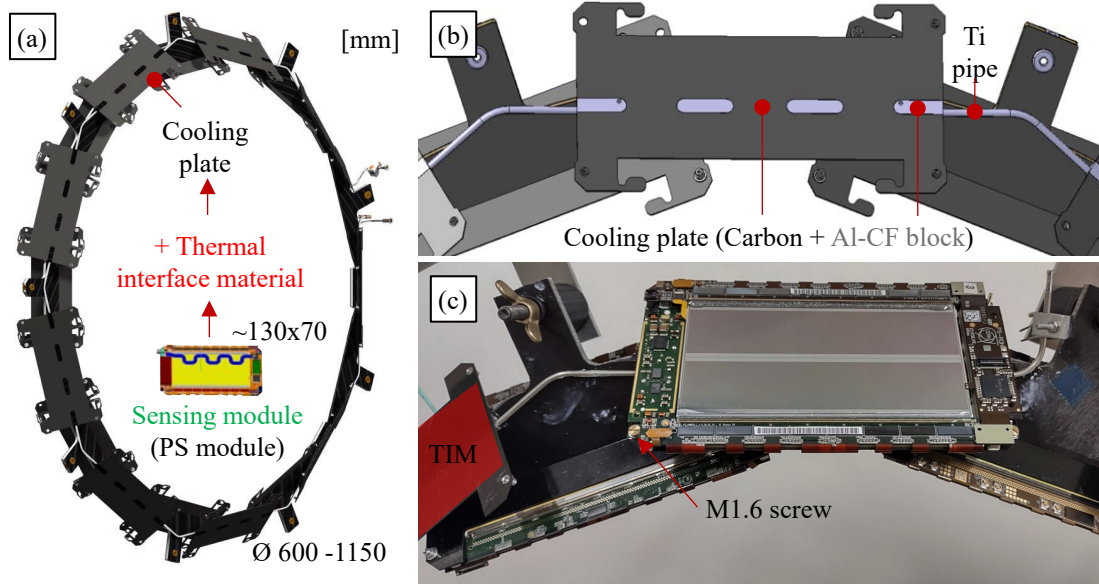


Figure 2.12: Re-workable CCS solution for the future CMS tracker. (a) CAD model and (b) detail of the ring, (c) detail of a sensing module assembled on the ring structure. The prototypes in the figure correspond to the prototypes of the future CMS Tilted Barrel Pixel and Strip (TBPS) ring. The pictures are taken from [80, 81].

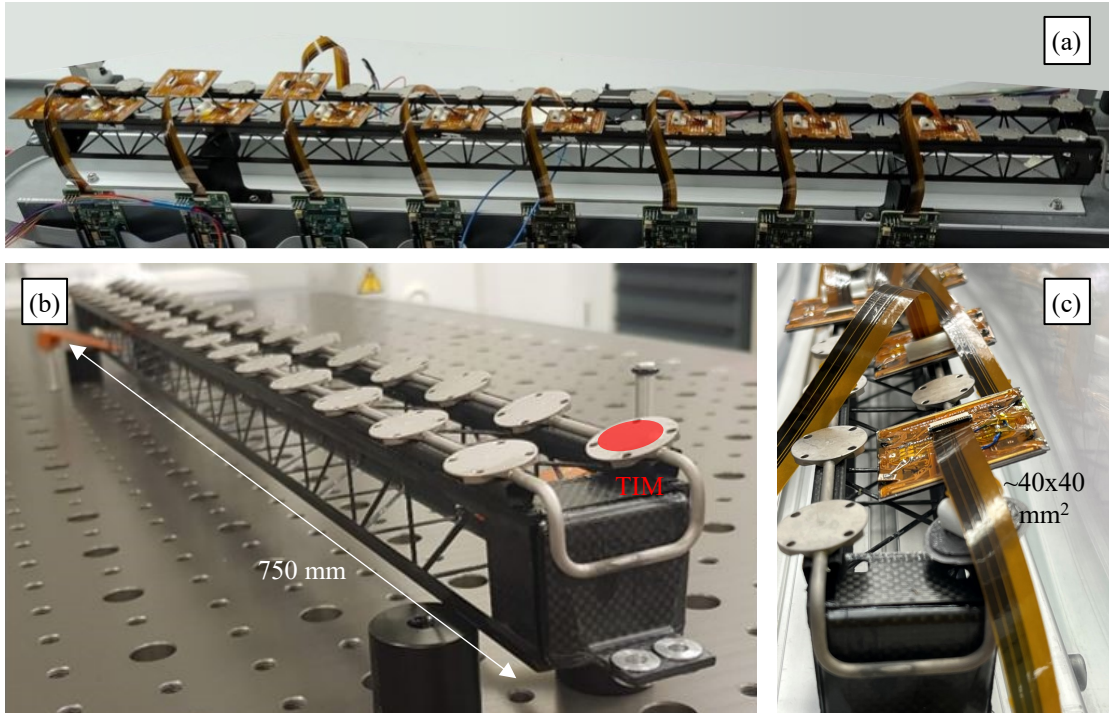


Figure 2.13: Re-workable CCS solution for the future ATLAS tracker. (a-b) Prototype of the space frame (named "longeron") integrated with metal pipeline and (c) detail with some sensing module prototypes and their CCS mounted on the space frame. The prototypes in the figure correspond to the prototypes of the centre area of the future ATLAS Inner Tracker (ITk) pixel outer barrel. The pictures are taken from [82].

2.3 Review of microchannel cooling substrate solutions

Microchannel cooling substrates, or microchannel heat sinks, were introduced for the first time by Tuckerman and Pease [83] in 1981. Narrow channels in a cooling substrate, increase the surface of heat exchange, while micro dimensions, i.e. small hydraulic diameter (<1 mm), increase the heat transfer coefficient, as the channel wall is closer to the bulk of the fluid. At the same time, the thin wall thickness of the channels minimizes the thermal resistance between the refrigerant and the electronic devices.

Tuckerman and Pease have demonstrated that electrical devices, dissipating up to 790 W/cm^2 , can be cooled by water in a laminar flow regime, pushing researchers on μCS and its implementation for different applications that require high thermal performance, from electronics (microchips and data centres [84–87]) to energy conversion systems (fuel cells and photovoltaic modules [88, 89]). High heat flux removal capability of the order of $0.1\text{--}1 \text{ kW/cm}^2$ is today achievable for μCS [90–92].

The μCS s can operate with single-phase and two-phase refrigerants [93, 94] and can be part of an active cooling system or work separately, acting as a thermal bridge (passive cooling system such as the heat pipes [95, 96]) between the heat sink (the primary active cooling system) and the heat source (the sensing modules). The mechanics of the heat transfer depends not only on the type of refrigerant, but also on μCS geometrical design [97]. Thinning of the thermal boundary layer, fluid mixing, increasing the fluid flow velocity gradient on the heated surface, rising pumping power, small channel width-to-depth ratio, microchannels with cavities, ribs, grooves or more sophisticated structures contribute to enhancing the heat transfer [98–100].

2.3.1 Silicon μCS in present HEP experiments

The μCS designs used today in HEP experiments consist of silicon cold plates with integrated multi-straight microchannels [101–103]. Beyond the high thermal performance and minimum dimension, the Coefficient of Thermal Expansion (CTE) of silicon perfectly matches with the CTEs of the silicon sensors and their front end chips. Two silicon tracking detectors, the NA62 GTK [104, 105] and the LHCb VeLo upgrade [22, 106] are today cooled with silicon (multi)-microchannel cooling substrate. A review of silicon μCS hydraulic connection to the feed-line is in Section 2.3.3.

NA62 GTK pioneered the Si μCS application in HEP; details are visible in Figure 2.14. It operates with single-phase C_6F_{14} , and the sensor ($60 \times 38 \text{ mm}^2$) is glued on top of the substrate. The silicon μCS is thinned down to $150 \mu\text{m}$ in the detection region; it keeps the pixel sensor at -10°C and removes 2 W/cm^2 of heat flux when the sensor operates.

As for the previous version, the new LHCb VeLo Upgrade detector is based on a two-phase CO_2 cooling system. The μCS has an elaborated geometry and larger dimension than the NA62 GTK; each silicon μCS cools four pixel sensors, two per side (Figure 2.15). The substrate

thickness is 500 μm , it keeps the sensors at -20°C , and a total heat of 13W can be removed.

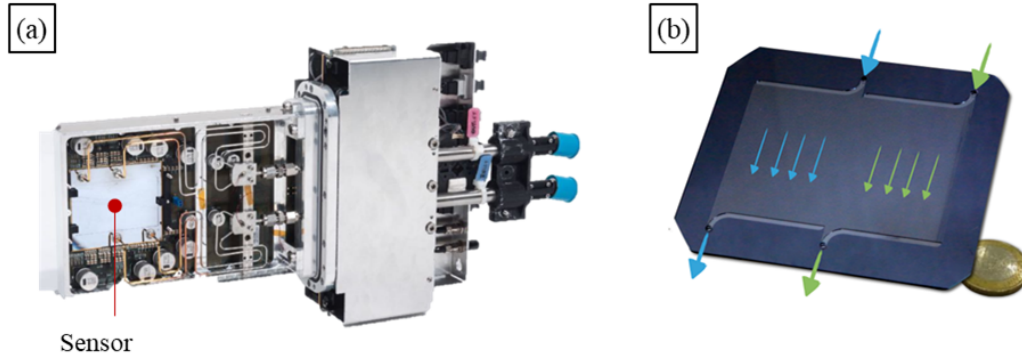


Figure 2.14: The NA62 GTK station. (a) Assembled GTK station and (b) the Si μCS (open) populated by 2 networks of 75 parallel microchannels 70 μm deep, 200 μm wide and separated by 200 μm thick walls. Pictures adapted from [107–109].

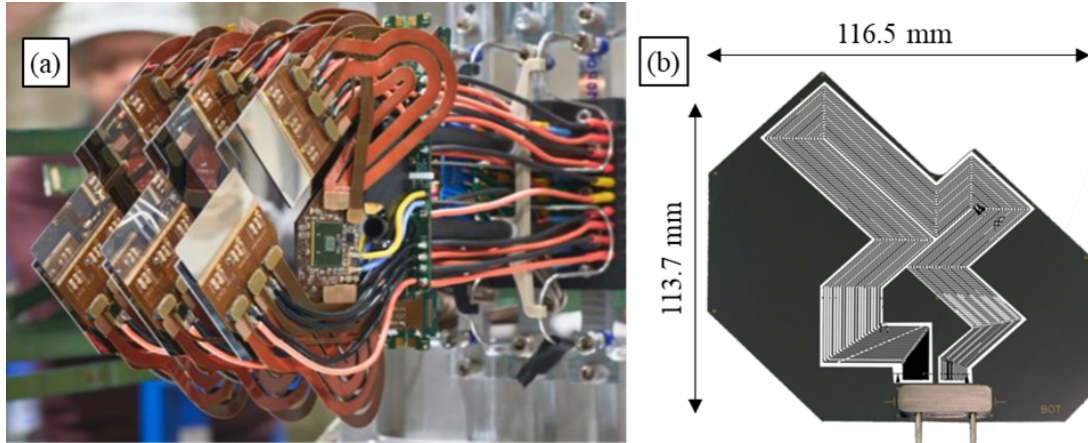


Figure 2.15: The LHCb VeLo module: (a) Three assembled VeLo modules in the test-beam and (b) the Si μCS is populated with serpentine of 19 channels 120 μm deep, 200 μm wide and with a pitch varying between 450 and 900 μm . In (b) the CAD drawing of the circuit is superimposed over the Si μCS . Picture adapted from [22, 106].

2.3.2 R&Ds on μCS for HEP experiments

Additional μCS solutions were investigated for the LHCb, ALICE [110, 111] and Belle II [112] experiments during R&D phase of their tracking systems, and further R&D on various μCS solutions are still ongoing in the particle detector community.

Proposals for LHCb VeLo Upgrade

Two other noteworthy μCS designs for the VeLo detector upgrade were studied during the previous detector developing phase (2011-2018). The first concept was based on a network of stainless-steel capillary pipes (500 μm inner diameter) brazed into aluminium nitride (AlN)

2.3 Review of microchannel cooling substrate solutions

cooling substrates, while the second concept consisted of a 3D printed cooling substrate in titanium grade 2 with integrated rectangular microchannels (down to $350 \times 350 \mu\text{m}^2$). They are shown in Figure 2.16.a and .b, respectively. Due to the well-advanced baseline design, i.e. silicon-based, the solutions were not adopted, but they remain valid candidates for future detectors.

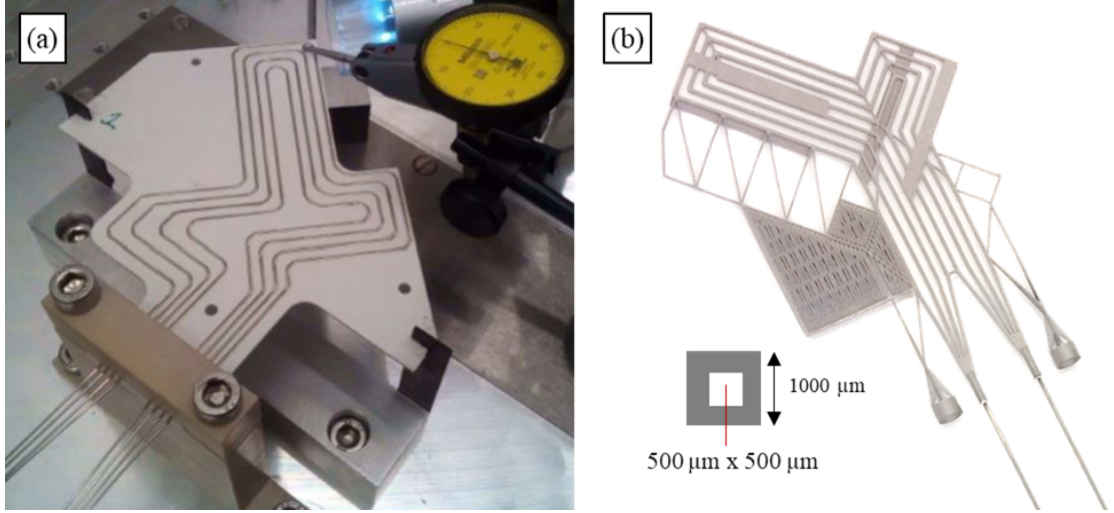


Figure 2.16: Alternatives μ CS solutions proposed for the present VeLo detector. (a) AlN cold plate with embedded stainless steel capillaries and (b) 3D printed titanium grade 2 cold plate [113–115].

Proposals for ALICE ITS2 Upgrade

Two additional μ CS options were proposed for the ALICE ITS2 during its development phase (2011-2016). The first option was based on polyimide (PI) microchannels [110] while the second option was based on interconnected silicon μ CS frames [111, 116, 117]. They are shown in Figure 2.17 and Figure 2.18, respectively.

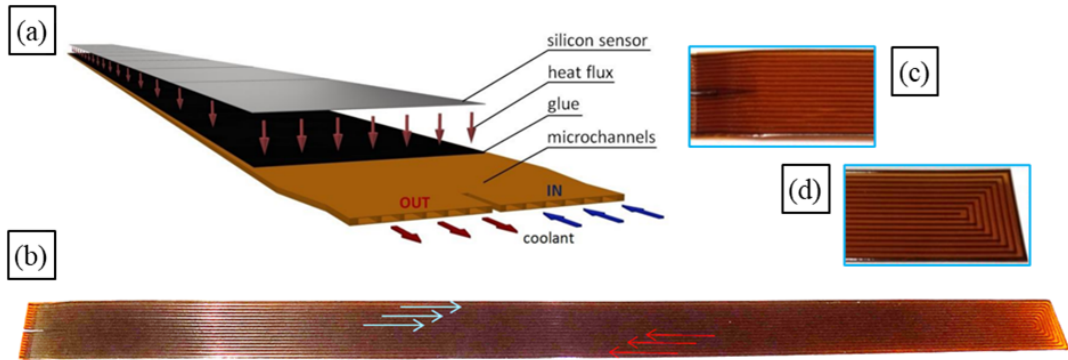


Figure 2.17: Prototype of the polyimide μ CS solution investigated for ALICE ITS2. (a) Sketch of the polyimide μ CS solution, (b) first prototype and (c-d) zooms of the inlet/outlet and the reverse flow zones. 16 microchannels were embedded on two polyimide films forming the multi-microchannel substrate. The picture is adapted from [110].

Chapter 2. State of the art

The polyimide pipe solution was planned to cool the full area ($15 \times 270 \text{ mm}^2$), dissipating 40 mW/cm^2 , with demineralized water at ambient temperature (below 30°C). Even if the solution was very promising from the material budget point of view (well below the requirement of $0.3\%X_0$), the microchannels ($0.8 \times 0.2 \text{ mm}^2$) couldn't work in leak-less mode and an important deformation (enlargement of the microchannels), under a pressure of 0.2 MPa , was noticed that could have impacted the stability and integrity of the glued sensors.

The silicon solution was designed to operate with evaporative Perfluorobutane (C_4F_{10}) at ambient temperature. Thermal tests demonstrated its ability to remove a heat flux of the order of 0.3 W/cm^2 while keeping the sensors below 30°C [116]. The frame design was intended to minimise the material contribution in the detection region. The coolant is supplied to the microchannels integrated into the silicon frame through a connector while a carbon fibre structure stiffens the assembly (Figure 2.18.a).

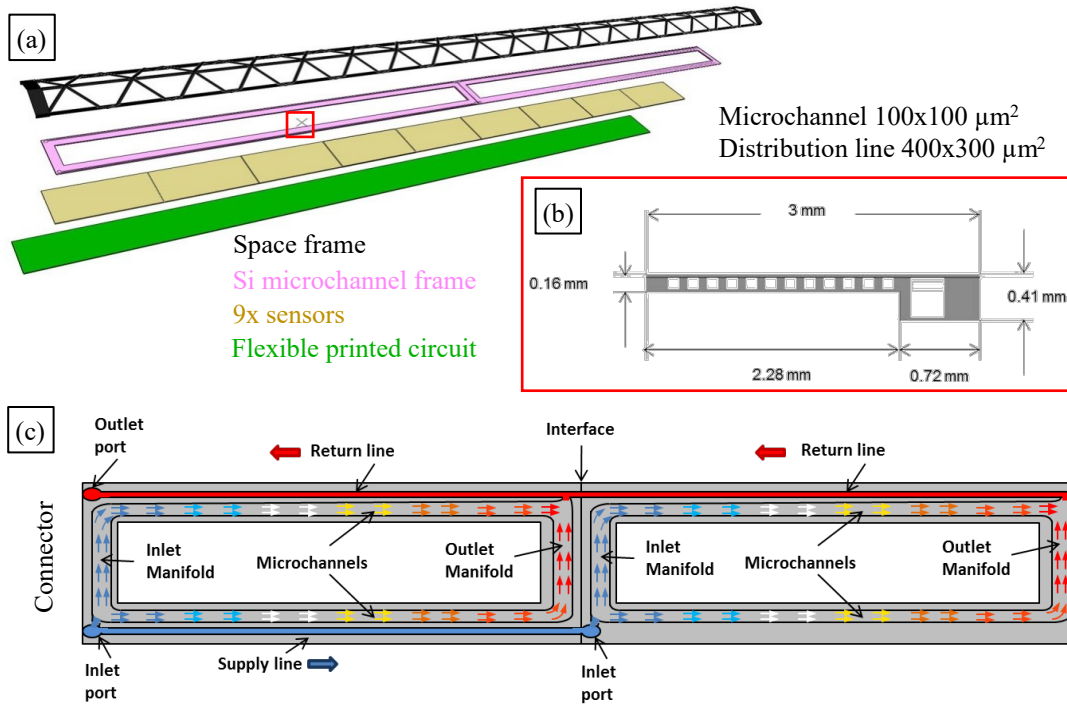


Figure 2.18: The silicon μCS solution proposed for the ALICE ITS2. (a) Exploded view of the silicon microchannel cooling frame solution, (b) cross-section and (c) schematic view of the two microfluidic sub-circuits interconnected in parallel. The picture is adapted from [116].

The cooling circuit was split into two sub-circuits to cover the 270 mm of length. The two silicon frames (135 mm in size) were fabricated on a single 6-inch wafer. The fluid distribution to the different microfluidic sub-circuits is obtained by introducing distribution lines (return and supply lines) which run in the frame thickness alongside each microchannel circuit (Figure 2.18.c). The distribution lines of the nearby frame were intended to be hydraulically interconnected. Additional information is in Appendix B.2, while details of the hydraulic

interconnection are in Section 2.3.3.

R&D on μ CS integrated into the silicon sensor

Microchannels can also be integrated into the substrate of the silicon sensor, providing higher thermal performance. Indeed, the temperature gradient between the sensor and the refrigerant is drastically reduced by removing all the possible thermal barriers (the thermal interface materials) and minimizing the wall thickness of the cooling substrate.

Microchannels can be integrated on a custom-made Silicon On Insulator (SOI) wafer before entering the standard semiconductor processing line or later, once the sensor is processed and diced. Both solutions were investigated and are being investigated.

The first solution was studied for the Belle II pixel detector [118] (Figure 2.19). Prototypes of the monolithic all-silicon ladder (i.e. the electronic module) with integrated microchannels were developed [112, 119]. These thermo-mechanical samples were equipped with deposited single-layer aluminium resistive circuits to simulate the heat load from the expected electronics. Thermal performance measurement with deionized water was conducted; they demonstrated that the temperature difference between the hottest sensor point and water can be kept below 2°K for a power density of 6 W/cm² and liquid flow of 1 l/h.

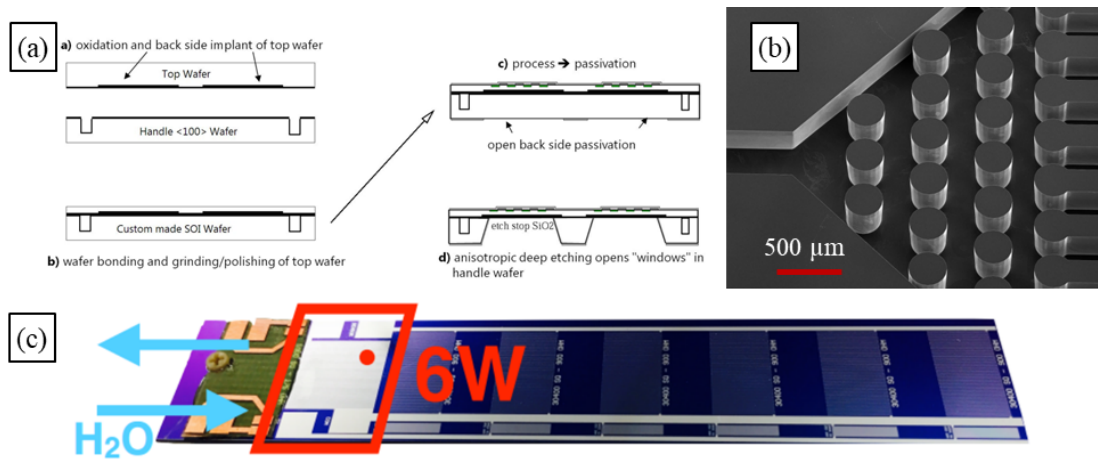


Figure 2.19: Prototype with integrated μ CS of Belle II pixel detector ladder. (a) Process flow, (b) zoom-in on the position where the inlet fans out into several cooling channels ($340 \times 380 \mu\text{m}^2$) and (c) 540 μm thick silicon μ CS ladder. Two silicon wafers are used in the process: the top ("sensor") wafer forms the active detector material, while the bottom ("handle") wafer forms the supporting frame of the all-silicon ladder. The bottom wafer hosts the microchannel cooling circuit. The picture is adapted from [112].

Unfortunately, most of the foundries where the silicon sensors are produced do not permit the use of already treated wafers in their processing line, in this case, with integrated microchannels.

For this reason, solutions to post-integrate microchannels on silicon sensor dies were investigated. Microchannels were directly etched in the backside of the MALTA monolithic active pixel sensor [102, 120]. The CMOS compatible process was developed by CERN EP-DT micro-fabrication group and the sensor was processed at the Center of Micro-Nanofabrication (CMi) at the École polytechnique fédérale de Lausanne (EPFL). The process relies on micro-trenches ($3 \times 10 \mu\text{m}^2$) etched in silicon. After that, the bottoms of the trenches are isotropically etched to create circular microchannels. Finally, the trenches are sealed by depositing a thin parylene layer forming the so-called buried channels. A 3D-printed connector is glued to feed the buried channels. Tests demonstrated that such microchannels withstand 11 MPa. A variant of this CMOS compatible process was also studied by L.Frehner [121].

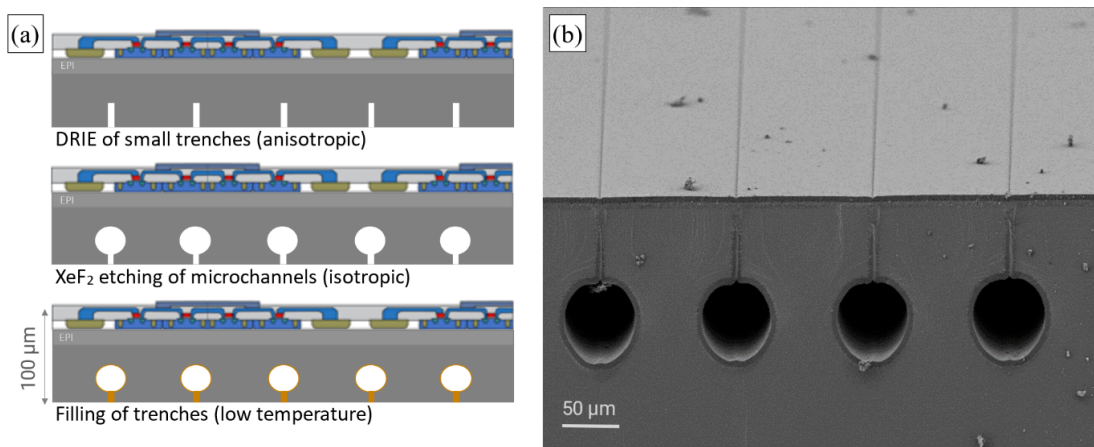


Figure 2.20: Prototype with integrated μCSof Belle II pixel detector ladder. (a) Details of the process flow and (b) SEM image of the cut Silicon buried microchannel. The picture is adapted from [102].

Note that similar solutions are also being investigated outside CERN; the Corintis start-up is developing similar integrated microchannel solutions for high-performance chips [122] and Kluba et al. developed a similar CMOS compatible process for high aspect ratio rectangular microchannels [123].

μOHP research at CERN

A fascinating solution based on microchannel Oscillating Heat Pipes (μOHPs) integrated into silicon substrates was investigated by T. Frei [95]. Oscillating Heat Pipes (OHPs), or pulsating heat pipes, were patented by Akachi in the 1990s [124–126]. The OHPs, and in general, the heat pipes, belong to the passive cooling solutions category. In an OHP, a two-phase coolant, enclosed in a serpentine-arranged single-loop capillary channel, rapidly transfers heat between heat sources and heat sinks.

The pressure-driven motion of the fluid results from the pressure difference between the evaporation and condensation of the alternating vapour plugs and liquid slugs. For HEP applications, the OHP can be used as a thermal bridge between the heat source, the sensors,

and the heat sink, an active cooling loop, providing an easy dismountable interface.

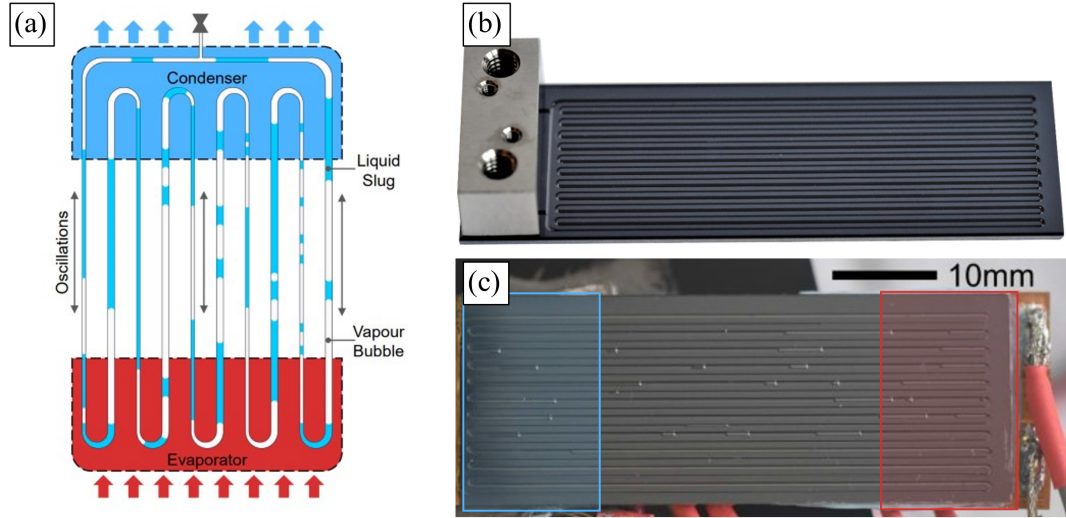


Figure 2.21: Silicon microchannel oscillating heat pipes. (a) Schematic of a typical OHP closed loop, (b) Prototype of the silicon μ OHP ($60 \times 20 \text{ mm}^2$) with connector and (c) details of a sample during operation. The picture is adapted from [95].

In addition, T. Frei demonstrated that the inlet charging port could be sealed by an innovative technique which relies on a compressed indium preform, yielding a minimum leak-tightness. For different coolant comparisons, the μ OHP was charged with Isopropyl Alcohol (IPA), Acetone or Perfluorohexane (C_6F_{14}). Tests at ambient temperature demonstrated that under a heat flux of 3 W/cm^2 the μ OHP filled with Acetone reaches an apparent thermal conductivity (k_{app}) of 375 W/mK . This value is close to the thermal conductivity of pure copper. On the flip side, at lower heat fluxes (below 0.75 W/cm^2) corresponding to most of the HEP Si tracker conditions, the k_{app} was close to the thermal conductivity of the silicon, as the flow boiling was not initiated in the μ OHPs. Nevertheless, other fluids that well operates at the desired low heat fluxes can be further investigated.

R&D on carbon micro-vascular networks at CERN

Further R&Ds are ongoing at CERN to miniaturise the vascular CCS solution and to produce carbon microvascular cooling substrates with integrated cooling circuits with channel diameters less than 1 mm by following two different R&D lines.

Because of the vast assortment of polyimide pipe sizes, with inner diameter down to $100 \mu\text{m}$ and wall thickness down to $25 \mu\text{m}$, microvascular circuits can be embedded on similar carbon lay-up used for the ALICE ITS2. In addition, metal braided polyimide pipes are also commercially available. Braided pipes can be bent down to a $2\text{-}3 \text{ mm}$ radius without buckling, and withstand high pressure.

The second option targets to eliminate any pipe inside the carbon laminate by using sacrificial material, i.e. modified PolyLactic Acid (PLA) polymer. This sacrificial material is co-cured with the CFRP laminate and later vaporised in an oven at 200 °C for 15 hours. This last solution has the potential to produce any type of microchannel network inside a CCS [1–3, 127]. The pipe-less CCS strategy was also investigated outside HEP applications [89, 128–130].

2.3.3 Hydraulic connections

Some efforts have been made to define guidelines for microfluidics interconnection. However, standards are not available. The wide variety of the developed solutions is mostly application-oriented. Besides the application, it is possible to group the interconnections into two main types: connection to the feed-line and substrate-to-substrate interconnection.

Connection to the feed-line

In the past years, a review of the possible connections to the feed-line applied inside and outside HEP communities was done by A. Toros [131], while the most relevant connections to the feed-line used in HEP applications are illustrated in the AIDA2020 report on "Standard connectors for microchannels" [132]. To connect a microchannel circuit to the feed-line, commercially available connectors, metal soldered connectors or adhesive-based connectors are used in HEP. In most cases, the substrate, often silicon, is out-of-plane connected to the feed-line.

Commercially available connectors [133] are typically used for prototypes. For example, the PEEK-based NanoPort base units, in Figure 2.22, stick to silicon, quartz, glass, and certain polymers. These base units withstand pressures of up to 6.9 MPa. They are attached to chip surfaces with prefabricated adhesive rings (cured for 2 hours at about 180 °C). These connectors are able to join different tube diameters. However, this connectivity approach requires a large area (the connector's diameter and height are close to 1 cm), which prohibits high-density interconnections.

Two metal solder solutions are applied in the HEP community to solder metal capillaries to microchannel μ CSs. The first method, which involves crimping ferrules around the SS capillaries, is preferred for prototypes (Figure 2.23).

In the second method, capillaries are connected to silicon plates using customised connectors that are machined from alloys such as Kovar and Invar. The CTEs of these alloys are close to those of silicon such to prevent thermo-elastic stresses induced in the interface connector-substrate. The LHCB and NA62 experiments employed this strategy; their connectors are in Figure 2.24 and Figure 2.25, respectively.

In both methods, direct soldering of stainless steel capillaries or based on customised metal connectors, the inlets and outlets of the microchannel cooling plate must be surrounded by a

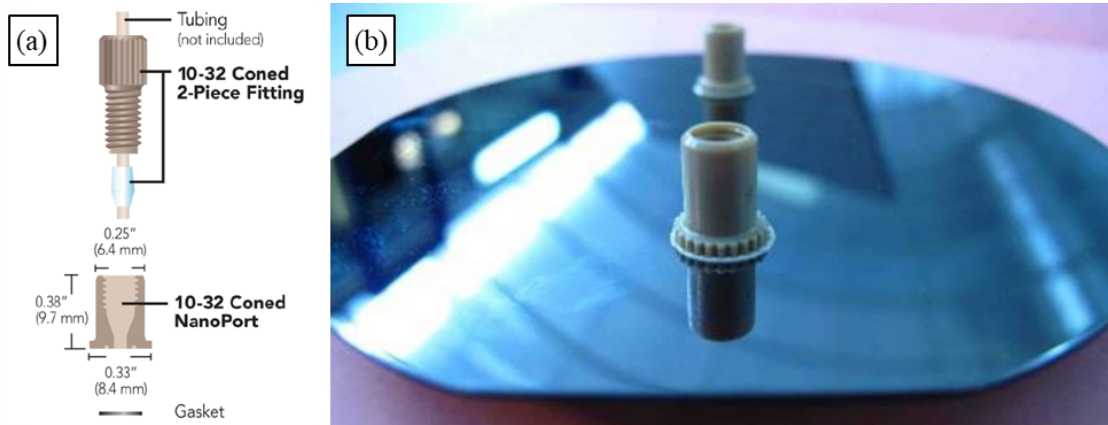


Figure 2.22: Example of a commercially available connector. (a) Exploded view of the NanoPort Assembly 10-32 [133] and (b) Nanoport connectors glued to a silicon/glass μ CS. The picture is adapted from [131, 132].

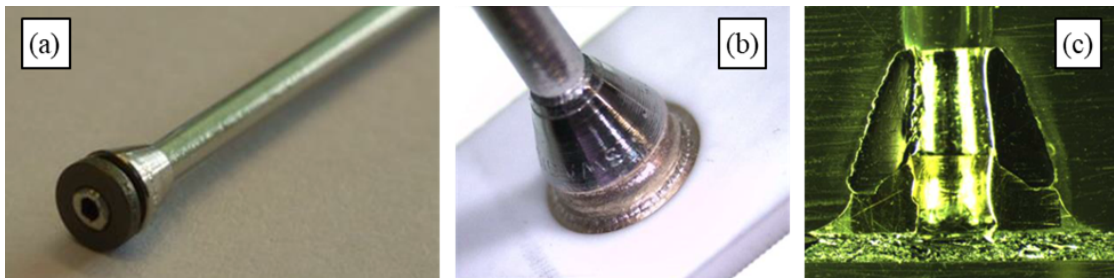


Figure 2.23: Direct soldering of stainless steel capillaries. (a) Ferrules crimped around a stainless-steel capillary, (b) Capillary with ferrules soldered to a ceramic substrate and (c) its cross-section. The picture is adapted from [131, 132].

stack of thin metallic films. Deposition of Ti (200nm), Ni (350nm) and Au (500nm) on the Si μ CS is a conventional stack utilised by CEA-Leti [134] in partnership with CERN. During the microfabrication process, the bond pads are patterned around the inlets of the microchannel device using a photolithography and metal etching sequence or metal lift-off. Bond pads can also be sputtered on whole wafers or single dies afterwards via a shadow mask.

The adhesive-based 3D printed connectors are intended for cases where a material reduction is essential. A 3D printed connector was developed for the BELLE II vertex detector [112] by IFIC (UEG/CSIC) Valencia, University of Bonn and the semiconductor laboratory HLL of the Max Planck Society (Figure 2.26). In this case, an in-plane low-mass connection seals (adhesive-based) the inlet and outlet of the microfluidic circuit at the sensor edge. The reverse side of the connector is plugged into hydraulic standards fittings. Destructive pressure and leak tests showed that the connectors withstand pressures up to 8 MPa, and their helium leak rate is of the order of 10^{-8} mbar l/s. Similarly, another adhesive-based 3D printed connector was developed for the silicon frame solution proposed for the ALICE ITS2; additional information is in Appendix B.6 (Figure B.12).

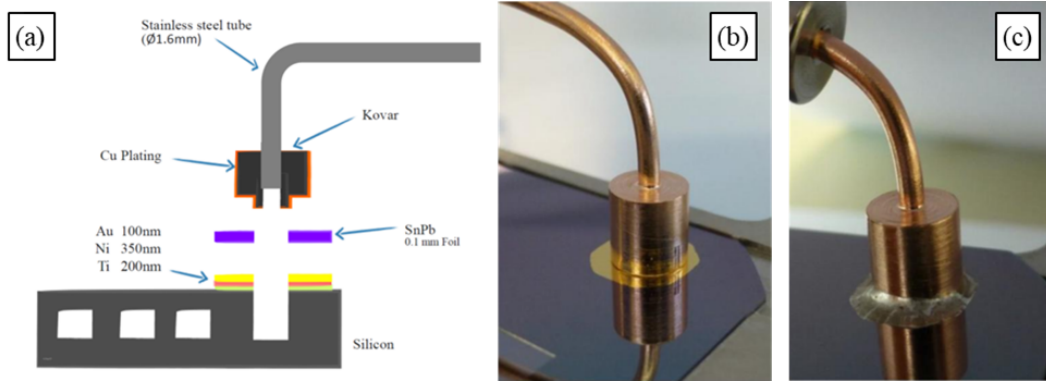


Figure 2.24: Kovar connectors of the NA62 GTK detector. (a) Schematic cross-section of the machined connector and before (b) and after (c) soldering. Four capillaries are welded to the Kovar connectors, which withstand 70 MPa of pressure. The picture is adapted from [131, 132].

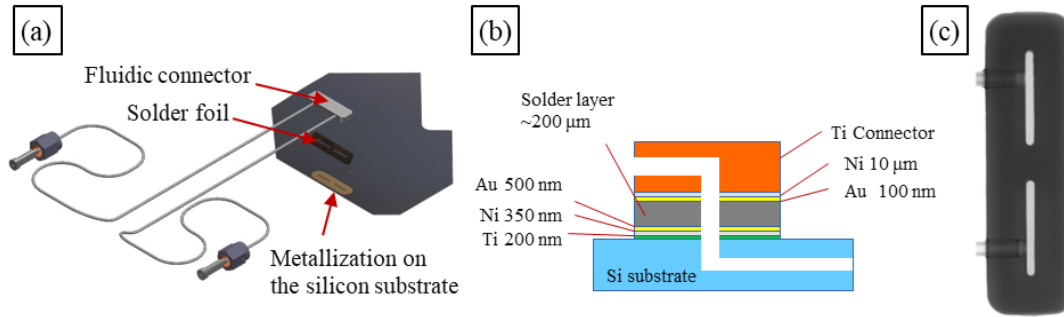


Figure 2.25: Invar connector of the LHCb VELO vertex detector. (a) Exploded view of the interface, (b) schematic cross-section of the interface and (c) X-ray of solder joints attaching the fluidic connector to the Si μ CS. The picture is adapted from [131, 132].

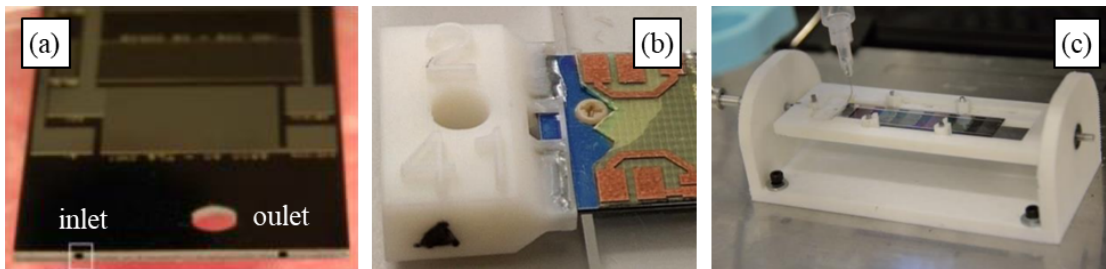


Figure 2.26: In plane 3D printed connector for BELLE II vertex detector. (a) Illustration of one DEFPFET ladder with the inlet and outlet channels, (b) 3D printed in-plane connector and (c) jig for automated glueing. The picture is adapted from [131, 132].

Substrate interconnection

Substrate interconnections are already implemented for modular Lab-On-a-Chip (LOC) devices [135–140]. In these cases, the fluids are driven by capillary force or the mass flow rate ($<0.1\text{g/s}$), and the operative pressures and pressure drop requirements are less demanding than typical HEP cooling applications. Among all the developed LOC interconnection solu-

tions that deserve a note, three examples are illustrated in Figure 2.27.

In Figure 2.27.a, the modular microfluidic system is constituted by a motherboard, fitting components and microchannel modular inserts. In this case, the fitting component, based on a miniaturised luer fitting, seals the two adjacent microchannel modules. The components were fabricated by stereolithography (SLA).

Figure 2.27.b shows high-precision LEGO® bricks modules where the fluid flows through tiny channels milled into the side walls, while the hydraulic interface is sealed with O-rings [137]. Figure 2.27.c [139] shows similar LEGO®-like modular microfluidic system with modules stack and parallel to each other. In this case, the LEGO®-like bricks were made in Polydimethylsiloxane (PDMS), and the elasticity of PDMS allows the material to conform into irregularities at the mating interfaces. In addition, the hydrophobic PDMS–PDMS sealing interactions helped against leaking.

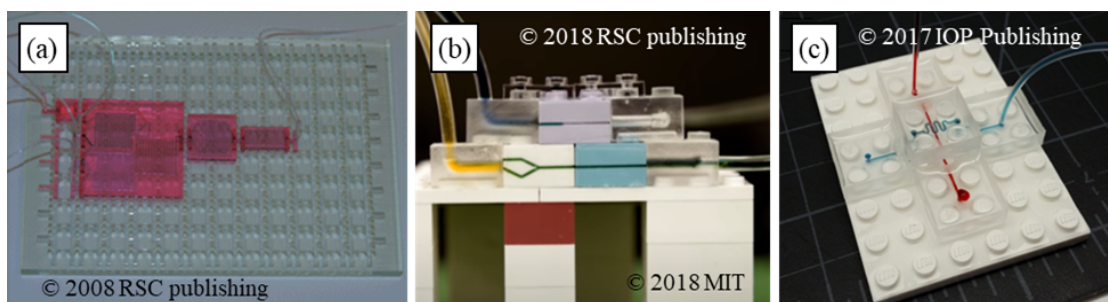


Figure 2.27: Interconnections for LOC devices in literature. (a) Modular microfluidic mixing system based on luer fitting concept [136], (b) high-precision modular microfluidics [137, 138], (c) PDMS LEGO®-like modular microfluidics platform [139]. Pictures reproduced with permission from "Royal Society of Chemistry (RSC)" and "Institute of Physics (IOP)" Publishing.

Microfluidic substrates for cooling applications, found in literature, are typically limited to single chip cooling. Interconnections between cooling substrates have never been implemented in real applications. However, some studies were performed [141, 142], also at CERN [111, 143].

In Figure 2.28.a, a Parylene deposited in vapour-phase is used to fix in-plane fluidic connections. In this case, the interface between the polyimide tubings and the silicon/glass chips sealed by Parylene-C can withstand pressures as high as 0.827 MPa [141]. Figure 2.28.b shows an interconnection solution based on micro polymer pipes and orifice (~ 0.2 mm of diameter) patterned on the Si wafer and used to transfer the cooling liquid [142].

At CERN, a similar bridge concept, but in large dimension ($\sim 4 \times 2$ mm²), was investigated (Figure 2.28.c) for the silicon frame μ CS solution proposed for the ALICE ITS2 [111]. A microbridge with an embedded channel connects the two Si substrate sub-circuits with minimum mass contribution and space occupancy. The bridge is aligned with respect to the inlet/outlet holes of the two substrates with a dedicated jig. After that, the interface is sealed using epoxy glue.

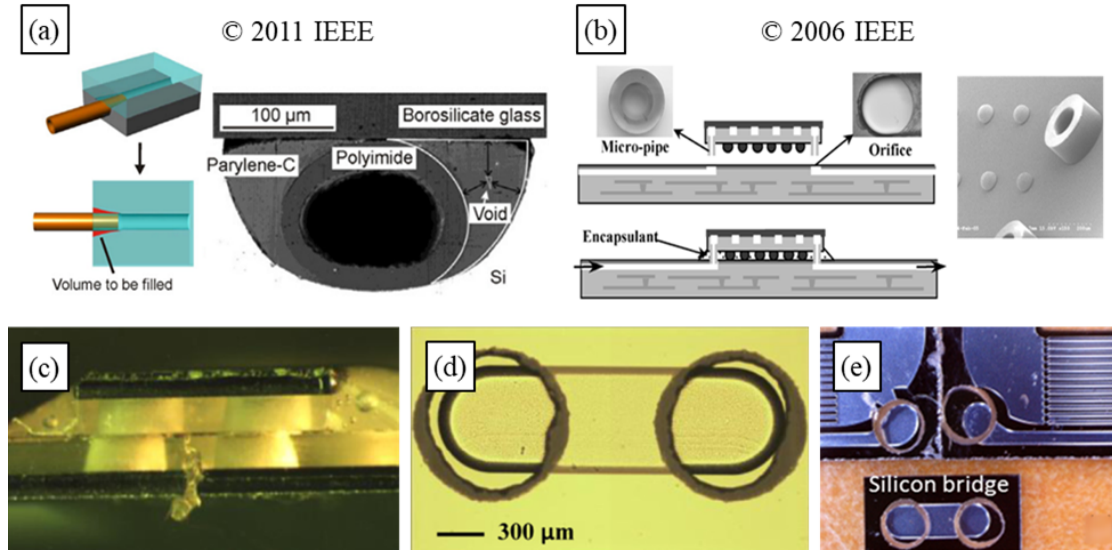


Figure 2.28: Interconnections for cooling applications. (a) In-plane Parylene sealing [141], (b) Si-polymer micro-pipe and orifice [142] and (c-e) silicon bridge solution investigated at CERN [111].

2.4 Cooling strategies comparison

The performances of different thermal management strategies, combination of the selected cooling substrate technology and coolant, are historically quantified by the Thermal Figure of Merit (TFM) calculated as follows:

$$\text{TFM} \left[\frac{\text{cm}^2 \text{K}}{\text{W}} \right] = \frac{\Delta T_{\text{sub}} [^\circ \text{K}]}{\dot{q} [\text{W}/\text{cm}^2]} \quad (2.3)$$

where \dot{q} is the heat flux and the temperature difference (ΔT_{sub}) is calculated as follows:

$$\Delta T_{\text{sub}} = \frac{1}{n} \sum_{i=1}^N T_i - \frac{T_{\text{in}} + T_{\text{out}}}{2} \quad (2.4)$$

where T_i are the maximum temperatures taken on the electronics surface, typically the temperatures at the furthest points from the coolant. While, T_{in} and T_{out} are the inlet and outlet temperatures of the refrigerant, respectively.

The TFM gives information on the average heat transfer resistance, or surface resistance, between the average temperature of the coolant and the average maximum temperature of the sensors and electronics along the substrate cross-section. Similarly to the Ohm's law, the TFM can be theoretically evaluated, in first approximation, as the sum of:

- The conductive heat transfer resistance of the substrate (R_s) between the channel wall and the electronics.
- The convective heat transfer resistance ($R_c=1/h_c$) between the channel wall and the

coolant (where h_c is the heat transfer coefficient between the channel wall and the bulk of the coolant).

The theoretical TFM (TFM_{theo}) can be therefore evaluated as:

$$\text{TFM}_{theo} = R_c + R_s = \frac{1}{h_c} + R_s \quad (2.5)$$

This approximation does not consider the contribution of the heat transfer with the environment that can have a positive (or negative) effect if the environment temperature (T_{env}) is lower (or greater) the temperature of the electronics (T_i).

When a large surface needs to be cooled, an evaporative refrigerant easily maintains an even temperature distribution along the sensing modules, as the vapour quality of the refrigerant increases while its temperature remains almost constant. It is essential to specify the operating temperature and the heat flux at the cooling lines as both parameters affect the flow pattern and, therefore, the heat transfer coefficient between the coolant and the cooling pipe wall. On the other hand, when gas or liquid refrigerants are chosen, their mass flow rate must be correctly settled to maintain an acceptable and minimum temperature difference between T_{out} and T_{in} .

Different values of TFM are shown in Table 2.2; while the expected arrangement of the cooling strategies for the four LHC experiments, foreseen to be installed during the 2026-2028 upgrade (LS3), is in Table 2.3.

The TFM's definition has severe limitations that can lead to a misleading comparison between cooling strategies as it assumes a uniform, or at least homogenised power dissipation in the electronics. In addition, it is not a constant value for a given design, since the convective contribution depends on the applied power and the coolant temperature (both of which affect the value of the local heat transfer coefficient). In addition, it should not be associated with a specific cooling technology, but with its implementation for a given sensor size and detector layout.

To conclude, the minimisation of the passive material in the sensor detection region, i.e. the material budget contribution of any cooling strategy, should be viewed as an equally important figure of comparison in selecting the cooling strategy.

Cooling substrate	Refrigerant	$T_{coolant}$ range [°C]	TFM range [cm ² K/W]
re-workable CCS (+TIM)	Evap. CO ₂	-45 / -15	20-45
vascular CCS	Evap. CO ₂	-45 / -15	12-15
Si μ CS	Evap. CO ₂	-45 / -15	3-1
vascular CCS	H ₂ O	10/30	8-12
Si μ CS	H ₂ O	10/30	3-1

Table 2.2: Thermal figure of merits in silicon tracking detectors. (non-exhaustive) This table is intended to give the reader the order of magnitude of the TFM's. The non-uniform heat dissipation, the size of the cooling system, the number of sensor modules to be cooled and the material budget contribution are some of the further aspects that must be considered for a correct cooling strategy comparison.

LHC Experiment	ALICE		ATLAS		CMS		LHCb
Active area [m ²]	9.4		170		200		0.12
Silicon detector	Tracker		Tracker		Tracker		Vertex
Type of sensor	Vertex	MAPS (large)	Hybrid 3D Pixel	Hybrid Pixel/Strip	Hybrid Pixel	Hybrid Pixel/Strip	Hybrid Pixel
*MB [%]	<0.1	<1.5%	<1.5%	>2%	<1.5%	>2%	<0.6%
*TID [MGy]	0.01	<0.01	10	<10	1.2	<1	4
*NIEL[10 ¹⁵ n _{eq} /cm ²]	0.01	<0.01	13	<10	23	<1.5	8
**Sensor Temperature [C]	30-40	30/35	-30/-15	-30/-15	-30/-15	-30/-15	-20
**Module power dissipation [W/cm ²]	<0.07	<0.05	0.25/0.8	0.25/0.8	0.3/0.8	0.3/0.8	1.5
Substrate	None	vascular CCS	vascular CCS	CCS (+TIM)	vascular CCS	CCS (+TIM)	Si μ CS
Coolant	Air	H ₂ O	Evap. CO ₂	Evap. CO ₂	Evap. CO ₂	Evap. CO ₂	Evap. CO ₂
**T coolant [C]	5-20	18-22	-25 / -45	-25 / -45	-25 / -45	-25 / -45	-35
**TFM [cm ² K/W]		8-12	12-15	20-45	12-15	20-45	2-1

Table 2.3: Expected cooling arrangement of the four LHC experiments after LS3. (non-exhaustive) (*)Value for the first layer, (**) Expected range for "an-irradiated sensor" and "sensor end of life" [20, 22, 47, 59, 60]

3 Requirements for future Si tracking detectors

This chapter describes the challenges that the modular microfluidic concept is addressing, with respect to the stringent mechanical and cooling requirements of future HEP experiments.

3.1 Mechanics and cooling challenges

The EP department at CERN, together with the ECFA committee, drew a roadmap for the R&D on future detector experimental technologies [1–4]. The requirements of future silicon tracking detectors are mainly driven by:

- Vertex measurements in high rate ($30 \cdot 10^9$ hit/s/cm²) and hostile radiation environments (TID ≈ 300 MGy, NIEL $\approx 10 \cdot 10^{17}$ n_{eq}/cm²) [144].
- Very high-resolution vertex measurements requiring a pixel size below 20 μ m, extremely low mass (0.05 % X₀) and hence low power consumption (<100 mW/cm²) [145].

These two R&D lines are intrinsically linked to the two different possible categories of experiments that will operate with either hadron-hadron colliders or lepton-lepton colliders. Other future experiments at lower energy, like fixed target experiments, will have requirements resulting from an overlap of the two previous categories.

Table 3.1 summarizes the relevant operating parameters for the impending upgrades of two of the experiments currently operating at the LHC. These can be compared (see table Table 3.2) with the corresponding parameters of the two generations of experiments currently foreseen at the Future Circular Collider (FCC-hh [144] and FCC-ee [145]).

The most evident difference is a significant increase in active surface area. Therefore, implementing a scalable concept for the sensing module will allow for a more streamlined production and testing and facilitate interventions at the commissioning stage for the correction of localized failures.

Chapter 3. Requirements for future Si tracking detectors

Table 3.1: Operating parameters of two present silicon tracking systems. Note that the ALICE experiment is a particular detector operating in a hadron collider. (*) Expected range for "an-irradiated sensor" and "sensor end of life".

Detector	ALICE[47]		ATLAS[59, 60]	
	Vertex	Tracker	Vertex	tracker
Detection area [m ²]	~ 10		~ 170	
Heat flux* [mW/cm ²]	~ 50	~ 40	~ 250-800	~ 250-800
MB (first layer) [% X ₀]	≈ 0.05	< 1.5	< 1.5	> 2
TID (first layer) [MGy]	~ 0.01	< 0.01	~ 10	< 1
NIEL (first layer) [10 ¹⁶ n _{eq} /cm ²]	~ 0.01	< 0.01	~ 10	< 1

Table 3.2: Operating parameters of future silicon tracking systems. The data are taken from [4]. "N.D." means Not Defined.

Detector	Lepton collider (FCC-ee [145], 2040)		Hadron collider (FCC-hh [144], >2045))	
	Vertex	Tracker	Vertex	tracker
Detection area [m ²]	>60		~400	
Heat flux [mW/cm ²]	≈ 20	≤ 100	N.D	N.D.
MB (first layer) [% X ₀]	≈ 0.05	≈ 1	≈ 1	≈ 2
TID (first layer) [MGy]	N.D.	≪ 0.5	~300	≤ 10
NIEL (first layer) [10 ¹⁶ n _{eq} /cm ²]	N.D.	≪ 0.5	~100	≤ 10

3.1.1 Si tracking system for future hadron collider

The reference experiment of the proposed hadron-hadron Future Circular Collider (FCC-hh), visible in Figure 3.1, provides a good baseline for the main objectives of the mechanics and cooling requirements for this category of future Si tracking systems. The overall detection area of the proposed tracking system is around ~ 400 m² (~ 200 m² for the barrel region and ~ 100 m² for one end-cap region), while the outermost detection layer area of the barrel tracker reaches ~ 45-50 m² (Figure 3.2 and Figure 3.3). The TID and NIEL at the vertex detector first layer will be in the order of ~300 MGy and ~10¹⁸ MeV n_{eq}/cm² respectively, while at the tracking layers doses of 1 MGy and fluences of <10¹⁶ MeV n_{eq}/cm² are to be expected. Harsher radiation environments will impose lower operating temperatures for the future detectors to extend the Si sensor lifetime.

As of today, the expected temperature domain of the coolant at the FCC is expected to have a lower boundary at -80 °C. while the dissipated heat fluxes should be within 0.1 and few W/cm². The actual values will, of course, depend from the technical advancements in sensor and electronics R&D. The lower admissible temperature at which an evaporative CO₂ coolant can correctly operate is ~-45 °C. Lower temperature domains will therefore require alternative coolant, such as 3M Novec®-649 fluid [50], evaporative Krypton [64, 65], Argon and Nitrogen gasses. Independently from the selected coolant, an efficient active cooling substrate must be employed to reduce the temperature gradient in the overall detector.

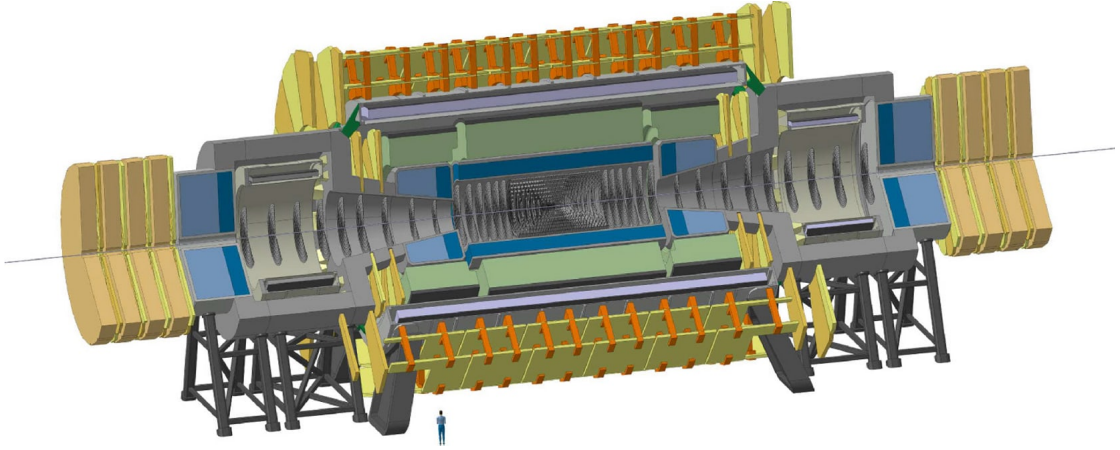


Figure 3.1: The FCC-hh reference experiment. The reference experiment has an overall length of 50 m and a diameter of 20 m [144].

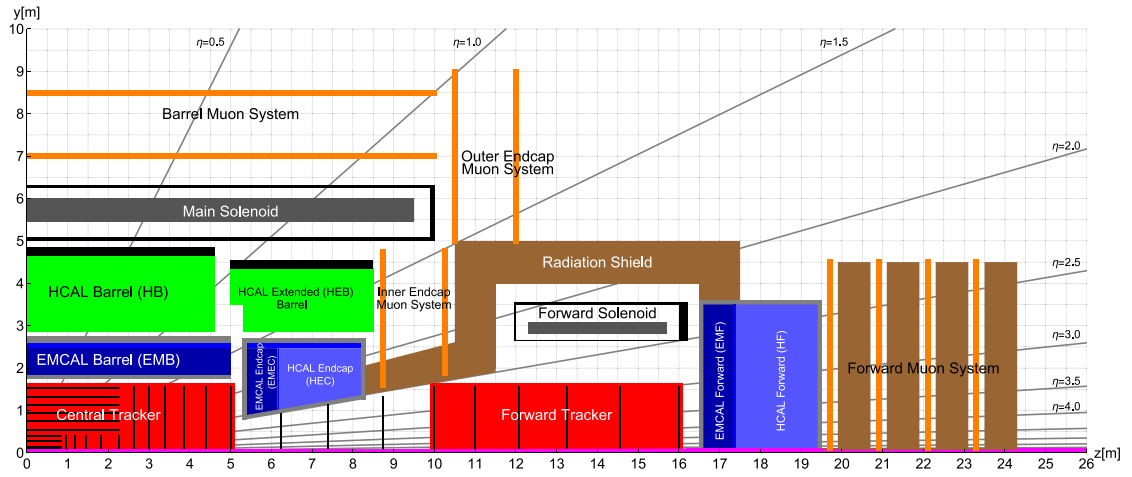


Figure 3.2: Longitudinal cross-section of the FCC-hh reference experiment. The area covered by the tracking system is highlighted in red [144].

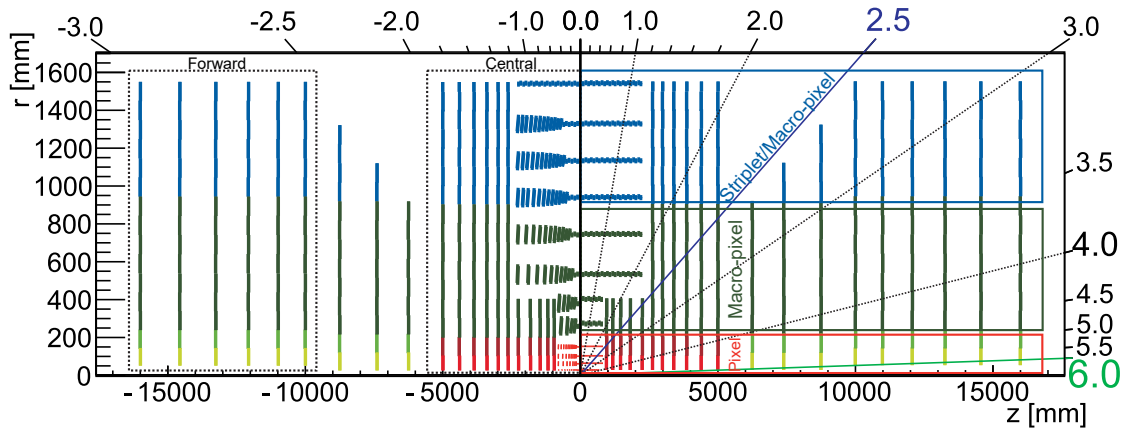


Figure 3.3: Tracking system layouts of the FCC-hh reference experiment. Tracking system layout using the so called “*tilted geometry*” (left) and “*flat geometry*” (right) [144].

3.1.2 Si tracking system for future lepton collider

Future lepton colliders will produce considerably lower levels of radiation. The sensing modules can therefore operate at ambient temperature, relaxing the design requirements for the cooling substrate, mainly driven by sensors' positioning accuracy ($\sim 5 \mu\text{m}$) and minimisation of the passive material.

The reference experiment, dubbed CLD (CLIC-Like Detector) is shown in Figure 3.4. The material budget of the vertex first layer should be $\sim 0.05 \%X_0$. It will most probably employ gas cooling. The MB of the tracker first layer is expected to be $\sim 1 \%X_0$, and the dissipated heat flux of its sensing modules is expected to be less than 100 mW/cm^2 over the entire detector lifetime. Such a low heat flux can be easily removed by demineralised water. The overall detection area of the proposed tracking system is in the range of $60 - 100 \text{ m}^2$.

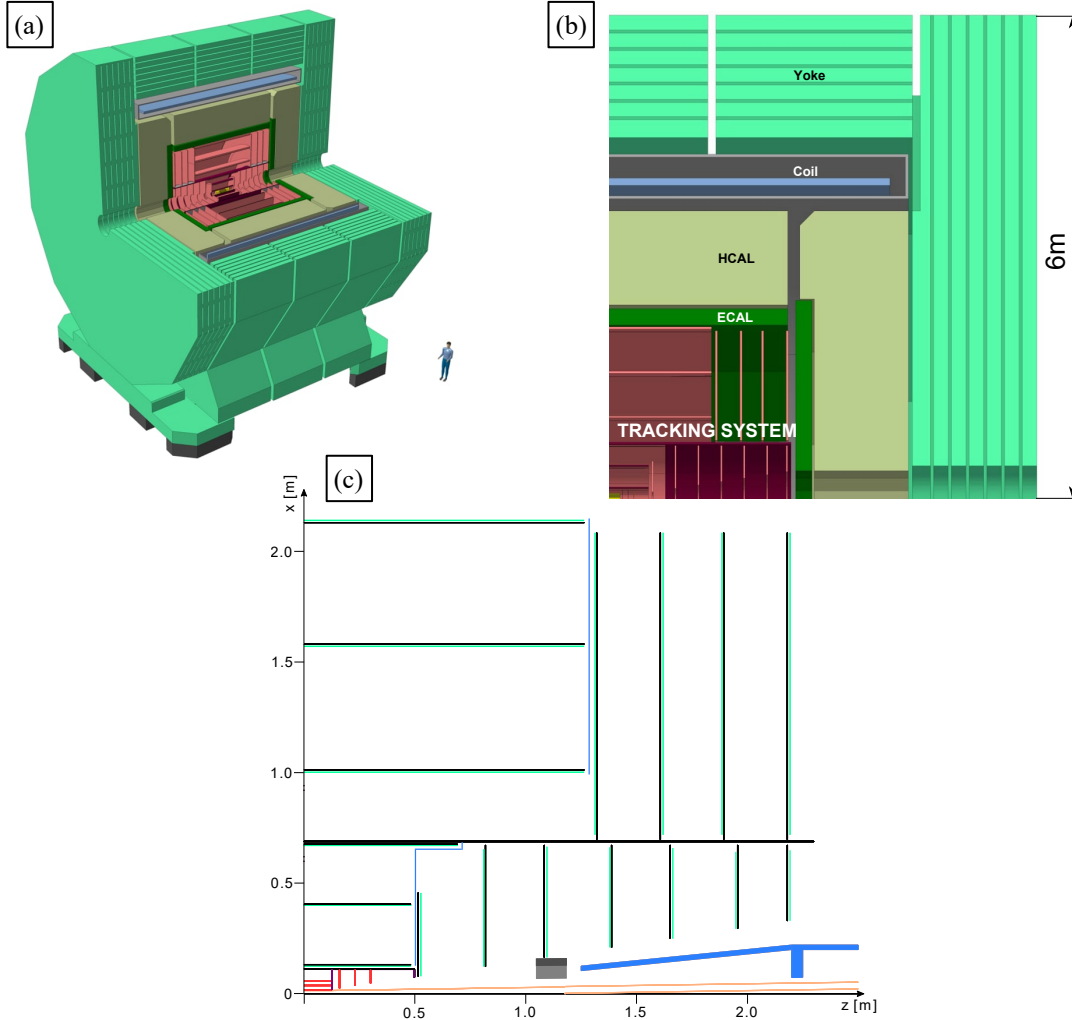


Figure 3.4: The FCC-ee reference experiment. (a) Isometric view, (b) longitudinal cross section (top right quadrant) of the proposed CLD experiment and (c) layout of its tracking system [146].

3.2 Modular implementation

The coverage of large surfaces with silicon sensing modules of a relatively small unit area ($\sim 100 \times 100 \text{ mm}^2$), implies assembling large units of elemental sensing modules into larger assemblies (up to 50 m^2). The sheer number of required modules introduces the problems typical of a production at scale. The modules will require a distributed production model, with several institutes or companies taking part to the endeavour. Subsequently, the modules are expected to be transported to one or more integration sites. This distributed model defines the constraints of the assembly and interconnection of the modules, which need to be compatible with such a large integration scale.

A modular concept still needs to address very specific challenges which are typical of particle tracking detectors. The constraints on material budget and cooling uniformity rule out the use of conventional heat transport techniques (e.g. heat pipes), that are not scalable to large surfaces. In order to minimize the amount of employed material, the heat extraction must happen as close as possible to the module, which is typically achieved through heat transfer to a fluid medium (liquid or gaseous).

Ensuring the leak-tightness of a fluid system in a reliable way is of paramount importance when considering detectors that will likely not be accessible over their lifetime, in the order of several years. Conventional (non-modular) systems, typically have a limited amount of fluidic connections. Implementing a modular interconnection system will result in a multiplication of fluidic interfaces, that need, therefore, to achieve outstanding reliability.

Along with the interconnection, the thermal interfaces to the heat load (sensor/readout electronics) need as well to be reliable. At present, several solutions are adopted for the thermal coupling between the fluidic system and the sensor (Section 2.2.2); the use of interface materials needs to be qualified for their mechanical and thermal performances in harsh environments.

In general, thermal interfaces (glued, soldered, brazed, TIM-based) represent one of the critical elements of the assembly. They introduce an uncertainty on the total thermal resistance between the sensing modules and the coolant; in addition, the late stage thermal coupling between the sensor and the cooling element, through the thermal interface material, allows to reveal of cooling weakness only in the final phase of the detector integration, and not at the level of a single component.

Electrical services, although not addressed in this work, will need as well to be compatible with a modular concept. Low voltage, high voltage interconnections, as well as data lines, will need to implement some degree of modularity, in order to allow distributed production and integration flexibility.

3.2.1 Limits of the re-workable thermal interfaces

The modularity would therefore impose constraints on the re-workable interfaces, that, while shrinking in surface, would multiply in numbers. On the flip side, larger interface surfaces result in larger stresses related to unavoidable CTE mismatches.

In typical applications, TIMs, like thermal pastes and thermal gap fillers, have to be deposited evenly on the surface, and this, most of the time, requires vacuum during deposition to avoid voids at the interface. This is particularly problematic for large assemblies, imposing the requirement of large autoclaves or similar.

Often thermal pastes have a problem with long-term reliability; after several thermal cycles, thermal expansion and contraction of the contact surface materials push the liquid components out of the interface ("*pump out phenomenon*"). At the same time, following thermal cycling, the paste components are gradually evaporated ("*dry out phenomenon*"). Both the phenomena produce performance degradation.

Compressible PGS is an alternative single-component thermal interface material that doesn't suffer from the above issues (dry-out, pump-out). However, in order to reach its nominal thermal resistance, a uniform compression is required, typically in the order of ~ 1 MPa, which is challenging to achieve on lightweight assemblies. Such compression should as well be maintained over the detector's lifetime, significantly limiting the number of mechanical options that can be employed to control it (such as adhesives).

Thermally conductive adhesives are as well a common choice for the realization of thermal interfaces. Among these, epoxies are commonly used, due to their outstanding radiation resistance. However, these are often permanent, not allowing reworkability. Their thermal conductivity is boosted by the introduction of various types of fillers, usually oxides or nitrides of aluminium or boron.

Boron-based fillers are, however, particularly problematic, due to their high neutron capture cross section, which can significantly boost the amount of TID and NIEL damage in the proximity of the interface. The conductivity is often limited to values that only slightly exceed ~ 1 W/m·K.

Special attention also needs to be paid to the filler particle size. Larger particles (larger than half the glue layer thickness) can cause cracks in the bonded elements when pressure is applied before curing the adhesive.

Other thermally conductive adhesive bases (e.g. acrylates) are often not sufficiently radiation hard, suffering from significant embrittlement after doses as low as ~ 1 MGy.

3.3 The proposed concept

The approach proposed in this research doesn't rely on TIM-based interfaces (Figure 3.5.a). It is instead based on modular microfluidic substrates with a novel fluidic interconnection (Figure 3.5.b). The cooling substrate and the cooling circuit are considered an integral part of the sensing module, glued at its backside. The concept defines a single bonded thermal interface, between the silicon sensor and the refrigerant. In-plane hydraulic interconnections are responsible for the transport of the cooling fluid between modules.

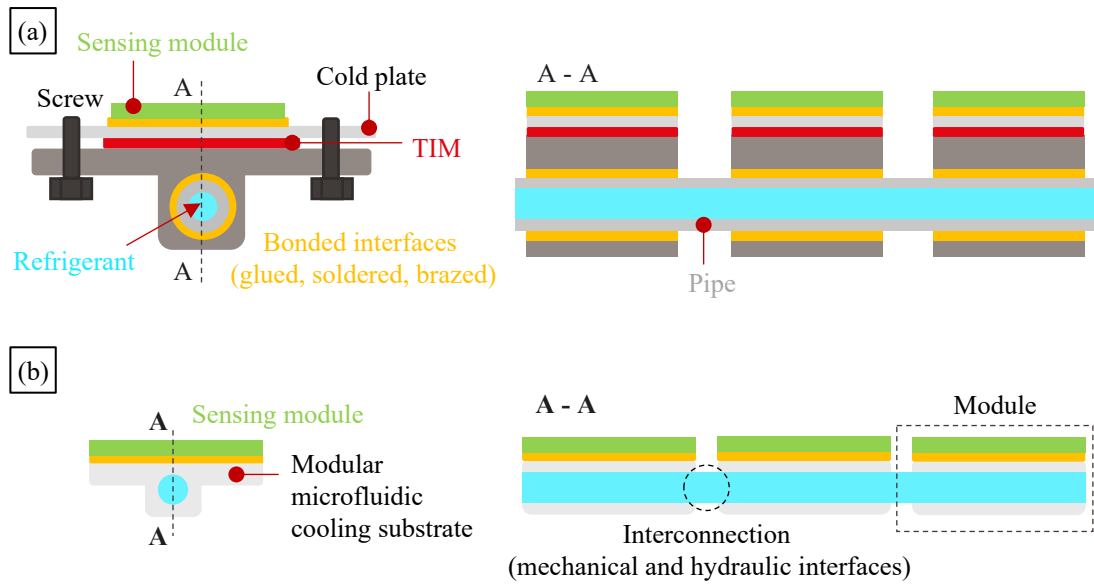


Figure 3.5: Concepts of modular implementation. (a) TIM-based and (b) modular microfluidic-based concept.

Such a concept allows for a distributed production and testing model. The single modules can be independently produced and qualified for their mechanical and thermal performances, before being shipped to an integration site where they are joined together. The thermal performances of the concept are improved by the reduction in the number of thermal interfaces. The simplified concept allows as well for significant improvements in terms of material budget.

An efficient and reliable interconnection, sum of a mechanical and a hydraulic interface integrated between modules, represents the key design feature for the new cooling substrate category denoted as "*interlocking Modular microfluidic Cooling Substrate*" (i-M μ CS).

The in-plane hydraulic interface is selected instead of out-of-plane interconnection, currently employed in microfluidic solutions. It minimises interconnection encumbrance and, at the same time, it reduces pressure drop, flow disruption and non-uniform forces at the interface induced by the refrigerant pressure.

3.4 Challenges of the modular microfluidic implementation

The fundamental challenge, which is the primary focus of this work, is to design a reliable and re-workable interconnection. Other challenges through the development of modular microfluidic substrates are mainly linked to the circuit design and to the manufacturing process and material.

Fluidic interconnection:

A reliable and re-workable interconnection must be integrated into modular microfluidic substrates while minimising the added material into the detection area. Therefore, the bulky metal connectors (brazed or soldered), typically used in present silicon cooling substrate applications, cannot be employed.

The study to overcome the present challenge starts from the analysis of existing re-workable interconnections at millimeter scale, and, following a miniaturisation to micro-features dimensions, proposes a new design. In addition, compatibility with the coolants and with cooling system requirements, like pressure resistance, must be investigated. Additional comments are reported in Chapter 5.

Circuit design:

Covering large meter scale distances, with a microfluidic circuit, requires deep studies on the total pressure drop and flow distribution uniformity that must ensure the proper working of the cooling system.

The miniaturization of the circuit, down to a sub-millimeter scale, allows for the achievement of high thermal performances (dissipation of heat fluxes at the order of W/cm^2) and minimisation of the passive material contribution in the detection area.

However, a sub-millimeter scale circuit, produces a higher pressure drop, for both liquid and evaporative coolants, which suggests the use of parallel sub-circuits (Figure 3.6.a). This is also the case for more elaborated designs, for example, based on staggered pin-fin design [147–149].

Similarly to the interconnected microchannel solution proposed for the ALICE ITS2 (Figure 2.18), the fluid flow to the different microfluidic sub-circuits should be achieved through the introduction of distribution lines (return and supply lines), running in the substrate module. The re-workable interconnection across modules can then be foreseen at the distribution lines.

The design geometry of a sub-circuit strictly depends on the type of sensor to be cooled (e.g. heat flux to be dissipated, its non-uniformity over sensor area and sensor dimensions) and type of coolant. The mass, momentum and energy conservation equations must be employed together for the characterization of the flow distribution.

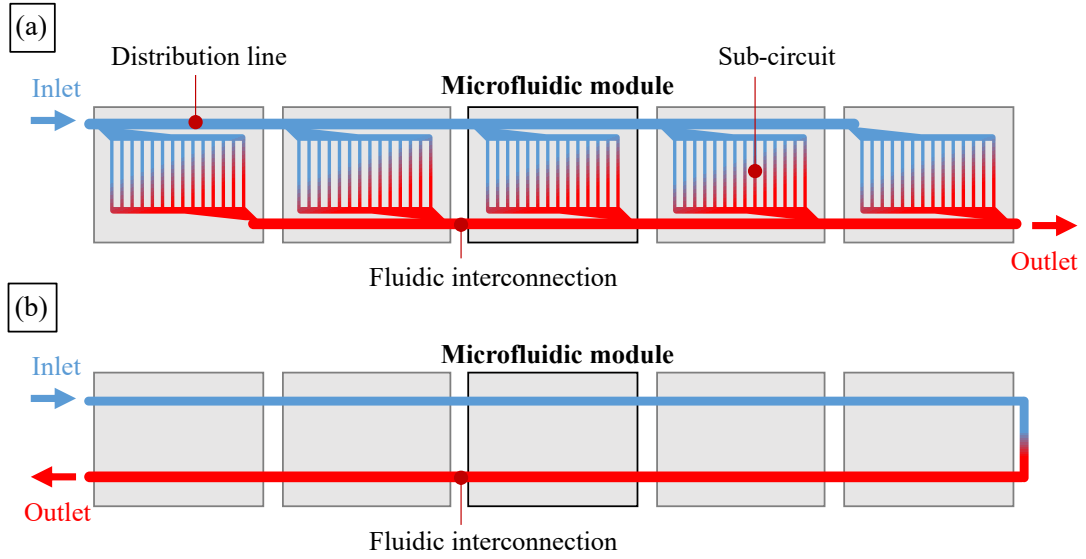


Figure 3.6: Schematic layout of microfluidic circuits. (a) Circuit composed of parallel sub-circuits and (b) single circuit.

In literature, guidelines on manifold sub-circuit design exist and are commonly applied to fuel cells, plate heat exchangers, radial flow reactors and irrigation systems. In addition, J. Wang produced several studies on flow distribution in fuel cell application [150, 151] and he unified the main models into one theoretical generalised model [152] that can be used as a starting point to develop sub-circuits for each specific use cases.

Computational Fluid Dynamics (CFD) analysis is, therefore, an essential tool for design optimisation in order to provide a better flow uniformity in the overall circuit and minimise inappropriate fluid re-circulation and stagnant zones. In Appendix B.2, the study performed on the flow uniformity inside the inlet manifold of the interconnected microchannel solution, proposed for the ALICE ITS2, is illustrated as an example.

On the other hand, simplified circuits, like the one in Figure 3.6.b, consisting of a single circuit and serial hydraulic interconnections, between adjacent substrates, can be employed when lower heat fluxes ($< 1 \text{ W/cm}^2$) are considered; in this case, the heat transfer relies on the thermal conductivity of the cooling substrates.

Manufacturing process and material:

Microfluidic substrates are mainly based on microchannels etched into a silicon wafer, closed by direct bonding of silicon top cover. In addition to the previous considerations, the production of a Si μ CS presents additional challenges strictly related to the material and present manufacturing processes when large dimensions and series productions are targeted.

The Si substrate size is limited to the wafer scale (up to a diameter of 300 mm). These dimen-

Chapter 3. Requirements for future Si tracking detectors

sions are adequate for most sensing modules. However, most of the steps for embedding microchannels in silicon take place in a clean room environment, with a steep run-up of the production costs. An alternative silicon manufacturing technology can be investigated to reduce production costs.

Moreover, for large detectors, requiring long distribution lines, the size of the microchannel needs to be increased from a micro-scale to several millimeters. Embedding such a large channel in a typical wafer (thickness $\sim 500\ \mu\text{m}$) is therefore not directly feasible, requiring workarounds such as piling-up several wafers through wafer bonding.

An alternative solution to the wafer piling-up could be the use of an auxiliary substrate for the distribution lines. In this case, the auxiliary substrate, made of a different material, provides the fluid distribution to the micro-patterned Si μCS bonded on it (Figure 3.7).

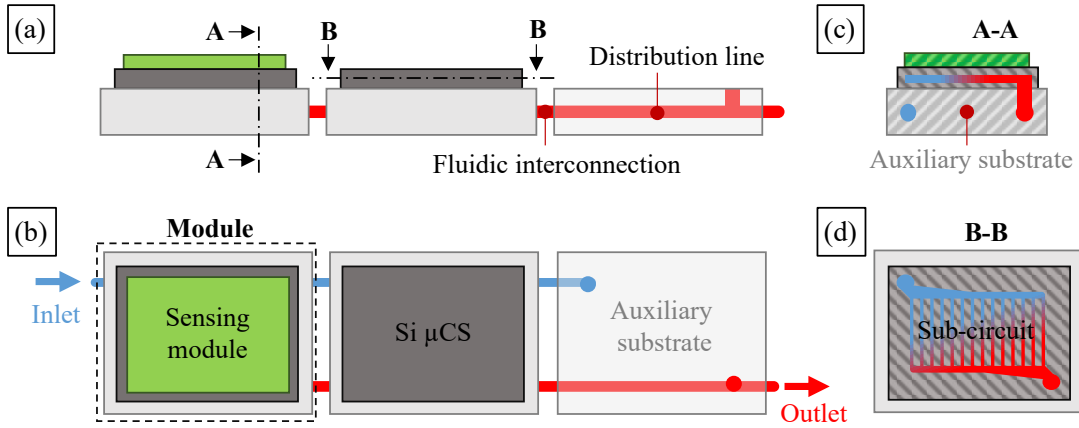


Figure 3.7: Schematic layout of a modular Si μCS concept with auxiliary substrates. (a) Lateral view, (b) top view and (c-d) cross-sections.

In alternative to the silicon solution, several materials and processes can be employed for realising modular microfluidic substrates. The materials should satisfy the requirements for the implementation in HEP applications, such as material budget, CTE matching with the sensors and high thermally conductive. In this case, the feasibility to realise such microfluidic substrates, with alternative material and processing like polymer and ceramic AM, composite materials (CFRP) or injection molding, composite material must be demonstrated.

Guided by the main challenges for a modular microfluidic implementation, the studies in this thesis followed the path stated in the [Introduction chapter](#).

4 Silicon microfluidic channels by femtosecond laser engraving

In this chapter, silicon microchannel cooling substrates, as state-of-the-art for microfluidic cooling solutions in the present HEP detectors, are considered. An alternative solution for the Si microchannel production, based on femtosecond laser engraving, is investigated and compared to the typically used "photolithography-etching processes".

4.1 Purpose of the research

The research investigates the possibility of producing silicon microchannel cooling substrates by femtosecond (FS) laser engraving as an alternative to the “*standard*” photolithography and DRIE/wet etching steps. Laser engraving has two main advantages:

- It minimises the production steps in the clean room and allows the quick production of low-cost prototypes.
- It allows pattern microchannels on Si plate shapes different from the Si wafer geometry. It means producing silicon μ CS on large wafers, minimising the fabrication cost, and engraving microchannels directly on diced chips.

FS laser technology was considered because ultra-short pulsed photons interact with the electrons of the substrate on a time scale shorter than is needed to transfer energy from the electrons to the lattice (of the order of picoseconds). This avoids significant thermal degradations of the surrounding zone and continuous heating of the etched surfaces. It results in a cold ablation of the target material and minimisation of the Heat Affected Zone (HAZ) [153–155].

The research tried to understand the limitations and advantages of the FS engraving compared to the standard production procedure focusing on achievable microchannels dimensions and the quality of the bonding interface.

Nevertheless, the closure of silicon μ CS by standard bonding procedures, such as Si-Si direct bonding, still implies subsequent clean room steps. Therefore, a simple adhesive-based alternative to close the microchannels was developed.

The Sirris [156] company was responsible for the femtosecond laser engraving step. Sirris references persons involved in the project are E.Kunnen and S.Lambrechts.

4.2 Methodology

The engraving was done on a LASEA LS5-1 10W fs-laser [157]. The laser emits photons at wavelength $\lambda = 1030$ nm, with 20 μ J as pulse energy and 250 fs at Full Width at Half Maximum (FWHM). The spot diameter is ~ 15 μ m, and the maximal operation frequency is 500kHz at 10W power. Eight Silicon wafers (crystal orientation $\langle 100 \rangle$, diameter $\varnothing 100$ mm, p-type doped, resistivity 1-10 Ω cm) were processed, 4 bare silicon wafers and 4 silicon wafers with 2 μ m oxide layer hard mask on both sides (Table 4.1). The wafers were double-side polished, their thickness was 380 μ m, and their Total Thickness Variation (TTV) was 5 μ m.

The project was executed in four phases.

1. Firstly, a Design Of Experiments (DOE) was carried out to calibrate and parameterise the FS laser engraving of the Si wafers. The lowest roughness, possibly similar to the DRIE etched surfaces (< 1 μ m), was targeted. In addition, the silicon temperature increase was controlled during engraving.
2. After that, a learning cycle was executed on three wafers to demonstrate the feasibility of anodic bonding of Si wafers after FS laser engraving. The wafers were anodic bonded to borosilicate wafer covers (Borofloat 33 [158], 525 μ m thick). A metrology survey (i.e. engraving uniformity, channel surface finishing and aspect ratio of the engraving) was performed.
3. Two wafers were then processed to produce microchannel samples for the burst pressure test. This test aimed to find any difference at the bonding interface compared to Si microchannels produced through DRIE etching.
4. Finally, another engraved wafer was used to investigate the novel adhesive-based bonding procedure.

The wafers' inspection, cleaning, and anodic bonding steps were performed at the EPFL CMi clean room. A surface profiler (Bruker Dektak XT) and a scanning electron microscope (SEM, Zeiss LEO 1550) were used to inspect the microchannels, while the Süss SB6 machine was used for the anodic bonding [159]. Burst pressure tests were performed at the CERN EP-DT department [160] in a standard pressure test set-up for silicon devices.

Table 4.1: Summary of Si wafer labelling.

Label	Type	Usage
CMI 1 1 10 7345	Silicon only	DOE – experiments
CMI 1 1 10 7240	2 µm silicon oxide	DOE - experiments
CMI 1 1 10 7236	2 µm silicon oxide	Anodic bonding test
CMI 1 1 10 7630	Silicon only	Anodic bonding test
CMI 1 1 10 7260	2 µm silicon oxide	Anodic bonding test
CMI 1 1 10 7497	Silicon only	Burst pressure test
CMI 1 1 10 7445	Silicon only	Brust pressure test
CMI 1 1 10 6999	2 µm silicon oxide	Other bonding test

4.3 DOE

Laser parameter variations considered in the DOE are in Table 4.2.

Table 4.2: FS laser parameters for DOE.

Pulse frequency:	100-500 kHz
Head speed:	1000-3000 mm/s
Laser power:	50-80%
Hatch pitch:	7-15 µm

A first run was conducted to determine the removal rate during a single lasering step. In a second run, the number of layers was repeated to target a depth of 200 µm. With respect to the lowest roughness, the best result was achieved at the pulse frequency of 100 kHz, head speed of 3000 mm/s, laser power at 80% and 7 µm hatch pitch requiring 768 layers to reach 200 µm. Operating at 100 kHz corresponds to an output power of 2W, resulting in a sub-optimal process time.

The results on a square 1x1 mm² are shown in Figure 4.1.

On a large scale, the roughness was of the order of $S_a = 2.8 \mu\text{m}$ and $S_z = 30.6 \mu\text{m}$. A texturing and some craters appeared on the engraved surfaces (Figure 4.1.a-c). The craters also appeared in other materials, e.g. steel, and could be reduced by subsequent DOE's. Typically, texturing is induced by the Laser Induced Periodic Surface Structures (LIPSS) phenomenon. This phenomenon happens on most of the solid materials that are exposed to linearly polarised laser radiation [161–164]. Typical produced surface structures are "ripples".

In addition, debris likely due to material re-deposition during the plasma phase was observed, which implies a cleaning step before proceeding to bond. During the process, the temperature of the Silicon substrate remained close to the room temperature (20-23 °C) as evidence of the minimum heating of the etched surface, Figure 4.1.d.

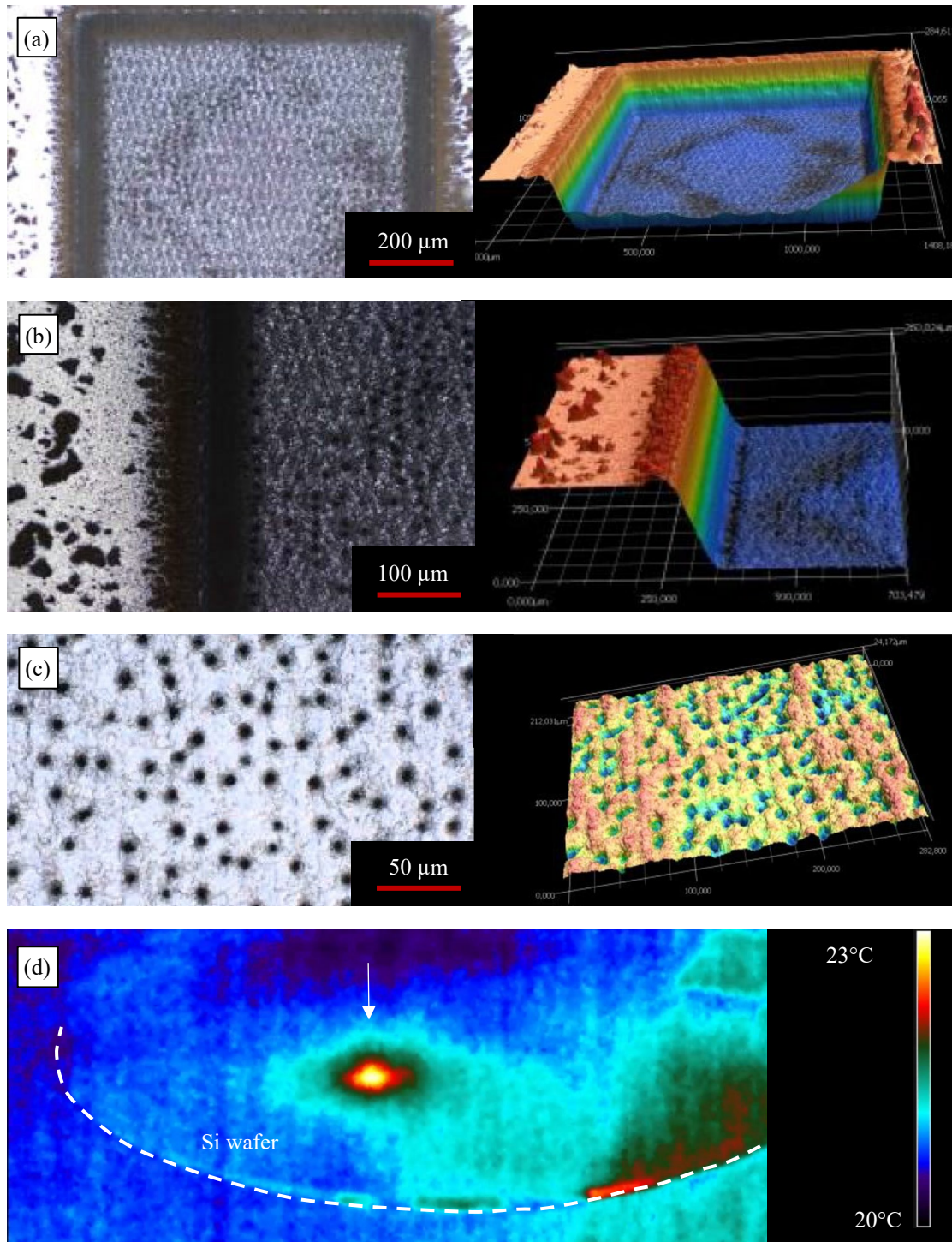


Figure 4.1: The outcomes of the DOE. (a) Picture of a 1 mm etched channel, (b) channel wall, (c) detail of the craters at the bottom surface and (d) thermal imaging during the FS laser engraving of a circle with a diameter of 4 mm. The pictures were taken by Sirris company. The first metrology was done by using a Keyence VK 1100 3D confocal microscopy [165].

4.4 Anodic bonding test

Re-deposited material on the top wafer surface did not allow the anodic bonding of the wafer as it is and required an intermediate step to eliminating it. Two different solutions were investigated:

- The first solution corresponded to processing a silicon wafer (CMI 1 1 10 7236) with 2 μm of silicon oxide layer deposited on the surfaces by Physical Vapour Deposition (PVD). The silicon oxide hard mask served to protect the top surface. The SiO_2 layer was removed, together with the debris, by Buffered HydroFluoric acid (BHF) etching right before the piranha cleaning step.
- The second solution was polishing the wafer (CMI 1 1 10 7630) to remove the deposited Si debris before the piranha cleaning and bonding steps. This procedure was also followed by other studies of Si engraving with different laser technologies.

The laser pattern and the processed wafers are shown in Figure 4.2. Surface contact was avoided since cleaning is known to be sensitive to prehistory. Five different sets of trenches were designed. Five channels with different widths (100, 250, 500, 750 and 1000 μm) composed a set of trenches. Each set had a different channel inter-distance (100, 250, 500, 750 and 1000 μm). The sets were allocated far from each other to minimise possible influence during the bonding procedure. The sets were named "Centre", "North", "South", "East" and "West" based on their position in the wafer (Figure 4.2.a).

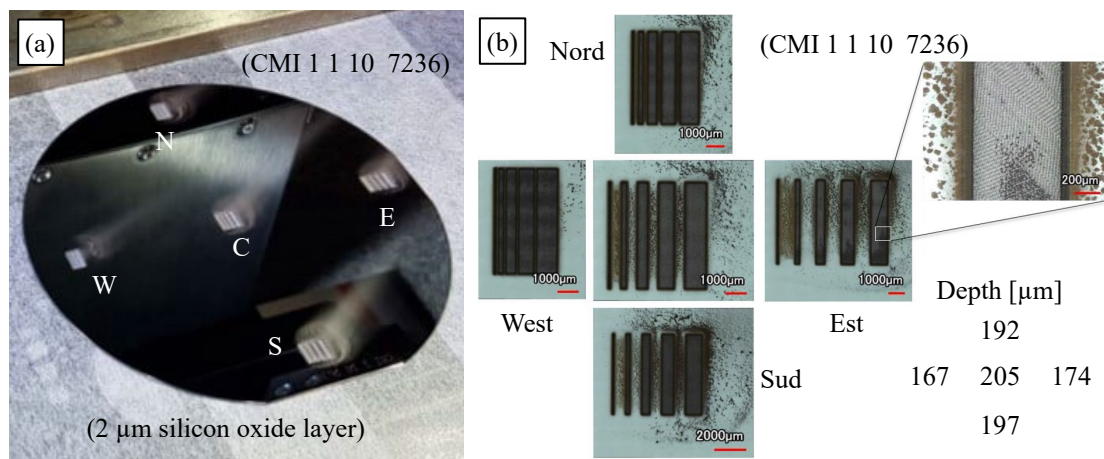


Figure 4.2: Laser pattern for anodic bonding test. (a) Silicon wafer with silicon oxide hard mask after the FS laser engraving and details (b) of the sets of the trenches. The 4" design was too large for the laser scanner to handle at once. Therefore, the wafer design was chopped into dies, one of the dies for each set. The micrometer stage moved the wafer to the center of a die before lasering it. Moreover, a job queue was used because of software limitations to handling many structures inside one job. The pictures are taken by Sirris company.

Chapter 4. Silicon microfluidic channels by femtosecond laser engraving

At CMi, the wafers received a preliminary deionised water (DI) rinse before going to the following cleaning and inspection steps. Figure 4.3 shows the wafer (CMi 1 10 7236) used to investigate the first solution, i.e. based on a silicon oxide hard mask for protection.

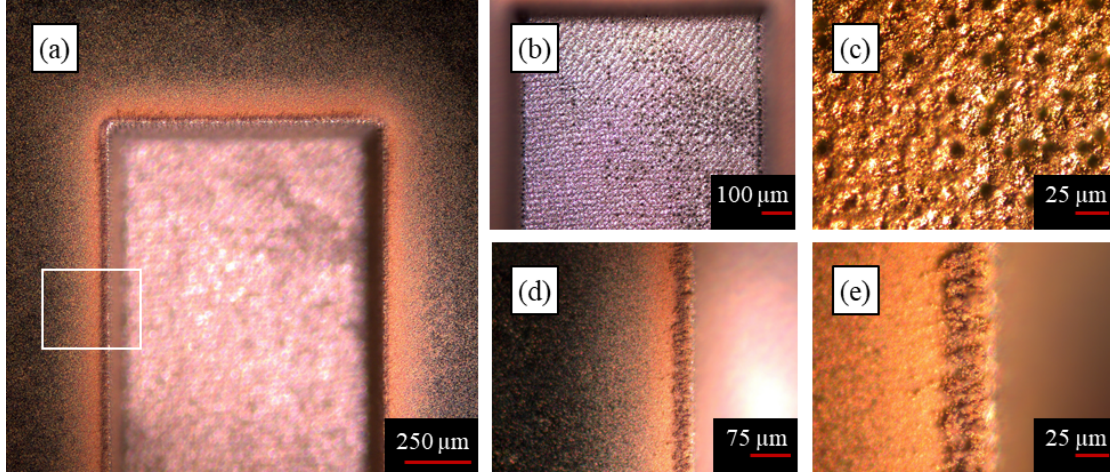


Figure 4.3: Silicon wafer (CMi 1 10 7236) with SiO_2 hard mask after DI rinse. (a) The 1 mm trench in position "Est" and (b-e) details of the engraved surface and residues present at the edge of the trench. Pictures were taken with a Leica DM800 microscope [159].

The SiO_2 stripping with BHF etching was unable to remove all the residues (Figure 4.4). Also, the subsequent piranha cleaning step was inefficient.

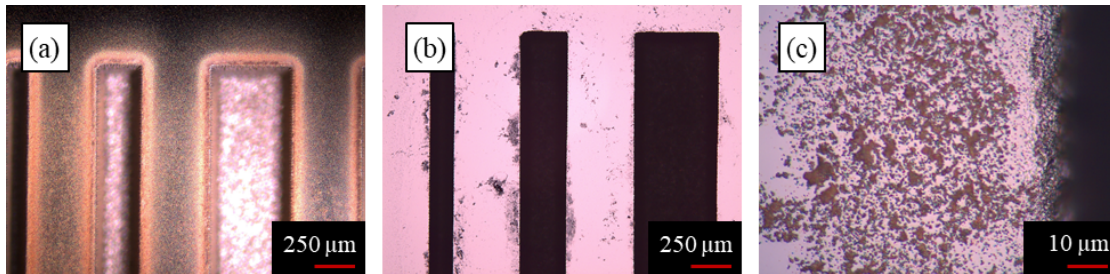


Figure 4.4: Silicon wafer (CMi 1 10 7236) after SiO_2 hard mask removing. Detail of trenches in position "Centre" (a) before and (b) after buffered HF etching and (c) details of residues. Pictures were taken with a Leica DM800 microscope [159].

It was then decided to move the focus to the bare Si wafer (CMi 1 1 10 7630). The SEM inspection after DI rinse can be seen in Figure 4.5. Afterwards, the wafer entered the Steag Mecapol E 460 CMP machine [159]. Only deionised water (no slurry) between the wafer and polishing pad was used to remove the particles at the top surface, avoiding polishing the silicon surface.

As can be seen in Figure 4.6, the entire wafer surface was naked, and the debris was removed already after 30 seconds of polishing. This gave a reason that this debris was only Si particles re-deposited during engraving.

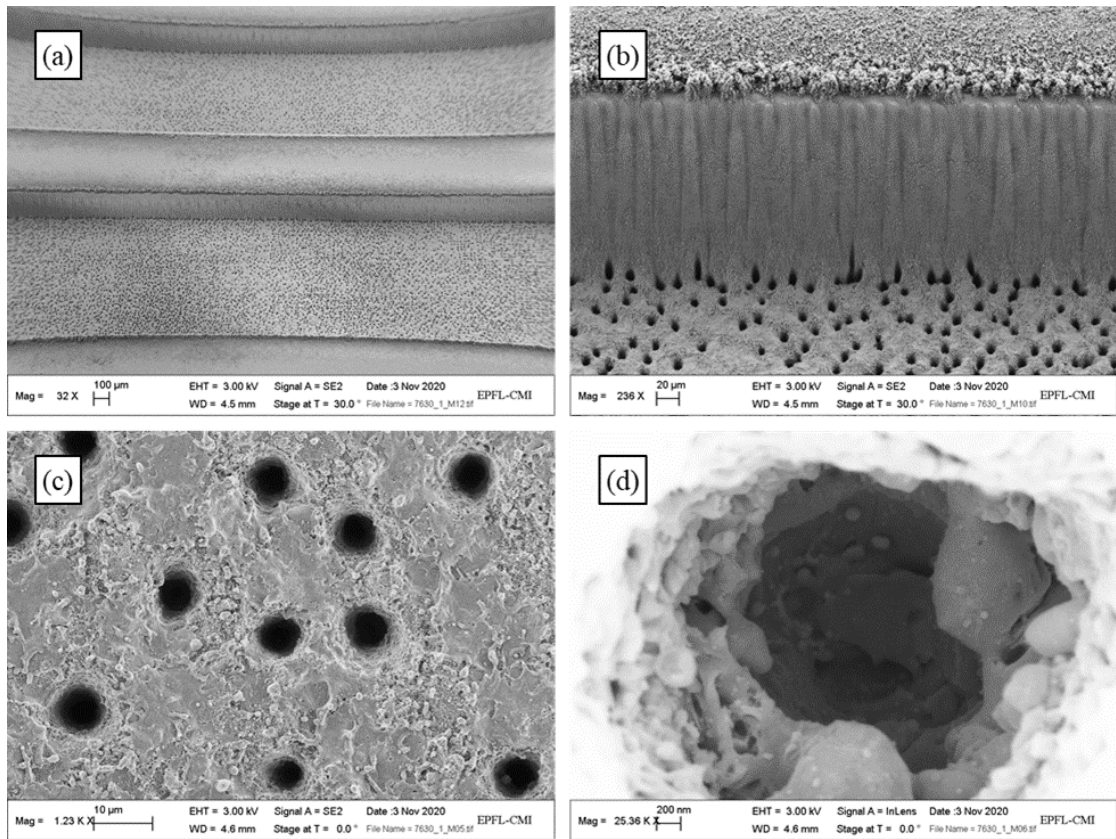


Figure 4.5: SEM pictures of the Silicon wafer (CMi 1 10 7630) after DI rinse. (a) Details of two trenches in position "Centre", (b) edge of a trench, (c) engraved surface and (d) crater. SEM images were taken with Zeiss LEO 1550 [159].

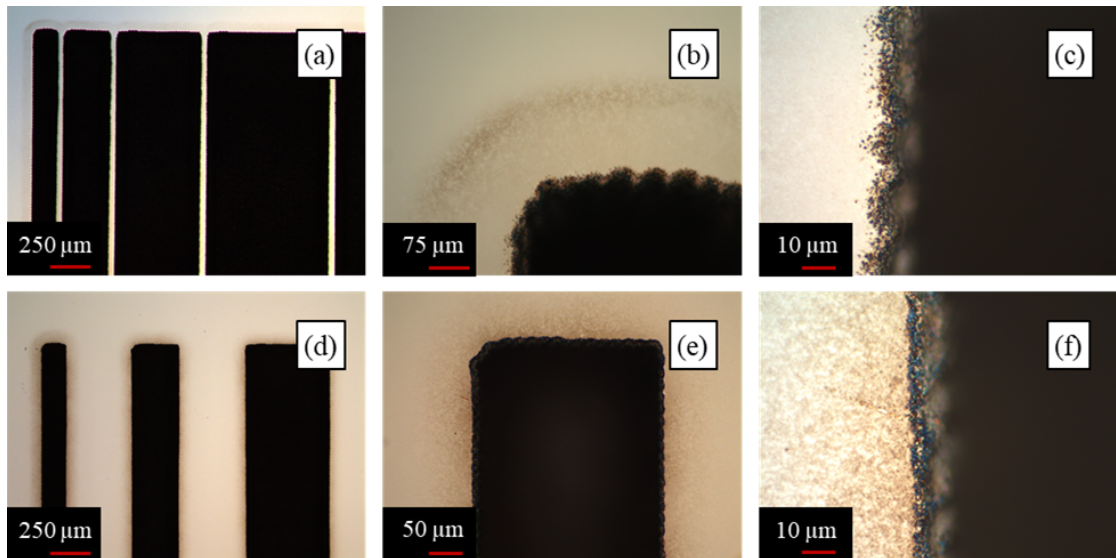


Figure 4.6: Silicon wafer (CMi 1 10 7630) after CMP polishing. (a-c) Details of trenches in position "West" and (d-f) details of trenches in position "Centre". Pictures were taken with a Leica DM800 microscope [159].

The wafer (CMI 1 1 10 7630) went under piranha cleaning and anodic bonding steps. The Si wafer and the cover were put in contact before anodic bonding. However, the "*cold adhesion*", which typically appears when clean Si and Borosilicate surfaces are put in contact, did not initiate (Figure 4.7.a). This can be a symptom of possible defects of the Si surface areas at the channel sides, which did not permit the cold adhesion. Nevertheless, the wafer was successfully bonded (Figure 4.7.b). The anodic bonding followed a standard CMi low-stress bonding receipt. The bonding was done at 350 °C, at ambient pressure (0.1 MPa), and 150 kPa pressure was applied to the wafer stack. The silicon and the borosilicate wafers were subjected to a voltage greater than 1100 V. The bonding ended when the current between the wafer stack reached 14% of the starting value.

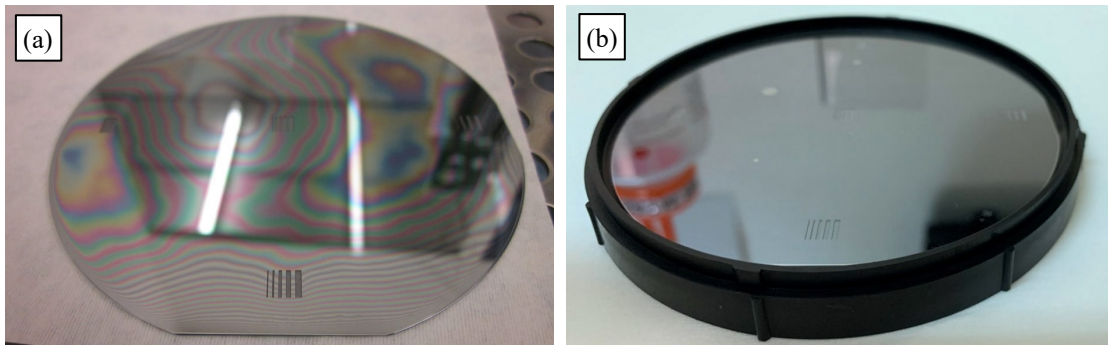


Figure 4.7: Anodic bonding of the silicon wafer (CMI 1 1 10 7630). (a) Before and (b) after anodic bonding. During the anodic bonding, an additional auxiliary borosilicate wafer is placed on top of the borosilicate cover to be bonded. It is typically added to collect Sodium (Na) ions that migrate from the bonding Si-SiO₂ interface to the top auxiliary glass surface. This standard procedure leaves the glass cover clean and transparent.

In addition, a third wafer, with the entire surface covered by trenches, went under mechanical brushing and mega-sound cleaning step (CMP Cleaning System GnP Cleaner 428) only before piranha cleaning and bonding (Figure 4.8). This demonstrated that a "*non-aggressive*" cleaning step is already sufficient to guarantee the anodic bonding.

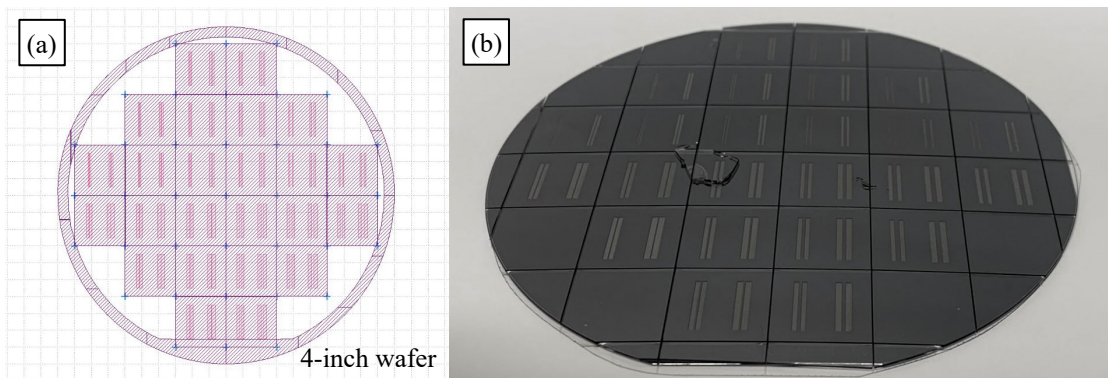


Figure 4.8: Anodic bonding of the silicon wafer (CMI 1 1 10 7260). (a) Layout and (b) wafer after anodic bonding and dicing. Trenches width and inter-distance between trenches range 100 -1000 μm . Unexpectedly, a piece of the auxiliary borosilicate wafer remained stitched on the borosilicate cover.

4.5 Pressure test

Two bare Si wafers, with 30 pressure samples each, were anodic bonded following the cleaning process of the wafer CMI 1 1 10 7630 (i.e. no slurry in the CMP polishing machine). The sample design corresponded to the “*standard*” one used for burst pressure tests at CERN EP-DT department [103] (see Figure 4.9). The set-up is shown in Appendix C. The tested channel width (W) of the samples varied from 250 to 1500 μm .

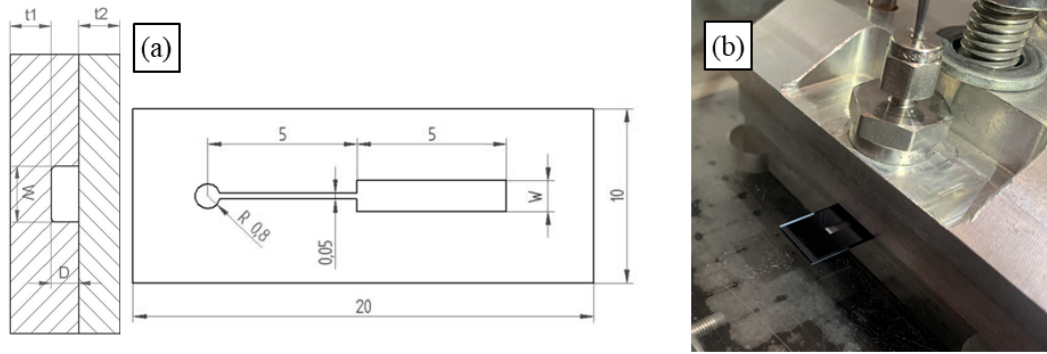


Figure 4.9: Burst pressure test sample. (a) Sample layout and (b) sample inserted in the set-up.

The burst pressure results were compared with the burst pressure results of previous samples etched with DRIE etching process by T.Frei [95]. The comparison can be seen in Figure 4.10.

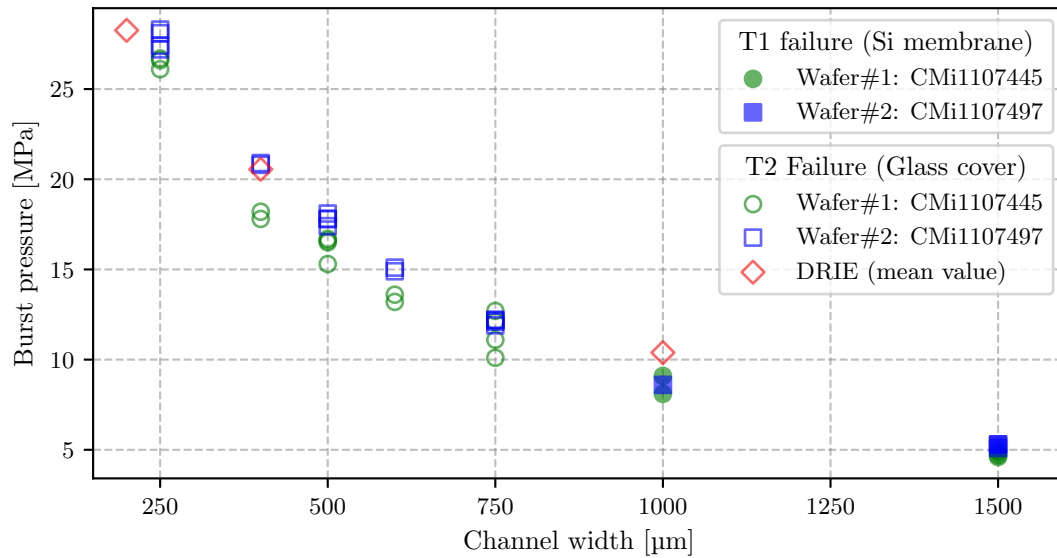


Figure 4.10: Burst pressure results. The burst pressure values of the Si samples are plotted as a function of the channel width. The samples failed at the 525 μm thick Borofloat 33 [158] cover (T2 failure) of the two wafers (CMi 1 10 7445 and CMi 1 10 7497) are compared with similar failed samples etched with DRIE process [95].

The burst pressure values of the engraved samples were in the same range of samples produced with DRIE etching process. Engraved samples with a width equal to or greater than 1000 μm failed at the silicon surface side. This failure is denoted T1 in Figure 4.11.a. While samples with a width lower than 1000 μm failed at the anodic bonding interface resulting in a detaching of the borosilicate top surface (T2 failure in Figure 4.11.b and c).

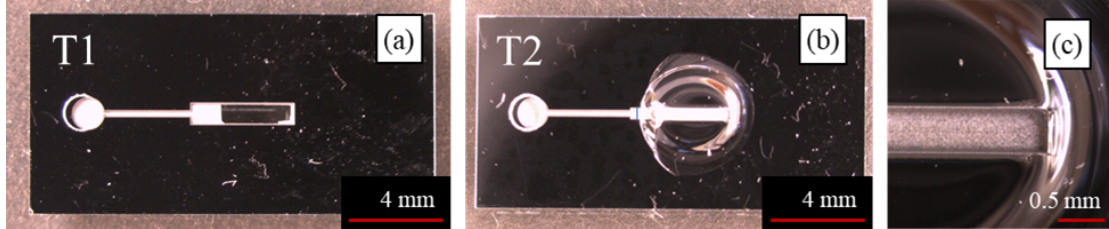


Figure 4.11: Failures of the burst pressure samples. (a) T1 failure (failure of the etched silicon membrane), (b) T2 failure (failure of the borosilicate cover) and (c) detail of T2 failure.

4.6 Metrology

A profilometer inspection was performed for all the wafers. An example of the profile measurement is in Figure 4.12, while a cross-section of trenches is in Figure 4.13. The depth of the trenches typically varied between 200, at the wafer centre, and 170 μm , at the wafer edge. This non-uniformity could be solved by further optimisation of laser parameters.

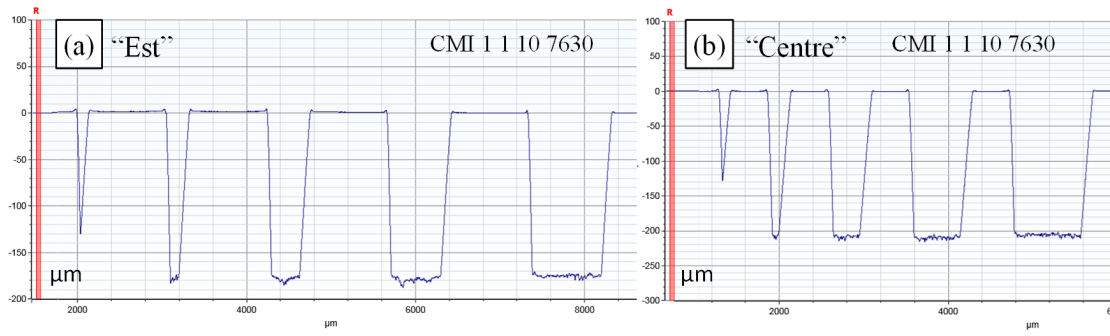


Figure 4.12: Examples of the profilometer inspection (CMI 1 1 10 7630). (a) Channels in position "Est" and (b) "Centre". The measurements in the picture were performed before the CMP polishing. It is possible to notice debris at the top of the channel walls. The radius of the Bruker Dektak XT was 12.5 μm , and the scan resolution was 0.56 μm . The stylus was not able to correctly enter inside the 100 μm microchannel.

High Aspect Ratio (HAR), usually realised with reactive ion etching (RIE) [166], can not be achieved by FS laser engraving. The trench's walls have a slope of approximately 20 degrees. This slope transforms the nominal rectangular cross-section into a triangular cross-section in channels with a width <100 μm (see Figure 4.13.b).

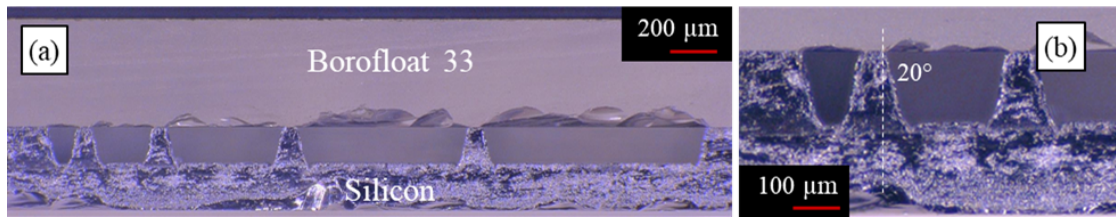


Figure 4.13: Cross section of a diced wafer (CMI 1 1 10 7630). (a) Channels in position "West" and (b) details of 100-250 μm wide channels.

4.7 Adhesive-based bonding procedure

A novel adhesive-based solution was investigated to seal the Si trenches, avoiding further steps in the clean room. It is based on the use of "*carbon fleece*" [167] impregnated with glue as a closing cover for the microchannels. The carbon fleece, or carbon veil, is a thin layer of woven carbon fibres orientated randomly. It is typically used in carbon composite materials to provide compactness in composite lay-ups. In our case, the carbon fleece serves as a retaining material (porous media) and avoids the penetration of the glue inside the microchannels. As far as the surface tension acting on the glue impregnated in the carbon fleece is greater than the capillary force induced by the empty channels, the glue does not spread in the channels.

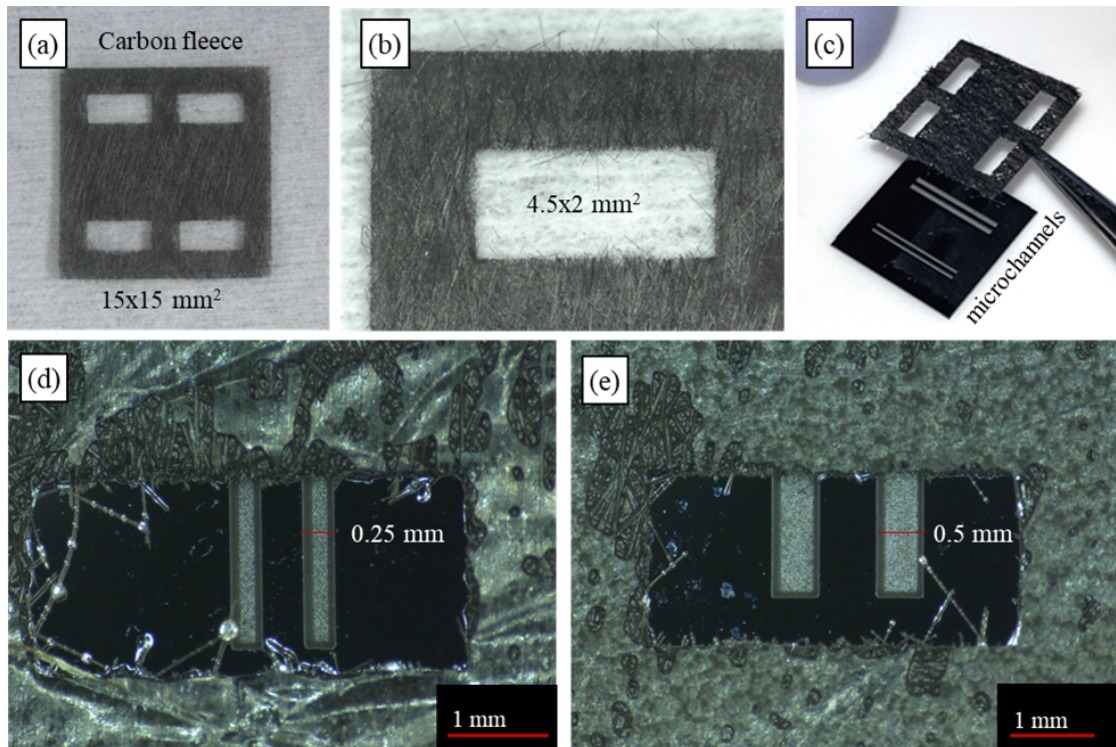


Figure 4.14: Si microchannels closed by a carbon fleece layer. (a) Dry Carbon fleece cut with CO₂ laser, (b) detail of windows opened with the laser, (c) impregnated carbon fleece during Si gluing and (d-e) detail of the cured carbon fleece cover.

In addition, the carbon fleece can be used as intermediate material between the silicon substrate and the feed-line connector, as depicted in Figure 4.15. The connector in the picture was 3D printed in ACCURA25 [168] by stereolithography (SLA).

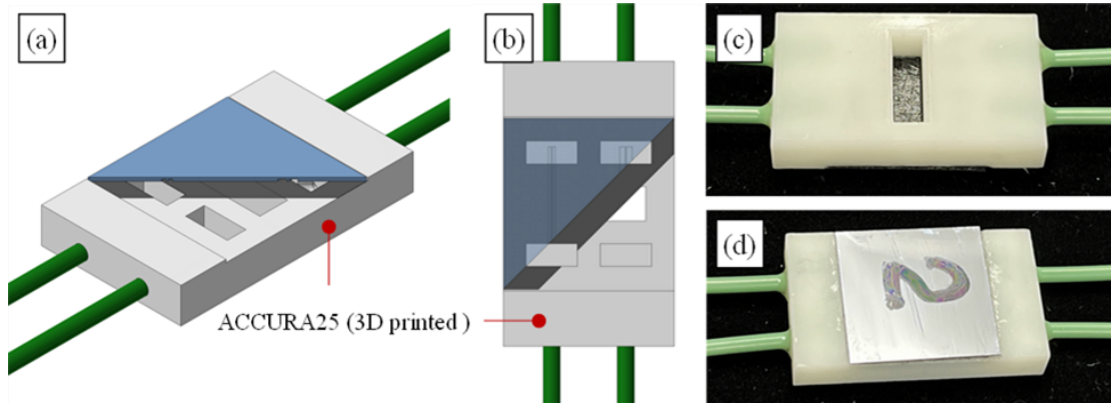


Figure 4.15: Si dice bonded to a 3D printed connector by a carbon fleece layer. (a-b) CAD design and (c-d) Si dice glued to the 3D printed connector. The carbon fleece was impregnated with Araldite 2011 [66]. The glue curing was at ambient temperature and pressure.

The selected carbon fleece has a $7\text{ }\mu\text{m}$ fibre diameter and an areal weight of 20 g/m^2 corresponding to a thickness of 0.24 mm (at 10 kPa of pressure). The veil cover was CO_2 laser cut (Trotec speedy 400 [169]) with an accuracy of $15\text{ }\mu\text{m}$. The cover was firstly impregnated with glue (Araldite 2011 [66]), and calibrated shims (0.1 mm) were used to control the glue quantity. After that, the impregnated cover was placed on the silicon dice ($15\times 15\text{ mm}^2$), and a pressure of 2 KPa was applied during the curing at ambient temperature.

The thickness of the cured cover was measured between 0.2 and 0.25 mm . Smaller (larger) thicknesses can be achieved by using a raw carbon veil with different areal weights or by tuning production parameters, i.e the pressure applied during curing or the shim thickness during gluing impregnation. The CTE of the carbon fleece ranges from 1 to $10\text{ }\mu\text{m/m}^\circ\text{C}$ depending on the applied compression of the lamina.

Different samples, with a width of the trenches ranging from 250 to $1500\text{ }\mu\text{m}$ and inter-distance between trenches ranging from 250 to $750\text{ }\mu\text{m}$, were bonded, and the channels remained open. The samples withstood pressures up to 4 MPa . The failure occurred in the silicon substrate in correspondence with the inlet of the microchannel (Figure 4.16). In addition, a He leak test was performed to investigate the leak-tightness of the solution (the set-up is in Appendix C). The He leak rate was $<3\cdot 10^{-9}\text{ mbar l/s}$ under medium vacuum ($<10^{-3}\text{ mbar}$).

A possible solution to improve the Si-carbon fleece bonding strength could be to pattern the silicon surface facing the carbon fleece. The Sirris company was able to FS laser engrave pillars on a large silicon surface (Figure 4.17). In this case, a well-calibrated force applied to the carbon fleece during curing could allow the braiding of the pillars with the carbon fibres. In addition, FS laser engraving alters the morphology of the silicon surface and, therefore, its hydrophobic property. A hydrophobic layer, FS laser engraved, could prevent the penetration

of the glue in the channels. All these aspects need further investigation.

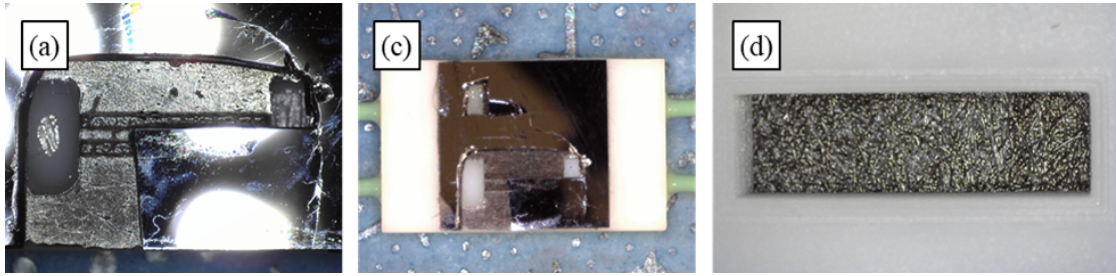


Figure 4.16: Burst failure of a Si sample closed by a carbon fleece layer. (a) Si failure at the manifold inlet, (b) Two different failures at the manifold inlet and (c) undamaged carbon fleece cover at the opposite side.

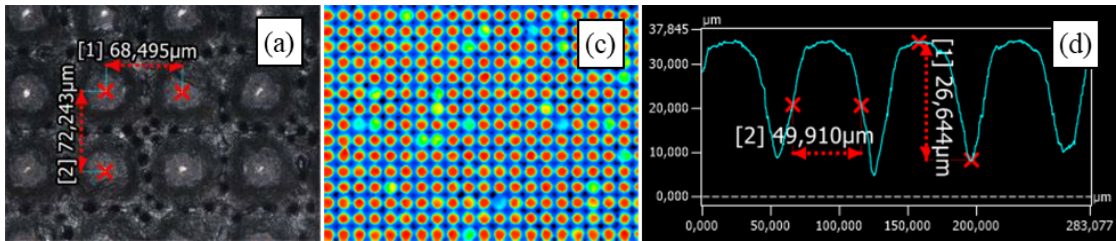


Figure 4.17: FS laser patterning of pillars on a silicon surface. (a) Patterned surface, (b) 3D scan and (c) profile measurement of the pillars. Metrology was performed at Sirris company with a Keyence VK 1100 3D confocal microscopy [165].

4.8 Outcomes

It was demonstrated that microchannels can be engraved inside a silicon substrate (380 µm thick) with FS-laser technology. We successfully produced 200 µm deep channels with a width down to 100 µm and an inter-distance between channels down to 100 µm. The depth difference between the channels at the wafer centre and the wafer side was 10%. The walls of the channels have a slope of approximately 20 degrees. This brings triangular cross sections for channels with less than 100 µm as nominal width. Therefore, the high aspect ratio typically achieved with the DRIE etching process was not reached with the FS laser.

No upstanding melting zone in the Si wafer was observed with the femtosecond laser (ultra-short pulse), but only re-deposition material from the plasma phase. The absence of melting zones represents a clear advantage compared to other laser engraving technologies, as it allows for reliable surface bonding. In addition, the low temperature (20-25 °C) kept during the FS engraving opens the possibility to realise channels directly at the back of diced chips. Nevertheless, the unavoidable material re-deposition requires an additional cleaning step. After a brush and mega sonic cleaning, it was possible to seal the microchannels with a borosilicate glass cover by anodic bonding.

Chapter 4. Silicon microfluidic channels by femtosecond laser engraving

FS process creates micro craters (diameter 5-10 μm) at the bottom of the engraved channels. The craters can trigger nucleation when evaporative coolants are considered. This effect is positive in the microchannel area when evaporation is the main target; it increases the heat transfer coefficient. On the flip side, it is negative when condensation is required. This aspect requires further research. Note that μCS s in HEP are mainly evaporative cold plates.

FS engraved channels withstood similar pressures compared to DRIE etched channels. Therefore, the surface quality at the bonding interface appeared unaffected by the FS process. This was demonstrated for the bonding interface between silicon and borosilicate wafers, and a similar investigation should be performed for Si-Si direct bonding.

Since no photolithography step is required, reducing process steps in the clean room could result in an economic gain. On the other hand, the silicon (oxide) wafer production took 11 hours (23 hours). However, the FS-laser technology is evolving fast. Today 100W lasers are already available. Such output power with a fast mirror could reduce the processing time to half an hour per wafer, which is a competitive time compared to the traditional deep silicon etch (5 $\mu\text{m}/\text{min}$).

Silicon dices (15x15mm², 380 μm thin) with FS engraved channels were successfully closed with a carbon fleece cover impregnated with epoxy resin. In this case, the carbon fleece serves as porous media (retaining material) and avoids the penetration of the glue in the microchannels. It was possible to close channels down to 250 μm in width and 0.5 mm as inter-distance between two channel walls. The samples reached pressures up to 4 MPa and He leak rate of the order of 10^{-9} mbar l/s. The silicon failed at the inlet of the microchannels while the carbon fleece cover remained intact. Higher pressures can therefore be achieved. Further research is required to investigate the potentiality of this bonding procedure in terms of minimum channel dimension, pressure resistance, channel leak-tightness and operative temperature.

Based on the presented achievement, a combination of FS laser engraving and Si-carbon fleece bonding could allow direct embed microchannels on real chips and find applications from electronics cooling (microchips and data centres) to energy conversion systems. Applying such a procedure to a real chip is a possible future development. The study of long-term reliability, considering several thermal cycles with different compatible fluids, should be pursued.

Regardless of the successful production and qualification of microchannels with femtosecond laser technology, no clear advantages were identified in terms of process simplification and cost saving with respect to the more standard etching process. It was, therefore, decided to refrain from investing additional time in analysing the other key aspect of the silicon cooling substrates design, i.e. the interconnection between Si substrates, and to move instead to other technologies (i.e. 3D printing).

5 Interlocking microfluidic interconnection

The developments of the novel interlocking interconnections for microfluidic application are described in this chapter. A baseline interconnection was identified, and its design was optimised and validated. This part of the chapter is based on the paper "First steps towards interlocking modular microfluidic cooling substrates (i-M μ CS) for future silicon tracking detectors in High Energy Physics (HEP)" [170]. After that, alternative designs were developed. The advantages and the disadvantages of all solutions were highlighted and compared.

5.1 Guidelines for the interconnection development

The development of the novel interlocking microfluidic interconnections started from studying the existing re-workable interconnections at the millimeter scale and followed a miniaturisation of such solutions to micro-feature dimensions. Two different interfaces make an interlocking microfluidic interconnection:

- The "*hydraulic interface*" which provides the sealing between modules.
- The "*mechanical interface*" which guarantees the modules' positioning and clamping.

The key parameter affecting the dimension scaling is the achievable manufacturing accuracy. As the limit case study, the minimum inner diameter at the hydraulic interconnection was set to 0.5 mm. Interconnections with smaller diameters are not intended to be applicable to the investigated modular cooling solutions. This is because a significant pressure drop will be induced by the considerable amount of mass flow (imposed greater than 0.3 g/s) distributed along prolonged cooling circuits or sub-circuits (Section 3.4).

The coolant choice drives the design evolution of the interlocking microfluidic interconnection. In this thesis, the fluid considered as the baseline is demineralised water at ambient temperature. Nevertheless, the design targets the use of different coolants whose long-term thermal behaviour will be studied in further research.

The hydraulic interface must be re-workable and as simple as possible. As a natural consequence, the research considered elastomer gaskets as sealing elements with the idea of considering more elaborated sealants (like metal-based) as the research moves forward. The mechanical interface must easily be integrated into a modular cooling substrate design while prioritising the minimisation of the added passive material in the active sensing area.

The selected production process and the material play a key role with respect to the achievable tolerances. Samples were produced in polymeric AM materials. This choice is based on the relative facility of 3D printing parts with micro features and the possibility to optimise their geometries rapidly. Nevertheless, polymeric cooling substrates can find applications in HEP trackers at lepton colliders where the sensors can be operated at ambient temperature (Section 7.2.2).

The developed interconnections should be designed to be minimally dependent on the type of material and manufacturing production process. Nevertheless, using different materials and manufacturing processes implies to re-assess the achievable tolerances and geometries. This will be done in Section 6.4 when ceramic AM is considered as cooling substrate material.

5.2 The baseline interlocking microfluidic interconnection

The interlocking microfluidic interconnection, proposed as a baseline in this research, is based on a LEGO®-like concept (Figure 5.1). Modules' positioning and mechanical clamping are realised through a "baseplate" whose "pins" engage "slots" located at the back of the cooling substrate. The interference between pins and slots guarantees the substrate's correct positioning and clamping. This mechanical interface is denoted hereafter as "pin-based".

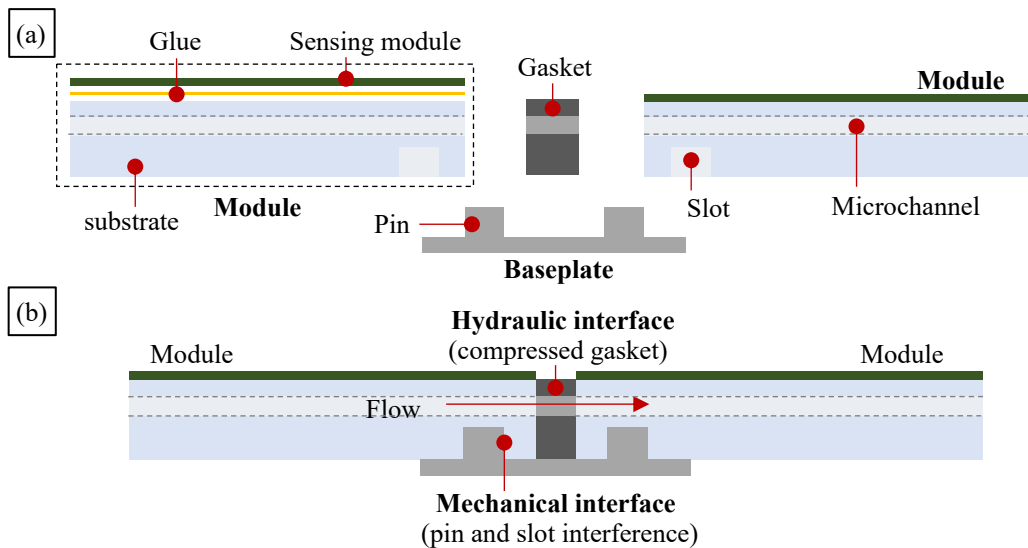


Figure 5.1: Interlocking modular concept. (a) Exploded view and (b) assembled view.

5.2 The baseline interlocking microfluidic interconnection

An in-plane hydraulic interconnection is realised through a gasket pressed between the substrates. This hydraulic interface is denoted hereafter as “*face seal*”. The compression force of the gasket is provided by the pins and slots anchoring. The design challenge comes from the micro-dimensions of the features in the substrate and in the baseplate, affected by the accuracy that can be achieved during production.

As a preliminary proof of concept, it was decided to produce a breadboard model prototype (Figure 5.2), taking inspiration from commercial LEGO® and preserving similar standard LEGO® dimensions, as in part was done by C. Owens [138]. Nevertheless, the geometry of the pin and slot, as well as their interface, differs from standard LEGO® design, based on the necessity to include channels in the sample and to minimise its thickness. No leaks up to 1 MPa have been detected in the experimental tests.

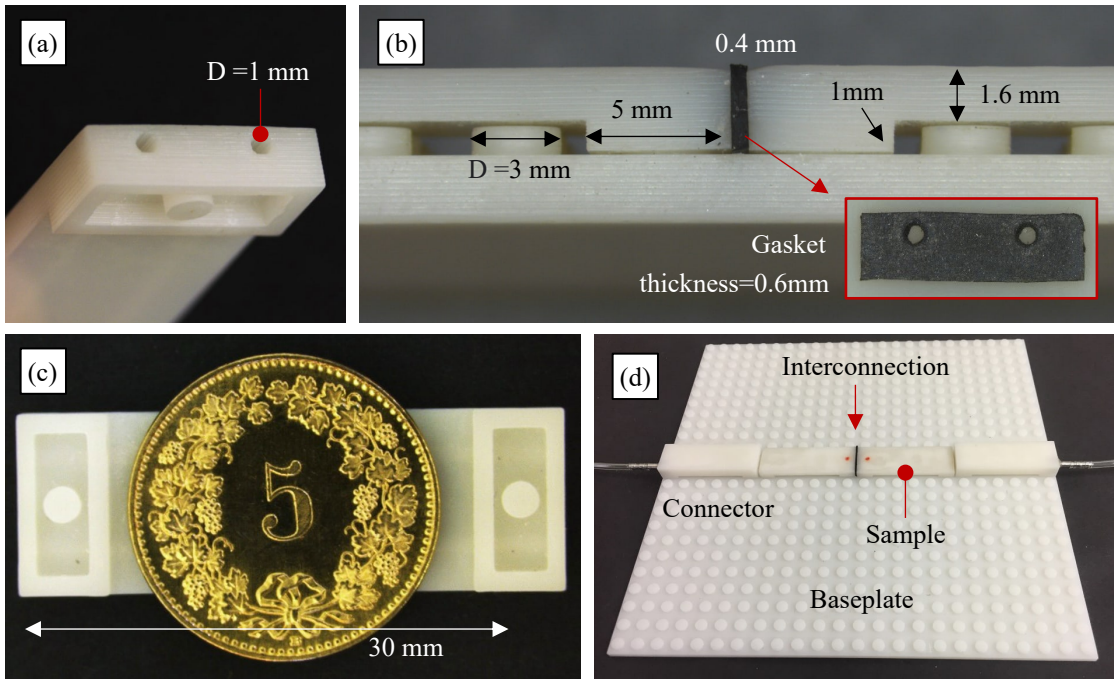


Figure 5.2: Detail of the first prototype. (a) Detail of the sample with two embedded channels with a diameter of 1mm, (b) detail of the sample slot, (c) samples and baseplate assembly and (d) detail of the fluidic interconnection.

5.2.1 Experimental methodology of the optimisation

The modular interconnection of the i-M μ CS should guarantee a stable mechanical connection within the elastic regime of the different components, not influence the precise module positioning and satisfy the cooling requirement in terms of hydraulic pressure resistance.

The experimental methodology to qualify the i-M μ CS interconnection followed an iterative process that involved analyses, prototypes production and tests. Different interconnection

designs and polymeric materials were investigated. Three relevant properties were identified to develop and validate the mechanical and hydraulic interconnection: substrate "*Plug-and-play*", "*Interchangeability*" and "*Sealing performance*". The key parameters affecting these three properties are the substrate and baseplate's dimensional accuracies.

- The "*Plug-and-play*" property can be represented by the pull force needed to mount and dismount a substrate from the baseplate. The force should avoid the sensor's damage during assembly while keeping in place the sensor stably. This force is determined by the static friction coefficient between pin and slot and depends on the materials of the baseplate and substrate. Therefore, the optimisation of the plug-and-play parameter in this phase of the design was not driven by the necessity to reach a specific range of pull force, but instead, by the design of a mechanical interface that can be tuned according to the requirements of the specific chosen materials.
- The "*Interchangeability*" is the ability to select components at random and fit them together within proper positioning tolerances, typically of the order of 50 μm for HEP tracker sensors [1], while fulfilling plug-and-play and sealing requirements.
- The "*Sealing performance*" is quantified through the pressure at which the leak appears at the interface between modules and depends on the coolant and its operational range. The requirement of 0.3 MPa is set for demineralised water applications that operate in leak-less mode. It corresponds to the safety margin with respect to the nominal operating pressure range that goes from 0.02 to 0.08 MPa [48]. However, the qualification to higher-pressure resistance will allow to consider the solution for applications that operate with more demanding coolants.

5.2.2 Design optimisation

Many variables influence the accuracy of 3D print parts, such as their orientation during the printing process, the printing layer's thickness and the printing technology. However, we can assume that the minimum dimensional accuracy obtained for the polymer substrates by commercial additive manufacturing is of the order of 50 μm corresponding to a total standard deviation (σ_{tot}) of 25 μm . With the substrate features' dimensions close to the achievable accuracy, the following criticalities were identified:

- The maximum contact pressure (p_{max}) between the pin and slot could cause punctual plastic deformation. For a given manufacturing accuracy, a corresponding minimum pin diameter must ensure to be within the elastic regime during all different assembly steps.
- The cooling substrate slots, and therefore the cooling substrate itself, absorb most of the deformation induced by the pin and slot interference. The cooling substrate deformation is seen by the silicon sensor glued on it. The design should then be optimised

such to have most of the deformation, coming from the interference between pin and slot, absorbed by the pin instead.

- The cooling substrate accuracy has an impact on the dimension of the clearance between two adjacent substrate surfaces where a sealed hydraulic interface is realised by a gasket, and this is reflected in a change of the pressure force compressing the gasket. Such force induces deformations that can compromise the alignment and, consequently, the sealing.
- The gasket dimension should be decreased down to the minimum admissible value, which guarantees the sealing, to minimise the required compressive force. Consequently, the contribution of the resultant force between the pins and the slots, due to the gasket compression force, is also minimised, and it will facilitate the module mounting.

Based on the above considerations, an optimised design for the substrate and the baseplate was developed (Figure 5.3). The pin diameter is set to 3 mm and sectioned in four quarters. This minimises the contact pressure p_{max} while not compromising the single pin's pull force contribution. The step between pins is 5mm, and the dimension of the square slot is also set to 3 mm by design. The drawing of the sample is in Appendix E (Figure E.1).

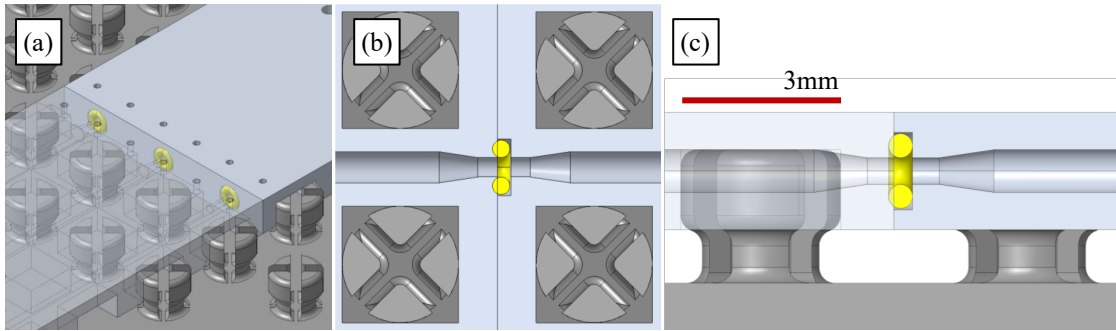


Figure 5.3: Optimised design of the interconnection. (a) Isometric view, (b) top section view and (c) lateral section view of the O-ring face seal.

Sectioning in four quarters allows the pin to absorb most of the displacements coming from the interference between pin and slot, minimising at the same time the deformation of the slots' wall in the substrate. An additional feature was introduced to enhance the pin compliance by shaping the pin's basis with a fillet whose radius can be adjusted at the design level to tune the final pin stiffness (Figure 5.3.c). The misalignment and possible uncoupling of the substrates were minimised by optimising its relative position with respect to the channel interconnection (Figure 5.3.c); the height in contact between pin and slot is 1.5mm. The acceptable manufacturing tolerances can be larger because of the larger elastic deformation of the pin.

Micro O-rings were considered for the hydraulic interconnection, minimising the surface in contact and, therefore, the force required for the correct sealing compression. A groove with a depth of 0.35mm, where the micro-O-ring sits (Figure 5.3.b), was implemented in the

design. The minimum elastomer thickness that guarantees the sealing, considering assembly tolerances, is 0.45mm. The minimum O-ring's production tolerance is $\pm 0.03\text{mm}$.

When the O-ring is squeezed between the two surfaces forming a seal, an initial contact pressure appears between the O-ring and the surfaces. The seal is guaranteed as far as the fluid pressure is lower than the initial contact pressure. A further increase of fluid pressure induces the O-ring to be tighter compressed into the groove and, therefore, it leads to a further increase of the contact pressure. This circular relationship of increasing pressure leading to increased sealing is called "*self-energising*" [171, 172]. In our configuration, the O-ring fails when the clearance between the two adjacent surfaces increases due to the involved forces in the O-ring.

A new module can be assembled at the end of a module array, without compromising the integrity of the micro O-rings. One possible assembly procedure is in Figure 5.4. Given the ability of the pins to absorb the deformation, the module at the end of the array can be tilted in correspondence with the previously assembled interconnection (Figure 5.4.b). The new module is then inserted without interfering with the micro O-ring of the previous module (Figure 5.4.c). During the assembly, the new module can be inserted with a small tilted angle (Figure 5.4.d). The minimum tilted angle is 3 degrees for the modules with 30 mm length. Any module in the array can be mounted and dismounted by tilting the adjacent ones.

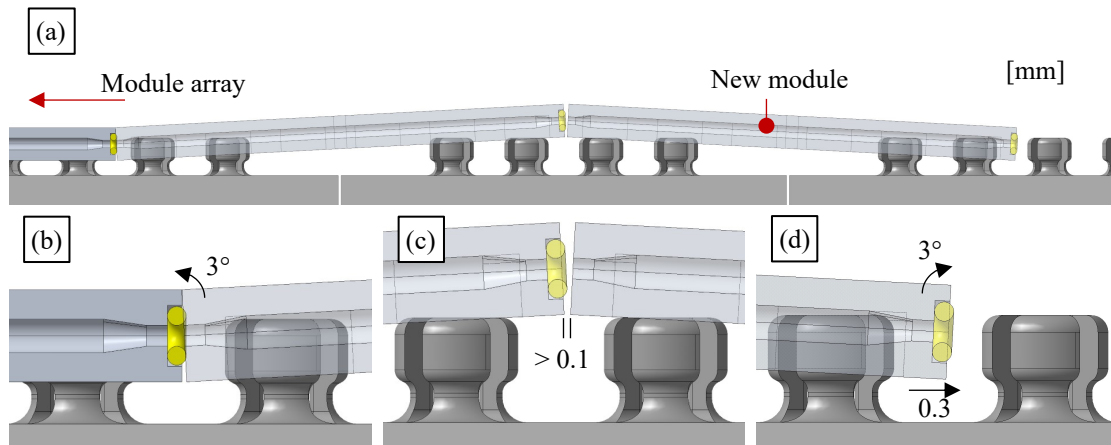


Figure 5.4: Module assembly. (a) Cross-section view of the three adjacent modules and (b-d) details of the interconnections (left, center and right ones) during the assembly.

The breadboard model to qualify the interlocking modular microfluidic interconnection can be seen in Figure 5.5.a. A specific AM material jetting technology, the "Stratasys Polyjet" [173], based on the use of sacrificial material inside the cooling channels, removed at the end of the process, was demonstrated to be the most promising process and affordable solution for prototyping. Straight and clear channels with inner diameters of 1, 0.7 and 0.5 mm were embedded in samples produced in Vero resin (acrylate photopolymer, [174]). The samples used to test the interlocking interconnection were 30mm x 15mm large and 2.2 mm thick,

5.2 The baseline interlocking microfluidic interconnection

while the baseplates provided a different number of pins depending on the substrate position.

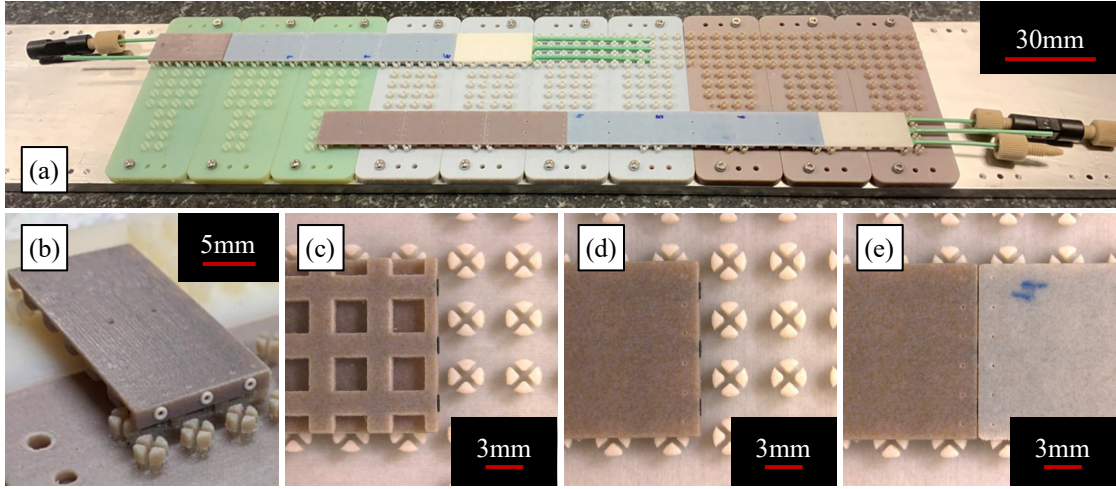


Figure 5.5: Breadboard model of the optimised interlocking configuration. (a) Assembly of substrates and baseplates, (b) isometric view of the substrate, (c) detail of the substrate slots and (d-e) top view of the interconnection assembly.

5.2.3 Validation and tests results

Analysis of pin and slot interference

Based on the estimated values of position tolerance (σ_{pos}) and dimensional tolerance (σ_{dim}) for both substrate and baseplate, the pin coupling in the slot has an interference that goes from 0 to 54 μm , assuming zero interference as a design specification (Figure 5.6).

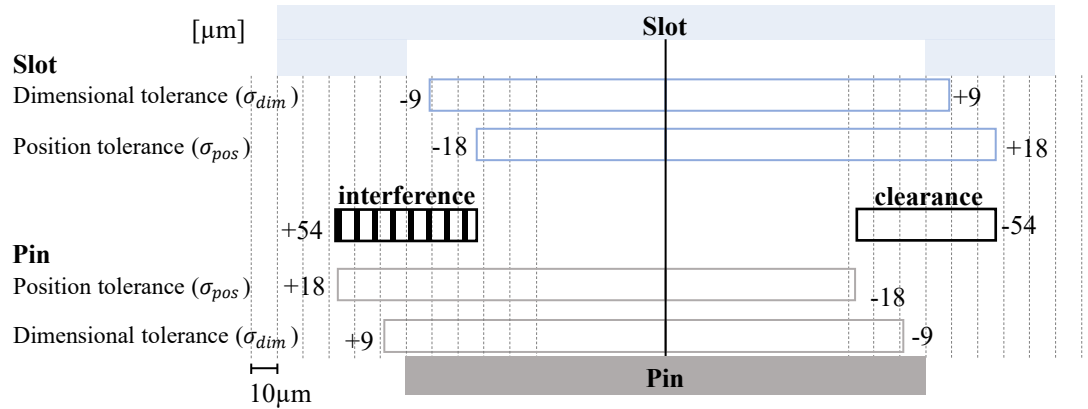


Figure 5.6: Pin-slot interference dependence on accuracy. This schematic picture summarises the position and dimensional tolerances for the pin and the slot. The total tolerance ($\sigma_{tot} = 25 \mu\text{m}$) is the sum in quadrature of position tolerance (σ_{pos}) and dimensional tolerance (σ_{dim}). Conservatively, we assumed σ_{tot} is equally shared between σ_{pos} and σ_{dim} . This results in a value of 18 μm for each term.

Finite element analysis (FEA) of the contact stress was performed to determine the effective interface behaviour (Figure 5.7).

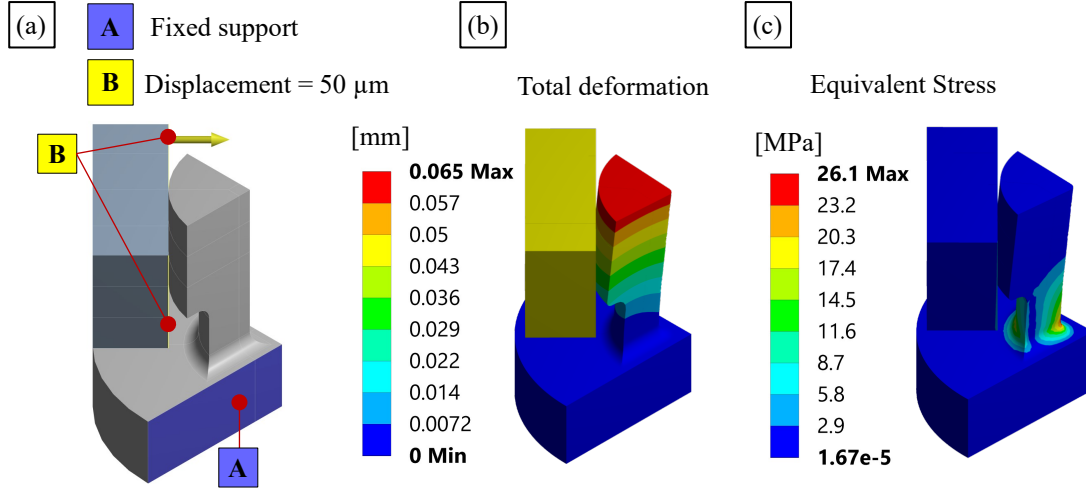


Figure 5.7: FEA Analysis of the pin-slot interface. (a) Boundary conditions, (b) deformation of the pin and slot and (c) contact stress. Non-linear frictionless contact was conservatively assumed between the pin and slot. The analysis was performed on a quarter of pin, and interference of 50 μm, corresponding to a rounded value for the calculated maximum interference, was considered. The Ansys Workbench 2019 [175] software was used to perform the analysis. The solution was obtained through iterative steps based on force convergence criteria. Large deflection effect was considered.

As expected, the pin's elastic deformation absorbs the interference. There is no relevant deformation or stress in the slot, while the stress in the pin is well within the yield strength of Vero material (50-65 MPa [174]). The maximum Von-mises stress is 26 MPa giving a yield safety factor of 1.9. The perpendicular force acting into a pin quarter (F_{\perp}) is of the order of 0.45 N and can be tuned by changing the pin's tapering.

Substrate Plug-and-play

The pull force needed to dismount a sample from the baseplate was measured by a dynamometer attached to the sample (Figure 5.8.a). Different baseplate layouts that would provide different numbers of pins engaging the samples were considered. The number of pins engaging the samples and, therefore, the number of contact points (28, 56 or 84) depends on the number of rows of the breadboard model baseplate (2, 4 or 6) on which the samples are mounted (Figure 5.5.a).

In Figure 5.8.b, the average pull force value of each tested sample ranged between 1.5 and 7 N depending on the number of contact points, and it linearly depends on them. The obtained pull force values point out that the specific design for the tested polymeric solution can provide a stable connection. At the same time, the baseplate design features, such as the number of pins and pin geometry, guarantee that stable connections can also be achieved for different materials by simply tuning these features. The achieved flexibility of the pin design also minimises the design dependence on the modules' material choice, allowing to consider

ceramic materials for the final substrate.

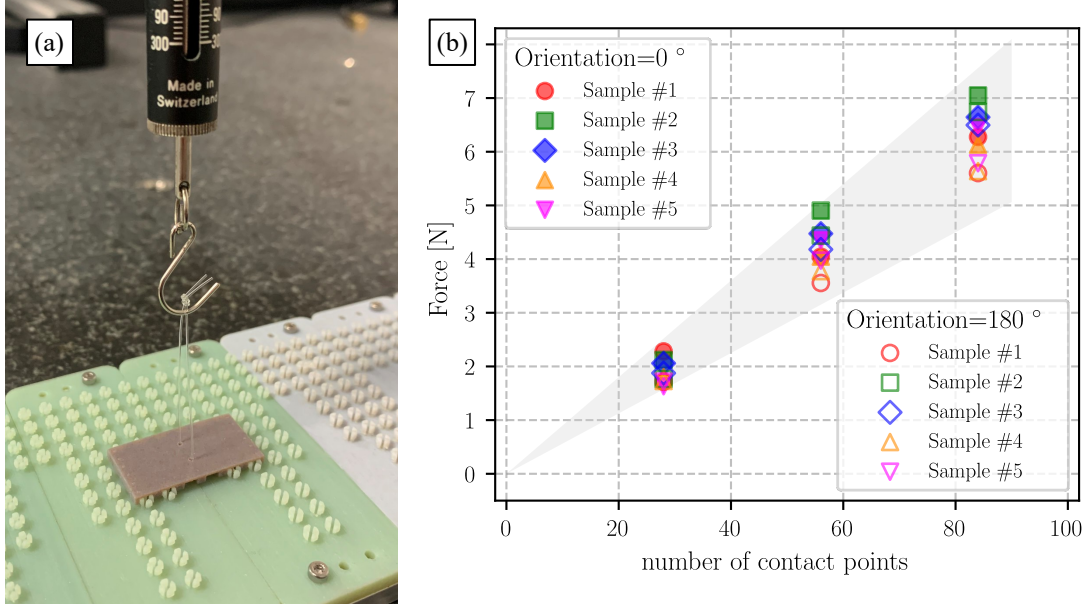


Figure 5.8: Pull force due to pin and slot interference. (a) Each sample (S1-S5) was tested eight times, and the orientation with respect to the baseplate pins (0° or 180°) was inverted to verify the influence of pins position accuracy only. (b) The plot shows the average pull force value of each sample for each contact points configuration.

The force to correctly compress one O-ring was measured in the range of 1.5 - 2 N. This force, even if minimal, positively contributes to the module anchoring and to the pull force required for the dismounting of a module from a module array. However, the modules must be designed such that their anchoring to the baseplate is guaranteed only by its pin's contact points. The dismounting force was experimentally evaluated in the same order as the pull force measured to mount a single sample.

Substrate Interchangeability

The Interchangeability (I_s) is the ability to select components at random and fit them together within proper “Repeatability” (R_s) and “Exchangeability” (E_s). The accuracy of the Repeatability can be described as the accuracy in the position of the same module once it is dismounted and mounted from the baseplate. While the accuracy of the Exchangeability is the accuracy in the position of different modules on the same baseplate. Assuming the respective variances are independent and normally distributed, I_s can be defined as the root mean sum of R_s^2 and E_s^2 .

$$I_s = \sqrt{R_s^2 + E_s^2} \quad (5.1)$$

The elastic averaging theory must be considered to investigate the Interchangeability property [176, 177]. When several pins fit into several slots, the compliant pins deform slightly, causing an elastic averaging of the module position and minimising its total error. R_s and E_s are approximately inversely proportional to \sqrt{n} where n is the number of contact points. E_s also depends on the production process accuracy and precision as well as correlated to component orientation during printing. The Repeatability is considered accepted when it is negligible compared to E_s accuracy.

Several measurements on the prototypes were performed for the experimental characterisation of the Interchangeability. The measurements were carried out under a Coordinate Measuring Machine (CMM) by using a touch trigger probe as in Figure 5.9.a. R_s was evaluated by mounting and dismounting the same sample ten times and calculating the standard deviation of the ten measurements (Figure 5.11.b). While E_s was evaluated by calculating the standard deviation of the average position of the different samples mounted on the same baseplate (Figure 5.11.c).

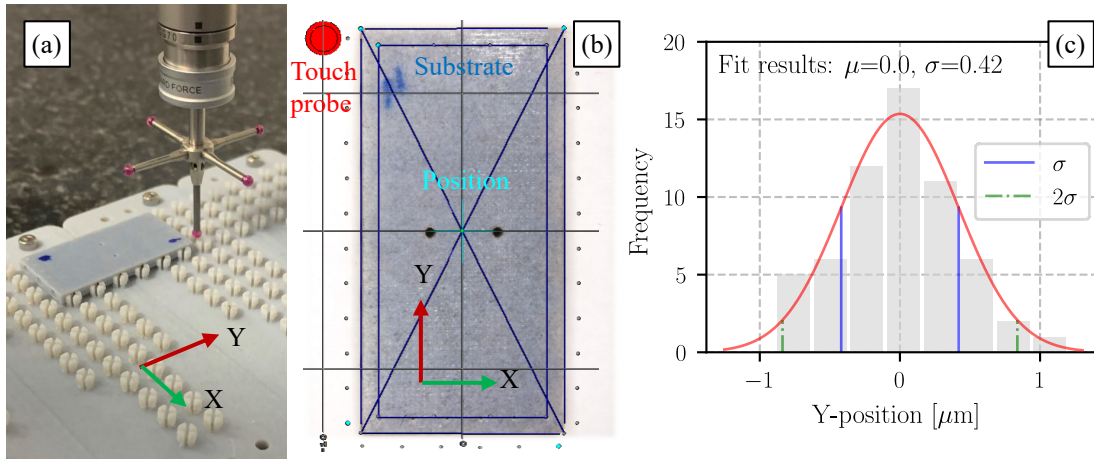


Figure 5.9: Measurement of the sample positioning. (a) A touch trigger probe (Renishaw TP200), integrated into the Mitutoyo CRISTA Apex S9206 CMM was used [178]. (b) The position of the sample centre is derived from the measurement of the sample edges (b). (c) A study of the machine's accuracy and precision was also performed. In this case, the position of an unmoved sample was measured, and the measurement was repeated 60 times. The error measurement standard deviation was $< 0.5 \mu\text{m}$.

The evaluated standard deviation of the Repeatability is approximately $1 \mu\text{m}$ (Figure 5.11.b) while the Interchangeability standard deviation goes from $10 \mu\text{m}$ to $8 \mu\text{m}$ depending on the number of contact points (Figure 5.11.c). In our case, the Repeatability dependence on contact points was almost negligible. The study was limited by the number of available samples and the number of performed measurements. However, the interlocking design showed to provide alignment tolerances within $10 \mu\text{m}$ even being the 3D printed parts within $25 \mu\text{m}$ accuracy, thanks to the multi-pin elastic contacts. This has also positive implications in the hydraulic interconnection that relies on the compression of the sealing O-ring, dependent on the clearance between modules.

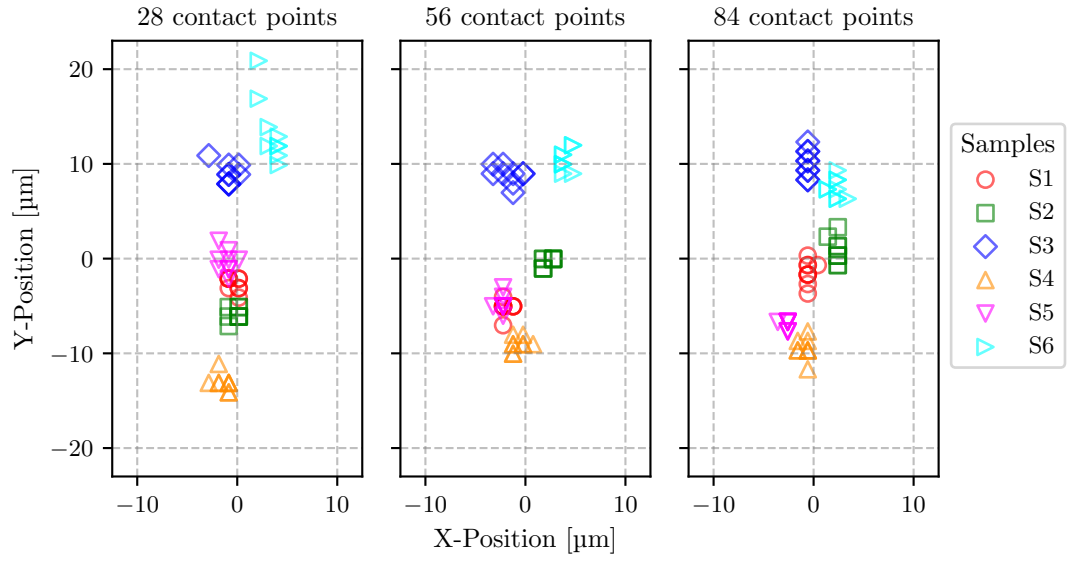


Figure 5.10: X-Y measurements of the samples. The three plots are referred to the three tested configurations with different numbers of contact points (pins).

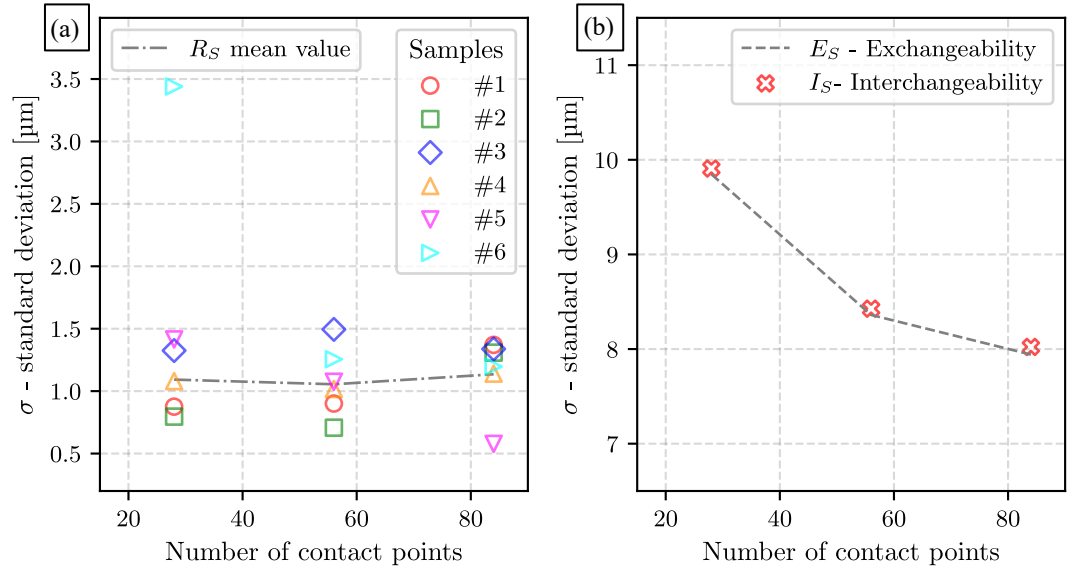


Figure 5.11: Repeatability and Interchangeability. (b) The standard deviation of the Repeatability for each sample and the Repeatability mean value, (c) The standard deviations of the Interchangeability and Exchangeability.

Substrate Sealing

The design of the hydraulic interface was driven by the necessity to guarantee a minimum elastomer compression of 10% considering all the component tolerances [171], Table 5.1. The silicone O-ring, utilised for the test, has a Cross-Section diameter (CS) of 0.45mm, an Inner Diameter (ID) of 0.5 mm and Shore A70. The depth of the sample groove is 0.35 mm, and the nominal clearance between two adjacent samples is set to zero, corresponding to a nominal O-ring compression of 22%.

Table 5.1: Design parameters of the hydraulic interface.

Micro O-ring		Groove		O-ring Compression	
Material	Silicone	OD [mm]	1.4	Minimum	11%
Durometer [Shore A]	70	Depth [mm]	0.35	Nominal	22%
ID [mm]	0.5	Clearance [mm]	0	Maximum	40%
CS diameter [mm]	0.45	Tolerance [mm]	± 0.025		
Tolerance [mm]	± 0.03	Assembly tolerance [mm]	± 0.025		

Tests to evaluate the pressure at which the hydraulic interface fails were carried out (Figure 5.12). Samples were mounted in series, up to 5 samples, and their order was modified for each trial. Different numbers of contact points were considered.

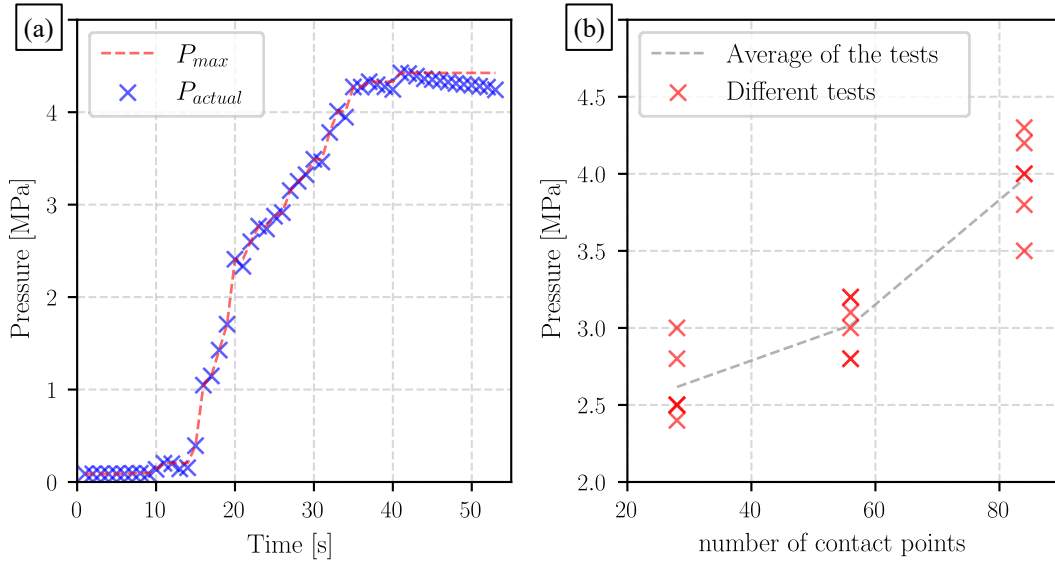


Figure 5.12: Pressure test results. (a) Single pressure test and (b) evaluation of the average pressure failure for different contact point configurations. The pressure sensor utilised is MEAS U5156-000005-100BA [179], and its pressure range goes from 0 to 10 MPa absolute with an accuracy of $\pm 0.75\%$ full scale (FS) corresponding to an accuracy of ± 0.075 MPa.

Figure 5.12.a shows that the samples anchored to 84 contact points can reach pressure up to 4 MPa, before having a small leak at one of the hydraulic interfaces at the extremity of the

substrate chain. The leak pressure depends on the number of engaged pins (Figure 5.12.b), and higher pressure can be reached by increasing the rigidity of the pins within elastic limits.

5.2.4 Outcomes

A completely new interlocking microfluidic interconnection for modular microchannel cooling substrates was developed. The microfluidic interconnection design relies on a mechanical fixation based on a LEGO[®]-like concept where sealing across microfluidic modules is realised through a gasket pressed between them.

The feasibility of the interconnection was demonstrated through additive manufacturing. For the first assessment, polymeric prototypes were produced and tested. It was shown that samples can be easily assembled, overcoming the typical μ CS inter-connectivity problem while keeping the possibility to rework and replace a single module. Based on the first optimisation, several parameters, both for the mechanical and the hydraulic interface, were tuned to match specific design requirements.

The pull force needed to remove a sample from its base was measured in the range between 1.5 - 7 N as proof of the stable LEGO[®]-like module positioning while allowing, at the same time, a perfect dis/mounting capability. The Interchangeability, i.e. the ability to select modules at random and fit them together within proper tolerances, showed to guarantee the module's correct positioning and alignment within $\pm 20 \mu\text{m}$. The hydraulically interconnected samples were tested up to 4 MPa. This pressure condition already matches several cooling design solutions adopted in HEP, and the extension of these limits will be further investigated.

The production and testing of the microfluidic samples demonstrated that this new design concept works at a miniaturised scale where the part features approach the dimensional tolerances. Production process and material play a key role with respect to the achievable tolerance. 3D-printed polymer technology fulfils the requirements. Nevertheless, using different materials and manufacturing processes implies re-assess the achievable tolerances. The miniaturisation of the interconnection can be further pushed if better manufacturing accuracy can be achieved with different AM processes.

The sealing dependence on the coefficient of thermal expansion (CTE) is negligible when water is considered as coolant at room temperature operation. Nevertheless, a minimum and maximum operative temperature range must be identified for a more general characterisation of the final substrate, contextually with the baseplate and substrate materials choice. Another aspect that should be considered is the long-term reliability, as the interconnection should remain unchanged over time. Materials creep could affect long-term performance. Accelerated ageing tests with thermal humidity and radiation environment can be done to assess the component's end-of-life properties.

5.3 Guidelines for the development of alternative interconnections

Alternative solutions for the hydraulic and mechanical interfaces of the interlocking interconnection were investigated.

Hydraulic interface:

The face seal interface of the previous samples withstood pressures up to 4 MPa before having a small leak at one of the interconnection sides (Section 5.2.3). In our case, the face seal failed because of compliance with the walls of the sample tightening the O-ring. This resulted in an increase in clearance between the two adjacent walls when internal pressure was applied. Deeper investigations of the face seal interconnection dependence on the accuracy, understanding its limits, and possible improvements were then required.

At the same time, an alternative sealing solution denoted hereafter as "*radial seal*" was investigated. The radial seal solution aims to be applicable for cooling applications that require more demanding fluids in terms of high-pressure resistance. The new hydraulic interface was designed to minimise the inevitable O-ring compression dependence on substrates' accuracy, which also increase the interconnection reliability. The new hydraulic interface targets to withstand pressure greater than 15 MPa and to have a He leak rate of the order of 10^{-9} mbar l/s. They are essential prerequisites for cooling systems operating with two-phase CO₂ refrigerant (Section 2.2.1).

Customised micro O-rings, made with different materials compatible with different fluids and radiation resistance, are available. However, as preliminary assesment, commercially available micro O-rings [180, 181] with standard sizes were used for all the tests. They are made in silicone or nitrile butadiene rubber (NBR). More comments are in the outcomes Section 5.4.3.

Mechanical interface:

The baseline interface solution, pin-based, that relies on the interference between pins and slots to hold and keep in position the modules, is affected by wear effects caused by friction between different parts and materials, as well as by printing accuracy limits. For this reason, at the beginning of the research, alternative solutions, that rely on different ways to hold and keep the modules in position, were investigated in parallel.

Three main alternatives, denoted hereafter as "*Clip*", "*Spring*" and "*Rail*"-based mechanical interfaces, were developed; each of them can be considered as an evolution of the previous one. Also here, the development of the alternative solutions followed an iterative process that involved analyses, productions, and tests. In Section 5.5, the main highlights for each solution are presented.

5.4 Alternative hydraulic interface

5.4.1 Face seal limits

A pressure test set-up for testing the O-rings was done to investigate the limits and possible improvements of the face seal hydraulic interconnection. The entire set-up is presented in Appendix C, while the main information is visible in Figure 5.13. A summary of the different types of tested micro O-rings is in Table 5.2.

Table 5.2: Types of micro O-ring. The micro O-rings were purchased from Isoswiss [180]. Some of them were used to test the face seal solution, while others were used to test the alternative seal solution.

Type	Code	Material	Shore A	ID [mm]	OD [mm]	CS [mm]	Tolerance [mm]
O-ring gasket	73172	Silicone	70	0.5	1.4	0.45	0.05
O-ring gasket	11000	NBR	70	0.5	1.5	0.5	0.05
O-ring gasket	11003	NBR	70	0.6	1.5	0.45	0.05
O-ring gasket	11009	NBR	70	0.7	1.5	0.4	0.05
Flat gasket	15286	NBR	70	0.65	1.45	0.45	0.05

The tests intended to investigate the O-ring failure dependence on clearance between the surfaces tightening the O-ring, on the accuracy of the groove, as well as to obtain information on the needed compression force.

Two cylindrical brass "*adaptors*", top and bottom adaptors, compress the O-rings. The bottom adaptor has engraved the groove to house the O-ring, and it is connected to the pressure pump; while the top adaptor is connected to a reservoir. These adaptors are free to slide in a polymer suspended "*case*". The case also provides the correct alignment of the two adaptors. The bottom adaptor sits on a weight scale plate (Mettler toledo MS4002 [182]).

The O-ring failure is investigated with two different set-up configurations (Figure 5.13.a & .d):

- In configuration 1 (C1), a micrometric screw, acting on the top surface of the top adaptor, provides the O-ring compression, and a customised shim between the adaptors sets the clearance between the two walls of the adaptors (Figure 5.13.b and .c).
- In configuration 2 (C2), a constant weight is applied on the top surface of the top adaptor while a dial indicator controls the clearance and possible displacement during tests.

With the C1 configuration, the failure dependence on different clearances and depths of the groove is analysed. While, the C2 configuration provides information on the hydraulic failure under a constant force and, at the same time, a cross-check of the results acquired with the C1 configuration.

For the tests with the configuration C1, two groove depth sizes (0.3 and 0.35 mm) and 4

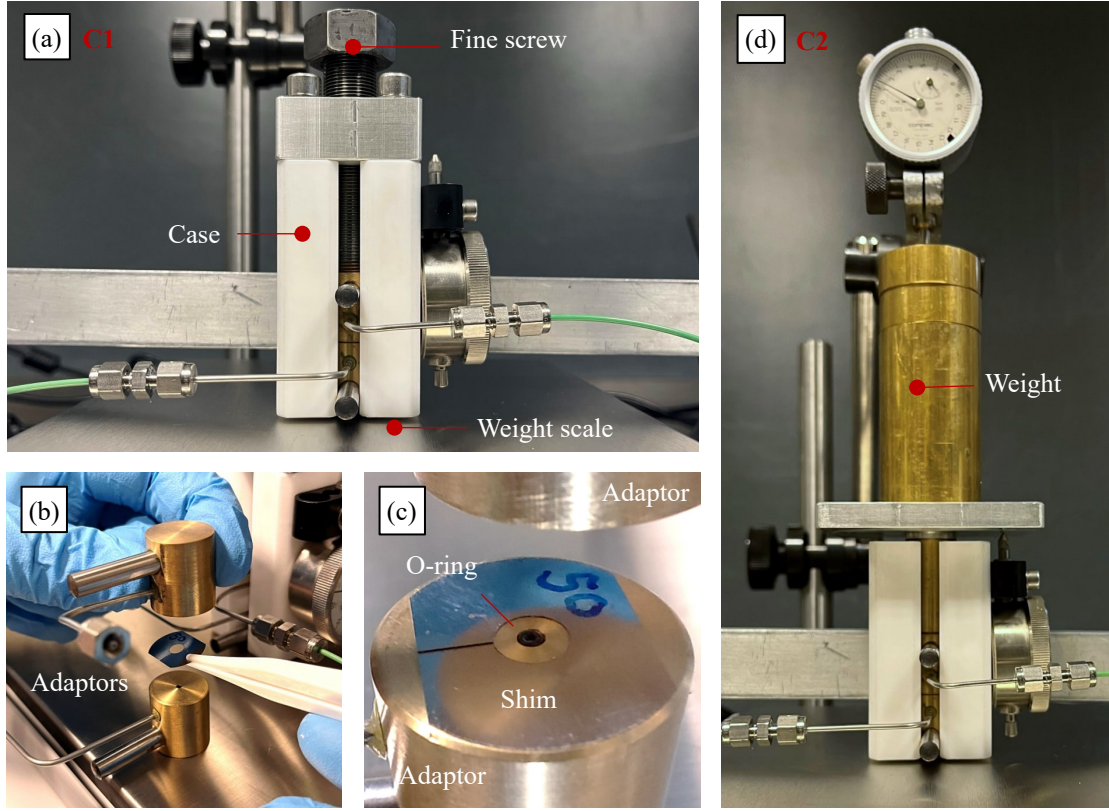


Figure 5.13: Set-up for the pressure test of the hydraulic interfaces. (a) Configuration 1 (C1), (b-c) details of C1 during the O-ring insertion and (d) configuration 2 (C2).

different shims (0, 0.03, 0.05, 0.1 mm), that provided different clearances between the brass adaptors, were tested. While for the tests with the C2 configuration, different weights, ranging from 5 to 30 N, were applied. In both C1 and C2, different NBR and silicone micro O-rings were tested. The compression ($C_{\%}$) is calculated as follows:

$$C_{\%} = \frac{CS - (CS + c)}{D} \cdot 100[\%] \quad (5.2)$$

Where H is the groove depth, D is the O-ring diameter, and c is the clearance. The results are summarised in Figure 5.14 and Figure 5.15. All the micro O-rings, with an inner diameter (ID) of 0.6-0.5 mm and CS of 0.5-0.45 mm, failed before 9 MPa. The flat gasket (15286 In Table 5.2) failed at 10 MPa because a greater surface is in contact with the brass adaptor. For a force of the order of 25 N, the compliance of the set-up (i.e. the tolerances of the brass adaptors and the flexibility of the weight scale plate) lets the o-ring be squeezed between the two compressing surfaces. It was not possible to reach higher pressures. However, we can conclude that:

- Tolerances of the order of $\pm 50 \mu\text{m}$ impact the pressure performance by 2 MPa.
- The force needed to hold the compressed O-ring and to guarantee a sealing up to 7 MPa of pressure, is of the order of 20-30 N (See Figure 5.15).

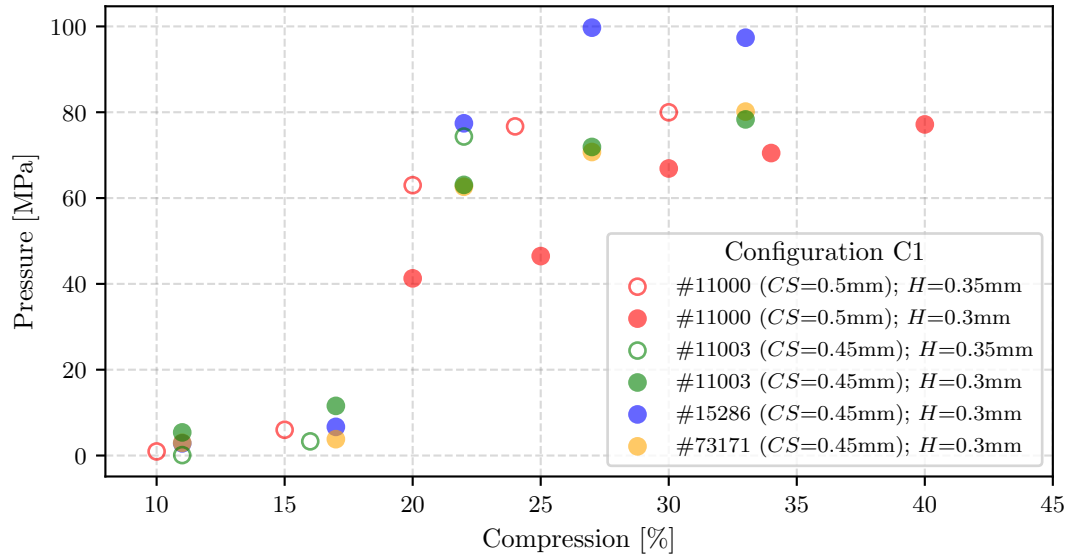


Figure 5.14: Failure pressure of the face seal as a function of the O-ring compression. Different micro O-rings (see Table 5.2), highlighted with different colors, were tested with the configuration C1 (see Figure 5.13). The pressures at which the O-rings failed are plotted as a function of the O-ring compression (See Equation 5.2). Two groove depth sizes (H), corresponding to the two different bottom adaptors, were used during the tests (filled and non-filled markers in the plot). Calibrated shims between the top and bottom adaptors were used to set c and $C\%$. A new O-ring was used for each test.

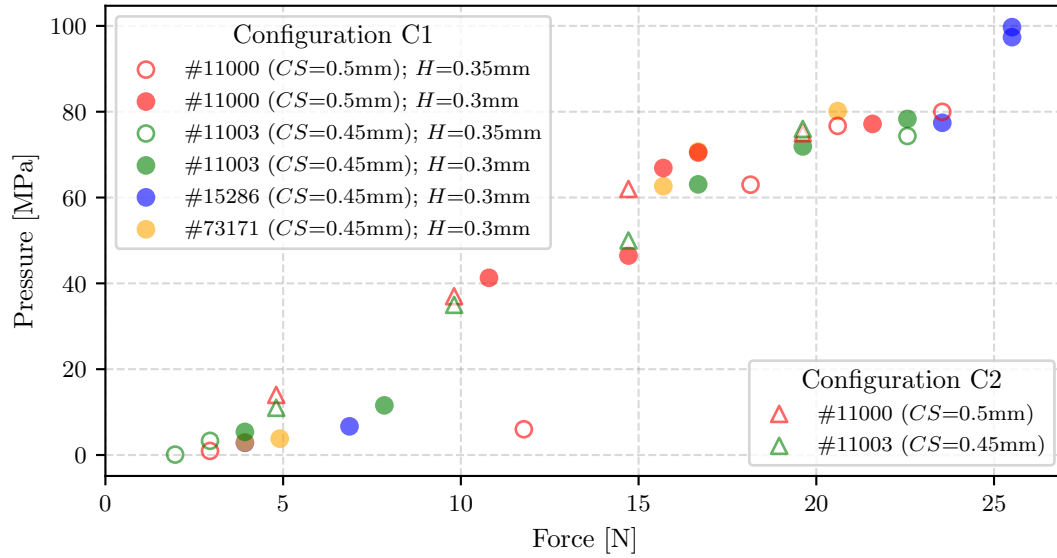


Figure 5.15: Failure pressure of the face seal as a function of the force. The pressure at which the different micro O-rings (see Table 5.2) failed is plotted as a function of the force measured by the weight scale. The results with the two configurations, C1 and C2 (see Figure 5.13), are highlighted with triangle markers and circle markers, respectively. Two groove depth sizes (H), corresponding to the two different brass adaptors, were used during the test (filled and non-filled markers in the plot). A new O-ring was used for each test. The failure pressure linearly depends on the applied force.

5.4.2 Radial seal

The direction of the O-ring compression, or squeeze, applied to the seal cross-sections differentiates radial seals from face seals. Face seals have compression applied to the top or bottom of the seal's cross-sections, whereas radial seals have squeeze applied to both the outside and inner diameters. Radial seals are frequently utilized in applications involving cap&plug, or piston&bore [171, 183].

To be the radial seal applicable in the miniaturised in-plane hydraulic interface, an additional insert, denoted hereafter as "*seal fitting*", is required (Figure 5.16).

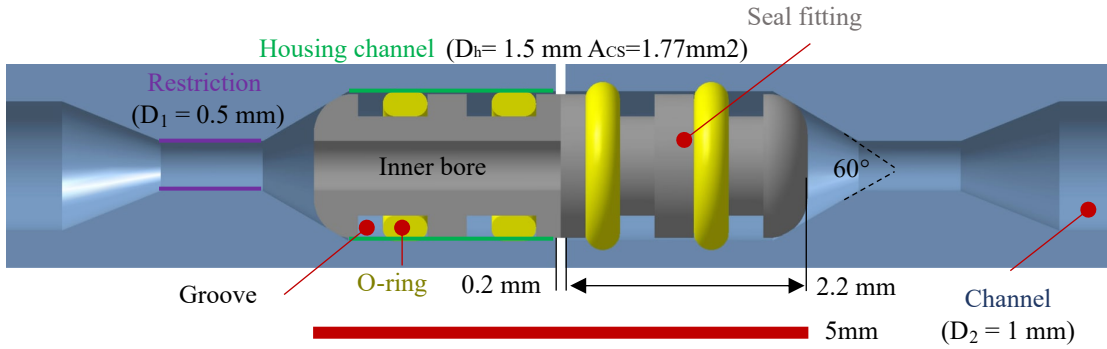


Figure 5.16: The radial seal solution. CAD design of the interconnection. The left side of the seal fitting is sectioned to highlight the inner bore.

In the proposed concept, a number of micro O-rings houses in a number of "*grooves*" present on seal fitting. The micro O-rings are radially compressed when the seal fitting enters into recessed holes, named "*housing channels*". The width of the seal fitting groove is designed to accommodate the micro O-ring deformation induced by the substrate housing channels. At the same time, an "*inner bore*", longitudinally engraved in the seal fitting, provides the channel interconnection. Two "*restrictions*" in the two cooling substrate channels are intended to keep the seal fitting in the correct position.

To improve the reliability of the radial seal, two redundant micro O-rings seal each substrate. If a leak appears in the first O-ring, the second one is ready to block the coming fluid.

The seal fittings used for the tests were CNC machined and produced in Carbon-PEEK (PolyEtherEtherKetone) material (Figure 5.17.c and d). Carbon-PEEK is a composite polymer material. The mechanical properties of the polymer PEEK matrix are enhanced by adding graphite powder. It is largely used in HEP applications for its high radiation resistance (>10 MGy [39]). The drawing of the seal fitting and its tolerances can be seen in Appendix E.

Similar pressure tests, previously shown, were performed for the seal fitting. Two new brass adaptors were produced to house the seal fitting. In addition, several O-rings, with different dimensions were tested, and the results can be seen in Figure 5.18.

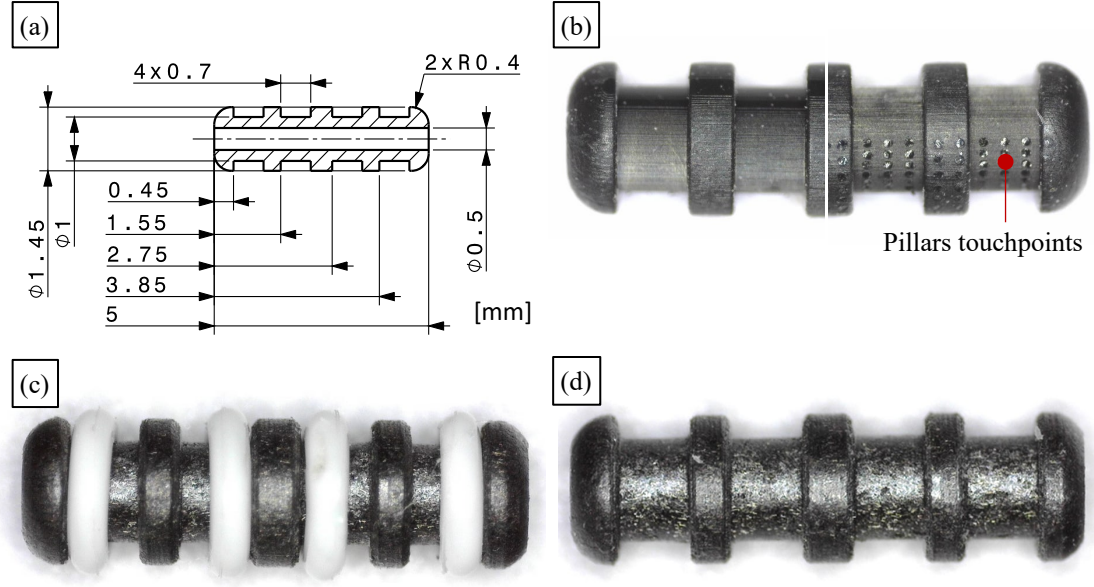


Figure 5.17: Seal fitting of the radial seal solution. (a) CAD drawing of the seal fitting cross-section, (b) first samples 3D printed and (c-d) CNC machined samples with and without O-rings. As proof of concept, seal fittings were 3D printed in ABS-like material (N-800 [184]) produced with Micro Digital Light Processing (DLP) AM system technology by Nanodimension Fabricagroup company [185] (b). The Micro DLP technology can reach 1 μm of precision. Preliminary pressure tests demonstrate that the radial interconnection withstands pressures up to 20 MPa.

All the seal fittings equipped with different O-rings were able to reach pressure higher than 20 MPa. At 20 MPa, the force needed to hold the interface is of the order of 40 N. The tests were stopped as the set-up was not intended to withstand pressure up to 28 MPa and a force of more than 40 N. The results show a linear correlation between the internal pressure (P) and the force (F) applied at the interface with the brass adaptor walls. It corresponds with the analytical estimate of the below equation:

$$F [\text{N}] = A_{CS} [\text{mm}^2] P [\text{MPa}] \quad (5.3)$$

where A_{CS} is the cross-section area of the housing channel (Figure 5.16) calculated as follows:

$$A_{CS} = \frac{\pi D_h^2}{4} = 1.77 [\text{mm}^2] \quad (5.4)$$

Note that a larger hydraulic interface (larger inner bore, seal fitting and housing channel) will require a higher force proportional to the square of the housing channel diameter (D_h).

To conclude, the additional use of the seal fitting applied to the pin-based (LEGO[®]-like) mechanical interface will require the assembly of the modules array prior to the modules' insertion on the baseplate (i.e. on the pins).

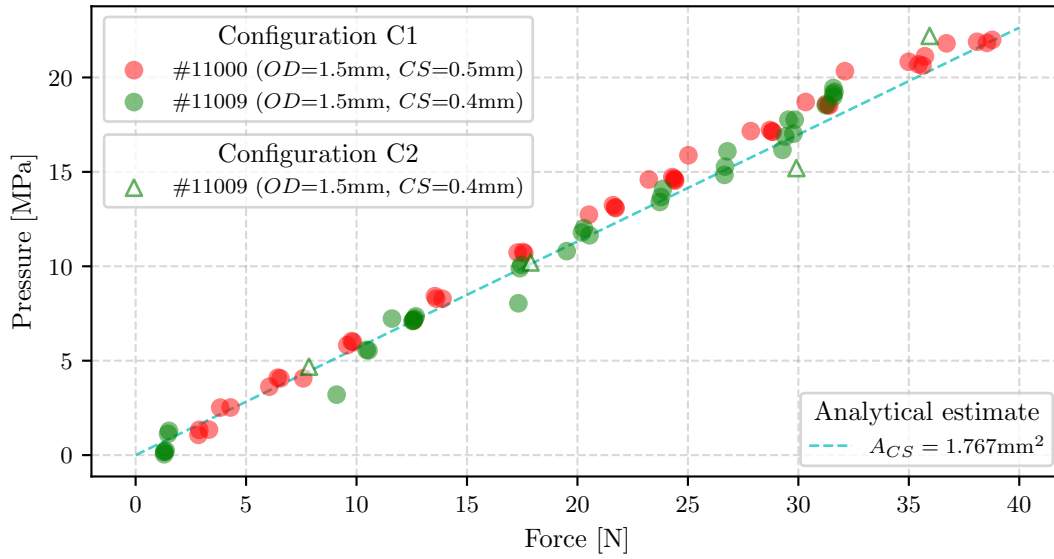


Figure 5.18: Test results of the radial seal solution. Nitrile micro O-rings, 11009 and 11000, were tested with C1 and C2 configurations. The plot also displays the linear correlation between the pressure and the applied force (see Equation 5.3).

5.4.3 Outcomes

A pressure set-up to test the hydraulic interconnection was built and was used to evaluate the behaviour of the face seal solution. Commercially available silicon and NBR micro O-rings were tested.

The maximum pressure reached was ~10-15 MPa due to the test set-up limits. Within this pressure range, it was observed that the force needed to hold the compressed O-ring is 20-30N. Note that in the pin-based solution, this force is counterbalanced by the simultaneous engagement of several pins. Manufacturing mechanical tolerances of the order of $\pm 50 \mu\text{m}$ degrade the hydraulic interconnection performance by 2 MPa as experimental observed.

Based on these experimental observations, a new hydraulic interface, less dependent on substrate accuracy, was designed and tested. The new solution is based on a radial seal.

The face seal is replaced by a seal fitting that engages in the two adjacent substrates. The seal fitting is equipped with a number of micro O-rings that are radially compressed, once inside the substrates, such to provide the required sealing.

The performance achieved with this new design is independent of the mechanical coupling of the substrate on its baseplate, i.e. from the manufacturing tolerances of the parts. Two adjacent modules can be displaced from their nominal position without affecting the hydraulic interconnection. Nevertheless, the accuracy of the housing channels, where the seal fitting is housed, still affects the maximum achievable pressure.

The radial seal interconnection was able to reach 20 MPa. The force needed to hold the interconnection linearly depends on the internal hydraulic pressure. For an internal pressure of 20 MPa, 32 N force was required, and it was proportional to the groove cross-section area ($D_h = 1.5\text{mm}$, $A_{CS} = 1.77\text{ mm}^2$) multiplied by the hydraulic pressure. In the case of radial seal interconnections in series, the force is only proportional to the groove cross-section area minus the cross-section area of the inner bore of the seal fitting.

The final sealing material must be compatible with the fluid and radiation resistance.

Concerning the evaporative CO₂ cooling system (Section 2.2.1), high-pressure cycles could initiate a phenomenon called "*explosive decompression*". This phenomenon causes blisters and ruptures on the surface of the elastomer [186–188]. Specific o-ring materials, compatible with evaporative CO₂, are PEEK, Perfluoroelastomer - FFKM (e.g. Kalrez® [189]) and hydrogenated nitrile - HNBR (e.g. Parker HNBR KA183-85 [190]). Once selected the material, the CO₂ qualification standard test NACE TM0297-2017 [191] must be followed.

At high radiation levels (>0.1 MGy), the elastomers change flexibility (durometer, elongation and tensile strength), and some of them become brittle. However, a recent study performed by L.Yuanyuan et al. [192] demonstrated that NBR and HNBR rubbers, irradiated in high-dose γ -ray field (up to 1.2 MGy), manifested a decreasing of elongation. Still, the strength, stress relaxation and abrasion resistance were significantly improved. Therefore, NBR and HNBR could be used for applications that achieve a dose of ~ 1 MGy, but their elastic deformation must be limited to a safe range.

To conclude, the studies of different elastomer materials suitable for high radiation doses and compatible with evaporative CO₂ should be foreseen. On the flip side, possible alternatives to elastomer materials are metals, such as indium (for radiation doses >10 MGy). In this case, the joint design should be adapted for their use.

5.5 Alternative mechanical interfaces

Similarly to the previous breadboard model produced for validating the baseline interconnection, the sample dimension printed to investigate the alternative mechanical interfaces was $\sim 30 \times 15 \times 2.2 \text{ mm}^3$. Most of them were produced in transparent Vero Clear resin (acrylate photopolymer, [174]) that allowed optical inspecting of the micro-features inside the channels.

5.5.1 Clip-based solution

This solution was intended to integrate the mechanical interface into the cooling substrate design. Standard buckles inspire it. Two features, the “Clips” and the “Drivers”, are implemented in the sample design. The final optimised design can be seen in Figure 5.19.

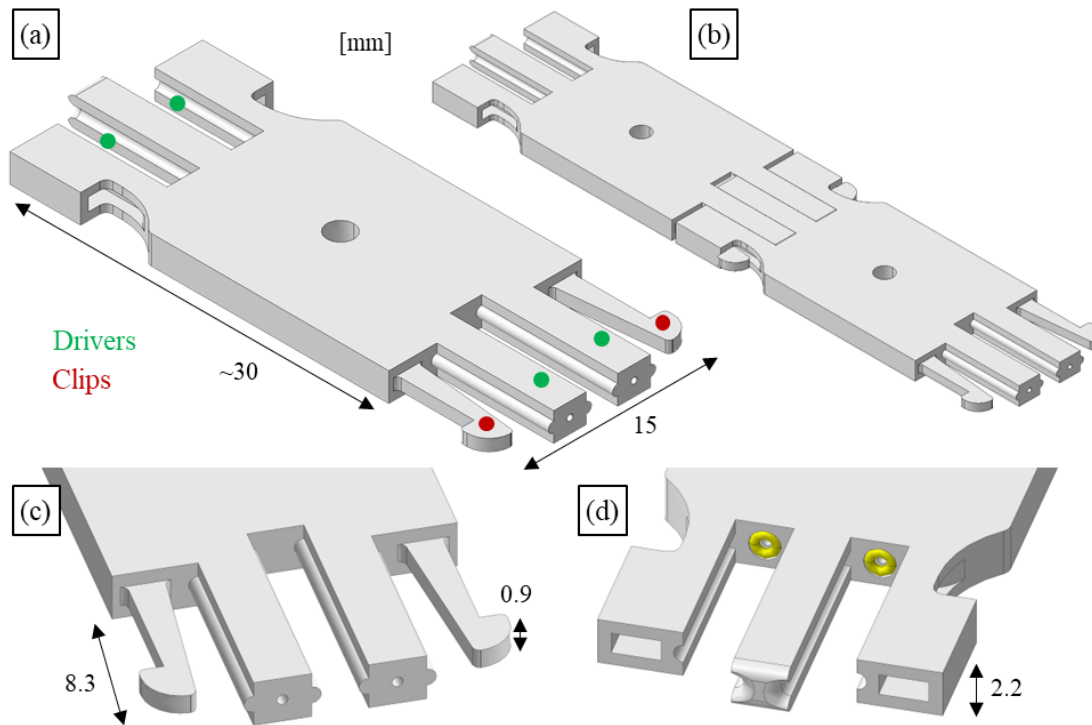


Figure 5.19: Design of the clip-based solution. (a) CAD model of the sample, (b) two assembled samples and (c-d) details of the two facing short sides. A similar design was also adopted for the radial seal solution. The hole at the center of the samples serves to handle.

Features optimisation followed the requirements:

- The clips have to elastically deform during assembly, hook the next sample and compress the gasket between them.
- The drivers have to guide the sample-sample assembly minimising their misalignment and reducing the clearance at the hydraulic interface.

The clip design was optimized and qualified through FEM analyses (Figure 5.20) and tests. During the optimization, the length of the clip was increased, and the width of the cross-section was reduced at the clip end. This allowed large displacement and maintained, at the same time, a sufficient stiffness of the clip. The clip can absorb a lateral displacement of 1 mm.

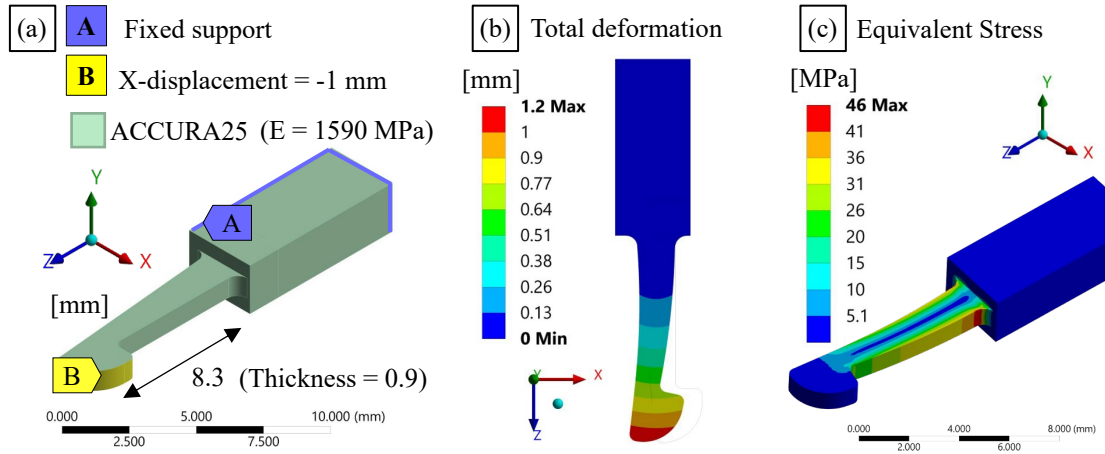


Figure 5.20: FEM of the clip-based solution. (a) Boundary conditions, (b) total deformation and (c) equivalent Von-Mises stress. The material in the analysis is ACCURA25 [168]; it has Young's modulus of 1590 MPa and flexural strength of 55-58 MPa. ANSYS Workbench 2021 [175] software was used for the analysis. Quadratic elements (mesh size = 0.05 mm) and large displacement effect were considered.

Wood joints inspired drivers' optimization. Contact surfaces between drivers were maximized to reduce the misalignment between samples. In addition, a concavity–convexity junction was created to avoid rotation around the X-axis. During the assembly, only the translation in Z is allowed. Details of the assembly steps are in Figure 5.21. In Figure 5.22, several spring-based samples are connected together for both the hydraulic solution, face seal and radial seal.

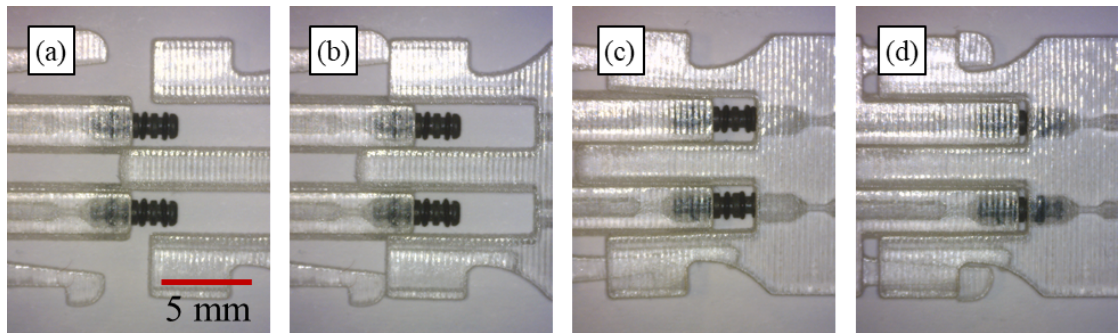


Figure 5.21: Assembly of the clip-based solution. The picture shows the main assembly steps of the clip-based solution for the radial seal configuration. A similar procedure is followed for the face seal configuration. In the beginning, (a) the drivers of the two samples touch each other providing the initial alignment. After that, (b) the drivers slide between each other. (c) During the sliding, the clips fit inside the corresponding buried slots. (d) The radial seal fittings reach their nominal position, and the two clip heads lock. The same procedure is followed for the assembly of the subsequent samples.

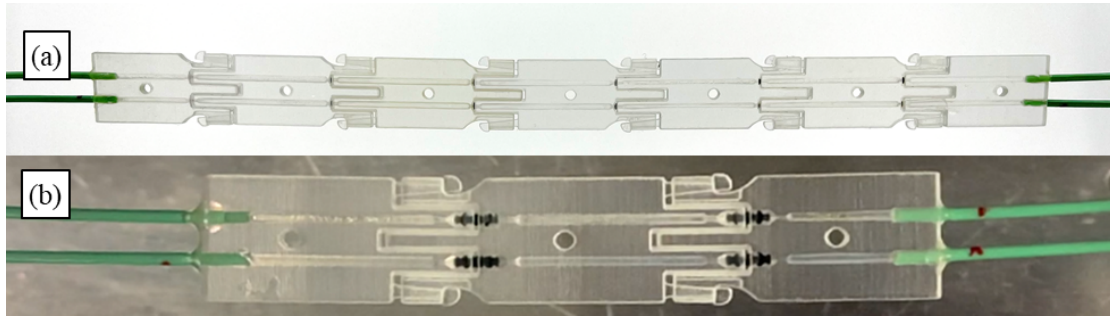


Figure 5.22: Array of samples with the clip-based solution. (a) Face seal and (b) radial seal hydraulic interfaces.

The clip-based solution with the face seal withstood pressures up to 1 MPa, in some cases 2 MPa, as the sealing highly depends on the accuracy of the clips. The samples implemented with the radial seal interface withstood 8 MPa of pressure. In this case, the compliance of the wall of the housing channels, where the O-rings of the seal fitting are compressed, did not provide sufficient sealing. A stiffer engineered material or a higher printing accuracy could allow withstanding higher pressures for both the hydraulic interface solutions. Nevertheless, the clip must be re-designed to withstand higher pressures (~ 15 MPa); its length and thickness must be increased with an impact on the design encumbrance and integration.

5.5.2 Spring-based solution

The compression force of the O-rings depended on printing accuracy in the previous mechanical interface solution. The spring-based solution (Figure 5.23) was developed to minimise this dependence. In this case, the clip features are substituted by "*spring*" features.

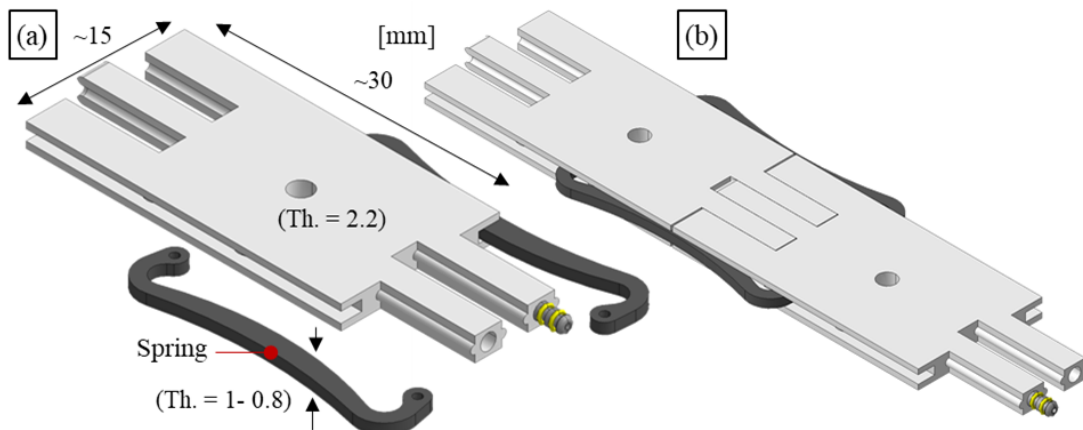


Figure 5.23: Design of the spring-based solution. (a) CAD model of the sample and (b) two samples assembled with the radial seal hydraulic interface.

Two planar springs hook the two samples (Figure 5.24.a). The spring passes from its relaxed position to its nominal extended position during assembly. It was designed such that it extends

to ~2 mm. Assuming that the substrate assembly accuracy is 0.1 mm (20 times less than the spring extension), the O-ring will be subjected to an almost constant compression force ($\pm 5\%$) induced by the spring. However, the position of the modules still depends on the tolerances of the module array.

Several FEM analyses of different spring geometries (Figure 5.24.b) were performed to select the best design of the spring (Figure 5.25). The spring dimension and its complexity were minimised within the limitations of the admissible maximum strain and stress of the selected material (polymeric material).

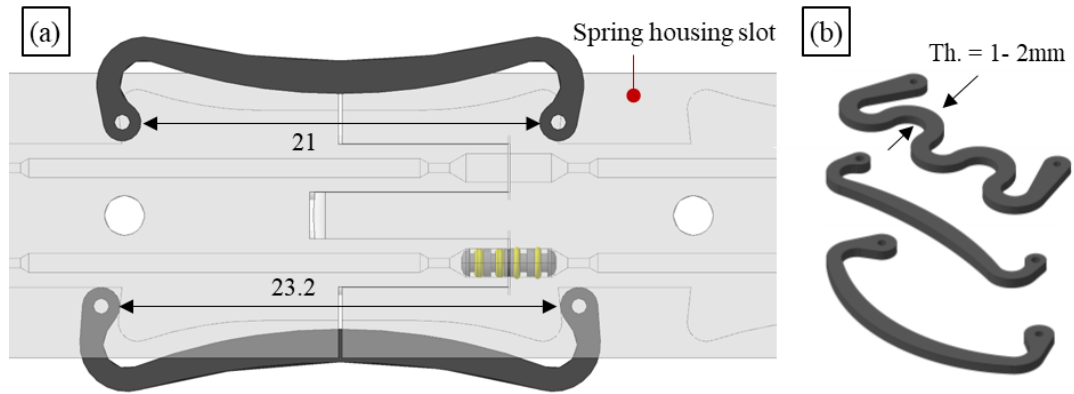


Figure 5.24: Design of the spring. (a) Detail of the spring assembled between two modules and (d) different spring designs. In (a), only one spring is extended and inserted in the spring housing slot.

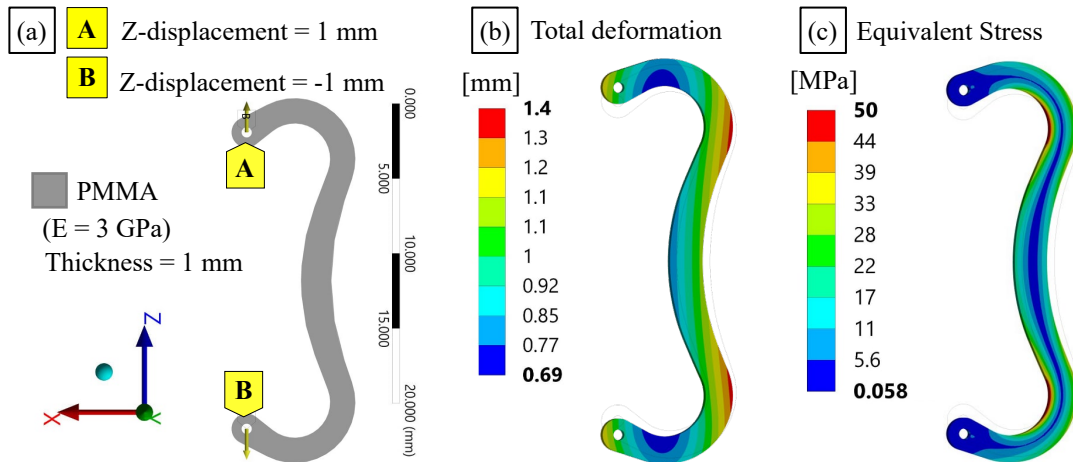


Figure 5.25: FEM of the PMMA spring. (a) Boundary conditions, (b) total deformation and (c) equivalent Von-Mises stress. The material considered in the analysis is PMMA (Young's modulus of 3000 MPa and flexural strength of 60-80 MPa). The reaction force at one spring extremity is 4 N; it corresponds to a spring constant (k_{spring}) of 4 N/mm. The spring was not optimised for high pressures (~15 MPa). ANSYS Workbench 2021 [175] software was used for the analysis. Quadratic elements and large displacement effect were considered. The mesh size of the hexagonal element was 0.05 mm.

Different samples with slightly modified designs were produced and tested to compensate for possible FEA error ($\pm 20\%$). The springs were made in Poly-Methyl MethAcrylate (PMMA) by CO₂ laser cut (Trotec speedy 400 [169]) for first attempts. Figure 5.26 shows the assembly procedure of two samples, while Figure 5.27 shows two arrays assembled with seven samples each for the two hydraulic solutions (face seal and radial seal).

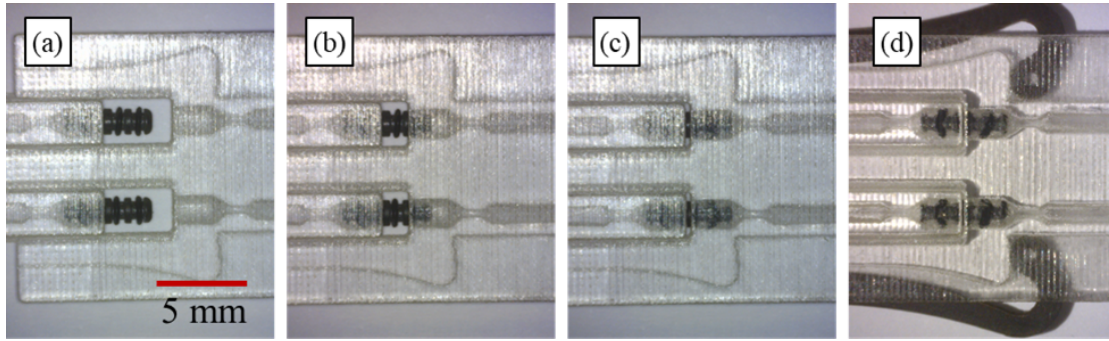


Figure 5.26: Assembly of the spring-based solution. (a) Sliding between drivers, (b) insertion of the seal fitting in the sample housing channel, (c) seal fitting inserted and (d) interconnection closing with the spring. The samples in the picture have the radial seal hydraulic interconnection.



Figure 5.27: Array of samples with the spring-based solution. (a) Face seal and (b) radial seal hydraulic interfaces.

The face seal and the radial seal interfaces withstood pressures up to 2 MPa and 8 MPa, respectively. Higher pressure could be reached by increasing the spring stiffness. Engineered (composite) polymeric materials (such as PEEK, Carbon PEEK) could be considered as the final choice. In this case, the design must also be re-adjusted; the spring dimension should increase with an inevitable impact on the substrate encumbrance. Metal springs cannot be considered because of material budget requirements. In addition, a stiffer substrate material is also required for the radial seal interface to minimise compliance of the housing channel wall and achieve higher pressures.

Similarly to the clip solution, the spring can be integrated into the module design. This aspect was not investigated as the mechanical interface was intended to be integrated independently on the final material of the substrate.

5.5.3 Rail-based solution

For the rail-based solution, the samples are kept aligned with respect to each other by two components called "*Rails*" (Figure 5.28). The sample presents two "*slots*" at the short side. These slots engage the two lateral rails. All the O-rings between the samples are pressed at once by using an additional external component called "*Pusher*" (Figure 5.28). The pusher is constituted by a "*screw*" mechanism, which exerts the correct force on the samples.

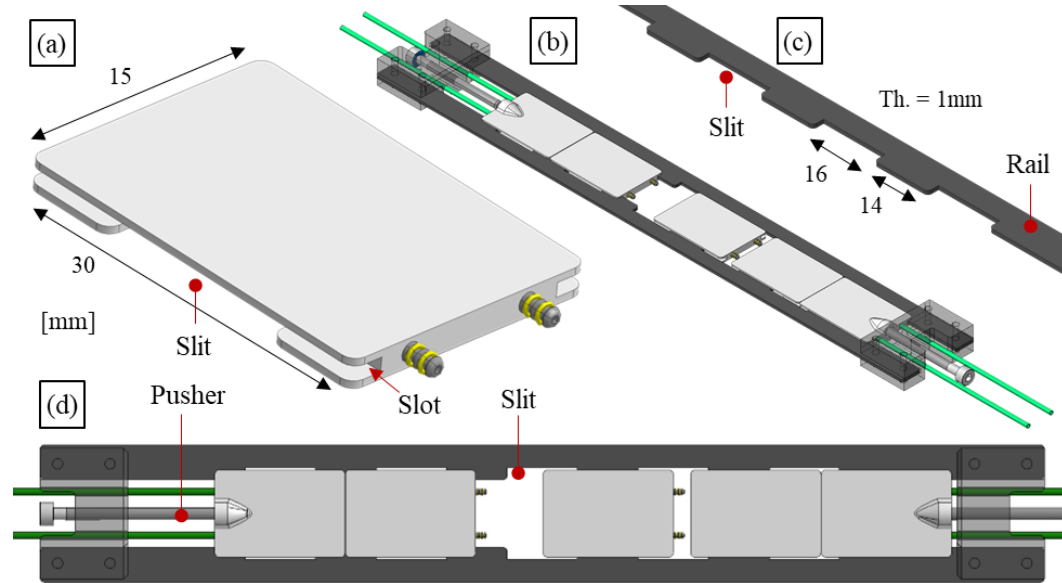


Figure 5.28: Design of the rail-based solution. (a) CAD model of the sample, (b) isometric and (d) top views of an array of samples and (c) detail of the rail.



Figure 5.29: Samples array of the rail-based solution. (a) Face seal and (b) radial seal hydraulic interconnections. Note that only one pusher is sufficient to compress the micro O-rings (b).

In addition, "*slits*" in the rails and in the back side of the samples (Figure 5.28.a and .c) allow to insert and replace a single sample with a minimum impact on the array of the samples. Indeed, it is possible to realise one pusher mechanism, let slide the adjacent samples, and remove the sample to be replaced without dismounting the entire assembly (Figure 5.28.d).

Substrates features consisting of slots and slits are more straightforward than previous mechanical solutions. For the face seal case, the gasket compression essentially depends on the force coming from the pusher and, in a minimal part, on the tolerance of the side wall and groove of the module. The face seal and the radial seal interfaces withstood pressures up to 7.5 and 8 MPa, respectively.

5.5.4 Outcomes

Three different options were proposed as alternatives to the pin-based mechanical interface solution: clip-based, spring-based and rail-based. The first two rely on a direct interconnection between two adjacent modules, based either on a clip or on a spring mechanism, while the rail-based one counts on two side rails that keep simultaneously in their correct position an array of modules. The force required to seal the hydraulic interfaces between the modules is provided by an additional. All the design solutions, applied to not yet optimised material choice, demonstrated to withstand pressures of more than 1 MPa and 8 MPa for the face seal and radial seal, respectively.

All three options try to solve some limits of the pin-based design with the face seal hydraulic interface, where the accuracy of the mechanical parts plays an important role.

The clip-based solution has the advantage of integrating the mechanical interface into the modules eliminating the use of a baseplate. Nevertheless, it was observed through a test campaign that clips manufacturing tolerances can still affect the hydraulic face seal.

The spring-based design relies on a calibrated spring that keeps two adjacent modules in contact with a force that does not depend on the module's accuracy and provides the required compression to the gasket at the hydraulic interface.

The rail-based solution fulfils the same performance as the spring-based solution with a simplified layout and a significant gain in terms of assembly procedure and system reliability.

In a subsequent development phase, the radial seal was adopted in all three design solutions, initially developed for the face seal configuration. All the mechanical interfaces demonstrated similar hydraulic performance being the radial seal solution less dependent on module manufacturing accuracy.

In addition, screws to hold and keep in position each substrate or to counterbalance the force coming from the hydraulic interface (face seal or radial seal) can be implemented. However, screws will impose constraints on the substrate's dimension, material and manufacturing process.

To conclude, the rail-based solution with radial seal is the best alternative to the pin-based solution as it simplifies the module layout, manufacturing, and dis/assembly while keeping the same performance as the other solutions.

6 Ceramic i-M μ CS

In this chapter, ceramics produced through AM are investigated as a potential candidate for the production of microfluidic cooling substrates. It introduces the reasons that make 3D printed ceramics interesting for HEP applications. Subsequently, the selection criteria and the description of the chosen printing processes and materials are discussed. The sample characterisation is then presented, followed by the ceramic interconnection validation.

6.1 Advantages of a 3D printed ceramic cooling substrate

AM allows the production of parts in a 3-Dimensional envelope. Ceramic AM solutions are, therefore, promising candidates for the fabrication of a new generation of cooling substrates. Ceramic materials suit several of the requirements for the mechanics of HEP detectors (Table 6.1):

- Coefficient of thermal expansion (CTE) comparable to the one of silicon ($2\text{-}6 \cdot 10^{-6} \text{ /K}$).
- Thermal conductivity (k) ranging from 12, for aluminium (di)oxide, to 200 W/mK for aluminium nitride.
- Radiation hardness (i.e no mechanical properties changing under doses $>100 \text{ MGy}$ for aluminium oxide based materials [40]).

On the flip side, the ceramics have higher densities ($2\text{-}6 \text{ g/cm}^3$) and, therefore, higher radiation lengths (2-12 cm) than the carbon composite laminates. This must be considered in the design of the cooling substrate.

Typically, an AM ceramic part is produced starting from micro or nano-powders mixed with various organic or inorganic additives to create the so-called "green part". The final product is then obtained after thermal post-processing (de-binding and sintering). The de-binding process removes the organic and inorganic binder through a thermal cycle (150-1000 °C). The subsequent sintering process, or firing process, involves consolidating ceramic powder

Table 6.1: Comparison of the ceramics with the silicon material. (Non-exhaustive) Requirements are labelled from **poorly satisfactory** to **satisfactory** and **highly satisfactory**. Mechanical properties are taken from [193] and radiation lengths were calculated using theoretical formulae [42].

Material	ρ [g/cm ³]	E [GPa]	CTE [10 ⁻⁶ /K]	k [W/mk]	X_0^* [g/cm ²]	X_0 [cm]
Silicon (Si)	2.33	130-188	2.6-3.3	149	21.82	9.37
Zirconium dioxide (ZrO ₂) - Zirconia	5-6.15	100-250	2.3-12.2	1.7-2.7	12.47	2.49-2.03
Aluminium Oxide (Al ₂ O ₃) - Alumina	3-3.98	215-413	4.5-10.9	12-38.5	27.94	9.31-7.02
Silicon dioxide (SiO ₂) - Silica	2.17-2.65	66.3-74.8	0.55-0.75	1.3-1.5	27.05	12.47-10.21
Silicon Carbide (SiC) - Carborundum	4.36-4.84	90-137	7.9-11	3.8-20.7	25.56	5.86-5.28
Silicon Nitride (Si ₃ N ₄) - Nierite	2.37-3.25	166-297	1.4-3.7	10-43	26.29	11.09-8.09
Aluminium Nitride (AlN)	2.92-3.33	302-348	4.3-5.6	60-200	27.46	9.41-8.25

particles by heating the part to a high temperature (up to 1500-2000 °C) slightly below the ceramic melting point.

Unfortunately, this step induces a non-negligible shrinkage, potentially introducing some geometrical deformations due to anisotropy phenomena and, in some cases, also some level of local porosity. Both these effects are highly undesirable for mini- and micro-fluidic applications. Indeed, respect for the exact geometries at the microscale is essential, and the wall's leak-tightness is of primary importance.

A possible alternative design choice is to skip the thermal postprocessing and directly produce the substrate as a “green part”. However, the polymeric binder, optimized for sublimation during thermal postprocessing, must be modified to provide good mechanical properties and radiation hardness. The binders presently in use are typically acrylic-based, a class of polymers with poor tolerance to ionizing radiation, while resins in the classes of epoxies and polyimides shall be considered as a replacement.

6.2 Method and materials

6.2.1 Methodology

Two possible ceramic AM technologies commercially available were selected. Their possible application to substrate production was investigated and discussed with the manufacturers. Process parameters were tuned to fulfil our desired requirements, and samples were produced for validation. The samples, having similar geometries to the previous polymeric ones, were inspected, and their interconnection (pin-based) was tested. The inspections on the samples can be grouped into two main categories: substrate and microchannel inspections.

The substrate inspection consists of the following:

- Investigation of internal defects of the samples
- Measurements of the dimensional accuracy of the features

- Measurements of the surface flatness and roughness

X-ray computed tomography was used to check possible internal defects that could compromise the substrate functionality, while a large 3-D scan was used to measure the substrate flatness and the accuracy of the main features for the interconnection. The roughness measurement was performed with a profilometer. The flatness and roughness of the substrate's top surface play an essential role in the interface with the sensor glued on it. Furthermore, a good flatness also guarantees control of glue thickness between sensor and substrate.

The microchannel inspection focused on studying:

- The roughness of the channels
- The leak-tightness of the channel wall

With channels close to the micro-scale size, the effect of the surface roughness on the heat transfer coefficient (h_c) should be considered. Rougher surfaces will tend to increase the heat transfer coefficient as they could initiate fluid mixing in the boundary layer. On the other hand, the surface roughness could increase the distributed pressure drop. Both the effects could not be negligible, especially when the two-phase refrigerants are considered.

Helium leak tests were performed to assess the leak-tightness of the channel wall. Large permeability values and, therefore, a significant value of He leaks can limit the use of ceramic 3D printed substrates for two-phase cooling applications.

Substrate and microchannel inspections were then followed by investigating the pin-based interconnection properties:

- Plug-and-play
- Interchangeability
- Sealing performance

A detailed description of the interconnection properties is presented in Section 5.2. Also, here, an iterative process based on testing the three properties and adjusting the design accordingly was followed to validate the interconnection.

This approach, even if not sufficient to demonstrate that a ceramic substrate fits all the requirements of HEP detectors, was intended to assess the feasibility of producing a cooling substrate and validate the hydraulic and mechanical interconnection.

6.2.2 Selected AM technologies

Several AM technologies for advanced ceramic materials appeared in the market during the past years. They continue evolving as the demand and interest in different engineering appli-

cations increase. An exhaustive review was carried out by Y. Lakhdar [194]. Some requirements were imposed for selecting the AM technologies to investigate among those available in the market:

- The printing accuracy must be within $\pm 50\text{-}100\text{ }\mu\text{m}$ to allow the correct working of the interconnection. Indeed, the accuracy is dependent on the part dimension. However, a post-machining could be considered to meet the accuracy requirement of specific features.
- The relative density of the final printed ceramic should be greater than 97% of the bulk material. This is a tentative requirement that was imposed to ensure the leak-tightness of the cooling channel walls.
- The ceramic material shall match the cooling substrate requirements. aluminium nitride is one of the best candidates for its CTE matching with silicon sensors and for its good thermal conductivity. However, aluminium oxide, with a lower thermal conductivity, can also be considered when less demanding cooling is needed.
- The printing machine shall produce parts larger than $100\times 100\text{ mm}^2$ to allow the printing of a substrate that suits the dimensions of a typical electrical module now present in silicon trackers.

Two different AM technologies were therefore chosen based on these requirements: the Nanoparticle Jetting technologyTM (NPJ) and the Lithography-based Ceramic Manufacturing (LCM).

The XJet company patented the NanoParticle JettingTM (NPJ) technology. It is based on liquid dispersion and inkjet process [195]. NPJ produces parts by jetting thousands of stochastic ceramic nanoparticles dispersed in a polymer matrix from inkjet nozzles. These nanoparticles vary in size and shape and are distributed on the building platform to allow natural packing, high density and super-thin layers almost as fine as $10\text{ }\mu\text{m}$. Simultaneously, a saline water-soluble support material is deposited in the same way. Both the build and support materials are suspended in a liquid that then evaporates at around $300\text{ }^{\circ}\text{C}$ in the build chamber, leaving behind the mechanical part and its supporting structure. The support material is then easily dissolved by a water-based solvent. Finally, the part is sintered ($T=1550\text{ }^{\circ}\text{C}$ for a few hours for aluminium oxide). Due to the effortless removal of the support material, finished parts of virtually any geometry can be produced, including those with very small holes, thin walls, challenging arches and sharp edges. A key point of this process is that the quality of the printed part is almost not dependent on the part orientation during printing. Resolution and accuracy of $20\text{--}100\text{ }\mu\text{m}$ are achieved depending on the dimension of the printed part.

The Lithography-based Ceramic Manufacturing [196], developed by Lithoz GmbH, is based on a layer-by-layer photopolymerisation process by digital light processing (DLP). Details of the LCM manufacturing system are shown in Figure 6.1. It uses a photocurable ceramic

suspension, consisting of a high-purity ceramic powder dispersed in a light-sensitive organic matrix, the "binder". The binder is composed of a photo-initiator, monomers based on (meth)acrylate chemistry and additives. It enables the layer-by-layer fabrication of a ceramic green body, and it is removed in a de-binding step ($T = 1000\text{ }^{\circ}\text{C}$). After that, a subsequent standard sintering process allows producing ceramics with high density, higher than 98% [197, 198]. For printing technologies based on lithography processes (i.e. DLP, stereolithography), the part orientation during printing plays a key role in the quality and accuracy of the final part.

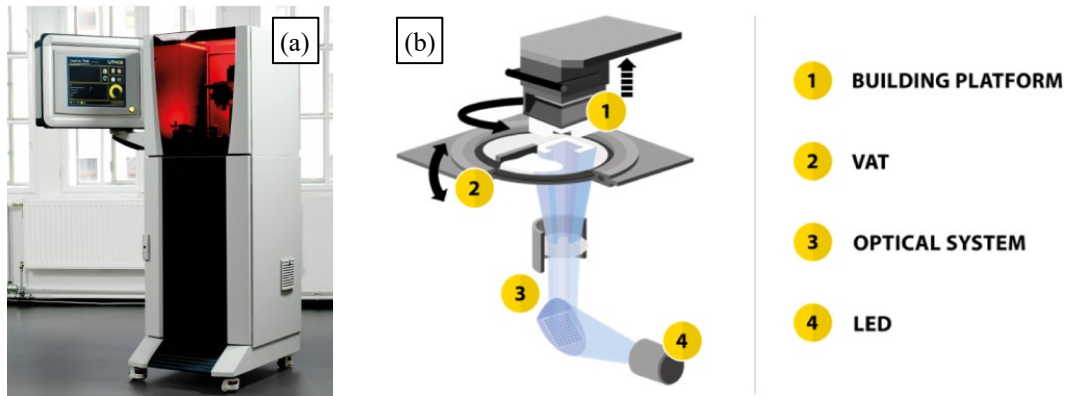


Figure 6.1: Lithoz CeraFab 7500 manufacturing system. In (a), the 3D printing machine is shown, while in (b), the schematic drawing of its LCM process is illustrated. The building platform (1) moves downward to the transparent vat (2). The DLP is constituted by light-emitting diodes (LEDs, 2) and an optical system (3) composed of a digital micrometer device (DMD) and dedicated projection optics. The DMD chip controls which area must be polymerised; its individual mirrors are tilted, causing the individual pixels to be turned on or off according to the cross-section to be projected onto the transparent vat bottom VAT (2). Once the layer is completed, the vat is separated from the cured layer, and the building platform (1) moves upwards out of the suspension. The projection optics guarantee a pixel resolution area of $40 \times 40\text{ }\mu\text{m}^2$ in the CeraFab 7500 and even lower, $25 \times 25\text{ }\mu\text{m}^2$, for the new CeraFab S25 manufacturing systems [196].

The polarity surface chemistry of each resin, the color of the ceramic powder, its reflective and absorption index affect the resin polymerisation. Therefore, some polymerisation parameters such as time of exposure, UV light wavelength spectrum and intensity are specifically adjusted and optimised for each ceramic powder. In this framework, most AM companies like XJet are developing their recipe for printing different ceramic materials. In addition, special attention must be given to the sintering process of particular ceramics like aluminium nitride (AlN). Indeed its sintering must be performed in a furnace at $1700\text{--}1800\text{ }^{\circ}\text{C}$ in an inert atmosphere (nitrogen gas only) to prevent oxidation of the aluminium.

The LCM technology is now capable of producing parts in AlN [199] even if not yet commercialised. Therefore, the ceramics samples were produced in aluminium oxide with the idea that similar results could be obtained with aluminium nitride in the future. Indeed, within the AIDA Innova framework [200], a collaboration with Lithoz was started on studies of aluminium nitride substrate production.

6.2.3 Samples

The ceramic samples are based on the polymeric design with some additional features and adaptations. Five different types of samples were printed, identified hereafter as S1-S5, and they are visible in Figure 6.2 with a sample summary information given in Table 6.2. The drawing of the sample type 4 (S4) is in Appendix E (Figure E.3) as an example of the implemented additional features and adaptations.

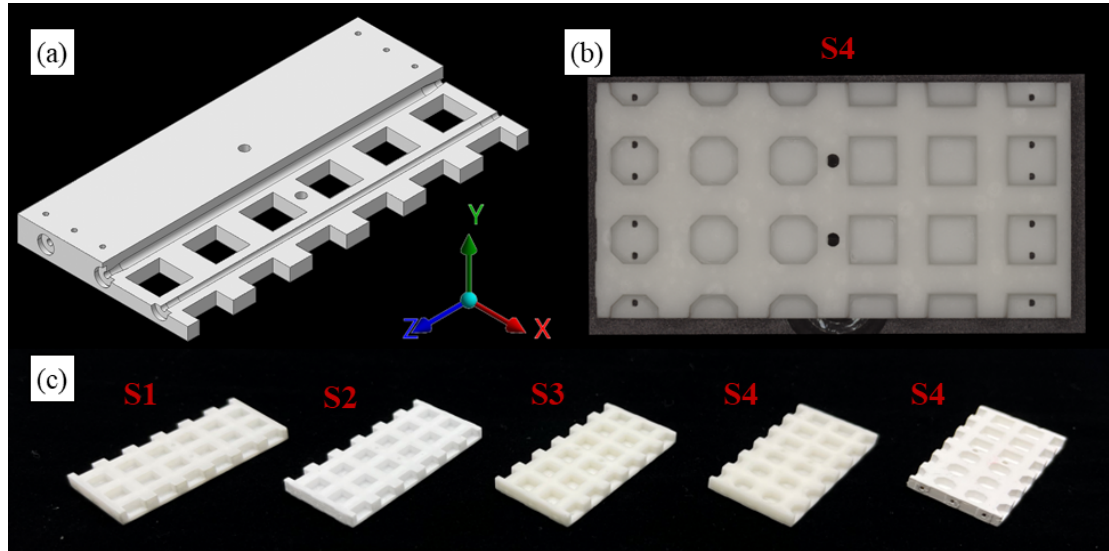


Figure 6.2: Samples for the ceramics characterisation. (a) Sectioned CAD model, (b) Bottom surface of sample type 4 (S4), and (c) Samples types S1-S5.

Table 6.2: Summary of the ceramic samples. NA* stands for Not Applicable.

Sample Type	Qty	Technology	Material	Sintering Temperature	Relative density	Orientation
S1	6	NPJ	C808 - Zirconia	1450-1500 °C	99.5%	XZ plane
S2	10	NPJ	C707 - Alumina	1550 °C	99.4%	XZ plane
S3	3	LCM	Lithalox 350 - Alumina	1650-1670 °C	99.3%	XZ plane
S4	3	LCM	Lithalox 350 - Alumina	1650-1670 °C	99.3%	XY plane
S5	3	LCM	350 (49vol%) - binder (51vol%)	NA*	NA*	XY plane

Samples type 1 (S1) and 2 (S2) were produced with NPJ technology and zirconia and alumina (aluminium oxide) materials, respectively. In this case, the result of the finished parts is not highly dependent on the orientation. Therefore, it was decided to orient the sample XZ plane parallel to the layer-by-layer growing plane. The sample reference system is displayed in Figure 6.2.a.

Samples type 3 (S3), type 4 (S4) type 5 (S5) are produced with LCM technology. Being LCM produced parts affected by the printing orientations, two different angles were considered:

- Samples type 3 (S3), XZ plane is placed parallel with respect to the layer-by-layer growing plane.

- Samples type 4 (S4), XY plane is placed parallel with respect to the layer-by-layer growing plane.

To improve the print quality of overhanging features, chamfers were added at the corners of the slots (45° angle and 0.7 mm length) of the sample of type 4 (6.2 .b). For each sample, half of the slots were printed with the chamfer and half without for comparison.

Samples type 5 (S5) are identical to S4 with the exception that they are not de-binded or sintered.

6.3 Ceramics sample characterisation

6.3.1 Substrate inspection

X-ray computed tomography (Zeiss METROTOM 1500 CT scanner [201]) measurements were conducted to find possible defects related to different AM processes and orientations. A sample for each type was scanned separately (Figure 6.4).

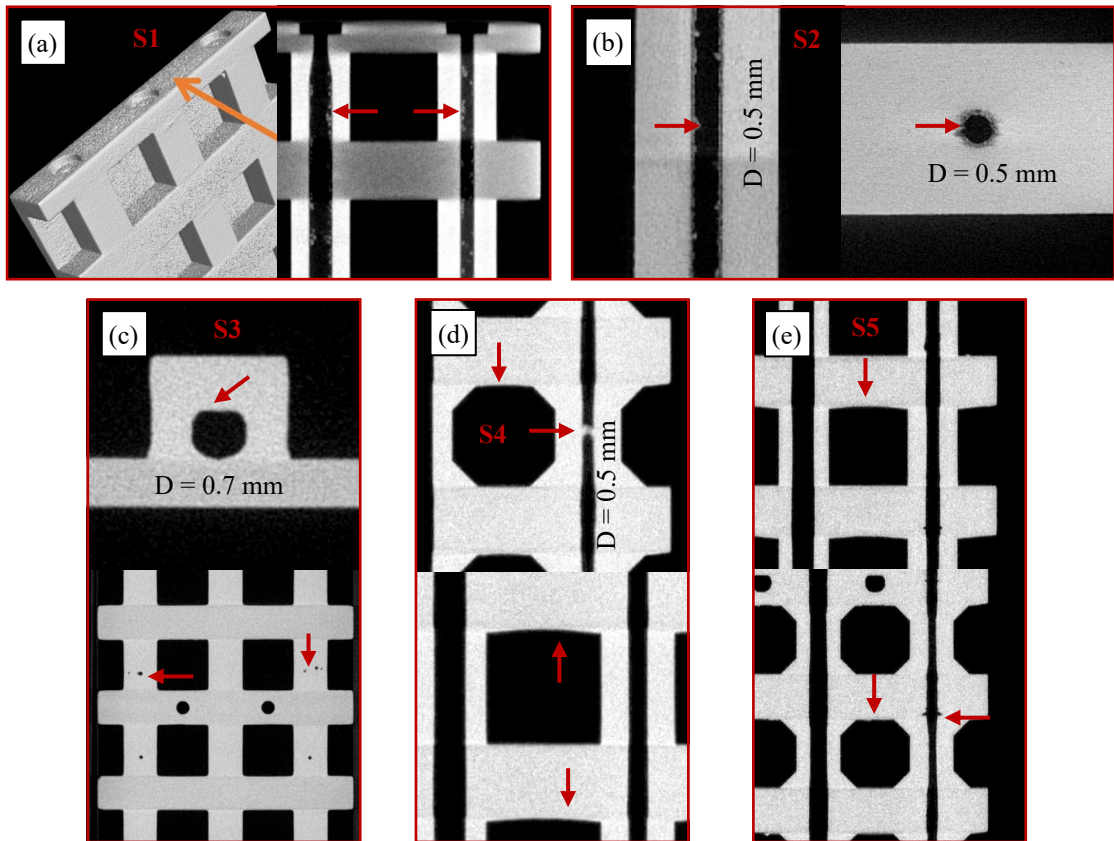


Figure 6.3: Details of the X-ray computed tomography. (a-e) Sample S1 - Sample S5. The accuracy of the scans (i.e. voxel size) performed for the sample types S1, S3, S4 and S5 was 19 μm while the accuracy of the scan for the sample type S2 was 9 μm .

Sample types (S1) and (S2) were produced with NPJ technology and Zirconia and Alumina materials. The S1, made in Zirconia, is much denser than the others made in Alumina, and therefore its scan quality was the worst. An artificial roughness effect, a common artefact of X-ray computed tomography, was present (Figure 6.3.a). Samples S1 and S2 channel cross-sections were perfectly circular, confirming the near independence from the printing direction for the NPJ technology. However, some powder leftovers were found inside the channels (Figure 6.3.b).

Samples types (S3), (S4), and (S5) were produced with LCM technology. The S3 showed a good quality of the slots' shape, glands depth and, in general, of all the features aligned with the printing baseplate. On the contrary, the cylindricity and the shape of the three channels were not respected. The channels presented flat regions aligned with respect to the print baseplate. As expected, overhanging regions of the channels were distorted (Figure 6.3.c top). In addition, some defects, corresponding to voids, were detected inside the materials, but their number and dimensions should not compromise the leak-tightness of the channel walls (Figure 6.3.c bottom).

For S4, rounded edges were present in the slots without chamfered corners because of the orientation (Figure 6.3.d). However, some deformation, even if minimal, was also noticed in the overhanging region of the chamfered slot (Figure 6.3.d top). In any case, they were minimal and will not affect the interface between the pin and slot. The channels had some powder obstruction and showed some irregularities. These irregularities were more evident in the smaller channel having a diameter of 0.5 mm.

The S5 was, among all, the sample with the largest number of defects, including all the defects observed in S4. It has to be said that S5 was printed on a 1:1 scale. Differently, all the other samples required a larger scale printing (1.2 : 1) in order to compensate for the subsequent shrinkage, due to the sintering process. A side effect of this is that the printing resolution of the sample 5 is intrinsically worst than that of the other "smaller" samples. It was also noticed that the parts appeared to be brittle due to the mixture of ceramics and binder that was not optimised to be used as a final part; further R&D is then required for the correct binder selection and the optimum mixture.

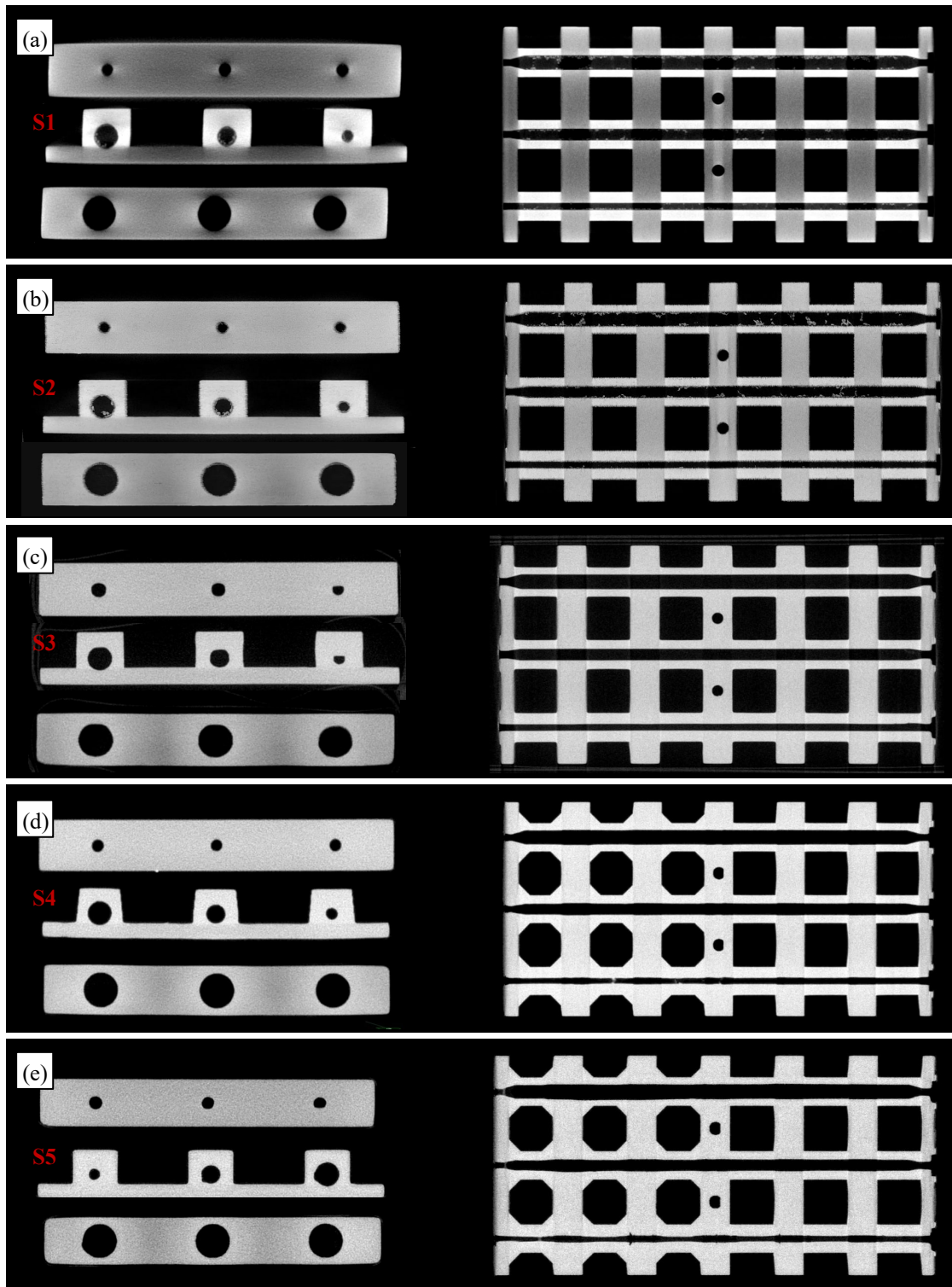


Figure 6.4: X-ray computed tomography of the samples. (a-e) All the sample types were analysed (S1-S5). The cross-sections of the channels in the left pictures refer to the short side of the samples, while the cross-sections in the right pictures are taken at the centre of the sample and are parallel to the top surface.

To investigate the dimensional accuracy and flatness of the samples, a wide-Area 3D measurement system head, the Keyence VR5200 machine, was used [202]. The 3D scan was set to "high magnification" and "stitching mode" options. The height measurement accuracy was $\pm 4 \mu\text{m}$ with a repeatability of $1 \mu\text{m}$. The accuracy in X-Y was $\pm 2 \mu\text{m}$ with a repeatability of $0.5 \mu\text{m}$. A profilometer with a needle of $2.5 \mu\text{m}$ was used for the surface roughness.

An example of a 3D scan measurement, of a sample bottom surface, can be seen in Figure 6.5. The measurement of all the slots was performed for all the samples, and the mean values and their accuracy are illustrated in Table 6.3. The "W1" dimension corresponds to the slot width along Z while "W2" is along X. The dimensions "a1" and "a2" correspond to the angles of the slot aperture along Z and X directions, respectively (see Figure 6.5). The dimension "H" corresponds to the slot depth, along Y.

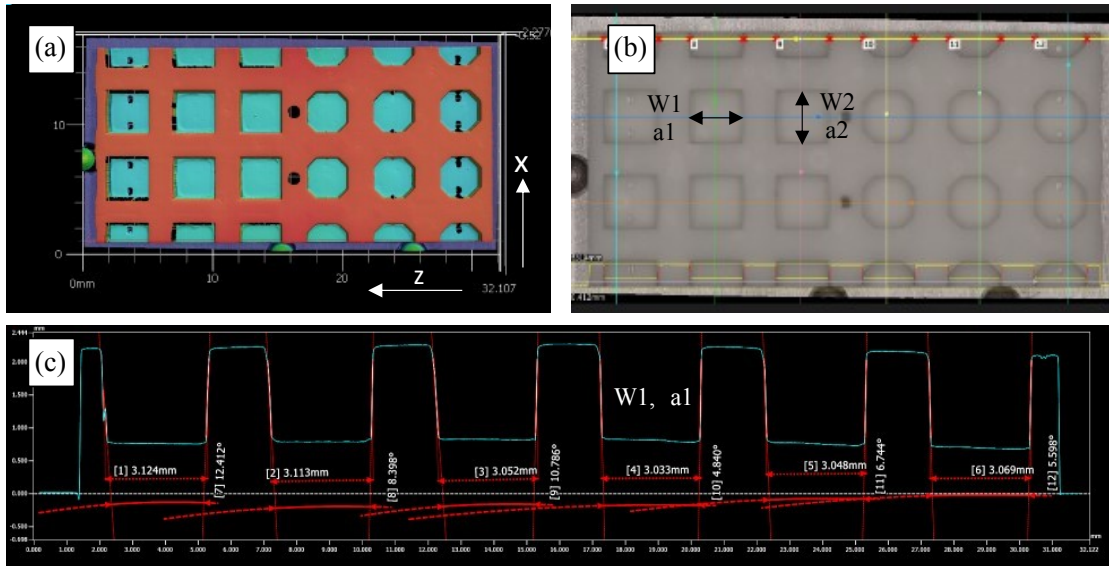


Figure 6.5: 3D scan measurement of a sample bottom surface. (a) Sample reconstructed image, (b) mapping of the surface and (c) Profile measurement. The sample illustrated in the pictures is the S4.

All the samples reached a dimensional accuracy (repeatability) of the slots within $50 \mu\text{m}$; the results are in Table 6.3. The mean values (μ) of samples S3, S4, and S5, obtained with LCM, were close to the design nominal values, 3mm for the width and 1.5mm for the slot depth. Mean values of S1 and S2, obtained with NPJ, slightly differed from the design nominal values. This indicates that the initial model adjustment to compensate for the shrinkage effect needs to be improved; on the other hand, the samples showed good repeatability ($\pm 50 \mu\text{m}$).

The 3D scan of the top surfaces can be seen in Figure 6.6 while the results of the top surface flatness and roughness are summarised in Table 6.4.

For all cases, the surface finishing was within the class number N9 on standard ISO 21920 [203]. It corresponds to a roughness R_a of less than $6.3 \mu\text{m}$. While the flatness was in the order of $50\text{-}100 \mu\text{m}$ for each sample type. The value of the flatness corresponds to $30 \times 15 \text{mm}^2$ printed

6.3 Ceramics sample characterisation

Table 6.3: Summary of surface 3D scan feature measurement. The nomenclature is in Figure 6.5.

Sample type		N. samples	W1		W2		a1		a2	
			μ [mm]	σ [mm]	μ [mm]	σ [mm]	μ [°]	σ [°]	μ [°]	σ [°]
S1		5	2.922	0.016	2.947	0.014	5.6	0.6	4.6	0.7
S2		6	2.937	0.015	2.851	0.031	4.7	0.6	3.9	0.6
S3		5	2.990	0.030	2.997	0.019	3.7	0.8	3.5	0.4
S4	no chamfer	3	3.098	0.039	3.103	0.015	8.8	2.0	7.9	1.6
	chamfer	3	3.008	0.036	3.033	0.014	5.4	1.7	4.1	0.5
S4	no chamfer	2	3.096	0.027	3.115	0.013	12.4	2.0	6.5	1.5
	chamfer	2	3.004	0.025	3.019	0.022	7.0	2.5	4.5	0.9

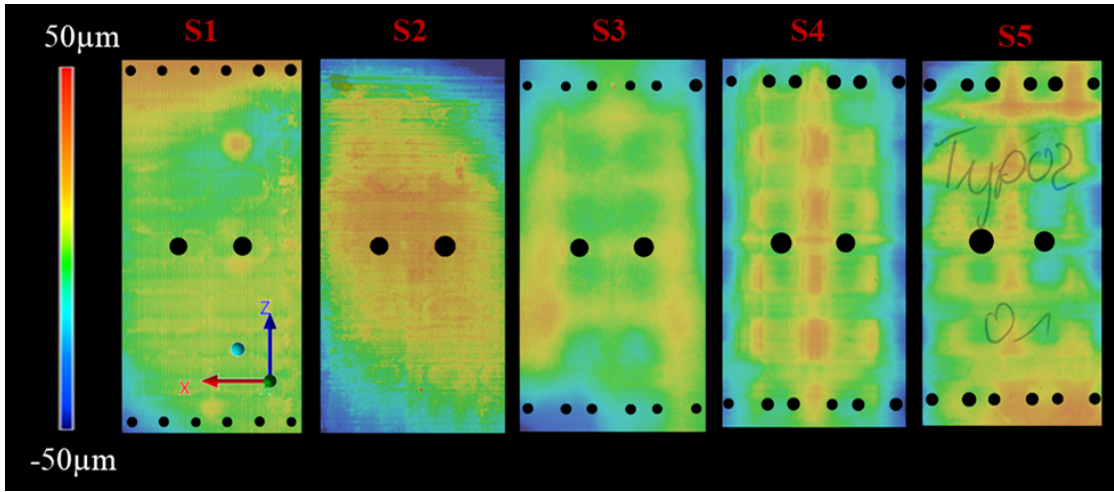


Figure 6.6: 3D scans for the measurement of the samples flatness. The picture shows the 3D scanned areas of the five sample types. The scanned area is approximately 15x30mm².

parts having a thickness that varies from 2.2 mm to 0.7 mm in correspondence with the slots. Based on the 3D scans, the effect of the slots at the bottom and, therefore, the effect of different thicknesses on the top surface is minimal and does not influence the chip sensor gluing. In addition, a thin layer of stitched power covered the S1 and S2 top surfaces. Presumably, it derived from printing technology. If needed, a post-surface finishing can be considered to remove the thin powder layer.

Table 6.4: Summary of the roughness and flatness measurements. The measurements of the arithmetic average roughness (R_a), root mean squared roughness (R_q) and the ten-point mean roughness (R_z) were taken along the two dimensions (Z and X) of the samples' surface (Figure 6.6).

Sample type	Direction Z [μ m]			Direction X [μ m]			Flatness [μ m]		
	R_a	R_q	R_z	R_a	R_q	R_z	Total	Upper	Lower
S1	1.54	1.96	9.89	1.27	1.64	8.53	56	27	-29
S2	3.87	4.88	9.31	2.05	2.5	11.29	94	35	-57
S3	0.63	0.82	4.89	0.53	0.68	4.19	58	16	-41
S4	0.41	0.51	2.76	0.47	0.57	2.78	65	24	-41
S5	0.49	0.6	3.34	0.36	0.53	4.25	67	28	-40

6.3.2 Microchannel inspection

Channel roughness and leak-tightness were inspected for all samples. For the roughness measurement, each sample type was cut and grounded, after being embedded in a resin potting, such to expose the channel. A profilometer with a tip of 2.5 μm was used to perform the measurements (Figure 6.7).

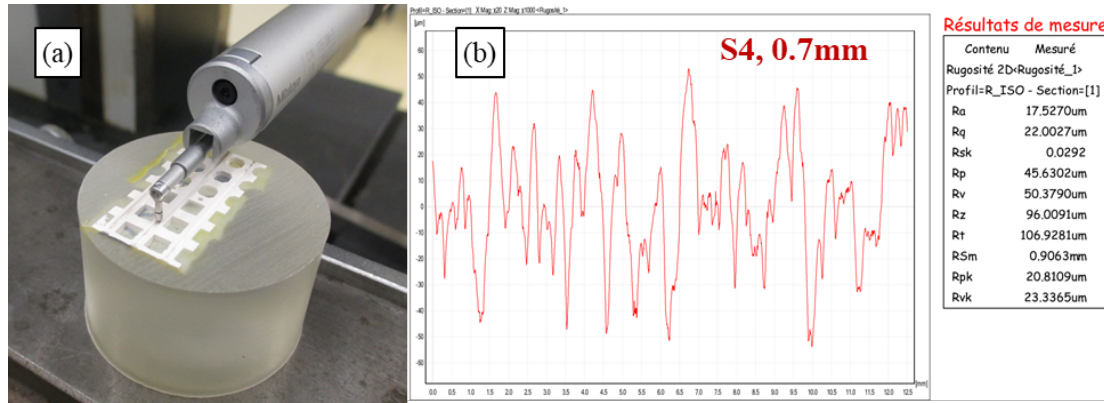


Figure 6.7: Measurement of the channel roughness. (a) Polished sample under the tip and (b) example of a roughness profile.

The arithmetic average of the roughness (R_a) was measured to be in the range 4 – 27 μm across the samples. The presence of protruding particles inside the channels was observed both by visual and X-ray inspections, in particular in samples S1 and S2. Channels were “cleaned” by mechanical abrasion with a metal brush, and roughness measurements were repeated. After cleaning, the roughness decreased. The results are reported in Table 6.5.

Table 6.5: Summary of the channel roughness measurements. Measurements of R_a , R_q and R_z before and after brush cleaning of the samples. The roughness profiles were taken on 7 mm sample length.

S. Type \emptyset [mm]	S1			S2			S3			S4			S5		
	1	0.7	0.5	1	0.7	0.5	1	0.7	0.5	1	0.7	0.5	1	0.7	0.5
R_a [μm]	13.8	12.4	14.1	20.0	31.8	8.6	22.1	18.4	11.6	26.4	17.5	15.6	7	4.2	9.5
R_q [μm]	19.4	17.6	20.5	24.8	37.7	11.0	26.2	23.1	14.8	32.1	22	19	9.2	5.7	13.5
R_z [μm]	98.7	98.8	101.5	107.6	139.6	52.7	100.1	96.8	62.6	133.7	96	72.4	45	32.2	81.7
After brush cleaning															
R_a [μm]	7.4	2	11.5	2.8	2.8	3.3	7.4	14.6	1.1	14.8	15.5	3.9	4.9	8.1	7.6
R_q [μm]	9.2	2.5	14.2	3.5	3.6	4.1	9.1	17.4	1.5	19	19	5	6.2	10.4	10.9
R_z [μm]	43.9	12.2	63.7	16.6	18.3	20.5	35	64.6	8.1	85.8	77.1	28.3	24.1	32	55.5
Reduced	Yes	Yes	Yes	Yes	Yes	Yes	Yes	Yes	Yes	Yes	Yes	Yes	Yes	No	Yes

A first assessment of the channel hermeticity was performed for all samples (Figure 6.8). A helium leak test set-up (Appendix C) was used. The channels were put under vacuum while helium was sprayed on the substrate’s external surface, looking for helium traces within the channel.

The results are summarised in Table 6.6. The He leak rate of all the channels for all the samples was in the order of 10^{-10} mbar l/s (under a vacuum of 10^{-3} mbar).

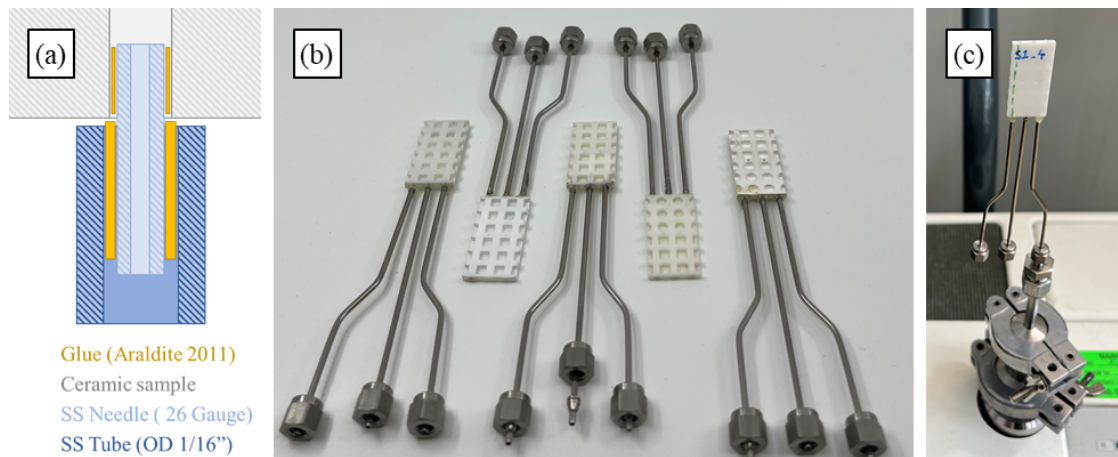


Figure 6.8: Samples for the helium leak test. (a) Schematic view of the interface between the ceramic channel and the stainless steel tube, (b) samples and (c) S1 sample connected to the set-up.

Table 6.6: Summary of the helium leak test. For all samples the vacuum pressure was 10^{-3} mbar. The glued interface was leaking for the channel marked with (*).

Sample type	S1			S2			S3			S4			S5		
D [mm]	1	0.7	0.5	1	0.7	0.5	1	0.7	0.5	1	0.7	0.5	1	0.7	0.5
He leak rate [10^{-10} mbar l/s]	3.4	2.6	3.2	3.9	4.0	14*	4.3	4.3	4.3	4.5	4.4	4.3	4.5	4.5	4.5

6.3.3 Outcomes

Two ceramic AM technologies, the NPJ and LCM, were considered for the final ceramic substrate production. Substrate inspection (defects, accuracy, roughness and flatness) and microchannel inspection (channel roughness, wall leak-tightness) were performed on samples produced by either NPJ (S1, S2) or LCM (S3, S4, S5). Both technologies are suitable for microchannel cooling substrate production.

Substrates inspection

Defects: Samples printed in Zirconia (S1) and Alumina (S2) with NPJ technology showed a good quality of all the features as the accuracy is almost independent of sample printing orientation. For samples printed with LCM technology, S4 had less design distortion. In this case, the XY plane of the sample design was placed parallel with respect to the layer-by-layer growing plane. Added chamfers at the corners of the slots (45° angle and 0.7 mm length) minimised feature distortion. However, some voids were detected inside the materials, but their amount and dimensions would not affect their suitability for cooling substrate application. Particular attention was devoted to the ceramics composite green part (ceramic+binder, sample type S5). The latter appeared to be brittle due to the mixture of ceramics and binder that is not optimised to be used as a final part; further R&D is required for selecting the correct binder choice and the optimum mixture. The use of composite materials shows promise for the production of cooling substrates. The investigation of possible compositions will be addressed

within the AIDAInnova project [200]. It is to be noted that composite materials must be radiation hard, and a radiation campaign is needed to qualify them.

Accuracy: All the samples had a repeatability of the features within $\pm 50 \mu\text{m}$. However, the NPJ samples need an initial best tuning of the printed model dimensions to take into account shrinkage during sintering. The samples produced with LCM went through a first-dimensional tuning to reach feature nominal dimensions.

Roughness and flatness: Both NPJ and LCM technologies showed minimum roughness and flatness values acceptable for HEP sensor gluing requirements i.e. $R_a < 5 \mu\text{m}$; Flatness $< 100 \mu\text{m}$. LCM samples gave slightly better results, with a $R_a < 1 \mu\text{m}$. The local flatness of the measured sample top surface, relevant for the glued interface with the sensors, will not be affected by the substrate geometry (below slot pattern). Nevertheless, overall flatness depends on substrate dimensions. The flatness of large substrates is more sensitive to the substrate thickness and to the printing process parameters; it must be therefore evaluated for each specific geometry.

Microchannels inspection

Channel roughness: Micro-particles, protruding from the channels' walls, were found in all the samples, with larger evidence in samples by NPJ. Roughness was measured to be in the range of $R_a = 4\text{-}27 \mu\text{m}$, and the impact on cooling performance must be evaluated according to the applications (depending on channel dimensions, mass flow rate, heat flux and type of refrigerant). A channel cleaning procedure to remove micro-particles protruding from the channel's internal wall can be implemented. In most of the cases, where cleaning was tried, the roughness was measured to be 50% lower than the initial.

Wall leak-tightness: All the channels of all samples had a He leak rate of 10^{-10} mbar l/s (under a vacuum of 10^{-3} bar). The minimum channel wall thickness was 0.5 mm. The results confirmed that ceramic substrates can operate also with more demanding refrigerants, like two-phase CO_2 .

6.4 Interconnection validation

A procedure similar to the one used for polymer samples was followed to assess the three properties: substrate plug and play, interchangeability, and sealing (see Section 5.2.1). In this case, samples corresponding to the S2 (NPJ), S3 and S4 (LCM) types were tested, and the main outcomes are illustrated below.

As done before, an iterative process, which involved analysis, production and tests, was followed that brought to the optimised design shown in Figure 6.9. The design of the pin geometry was modified. The pin head was rounded (radius = 0.8 mm) to offer a smoother engagement, and the height of the pin was increased (up to 3 mm) to have larger flexibility.

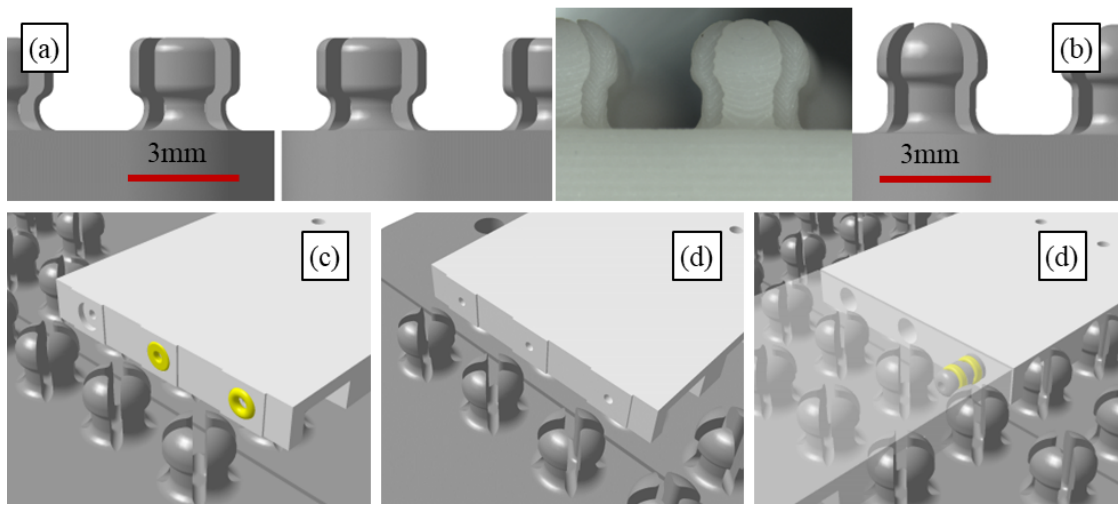


Figure 6.9: Design modifications for the ceramic samples. View of the pin (a) before and (b) after its modification. (c-d) Modification of the wall of the face seal solution and (e) samples with implemented radial seal design. In (b), the pin CAD design is overlapped with the 3D printed baseplate pin (ACCURA25[168]).

Different plastic materials for the baseplate were considered; in the following sections, tests were performed on baseplates printed in ACCURA25 [168], while other tested materials were demonstrated to be more sensitive to the wear effect.

For the face seal solution, to minimise the O-ring compression dependence on the accuracy at the edge of the matching substrates, it was decided to reduce the contact surface to the area of the seal. A step of 0.1 mm around the O-ring groove was implemented at the face seal interface (Figure 6.9.c and d). It guarantees that the modules facing each other will be in contact only in this area. The sample design of the radial seal interconnection is based on the same dimension described in Section 5.4.2.

X-ray computed tomography analyses were performed to evaluate the different mechanical and hydraulic interfaces (Figure 6.10). It was noticed that the radial seal interface was affected by the manufacturing tolerance of the ceramic housing channels. In some cases, the O-rings

of the seal fitting were not perfectly positioned along the housing channels (Figure 6.10). In this case, the oversized O-ring groove caused the sliding of the O-ring during the fitting insertion. The O-rings at the middle of the seal fitting were not completely inserted into the housing channels. The seal fitting position with respect to adjacent modules was affected by the sum of the tolerances of the different parts. Therefore, an additional dimensional tuning to compensate for greater ceramic and assembly tolerances must be performed to optimise the interconnection reliability.

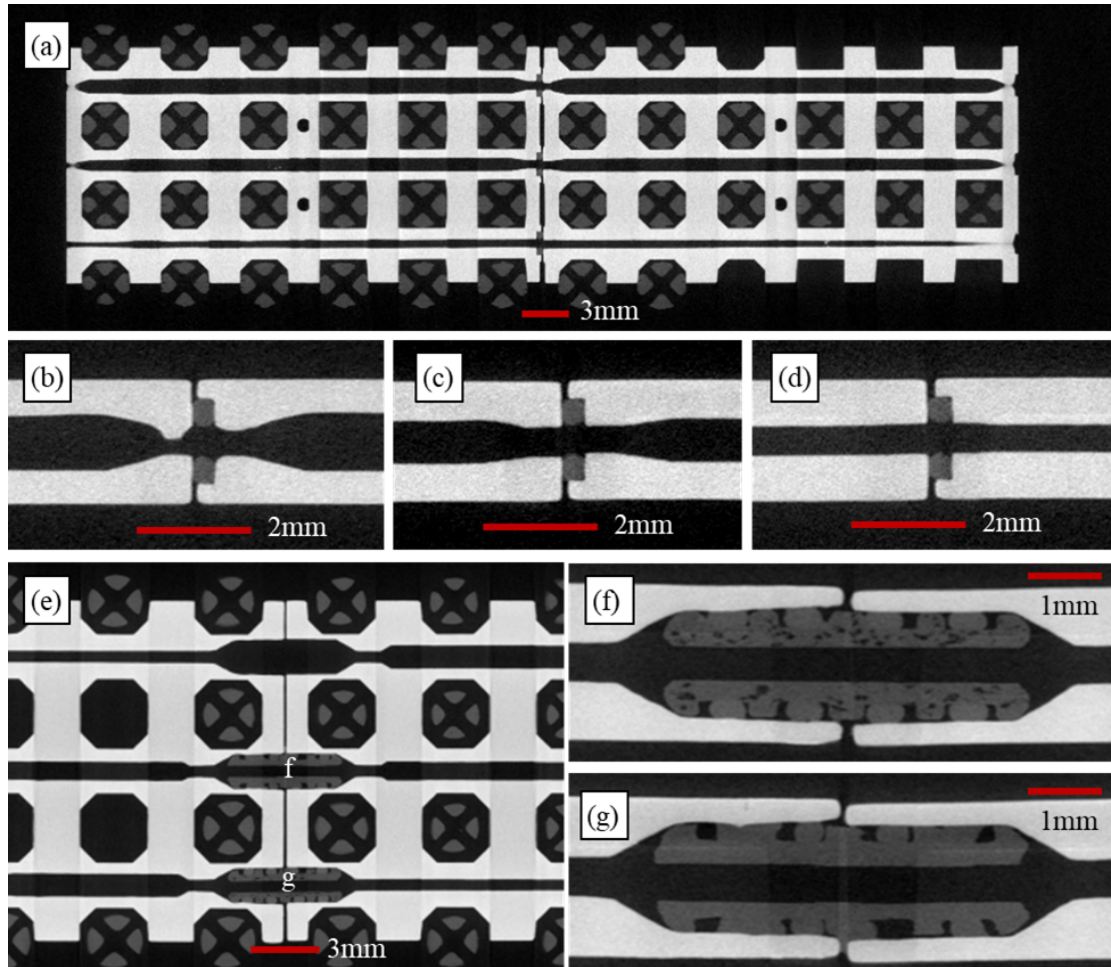


Figure 6.10: Details of the hydraulic interconnection of the alumina samples. (a) Two S3 samples placed in position, (b-d) details of the face seal hydraulic interconnections, (e) S3 samples in position with radial seal interconnection and (g-f) details of the two seal fittings. The pins (baseplate) in the picture (a) correspond to the previous design. The images were taken by using an X-ray computed tomography. The accuracy of the scans (i.e. voxel size) was 19 μm .

6.4.1 Substrate plug-and-play

NPJ (S2) and LCM (S4) sample types were tested with a dynamometer attached to the sample (Figure 6.11). One of the main parameters which affect the pull force is the interference between the pint and slot. The interference is set to 0, and the nominal width of the slot and pin diameter is set to 3mm by design. However, the average dimensions (W1 and W2) of the slot for NPJ (S2) and LCM (S4), measured in Section 6.3.1, were respectively 3.05 mm and 3.02 mm for the LCM (S4) and 2.9 and 2.85 mm for the NPJ (S2). Based on these measurements, the interference of the NPJ (S2) should be larger with respect to the design one, and this can help to investigate the possible effects that could appear by increasing the interference between pin and slot.

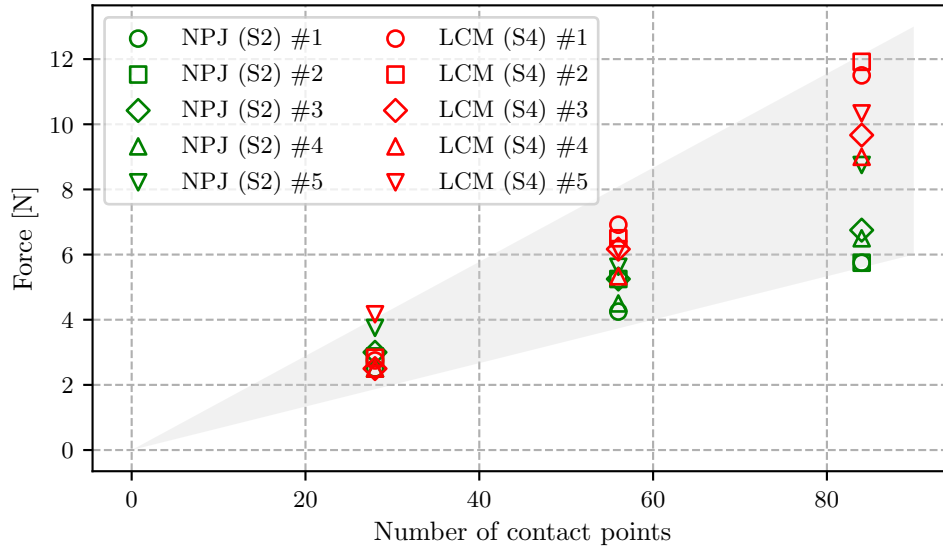


Figure 6.11: Pull force results of the alumina samples. The pull force of the alumina sample types S2 (NPJ) and S4 (LCM) are plotted as a function of the number of contact points (proportional to the number of pins in contact, see Section 5.2.3). Five samples (#1 - #5) are tested for each sample type. The markers show the average pull force of each sample tested 5 times.

Unlike with the polymer samples, where the pull force was almost constant during different tests, the wear effect, after the first tests, was noticed for both sample types. However, after a few (3-5) pull tests done on the same baseplate, the samples' pull force stabilized to the ones shown in Figure 6.11. The reductions of the pull force value were of the order of 30%.

Contrary to expectations, despite having an equal number of contact points, the pull force of the LCM (S4) samples was greater than the pull force of the NPJ (S2) samples, even if the dimensions of the slots of LCM (S4) samples were smaller compared to the slot dimension of the NPJ (S2) samples. This can be explained by the fact that the surfaces of the NPJ samples were covered by the stitched thin powder layers that were gradually detached during the un/plugging. Residual ceramic dust was noticed around the pin during the tests.

6.4.2 Substrate interchangeability

A procedure similar to the one described in Section 5.2.3 was followed for the assessment of the interchangeability of the NPJ (S2) and LCM (S4) sample types. The results of the Repeatability, Exchangeability and Interchangeability for the two sample types, NPJ (S2) and LCM (S4), are in Figure 6.12. While, the X-Y position measurements of the two sample types are in Figure 6.13 and Figure 6.14, respectively.

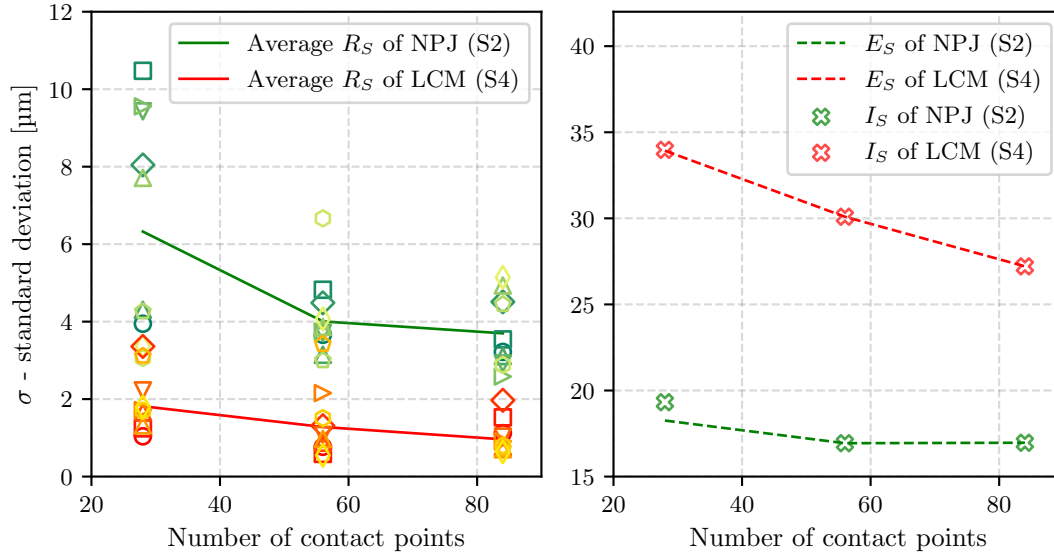


Figure 6.12: Interchangeability results for the alumina samples. (a) Repeatability standard deviation of each NPJ (S2) sample and Repeatability mean value and (b) Interchangeability and Exchangeability standard deviations.

The positioning accuracy of both ceramic sample types was within $\pm 50 \mu\text{m}$. Similarly to the polymer samples, lower accuracy in positioning is achieved along the Y direction corresponding to the 30 mm sample side. This is more evident for the LCM (S4) sample type that was printed vertically with respect to the printing baseplate. Therefore, it can be related to the printing accuracy of the sample in that direction.

The Repeatability values of the NPJ (S2) samples were less than the Repeatability values of the LCM (S4) samples. This could again be attributed to the stitched thin powder layer present on the NPJ (S2), which is gradually removed during the test.

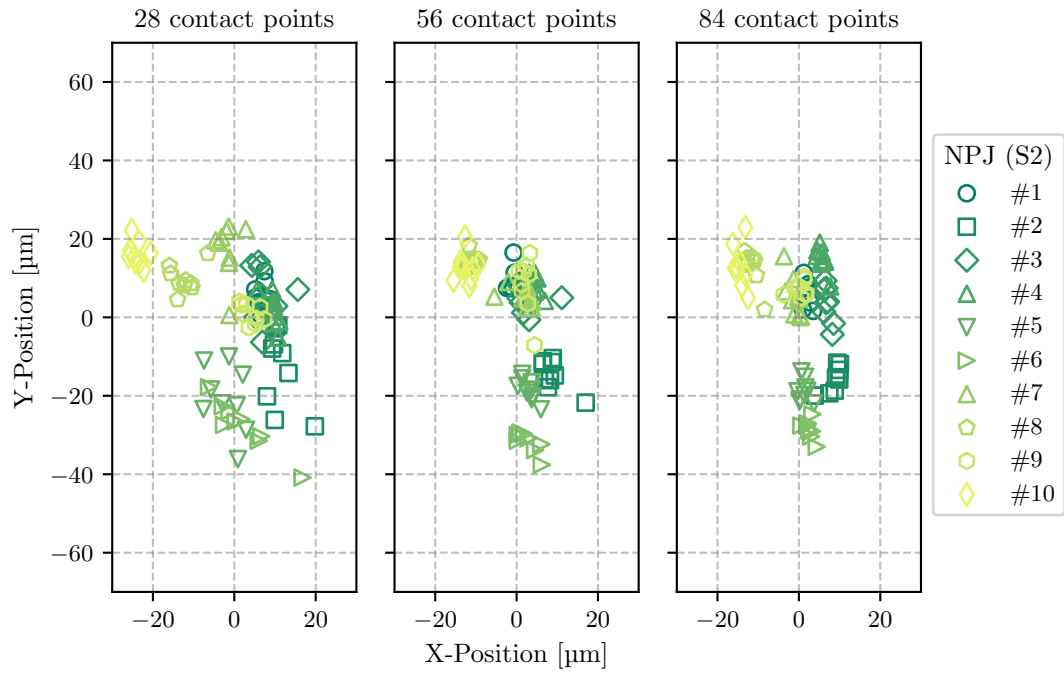


Figure 6.13: X-Y position measurements of the alumina NPJ (S2) samples. The three graphs are referred to the three tested configurations with different numbers of contact points (pins).

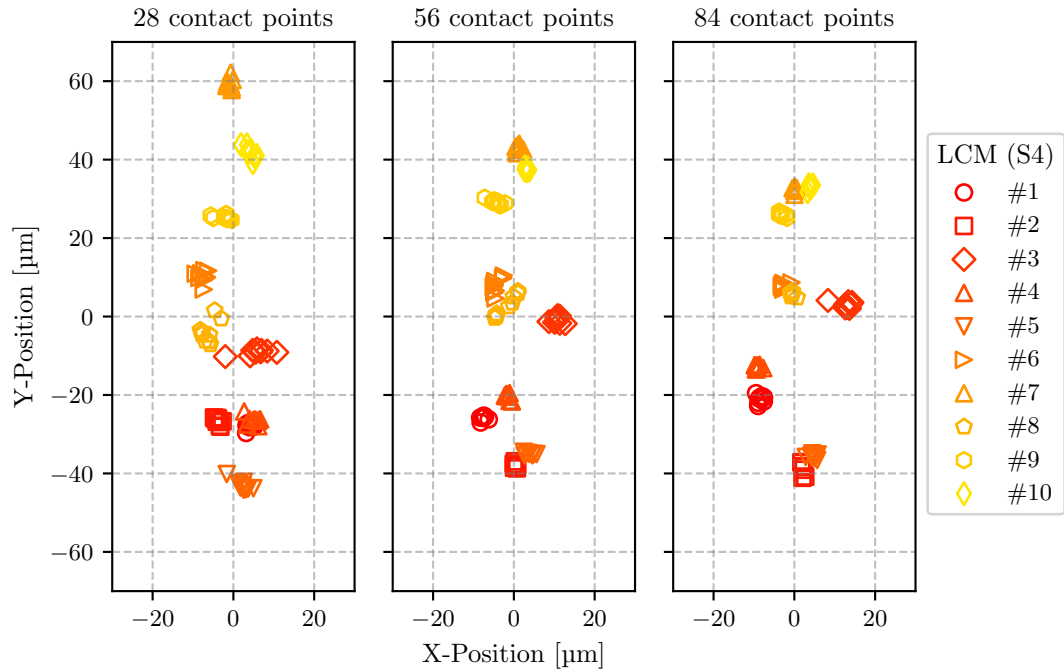


Figure 6.14: X-Y position measurements of the alumina LCM (S4) samples. The three graphs are referred to the three tested configurations with different numbers of contact points (pins).

6.4.3 Substrate sealing

Face seal

The NPJ (S2) samples did not withstand pressures higher than 2 MPa. The cause can be traced to improper tolerances of the samples and surface roughness of the two facing surfaces at the interconnection. R_a greater than 2 μm is known to influence elastomer compression. Further tuning of the production steps parameters or post-surface machining is therefore required for NPJ samples.

For the LCM (S3) samples, the R_a ($<1 \mu\text{m}$) was less of a concern. LCM (S3) samples were tested with micro O-rings (11000, 73172) and micro flat gasket (15286) types. Elastomers geometry slightly differs by $\pm 50 \mu\text{m}$ (Table 5.1). The results for the LCM (S3, S4) are reported in Figure 6.15. The tests with the micro O-rings (11000 and 73172) were performed following the same procedure as the tests in Section 5.2.3. The samples with their O-rings were mounted in series, up to 5 samples; their order was modified for each trial, and only the failed o-ring was substituted for the next trial.

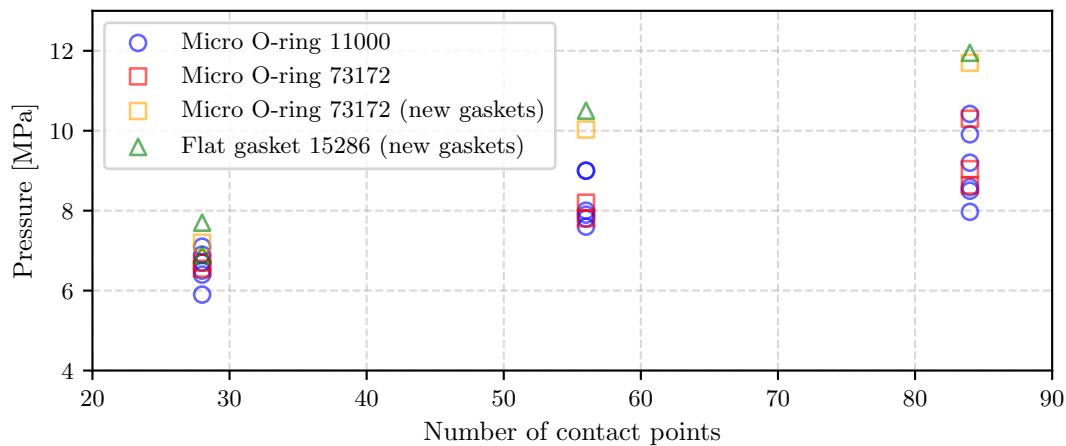


Figure 6.15: Burst pressure results for the LCM (S3) samples with face seal. The dimensions of the O-rings are in Table 5.1.

The micro O-rings withstood pressures from 6 to 11 MPa. The flat gasket having more surface in contact with the samples reached ~ 15 MPa of pressure in one test; however, more attention was required not to touch and misalign the flat gaskets between the samples. The failure typically appeared at one of the two samples at the array end.

In addition, tests with the micro O-ring 73172 and the flat gasket 15286 were done by changing all the elastomers of the 5-sample array every time. These tests are named "*new gaskets*" in Figure 6.15. In these cases, the samples reached higher pressures; the difference was of the order of + 15%.

The achievable pressure depends on the number of contact pins (points) as it increases assembly stiffness and minimises the clearance between the two samples. The failure manifested itself as a "*water jet*" at the interface and to a pushing of the O-ring in the clearance. Figure 6.16 shows a micro O-ring in the correct position and a failed micro-O ring. The He leak rate was of the order of 10^{-8} - 10^{-9} mbar l/s for all the elastomer types.

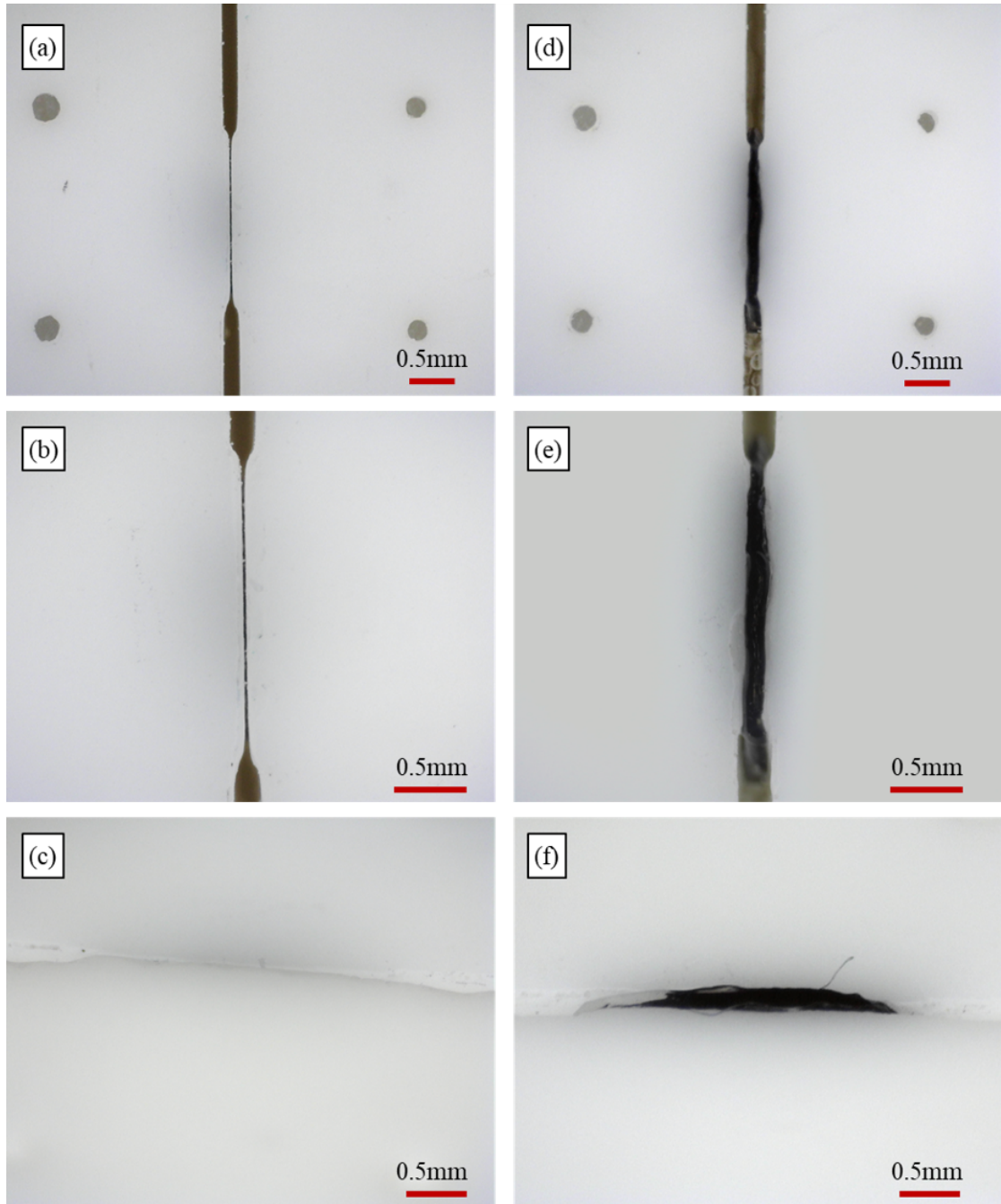


Figure 6.16: Micro O-ring squeezed between the alumina LCM (S3) samples. (a,b) Top and (c) tilted view of a micro O-ring in the correct position, and (d,e) top and (f) tilted view of a failed micro O-ring.

Radial seal

For the radial seal solution, LCM (S4) samples were tested with micro O-rings 11009 (NBR) and 73172 (silicone). Both the O-rings reached pressures up to 30-35 MPa (Figure 6.17). Higher pressures were not investigated because of set-up limitations. However, 30 MPa is well beyond the requirements for operating with higher pressure fluid refrigerants (~ 15 MPa for CO₂). For all the elastomer types, the He leak rates were of the order of 10^{-10} mbar l/s.

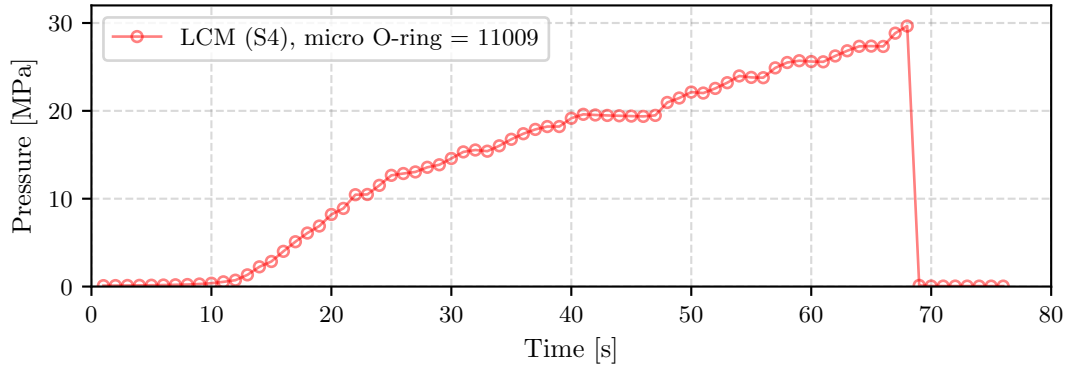


Figure 6.17: Burst pressure test for the LCM samples with radial seal. The O-ring size is in Table 5.1.

For the NPJ (S2) samples, their housing channels were too small to insert the seal fitting correctly. The NPJ samples were re-machined and reached 15 MPa of pressure before leaking at one of the interconnections. The cause was identified in the increase of conicity and surface roughness inside the re-machined housing channels of the O-rings that affected O-ring positioning and integrity. Seal fittings were optically inspected; deterioration of the O-ring was noticed for most of the O-rings once dismantled from the NPJ samples (Figure 5.1).

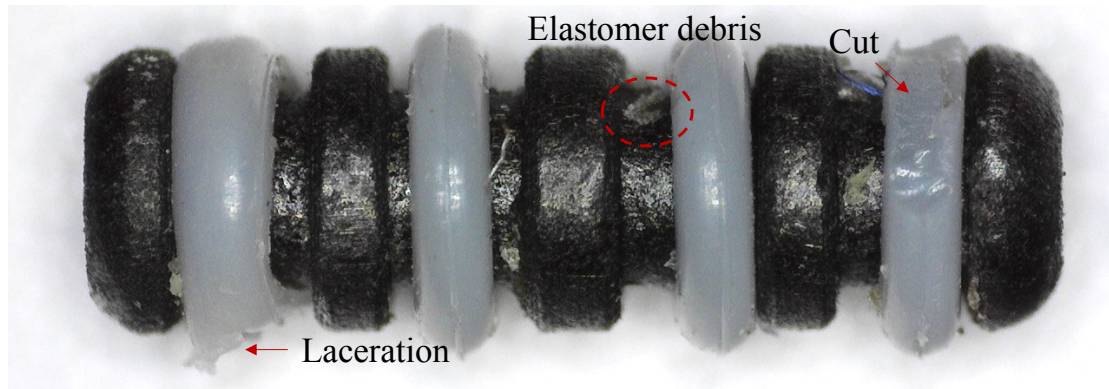


Figure 6.18: Example of a deteriorated micro O-ring. Example of a deteriorated micro O-ring after being extracted from the re-machined NPJ (S2) samples. Typically, deterioration, laceration or cut of the O-rings, occurred for the O-ring at the seal fitting extremities. Elastomer debris was also noticed. The micro O-ring in the picture is the 73172; its dimension is in Table 5.1.

6.4.4 Outcomes

The validation of the hydraulic and mechanical interface for the ceramic prototypes followed a procedure similar to the one employed for polymer samples.

The mechanical interface between the hard ceramic slots in the module and the polymer pins in the baseplate is subjected to the wear effect. A compromise between desired pull force, required to engage the pins, and the wear effect can be reached by tuning the pin's geometry and the number of pins. The pins design was optimized to offer a smoother engaging interface (rounded pin heads) and larger flexibility (longer pins). Nevertheless, a minimal wear effect was observed, translating into a reduction of the pull force value by 30%. However, this effect reduces sensibly after the first few (3-5) un/plugging steps and does not compromise the functionality of the pin base mechanical interface. Further optimizations, such as the tapering of the sample slot walls, can be foreseen. In addition, stiffer materials for the baseplate, like PEEK and Carbon PEEK, can be considered. Different manufacturing technologies like injection moulding or CNC machining can be adopted if more stringent dimensional accuracy, material rigidity or higher radiation tolerances are required.

The ceramic sample position, driven by the baseplate, is guaranteed within $\pm 50 \mu\text{m}$. It corresponds to the minimum achievable tolerance imposed by the 3D printing accuracy ($\pm 50 \mu\text{m}$). The wear effect did not influence the sample position due to multiple pins engagement and its elastic averaging effect (Section 5.2.3).

Specific improvements were implemented for the hydraulic sealing at the interface of the ceramic samples. In order to minimize the dependence of the face seal on the accuracy of the edges of the matching modules, the contact surface was reduced to the area of the seal. The face seal withstood pressures from 6 to 11 MPa depending on the number of engaged pins. A He leak rate of 10^{-8} mbar l/s was measured.

For the radial seal solution, the LCM samples reached pressures higher than 30 MPa and low He leak rates (10^{-10} mbar l/s). However, the radial seal was affected by the manufacturing tolerance of the ceramic housing channels. X-ray metrology highlighted that, in some cases, the O-rings of the seal fittings were not perfectly positioned along the housing channels. Indeed, the oversized O-ring groove caused the sliding of the O-ring during the seal fitting insertion. In addition, the seal fitting position with respect to the adjacent modules was affected by the sum of the tolerances of the different parts. Design adjustments can solve these effects.

The housing channels of the NPJ samples were too tiny to insert the fitting properly. The NPJ samples were re-machined and reached 15 MPa, before slightly leaking at one of the interconnections with respect to the 30 MPa of the LCM samples. The cause was identified in the increase of conicity and surface roughness inside the re-machined O-ring housing channels that affected O-ring positioning and integrity. To overcome this issue, dimensional tuning of the printing model to compensate for the manufacturing tolerances must be foreseen.

If re-machining is required, a fine method that minimizes surface roughness must be followed.

7 i-M μ CS implementation in silicon tracking systems

This chapter provides an idea of possible i-M μ CS implementations into the detector layout, taking as an example the future silicon tracking detector of ALICE 3 [204]. Some fundamental aspects of the i-M μ CS implementation are examined with emphasis on 3D printed ceramics, such as material budget contribution, the flatness of a large cooling substrate, the assembly with monolithic active pixel sensors, and the hydraulic and thermal performances of i-M μ CS.

7.1 Guidelines of the research

Two designs of the interlocking interconnection, that emerged from previous research, were considered for their implementation in an actual detector layout. They are the pin-based and the rail-based mechanical interface (see Section 5.2 and Section 5.5.3, respectively). Both designs can operate with face and radial seal hydraulic interfaces seen in Section 5.4.

The i-M μ CS does not imply the exclusive use of polymer or ceramic AM technologies; other materials (e.g. silicon and CFRP) and manufacturing technologies (e.g. laser engraving, CNC machining and injection moulding) can be employed. For this reason, different materials and manufacturing processes were reviewed, some prototypes manufactured and possible future developments defined.

Taking as reference the future tracker of the next ALICE 3 experiment [204], the implementation of the interlocking concepts into a real detector layout was explored, and the first prototypes of support structures assembled with polymer and ceramic i-M μ CS were fabricated.

Based on the interest in ceramic AM, as new materials and processes for HEP cooling applications, special attention was given to the i-M μ CS printed in alumina. Alumina AM prototypes (up to 30x210 mm²) were used to assess fundamental aspects of the detector implementation like the substrate flatness, gluing interface with thin monolithic pixel sensors (100 μ m thin) and hydraulic and thermal performances.

The requirement of the flatness was set to 100 μ m; a large area 3D scan was used for the

investigation of different cooling substrate designs. A possible solution to optimise the flatness was as well investigated.

A real sensing module (30x210 mm² large) of the ALICE ITS2, was glued to the i-M μ CS substrate following the standard procedure used for this detector. This allowed a direct comparison with the experience developed previously and the identification of specific issues due to ceramics stiffness and roughness that could affect, i.e. break, the MAPS sensors (ALPIDE sensors [19]).

In addition, plug-and-play hydraulic interconnection is a new concept for HEP cooling applications. For this reason, a general assessment of the dependence of the hydraulic and thermal performances on the interconnection and the interconnected substrates was performed, knowing that a final detector implementation requires a deeper and more specific characterization outside the scope of this research.

To summarise, the aspects examined in the following Sections, are:

- Materials and manufacturing processes
- Detector layout implementation
- i-M μ CS in ceramic AM
 - Flatness dependence on substrate dimension
 - Gluing interface with the sensing module
 - Hydraulic and thermal assessments

7.2 Materials and manufacturing processes

A simple baseline design for the cooling circuit, towards several microfluidic modules, was considered to demonstrate the feasibility of making i-M μ CS with different materials and manufacturing processes. Two parallel channels with a diameter of ~ 1 mm were integrated into the i-M μ CS prototypes. These channels are meant to be connected with the channels of the adjacent modules by face seal or radial seal interfaces.

At this stage, the investigation was limited to the serial hydraulic interconnection between adjacent cooling substrates, with no sub-circuits connected in parallel and integrated into the i-M μ CS. As described in Section 3.4 and Appendix B.9, the design of a more elaborated circuit strictly depends on constraints coming from the final detector requirements and the type of sensor (e.g. heat flux to be dissipated, its non-uniformity over the sensor area and the sensor dimension).

The surface dimension of most of the prototypes ranges from 30x30 to 30x210mm². These two dimensions derive from the size (30x15mm²) of the ALPIDE [19] sensor and its sensing module, named Hybrid Integrated Circuit (HIC) module, which is composed of 2x7 ALPIDE sensors electrically connected through a flexible printed circuit (FPC).

7.2.1 Ceramics

Prototypes, with a thickness of 0.7mm, were produced in alumina (Figure 7.1, "*plate design*"). The main drawback of using ceramics, for HEP cooling applications, is their significant radiation length that must be taken into account, especially for detectors operating at lepton colliders. In lepton colliders, the total MB of the tracker is targeted to be within 1%. Taking the ALICE ITS2 as an example, its sensing module (FPC, sensors and their interconnection) already contributes to 0.5% for the MB of a single layer. This implies that the ceramic substrate should have a thickness of less than 0.4 mm. This does not take into account the contribution of the coolant to the material budget.

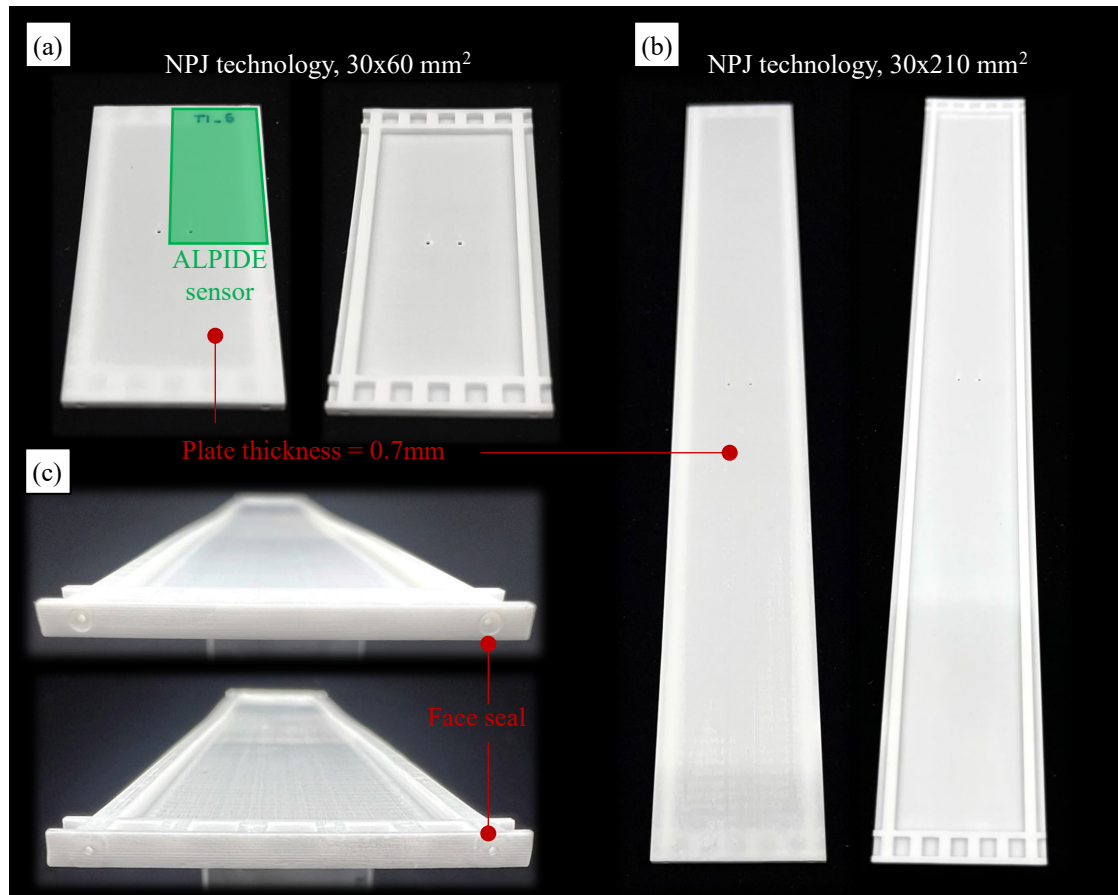


Figure 7.1: Ceramic i-MuCS with plate design. (a) 30x60 mm² sample, (b) 30x210 mm² sample and (c) detail of a face seal interface. They are printed by NPJ technology. The thickness of the sample plate is 0.7 mm.

Producing thin ceramics substrates, down to 0.4 mm of thickness, is challenging because of the flatness tolerance requirement; this aspect is later addressed in Section 7.4.1. However, going with a thin substrate is not the only possibility. Similar to the silicon microchannel frame solution (Section 2.3.2), the areas in which high thermal performance is not required (e.g. in correspondence with the pixel matrix region of the ALPIDE) can be thinned down or

completely removed ("*frame design*"). In this case, the average thickness, and therefore the MB contribution, is minimised at the cost of increasing the MB non-uniformity in the detection layer. Although the layer regions with higher MB contribution will not be within the active sensing area, this non-homogeneity can impact the overall detector resolution as it influences the active sensing area of the nearby detection layers. This aspect must be investigated for each specific application. Prototypes with "*reduced thickness areas*" and "*frame design*" are shown in Figure 7.2. The thickness of the frame is 0.5 mm, while the thickness of the thin plate is 0.2-0.3 mm.

The samples were 3D printed in alumina by using the two AM technologies previously described, LCM and NPJ. In parallel to the evolution of Additive Manufacturing technologies, which will enable the production of prototypes with 3D printed aluminium nitride (Section 6.2.2), alternative ceramic manufacturing processes, such as Ceramic Injection Moulding (CIM), should be explored.

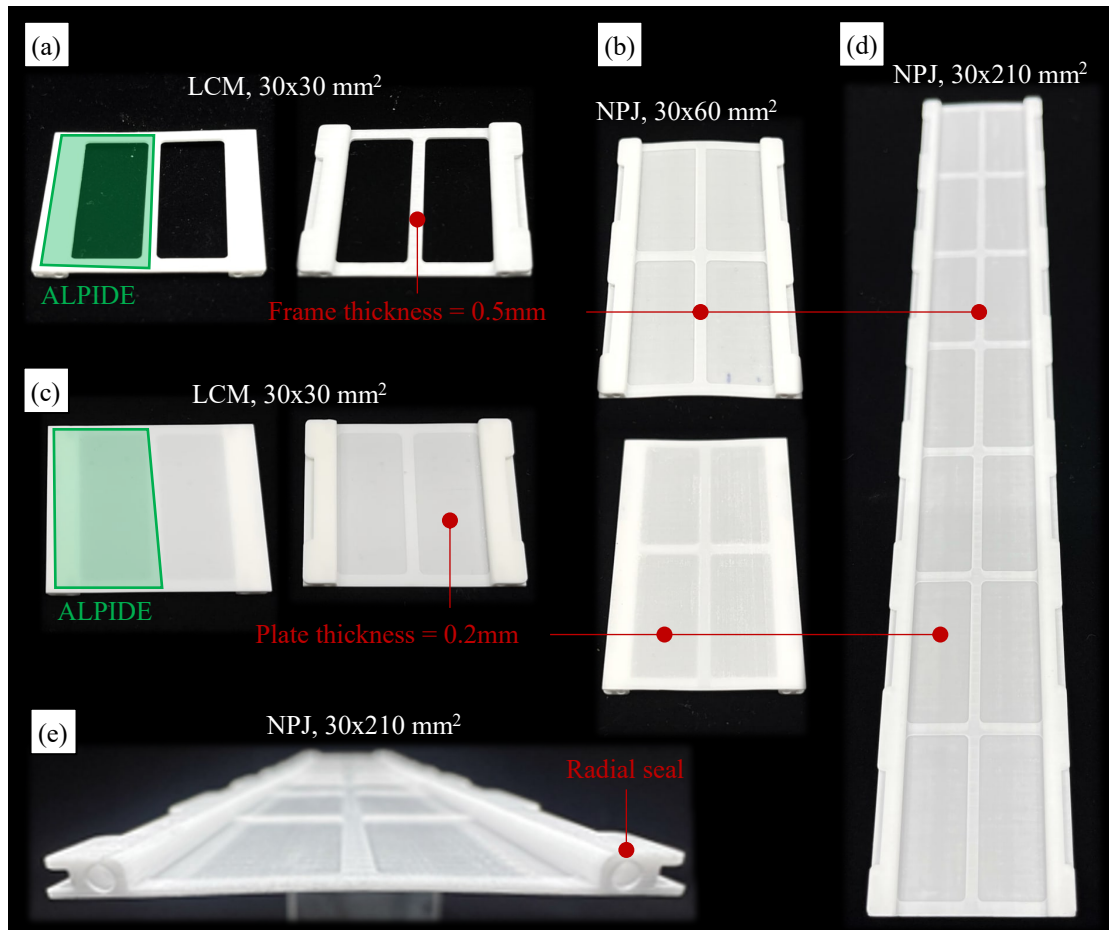


Figure 7.2: Ceramic i-M μ CS with frame and reduced thickness designs. (a) 30x30 mm² frame design, (b) 30x30 mm² reduced thickness design, (c) 30x60 mm² sample with reduced thickness design, (d) 30x210 mm² sample with reduced thickness design and (e) detail of its radial seal interface.

7.2.2 Polymeric

Similar prototypes produced in Alumina AM were also produced in acrylate photopolymer (Vero Clear resin [174]) and they are later shown in Section 7.3.

A polymeric cooling substrate can find applications in HEP trackers for lepton colliders where sensors can be operated at ambient temperature. Indeed, limiting factors of polymers are their low thermal conductivity and the mismatching of their CTE with the silicon sensors (3-5 ppm/K). Taking as an example the 3D printable epoxy-based resin ACCURA25 [168], commonly used in the ALICE experiment for its radiation tolerance, its thermal conductivity and CTE are 0.150 W/mK and 107 ppm/K, respectively.

The minimisation of the substrate thickness at the interface between coolant and sensor can reduce the impact of the polymer low thermal conductivity. It has been demonstrated that wall thicknesses of 0.4 mm are printable while guaranteeing leak-tightness of the cooling channels. Further thickness reduction is also achievable, i.e. surface post-grinding. As an example, the ALPIDE[19] sensor, dissipating about 40 mW/cm², can be kept at an operating ambient temperature by a polymeric substrate with chilled water at 20°C as coolant, Figure 7.3. Ambient operating temperature also minimises the effect of the CTE mismatch between the silicon sensor and the polymeric cooling substrate with no relevant impact on sensor stability and integrity.

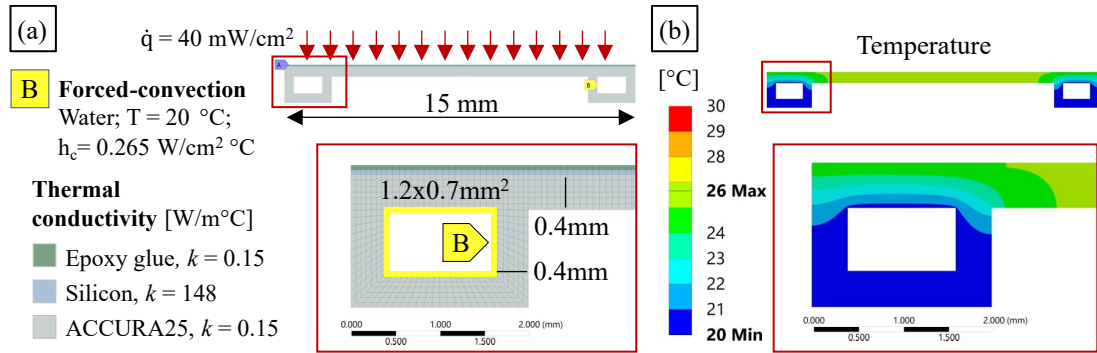


Figure 7.3: 2D thermal analysis of a polymeric cooling substrate. (a) Boundary conditions and (b) temperature results. The ALPIDE sensor is 15x30 mm² large and 50 μm thin. Conservatively, an epoxy glue thickness of 100 μm is considered at the interface between the sensor and cooling substrate. Two channels, with a rectangular cross-section of 1.2x0.7 mm², are engraved in the polymers. The channels are perpendicular to the short side of the ALPIDE sensor corresponding to 15 mm length. The coolant is water at 20 $^\circ\text{C}$ with a mass flow rate of 0.1 g/s. It operates in a laminar flow regime under the hypothesis of a constant axial wall heat flux. The corresponding Nusselt number is 3.92 and the convective heat transfer coefficient (h_c) is 0.265 W/cm²K [94, 205]. The maximum temperature, reached in the center of the sensor, is 26 $^\circ\text{C}$. The Ansys Workbench 2019 software [175] was used to perform the analysis.

In addition, the integration of the service circuitry and the electrical interconnections into the module cooling substrate is a possible future development for the polymeric i-M μ CS. Indeed, a circuit board can be 3D printed, the sensors can be electrically connected to its circuitry and a cooling circuit can be integrated inside. As an example, the NanoDimension

company is able to produce 3D PCBs having metal layers down to 17 μm [206] and embed electronic components, from capacitors to real chips. In this case, the materials of a 3D printed circuit board, with an integrated cooling circuit, should be radiation hard, and the electrical interconnection between metal layers and silicon sensor should be studied.

7.2.3 Silicon

As anticipated in Section 3.4, to overcome the limitations of the Si μCS for cooling circuits covering a meter scale length, an auxiliary substrate for the distribution lines, made of a different material, can provide the fluid distribution to the micro-patterned Si μCS bonded on it (Figure 3.7).

In Figure 7.4, Si μCS s were integrated on auxiliary substrates (3D printed polymers) having the radial seal and the pin-based interfaces for the interlocking interconnection. The adhesive-based carbon fleece solution, shown in Section 4.7, was used to seal and connect the cooling circuit of the Si substrates with the cooling circuit of the auxiliary substrates.

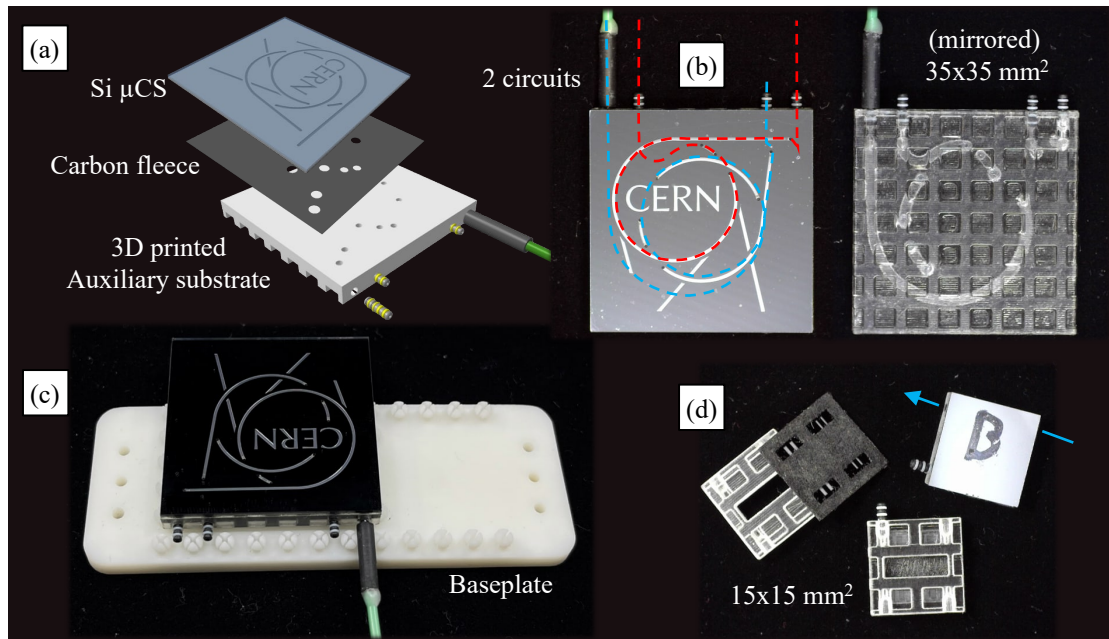


Figure 7.4: Si μCS integrated on a modular concept. (a) Exploded view of the Si i-M μCS with 2 embedded circuits, (b) assembled Si i-M μCS prototype (top and bottom view), (c) prototype inserted on a baseplate and (d) 15x15 mm² Si i-M μCS . The parts shown in the picture were made for educational purposes only. The CERN logo bi-circuits (a-c) was produced for the CERN Open days 2019.

The carbon fleece interface already demonstrated to withstand pressures up to 4 MPa and to guarantee leak-tightness (He leak rate $<3 \cdot 10^{-9}$ mbar l/s). Long-term reliability, thermal-cycle behaviour, lower temperature operation and accelerated ageing with temperature, humidity and radiation are some of the aspects that need to be further investigated to qualify the adhesive bonding interface. In addition, different materials for the auxiliary substrates, like

composites, and alternative bonding solutions, like gold thermo-compression bonding, can be explored and characterised.

7.2.4 CFRP

The vascular carbon cooling substrate solution used for the ALICE ITS2 (Section 2.2.2) can be integrated with an interlocking interconnection. The carbon substrate can be longitudinally segmented (Figure 7.5.a), and radial seals can be applied between the adjacent segments while rails hold and stiffen the assembly. The vascular cooling substrate of the ALICE tracker, with embedded 2 mm polyimide pipes, withstands pressures up to 2.9 MPa. Higher pressures can be reached by using thicker polyimide tubes or braided polyimide tubes. In addition, as demonstrated in recent R&D, this solution is compatible with boiling CO₂ [3]. In line with the present R&D, a modular design, compatible with two-phase CO₂ systems and integrated with the support structure, should be explored.

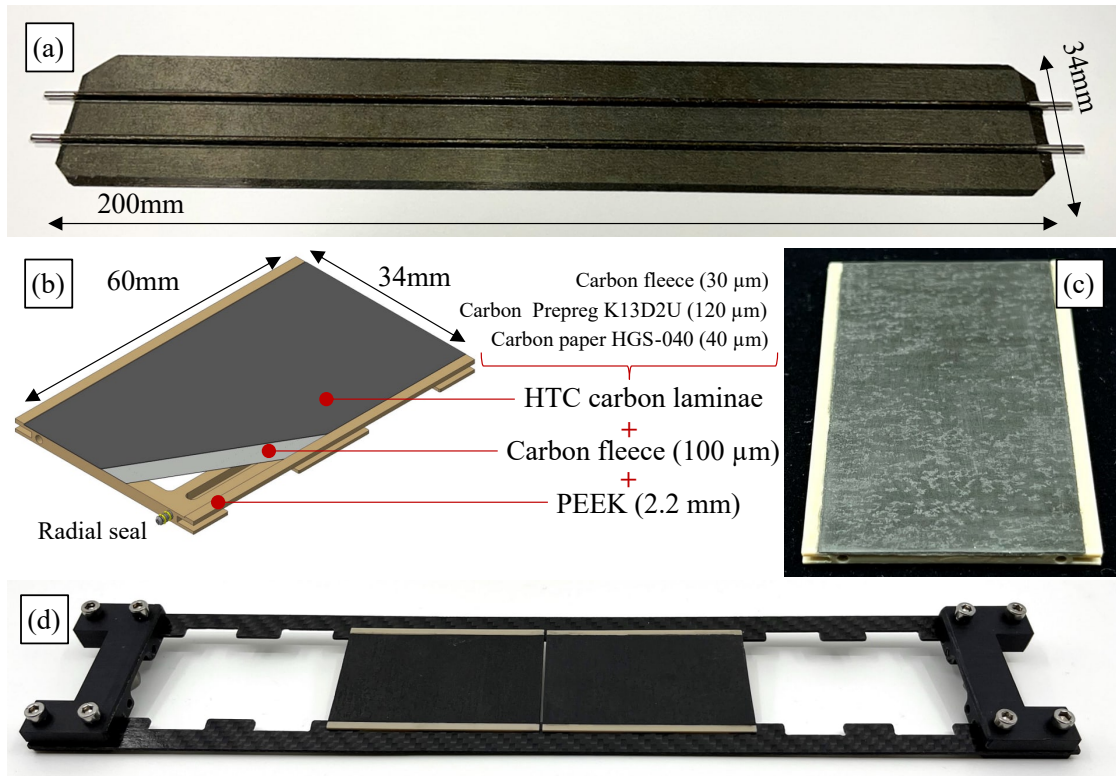


Figure 7.5: CFRP cold plates integrated on a modular concept. (a) Vascular CCS with embedded metal pipes, (b) sketch of a CFRP cold plate with auxiliary PEEK substrate (drawing in Appendix E), (c) assembled CFRP i-MμCS and (d) two modules inserted in the rails (rail-based mechanical interface).

Similarly, alternative design based on carbon cooling substrate should be investigated. In Figure 7.5.b. A high conductive CFRP laminate, can be bonded to a polymer substructure with added features for the rail-based mechanical interface, like slits and slots (Figure 7.5.b). The substructure shown in Figure 7.5.c was made in PEEK; however, alternative materials, like

carbon-PEEK or carbon Bulk Moulding Compound (carbon-BMC), should be used. Two rectangular channels having dimensions of $1 \times 1.2 \text{ mm}^2$ were machined into the PEEK substructure, and a carbon fleece layer, impregnated with epoxy resin (Araldite 2020), was used to glue the CFRP layer and, at the same time, to close the channel. In this way, the thermal path between the refrigerant and the silicon chips is minimised. The prototype withstood pressures up to 1 MPa, and no failure (leaking, substrate rupture) was detected. The drawing of the part is in Appendix E.6.

7.3 Detector layout implemented with i-M μ CS

ALICE 3 is a major detector upgrade proposed to study the properties of the quark-gluon plasma after further improvement of the luminosities ($L = 3.0 \cdot 10^{32} \text{ cm}^{-2} \text{ s}^{-1}$) available with ion beams at the LHC beyond 2030 [204].

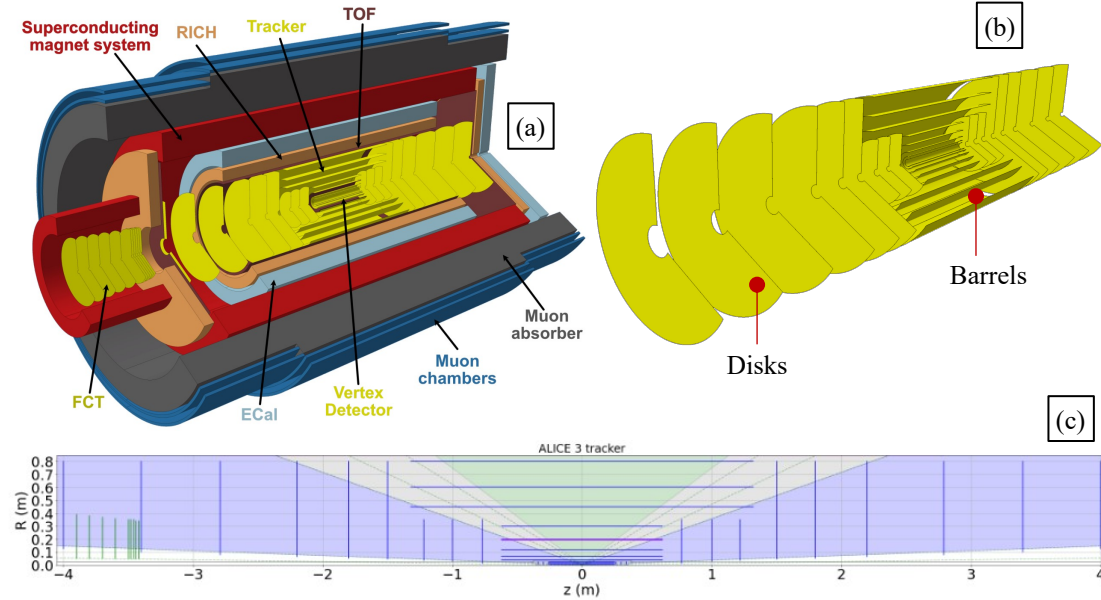


Figure 7.6: ALICE 3 detector concept. (a) ALICE 3 detector, (b) isometric view and (c) layout of its tracking system's layers [204] .

The tracking detector is based on 11 barrel layers and 2×12 forward discs. It is divided into a vertex detector and a tracker. The resulting active surface sums to around 60 m^2 . Accounting for an overlap of sensors of about 10% to cover inactive periphery and achieve layer hermeticity, 66 m^2 of silicon sensors have to be installed. The vertex detector and the outer tracker target low material thicknesses of 0.1% and 1% of a radiation length, respectively. The tracker is foreseen to be cooled by water at ambient temperature, and the MAPS sensor power consumption should be less than 40 mW/cm^2 for the tracker. Additional information about the possible sensing module can be found in Appendix D.1.

Modular concepts will be applied to the tracker. While the vertex will be a single integrated detector component.

Similarly to the ALICE ITS2, the main building block of the outer barrel tracker can be longitudinally segmented in staves where several sensing modules (named HIC) are present. As an alternative, the sensing modules could be installed onto a single large composite cylindrical shell forming a detection layer. In this case, the final assembly will be done in one construction centre.

For the disk layers, a carbon composite plate (or sandwich), that supports several HICs, is the baseline. Following similar concepts applied for ATLAS and CMS trackers, as described in Section 2.2.2, the HIC can be glued on a high thermal conductive carbon plate that is then thermally connected through TIM to a primary cooling circuit.

On the other hand, the i-M μ CS design could be applicable (Figure 7.7.a). Prototypes of the possible layouts, implemented with polymer and ceramics i-M μ CSs are shown in Figure 7.8. The pin-based or the rail-based solution can be integrated into a carbon laminate (Figure 7.8.a and .b) or space frame (Figure 7.8.c and .d) structures.

In addition, the inlet and the outlet of the coolant can be at the same detector side or at the two opposite extremities (Figure 7.8.c and .d). This aspect will depend on the possible achievable thermal performances and the service routing requirement.

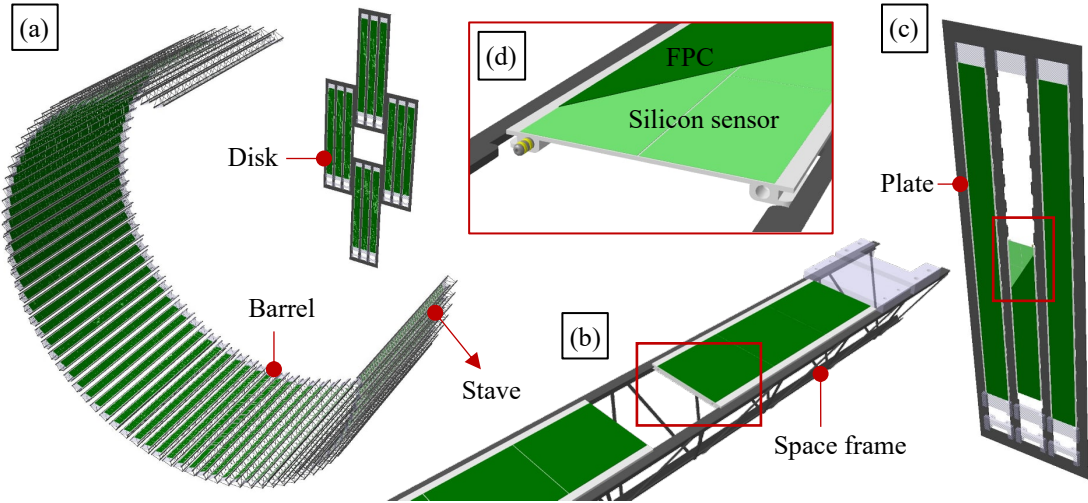


Figure 7.7: Layouts implemented with i-M μ CS. (a) Barrel and Disk layouts, (b) a space frame structure implemented with i-M μ CS (the modular stave), (c) a plate implemented with i-M μ CS and details of an i-M μ CS with the sensing module (Si sensors and electronics) on top. The modular microfluidic cooling substrates in the picture have the radial seal and rail-based configurations.

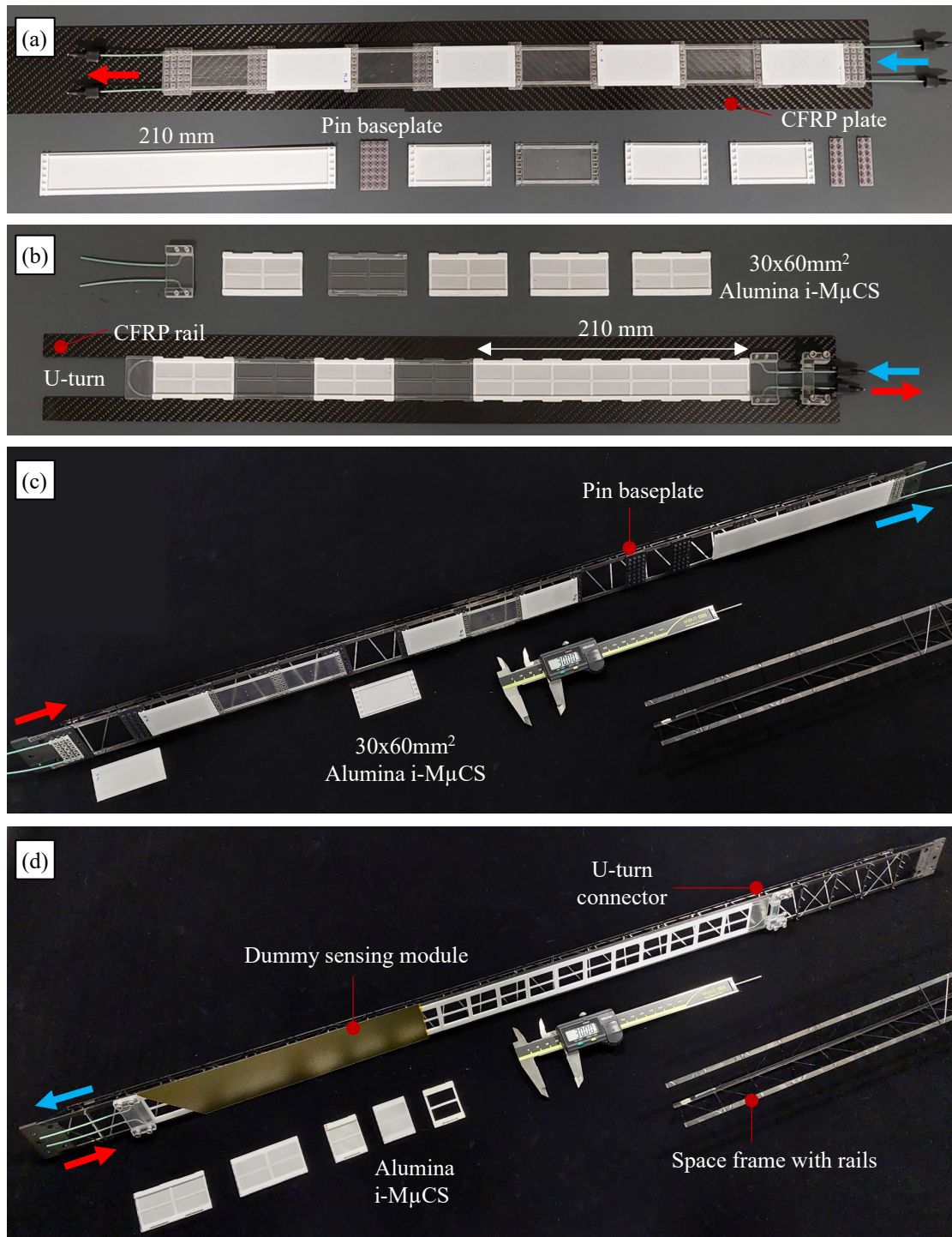


Figure 7.8: Prototypes of i-M μ CS with their support structures. (a) Pin-based and (b) rail-based solutions integrated on a CFRP plate, (c) pin-based and (d) rail-based interfaces integrated on a carbon space frame structure.

7.4 i-M μ CS in ceramic AM

7.4.1 Flatness dependence on substrate dimension

The flatness dependence on substrate dimension was explored. All ceramic prototypes, with different sizes, were measured with a large 3D scan (Keyence VR5200 [202]). The main outcomes of the measurements are described here (Figure 7.9 and Figure 7.10), while all the results can be found in Appendix D.2.

The flatness of all the prototypes was out of tolerance ($\pm 50 \mu\text{m}$). Thickness increasing is the basic solution to minimise warping and deflection effects after the de-binding and firing processes. Nevertheless, this is not a realistic solution for HEP experiments. A compromise can be found by increasing the thickness only at the substrate sides, where the minimum material requirement is less stringent. However, all previous prototypes were already stiffened by the presence of channels and features for the mechanical interface at the side of the prototype.

Better flatness can be achieved through deep studies and tuning of the de-binding and firing parameters. However, most of the production processes are subjected to non-disclosure agreements. Parameter tuning requires a deep investigation and close collaboration with the companies. In addition, each specific part requires an optimisation of the production parameters that are directly dependent on its geometry.

Alternatively, the shape of the green part can be "locked", by using calibrated weights during the firing step. Ceramic weight tools, that withstand higher temperatures (up to 1800°C) and customised ceramic powders, that avoid the bonding between the final part and the weight tools, can be used. Also in this case, the way of supporting the final part strictly depends on the final part geometry.

A less elaborated alternative, i.e. a post-machining solution, can be pursued. It is possible to produce thicker substrates and grind them later down to the nominal thickness.

Indeed, the grinding solution was employed for the $30 \times 30 \text{ mm}^2$ LCM samples with the frame and the reduced thickness configurations (Figure 7.10). A thickness of 0.8 mm was added to the top substrate. The sharp corners of the thicker surface were rounded to minimise possible chopping of the plate (Figure 7.10). The flatness of the reduced thickness and the frame design was $38 \mu\text{m}$ and $55 \mu\text{m}$, respectively (Figure 7.10). These values are well within the requirements. However, they are related to the sample dimensions of $30 \times 30 \text{ mm}^2$, and similar procedures have to be followed and demonstrated for larger substrates. In addition, the machined top surface can lose tolerance in position with respect to the rest of the substrate features. Also here, a deep study on the holding tool and the transferred force to the substrate during the grinding step must be done, and it is strictly related to the final substrate design.

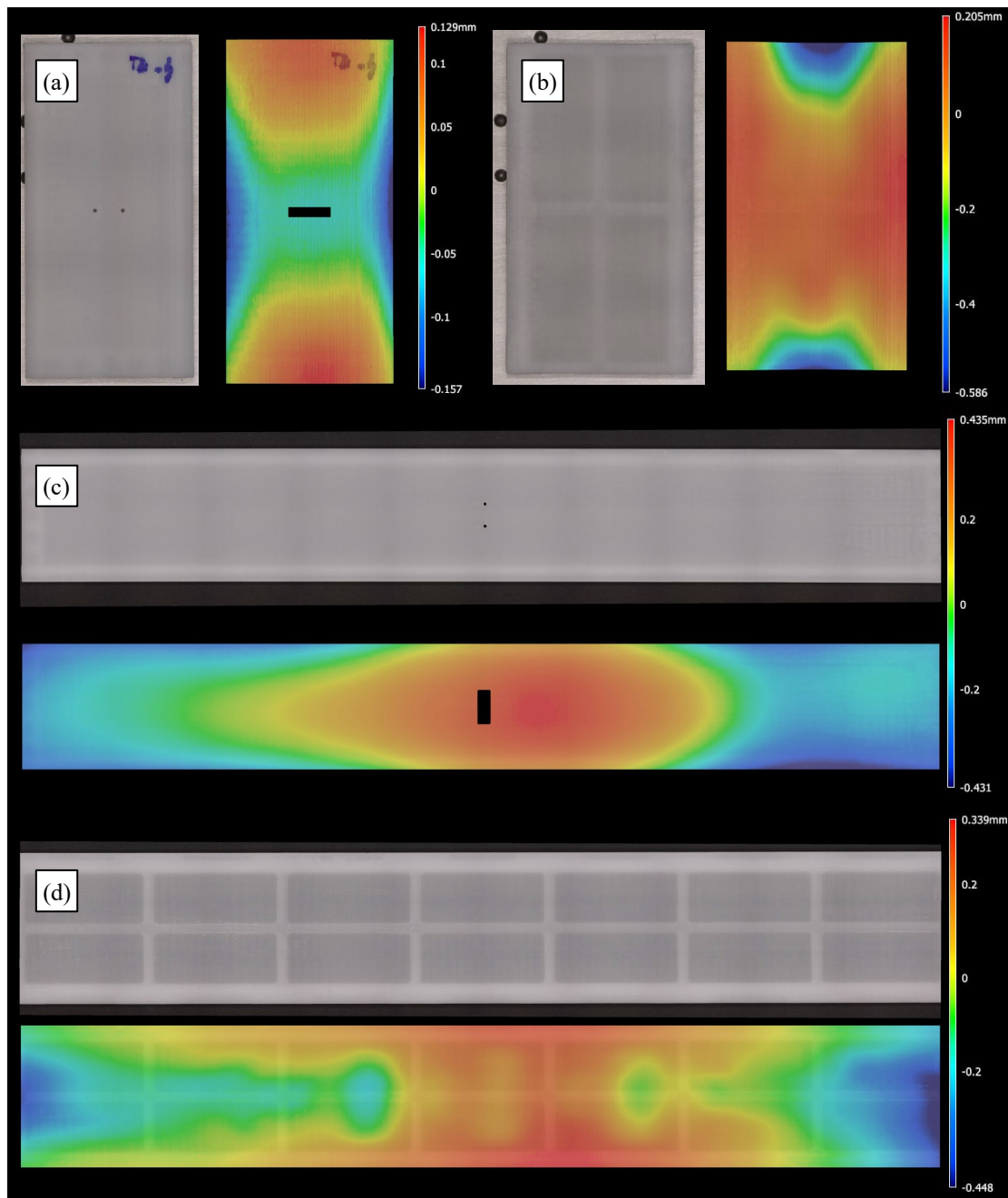


Figure 7.9: Flatness of the ceramic substrates. (a) 30x60 mm² plate prototype (0.7 mm thick), (b) 30x60 mm² prototype with reduced thickness (0.2 mm and 0.5 mm for the frame, see Figure 7.2), (c) 30x210 mm² plate prototype (0.7 mm thick) and (d) 30x210 mm² prototype with reduced thickness (0.2 mm and 0.5 mm for the frame). All these samples were produced with NPJ technology in aluminium oxide.

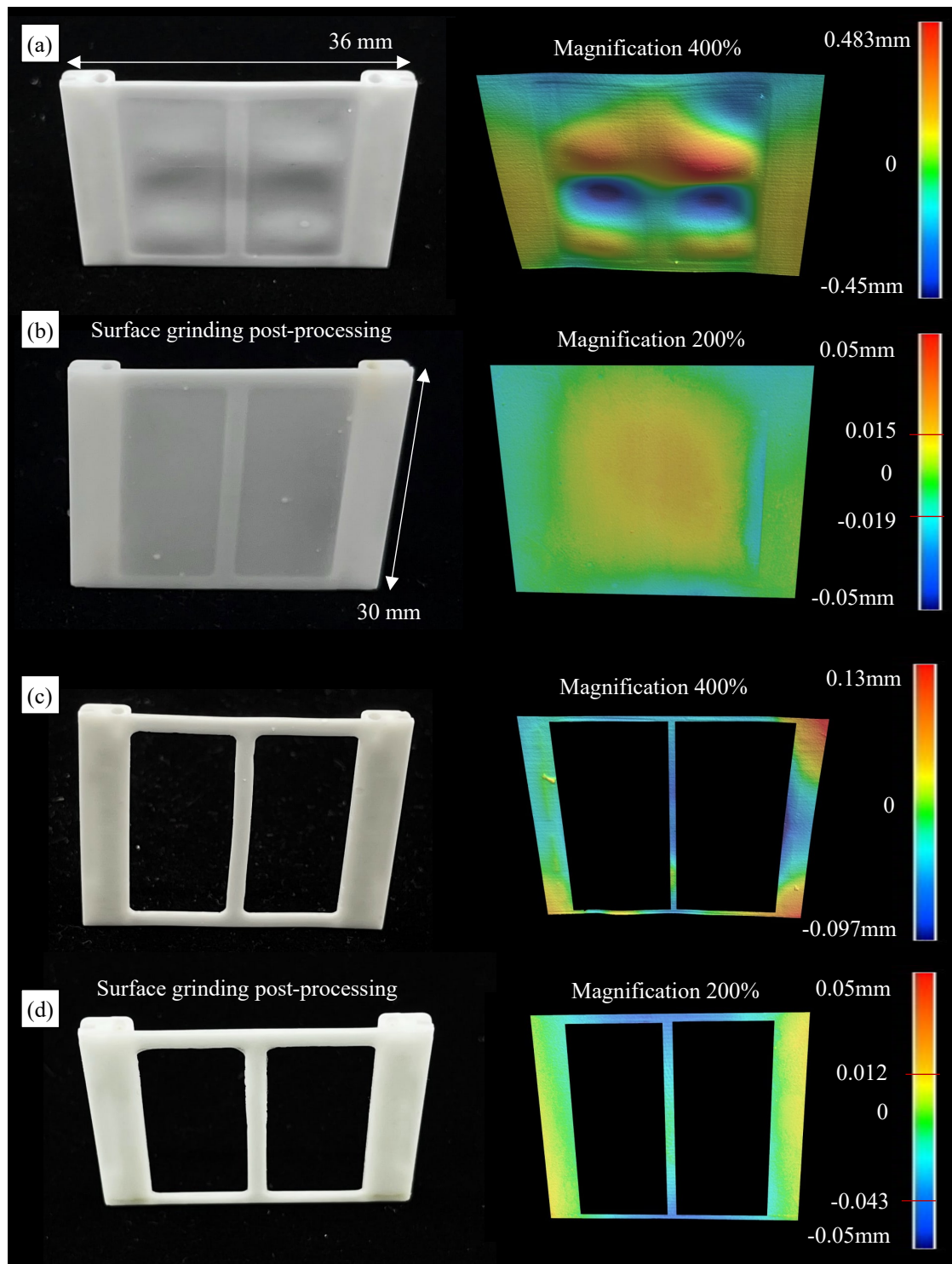


Figure 7.10: Flatness of the ceramic substrates with and without post-surface grinding procedure. Reduced thickness solution with (a) and without (b) post-surface grinding procedure and frame design solution with (c) and without post-surface grinding procedure. The samples were produced with LCM technology.

7.4.2 Gluing interface with the sensing module

The glue must cover most of the chip, avoiding glue penetration between chips and out of the module. The epoxy resin Araldite2011 [66] was selected for the ALICE ITS2, based on its compatibility with CERN requirements and on long experience with detectors applications. Any type of chosen glue must be radiation hard. The main characteristics of the Araldite2011 are the well-controlled glue flexibility, its curing at room temperature and its reliability in a radiation environment.

Gluing procedure

The procedure described here is based on the approach followed for the ALPIDE HIC gluing onto the vascular CCS for the ALICE ITS2 [70] (Figure 7.11). The alignment of the HIC is performed under CMM Mitutoyo machine equipped with an optical probe, CDD camera (Mitutoyo Quick Vision Probe, QVP [178]), and assisted by a semi-automated program. The same procedure can be applied to ceramic modules. However, the gluing procedure for the ceramic i-MuCS depicted in Figure 7.14 followed a manual alignment.

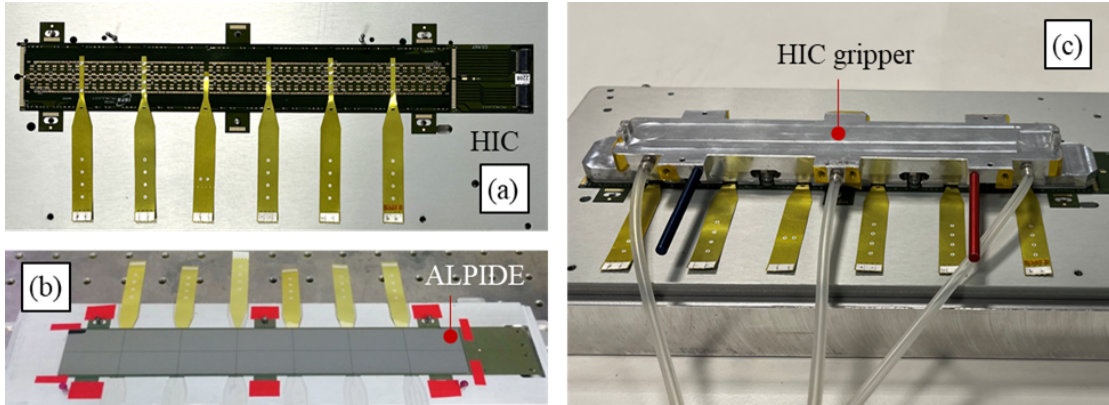


Figure 7.11: HIC of the ALICE ITS2 tracker. (a) Side view of the FPC, (b) ALPIDE sensors view and (c) HIC held by a vacuum gripper.

Glue deposition: A "glue sticker mask" is positioned on the ceramic module for gluing control. The geometry of the gluing mask is optimised to guarantee glue uniformity within $\pm 20 \mu\text{m}$ and to cover the entire sensor area. For the gluing of the ALPIDE HIC, the mask used is a polyvinyl adhesive with a thickness of $90 \mu\text{m}$ with rectangular windows for the gluing deposition (Figure 7.12.a). In the real procedure, these masks are inserted and aligned to the cooling substrates using a dedicated mask positioning tool and standard dowel pins. The glue is inserted in the windows through a glue dispenser, composed of a syringe and its holder that slides along the module (Figure 7.12.b). While a "glue-levelling spatula" (Figure 7.12.c) is used to spread the glue on the areas of the entire windows. A mask tab protrusion at the short side collects the extra glue and facilitates the mask stripping (Figure 7.12.d). At this point, it is possible to proceed with the HIC alignment (Figure 7.12.e).

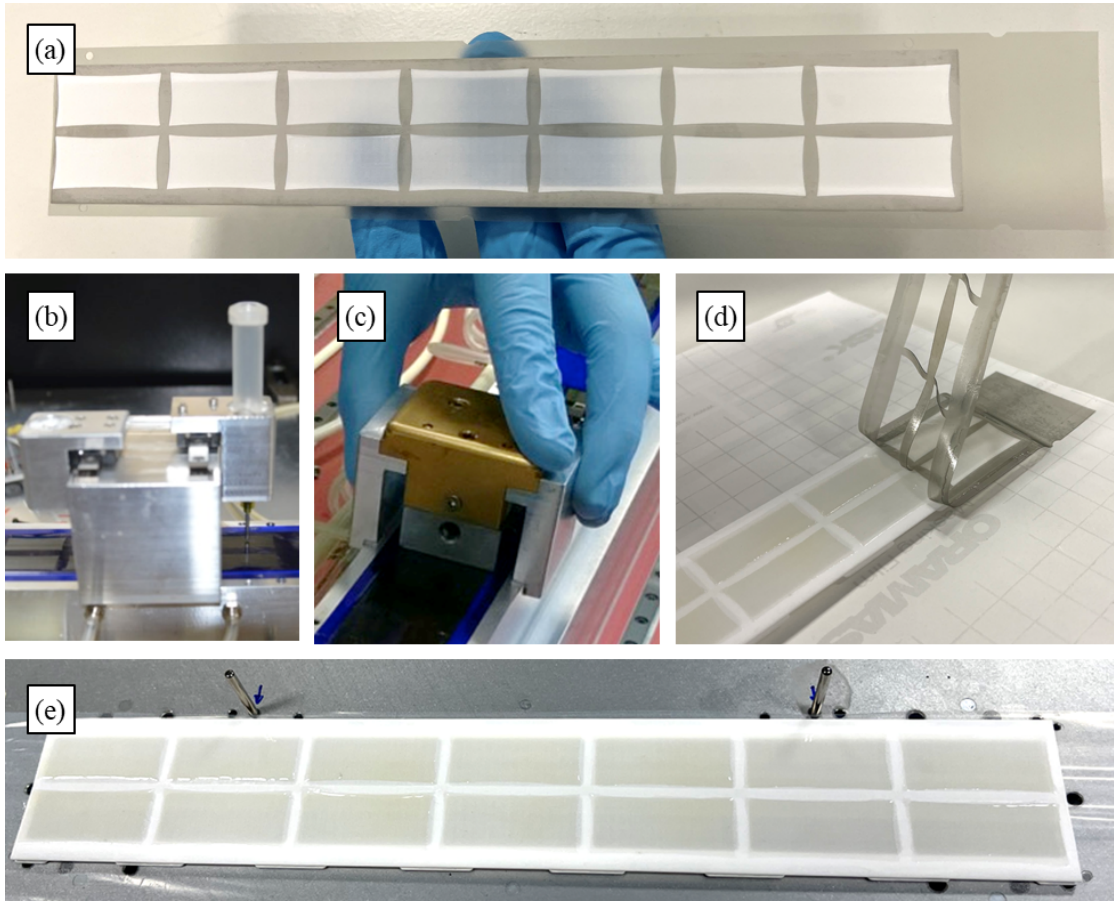


Figure 7.12: Glue deposition on ceramic i-M μ CS. (a) Polyvinyl adhesive mask inserted onto the ceramic cooling substrate, (b) glue dispenser, (c) glue-levelling spatula, (d) the substrate during the removal of the adhesive mask and (e) the ceramic cooling substrate with glue patterned (window area) on the top surface.

HIC alignment: The sensing modules have different types of reference markers. In the case of the ALICE ITS2 tracker, the cross markers patterned in the ALPIDE sensor are used to align the four HIC corners onto the substrate. An "*aluminium gripper tool*" holds the HIC by vacuum (Figure 7.11.c). Vacuum holes (or vacuum suction cups) are carefully designed and implemented in regions that do not interfere with the electrical interconnections between the sensors and the FPC (e.g. wire-bonding interconnection). The probe marker of the camera (green cross in Figure 7.13.a) is used to guide the alignment. The adjustment of the HIC (accuracy $\sim 20\ \mu\text{m}$) is performed with the help of the "*alignment station*". The alignment station has four motion micrometric stage screws (Figure 7.13.b). The descent of the HIC is controlled with an "*electronic safety device*". Four red lights, which correspond to the four corners of the HIC, are on during the descent. When one of the HIC corners touches the cooling substrate, the light switches off. The HIC is considered in position once all the lights are off. After that, a calibrated weight is applied during curing; in the case of i-M μ CS ITS2, the applied weight is 2N.

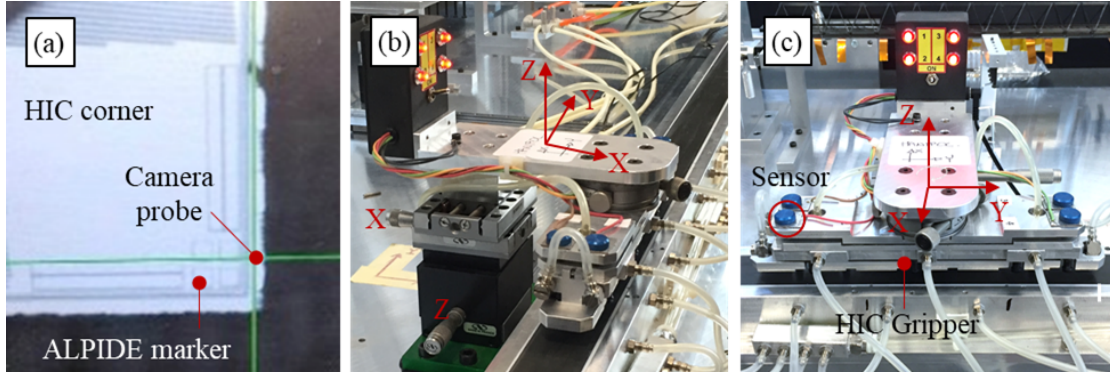


Figure 7.13: Procedure of the HIC alignment used for the ALICE ITS2 outer tracker. (a) Optical probe that frames the cross-reference marker of an ALPIDE sensor at the side, (b) lateral and (c) front view of the alignment station with HIC gripper used for the assembly of ALICE ITS2 outer tracker. The figure is adapted from [70].

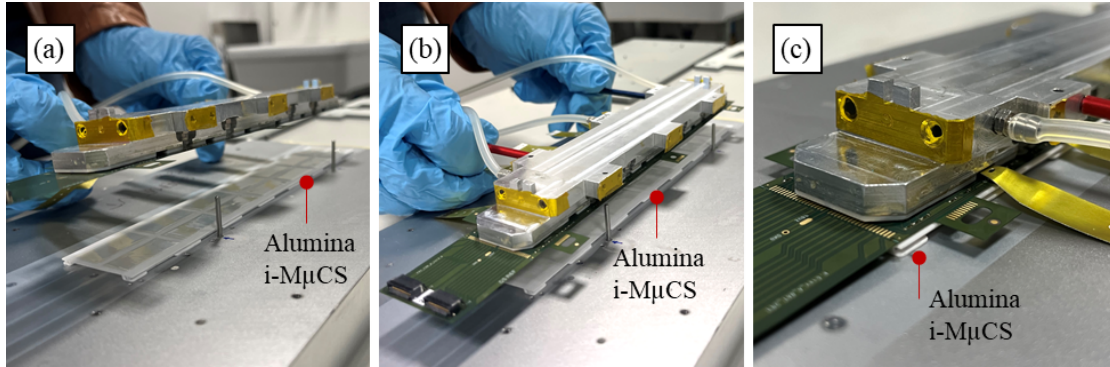


Figure 7.14: Manual alignment of the HIC onto the alumina substrate. (a-b) HIC and its gripper approaching the alumina i-M μ CS and aligned HIC onto the ceramics substrate.

Figure 7.14 shows the main gluing steps of the HIC onto the ceramics i-M μ CS (30x210mm²). In this case, the HIC was manually aligned to the cooling substrate, and the HIC descent was driven by two dowel pins.

Figure 7.15 shows the final assembled ceramic i-M μ CS. The out-of-tolerance of the flatness (Figure 7.16) produced irregularities at the gluing interface (Figure 7.15.b). Before gluing, the ceramic surface was cleaned with isopropyl alcohol. No de-lamination of the sensing modules from the ceramic substrate occurred. The assembled i-M μ CS was cooled down to -10 °C. The electronic test bench detected all the ALPIDE sensors (2x7). This demonstrated the integrity and correct working of the sensors after the gluing and the thermal cycle. Note that if the final detector requires to operate at lower temperatures (-20 or -30 °C), a more flexible thermal glue, e.g. Masterbond EP37-3FLFAO [207], can be used to minimise stress at the gluing interface induced by CTE mismatch.

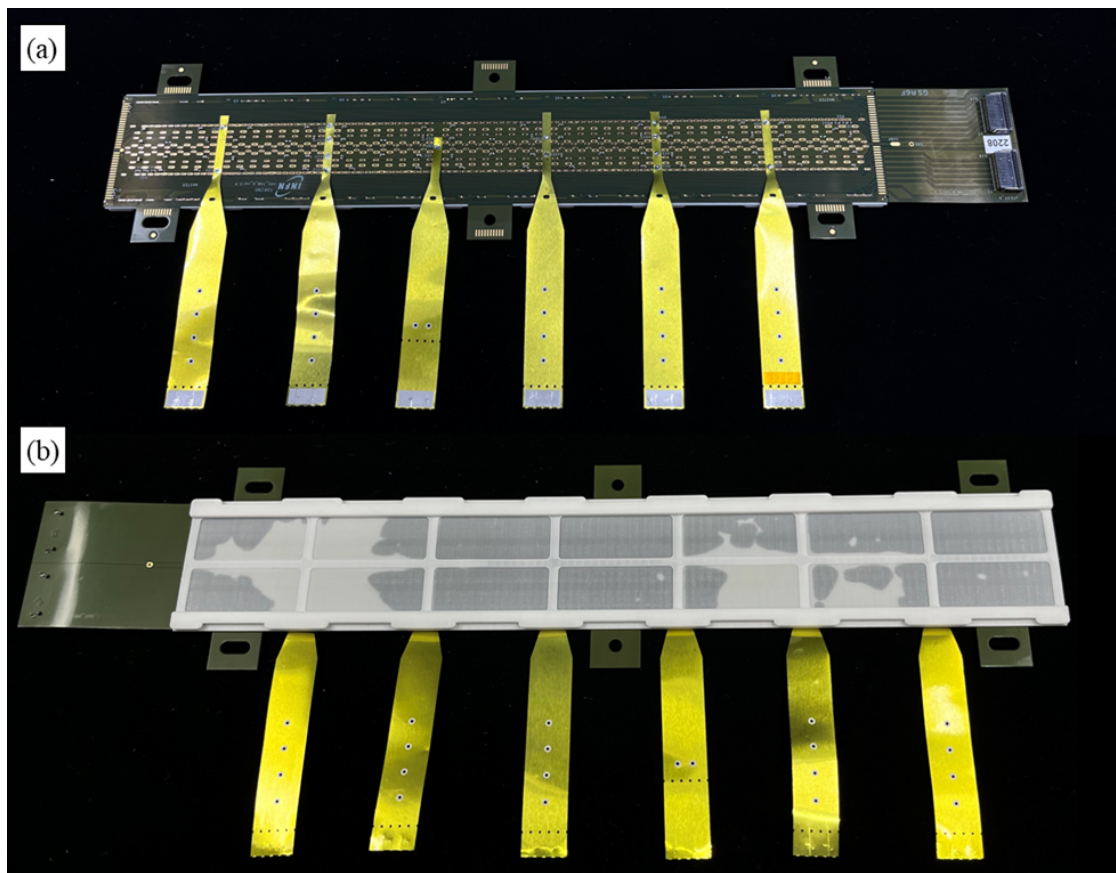


Figure 7.15: Assembled ceramic i-M μ CS. (a) Top view and (b) bottom view of the assembled alumina i-M μ CS.

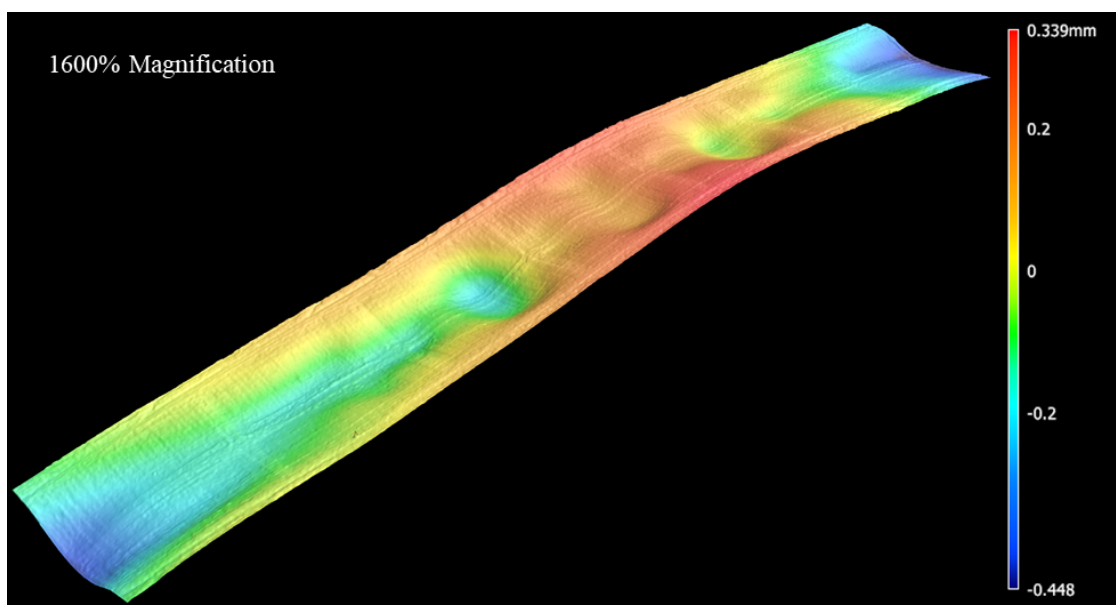


Figure 7.16: Flatness of the ceramic i-M μ CS used for the gluing of the HIC.

7.4.3 Hydraulic and thermal assessment

The hydraulic and thermal behaviours of a i-M μ CSs are influenced by interconnection features such as the restrictions and the enlargements in the fluid channels (Figure 7.20). In addition, production aspects coming from the 3D printed ceramics, such as channel accuracy and roughness, also need to be considered. Hydraulic and thermal assessments were performed on a theoretical laminar flow regime using deionised water at ambient temperature. The 30x60 mm² alumina modules were used for the tests. Radial seal and pin-based were, respectively, the hydraulic and mechanical interfaces under investigation. Taking as reference the minimum diameter (D_1) inside our modules, corresponding to the inner diameter of the seal fitting and the inner diameter of the module restriction (0.5 mm nominal), the Reynolds number (Re) ranges from 250 to 2000.

A rougher surface (in our case $R_a \sim 20 \mu\text{m}$) tends to increase the convective heat transfer coefficient (h_c) as it could initiate fluid mixing in the thermal boundary layer. In addition, when the fluid approaches an interconnection and escapes from it, the boundary layer is stripped, and a swirling of the liquid (eddy flow) is created. As a result, fluid mixing in the upstream channel section is formed until the fully developed flow regime is again established. Consequently, the distributed pressure drop in the embedded channel of the modules is greater than the theoretical distributed pressure drop of a fully laminar developed regime. At the same time, the local pressure drop, corresponding to the interconnection restriction and enlargement, must be considered. If the restriction and the enlargement are minimal with respect to channel size, these effects can be negligible, although in the hydraulic interconnection under investigation, these losses cannot be neglected, and they are responsible for most of the total pressure drop. Accordingly, the local heat transfer coefficient can increase, because of the eddy flow, and cooling performance locally improves.

When non-developed flows are present in a fluidic circuit, the hydrodynamic entrance length (L_h) and the thermal entrance length (L_{th}) must be analysed. The hydrodynamic (thermal) entrance length describes the distance for incoming flow in a channel to form a (temperature) flow profile of the stable shape. In the laminar flow regime, they are respectively described by equation 7.1 and equation 7.2:

$$L_{h,laminar} = 0.0575 \cdot Re \cdot D \quad (7.1)$$

$$L_{th,laminar} = 0.05 \cdot Re \cdot D \cdot Pr \quad (7.2)$$

where Pr is the dimensionless Prandtl number defined as the ratio of the momentum diffusivity to thermal diffusivity.

Furthermore, when the flow is approaching the next interconnection and if the hydrodynamic and thermal boundary layers are not yet restored, a cascade effect can be triggered, which can bring a further pressure drop and a heat transfer coefficient increase. This situation appears when the hydrodynamic entrance length is greater than the distance between two disturbances of the flow, i.e. two nearby interconnections (60 mm). It corresponds, in our

case, to a Re greater than 2000 and a transitional flow regime. Tests were performed before this situation took place because of set-up limitations.

In addition to the influence investigation of the above parameters (channel roughness, channel accuracy, interconnection features), a preliminary assessment of the TFM was done and compared with the theoretical prediction.

Sample preparation and set-up

Two channels with a diameter of 1 mm are present at the extremities of the alumina modules ($30 \times 60 \text{ mm}^2$). The modules were equipped with polyimide thin-film heaters to replicate the heat coming from the electronics (Figure 7.17).

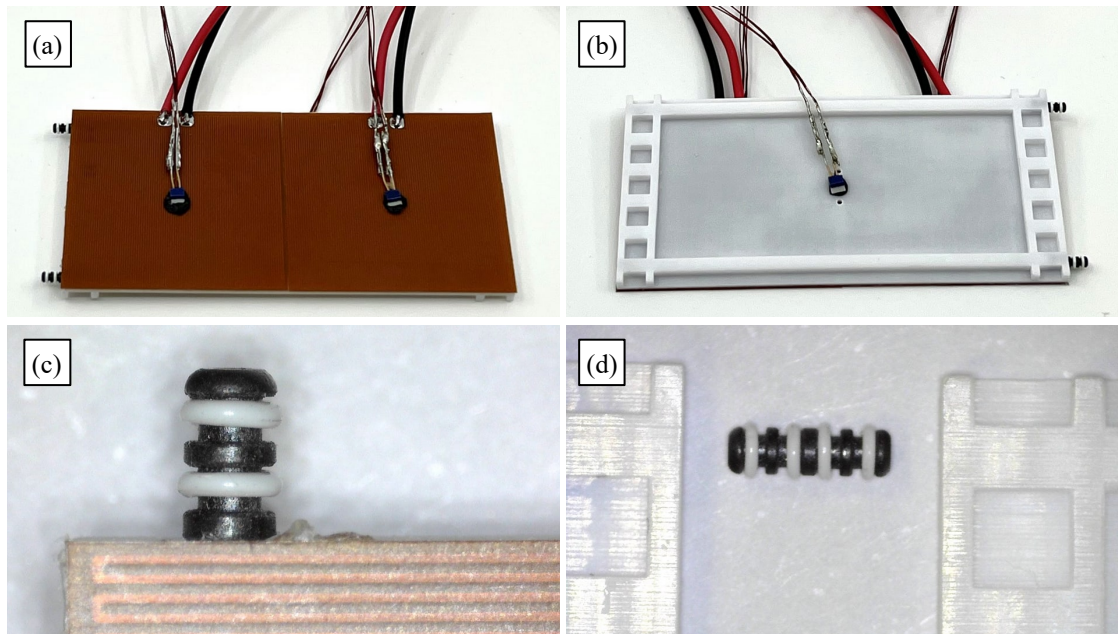


Figure 7.17: Ceramic i-M μ CS for hydraulic and thermal tests. (a) Top view and (b) bottom view of the assembled alumina i-M μ CS, (c) detail of the seal fitting inside a module equipped with two heaters and (d) exploded view of the hydraulic interface.

Two heaters ($30 \times 30 \text{ mm}^2$, resistivity = $22 \Omega \pm 2\%$) were bonded on the top surface of each alumina prototype by using 3M™ Adhesive Transfer Tape 468MP [208]. The bi-adhesive tape has a thermal conductivity of 0.19 W/mK and a thickness of 0.13 mm . From the thermal point of view, this bi-adhesive creates a non-negligible thermal barrier. Unfortunately, as seen in Section 7.4.1, the flatness of the samples, which ranges from 0.159 to 0.338 mm , could have compromised the thermal glue uniformity. It was then preferred to have a higher thermal barrier all along the modules than a non-uniform thermal resistance that could have impacted the thermal investigation.

The test set-up already present in the clean room of the ALICE ITS Upgrade at CERN was

used to measure the inlet and outlet pressures and the mass flow rate. In addition, a National Instruments (NI) Data Acquisition (DAQ) system and its acquisition program (LabView [209]) were employed to control the heaters and temperature sensors. Details of the set-ups are in Appendix C. A thermal infrared camera (FLIR E60 [210]) was used, and the modules were black-painted to take thermal images 7.18.

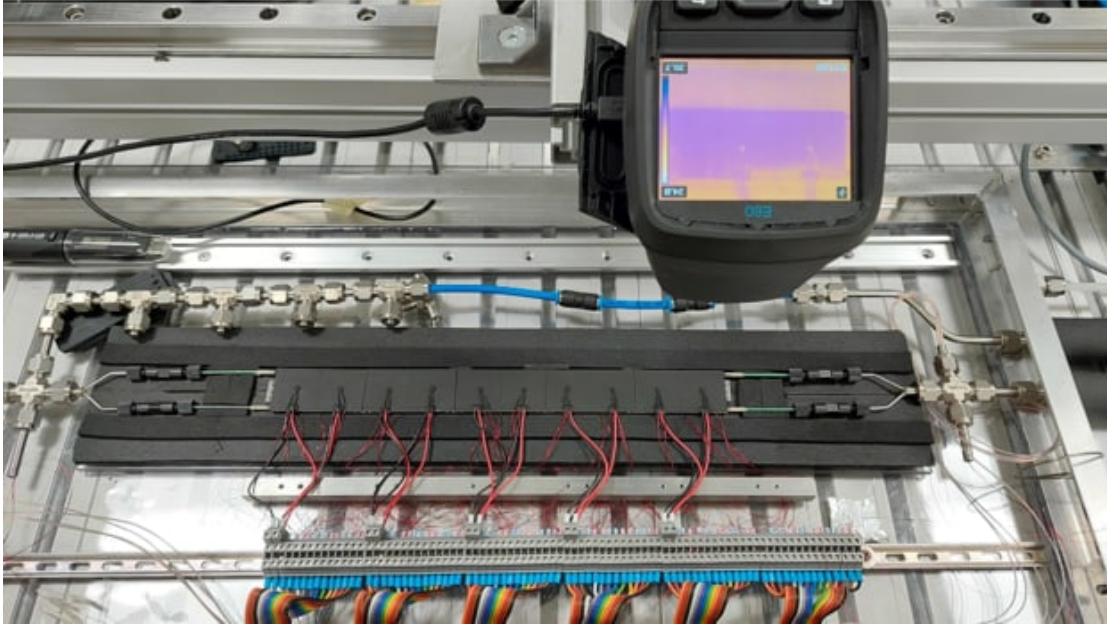


Figure 7.18: The module array connected to the hydraulic and thermal test set-up.

Two possible flow circuit configurations were analysed (Figure 7.19):

- One direction configuration: the inlet and the outlet flows are at the opposite side of the module array, and the water flows in the two parallel channels.
- Two directions configuration: the inlet and the outlet flows are at the first module of the array, while a U-turn tubing is connected to the last modules of the array.

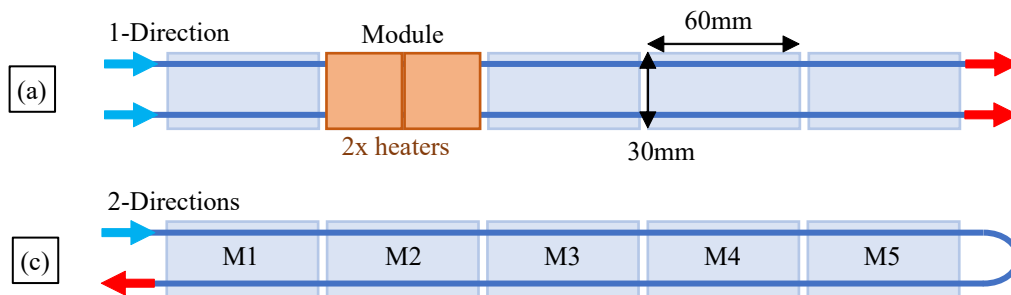


Figure 7.19: Set-up configuration for hydraulic and thermal tests. (a) 1 Direction and (b) 2 Directions.

During the thermal test, the module array was embedded in insulating foam (Armaflex [211]) to minimise convection with the environment. The environment's temperature and humidity were controlled. They were in the range of 19-22 °C and 35% -45%, respectively.

Hydraulic behaviour

The study aimed to compare the measured pressure drop to the expected analytical one. Several modules, up to five, were tested. The pressure drop values were normalised to a module channel dimension, corresponding to a circuit size of 60 mm (Figure 7.20). The transition section ($L_1 \sim 8$ mm) consists of diverging and converging (expansion or reduction) sections and a throat. The throat section comprises the seal fitting channel, restriction in the alumina module and the dead volume between the seal fitting and the alumina groove (highlighted in light red in Figure 7.20).

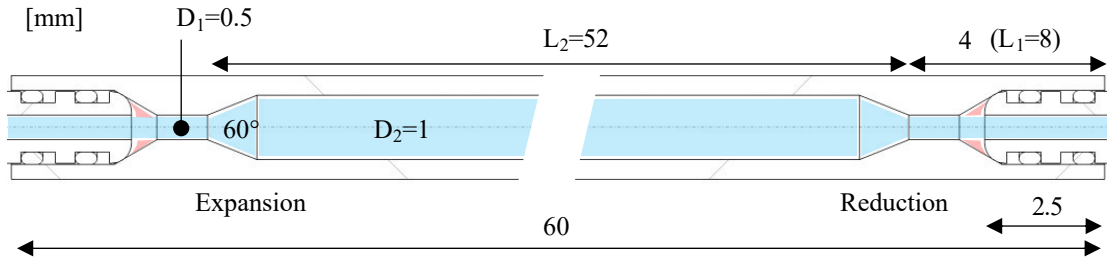


Figure 7.20: Cross-section of the investigated channel circuit inside the alumina module. The light blue and light red areas correspond to the channel circuit volume. The red light area corresponds to the dead volume between the seal fitting and the alumina module, which is also filled with water.

Additional samples, each of them made of stainless steel (SS) pipe glued to polymer CNC machined adaptors that serve to house the seal fitting (Figure 7.21), were used for comparison with the pressure drop of alumina prototypes. The SS samples have a total length of 60 mm, an outer diameter of 1.6 mm and an inner diameter of 1 mm. The SS samples were assembled, up to five in rows, and tested with both configurations (1 direction and 2 directions). As for the alumina prototypes, the pressure drops, measured with a different number of SS samples, were normalised to the module length (60 mm).

Theoretical total pressure drop (Δp_{tot}) values are calculated by:

$$\Delta p_{tot} = \sum_{i=1}^N \Delta p_{frict_i} + \sum_{j=1}^M \Delta p_{sing_j} \quad (7.3)$$

where Δp_{frict_i} is the distributed frictional pressure drop related to the i -th channel section and Δp_{sing_j} is the pressure drop in the j -th singularity. The distributed pressure drop for a i -th

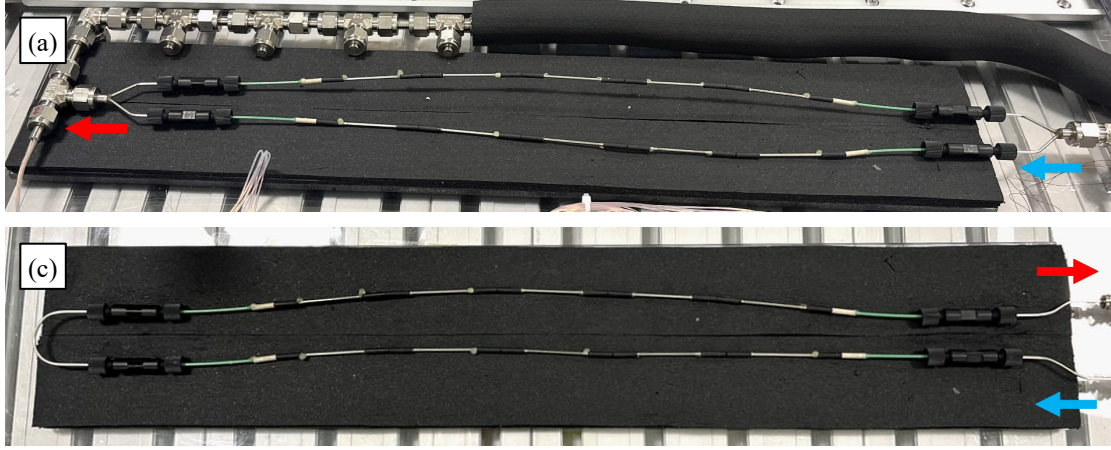


Figure 7.21: Modular SS samples for the pressure drop interconnection characterisation. (a) One direction configuration and (b) two direction configurations. The polymer CNC machined adaptors are the black components between the SS pipes.

channel of length L_i , inner diameter D_i , fluid density ρ and fluid velocity v_i is expressed by:

$$\Delta p_{frict_i} = \zeta \frac{L_i}{D_i} \frac{\rho v_i^2}{2} \quad (7.4)$$

where ζ is the Darcy friction factor. In our case (laminar regime, $Re < 2300$, circular channel), ζ is related only to the Reynolds number according to the Hagen–Poiseuille’s law:

$$\zeta = \frac{64}{Re} \quad (7.5)$$

Note that the more generic Churchill correlation that also takes into account the roughness gives the same value of ζ .

While p_{sing_j} are expressed by :

$$\Delta p_{sing_j} = K_j \frac{\rho v_j^2}{2} \quad (7.6)$$

where k_j is the friction factor of the singularity and v_j is the velocity at the singularity inlet. For our tapered reduction and expansion, both having angle (θ) of 60° , k_{red} and k_{exp} are respectively expressed by equation 7.7 and equation 7.8 according to I. E. Idelchik [212]:

$$K_{red} = \left(1.2 + \frac{160}{Re_2} \right) \left[\left(\frac{D_2}{D_1} \right)^4 - 1 \right] \sqrt{\sin \left(\frac{\theta}{2} \right)} \quad (7.7)$$

$$K_{exp} = 2 \left[1 - \left(\frac{D_1}{D_2} \right)^2 \right]^2 \quad (7.8)$$

The numbers (1 and 2) in the subscripts refer to Figure 7.20.

The pressure drops, experimentally evaluated and the analytical estimate, are reported in Figure 7.22. The experimental results of the SS samples matched with their analytical prediction when the restriction diameter is considered between 0.5 and 0.55 mm (light grey area in Figure 7.22).

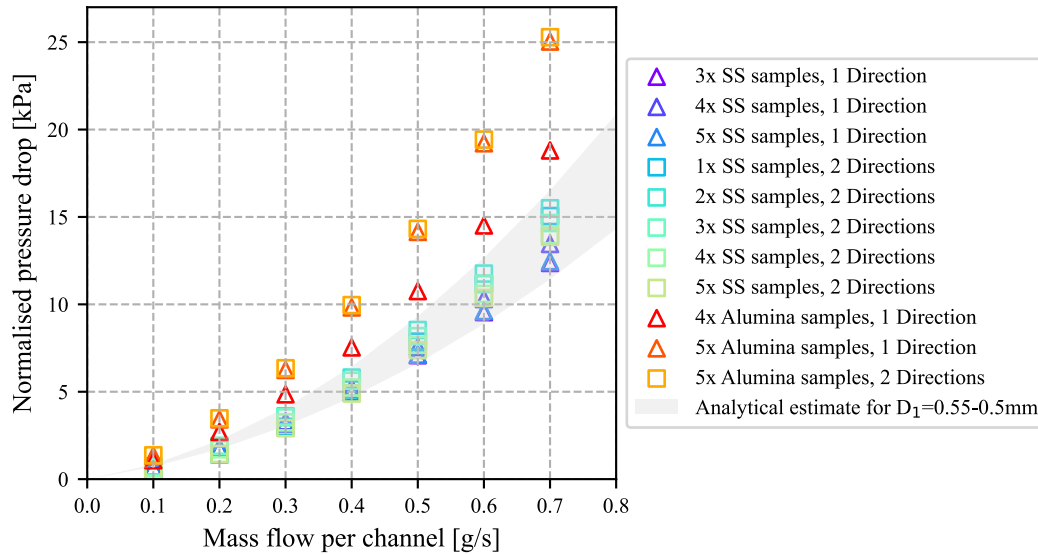


Figure 7.22: Results of the pressure drops for the stainless steel samples. The values of the pressure drop are plotted as a function of the mass flow rate inside a single channel. Several tests with a different number of the stainless steel samples (i.e. 1x SS, 5x SS) were tested with the two configurations shown in Figure 7.21. Depending on the number of samples and the tested configuration, the pressure drop values were normalised to the length of a module channel (i.e. 60 mm circuit unit in Figure 7.20). The experimental results are compared to the analytic estimate (light grey area) for D_1 ranging from 0.5 to 0.55 mm (see Figure 7.20). The experimental results of the alumina samples (i.e. 1x alumina, 5x alumina) are also plotted for comparison.

In contrast, the pressure drop of the tested alumina prototypes was greater than the pressure drop of tested SS samples. In this case, the measured pressure drops matched with the analytical prediction when the restriction diameter is considered between 0.45 and 0.5 mm (Figure 7.23). In addition, the local pressure drop, related to the interconnection features, is considerably greater than the distributed pressure drops in the L1 and L2 sections of the channel circuit (L1 and L2 in Figure 7.20).

The smaller dimension of the throat can be due to part accuracy but also to the prototype roughness inside the channels ($R_a \sim 20 \mu\text{m}$). This highlighted the great importance of the channel accuracy and, indirectly, of the channel roughness, which can influence feature dimensions. The analytical prediction does not take into account non-developed flow and the dead volume (light red in Figure 7.20). They clearly influence the total pressure drop. However, these influences can be considered as part of the restriction dimension uncertainty.

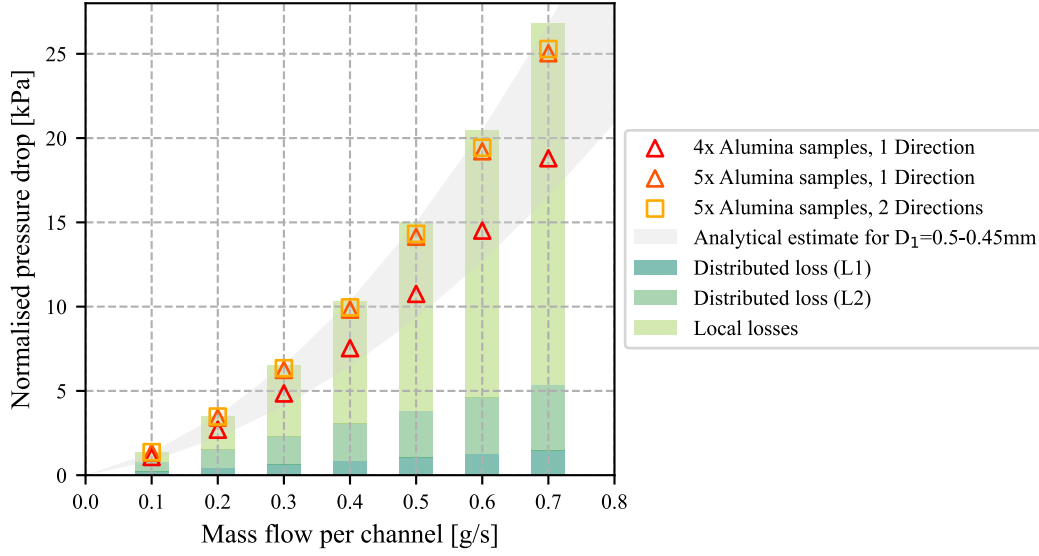


Figure 7.23: Results of the pressure drops for the alumina samples. The values of the pressure drop are plotted as a function of the mass flow rate inside a single channel. The experimentally evaluated pressure drops are compared to the analytic estimate (light grey area) for D_1 ranges from 0.45 to 0.5 mm (see Figure 7.20). The different contributions to the total pressure drop, coming from the distributed pressure losses (green and medium-green colors) and the local pressure losses (light-green), are plotted as a bar chart.

Thermal behaviour

A preliminary estimation of the influence of the interconnection on the heat transfer coefficient can be made using empirical numerical correlations of the Nusselt number (Nu). The dimensionless Nusselt number is the ratio between the heat transfer by convection (h_c) and heat transfer by conduction alone (k/D), and it can be expressed as follows:

$$Nu = \frac{h_c D}{k} \quad (7.9)$$

Several correlations can be utilized to obtain the Nusselt number. Among other factors, the correct correlation must be chosen depending on the fluid's physical state, the flow circumstances and the predominant heat transfer method. When a fluid in a fully developed laminar flow is heated by a constant heat flux at the channel wall, Nu is 4.364.

Grigull and Tratz [213] investigated the thermal entrance problem in the laminar flow regime under a constant heat flux at the wall channel. They empirical estimate the Nusselt number as a function of the Prandtl number, Reynolds number, and dimensionless axial distance (D/x):

$$Nu = 4.364 + \frac{0.00668(D/x)Re \cdot Pr}{1 + 0.04[(D/x)Re \cdot Pr]^{2/3}} \quad (7.10)$$

According to equation 7.10, the local heat transfer coefficient along the channel length ($L2$

~ 52 mm), before and after the flow disturbances (~ 4 mm per side), is evaluated in Figure 7.24.

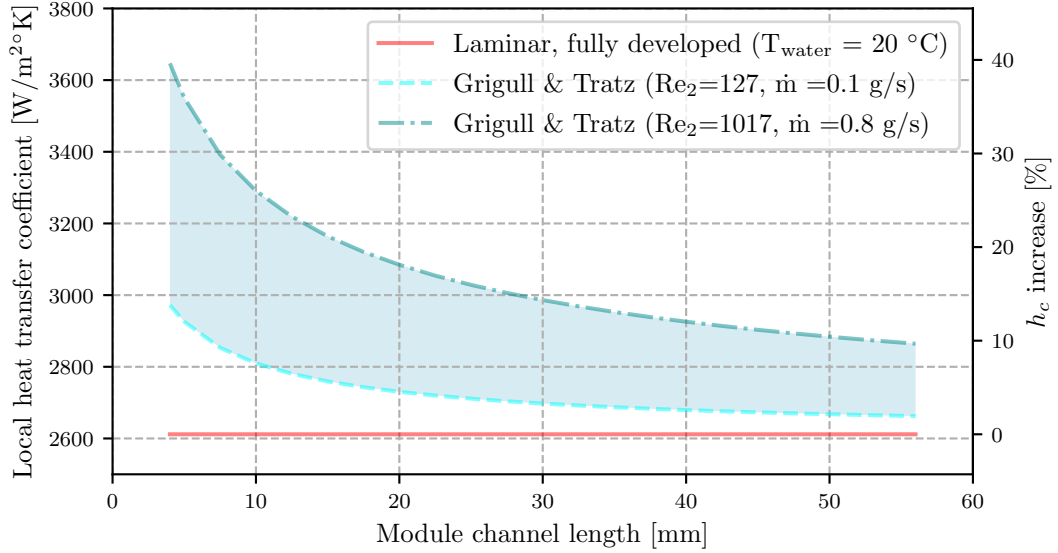


Figure 7.24: Analytical estimate of the local heat transfer coefficient. The analytical estimate of the local heat transfer coefficient is plotted as a function of the module channel length ($L_2 \sim 52$ mm and $D_2 = 1$ mm), before and after the flow disturbances (See Figure 7.20). The thermophysical properties of the water are referred at room temperature (20°C) and atmospheric pressure (101.325 Pa). The local heat transfer coefficients (blue and light-blue lines) calculated with the empirical correlation of Grigull & Tratz (Equation 7.10) are compared to the h_c in fully developed laminar flow regime (red line). The right Y-axis refers to the percentage increase of h_c with respect to the fully developed laminar flow case.

At $Re_2 = 1017$, corresponding to a mass flow rate (\dot{m}) of 0.8 g/s, the local h_c increases by 40% at the interconnection outlet compared to the h_c at the fully developed laminar flow regime (2612 W/m 2 K). While, at $Re_2 = 127$ ($\dot{m} = 0.1$ g/s) the increase is $\sim 12\%$.

Based on this preliminary estimation, it was decided to perform thermal tests and tune the mass flow rate and the heat flux to highlight the above-described effect. An array of five modules (named from M1 to M5) were tested with the configurations, 1 Direction and 2 Directions (see Figure 7.19).

Figure 7.25 shows the temperature profile taken with the thermal camera at the top surface along a channel circuit line (red continuous line) during a test (with 1 Direction; $\dot{q} = 0.8$ W/cm 2 ; $\dot{m} = 0.8$ g/s). While, Figure 7.26 and Figure 7.27 show the temperature mapping on the top surface of the modules array tested with the 2 configurations, different mass flow rates and dissipated heat fluxes.

In correspondence with the downstream of the interconnection, the thermal tests confirmed an increase of the local heat transfer coefficient with increasing the mass flow rate. While, in correspondence with the seal fitting, it is possible to notice a temperature increase (Figure

7.25) due to the thermal barrier induced by the seal fitting itself and the non-thermal contact between the modules.

In Figure 7.25, the profile of the temperature difference (ΔT between the top surface of the alumina module and the water in the channel) for the modules M1, M2, M4 and M5 is similar; while the ΔT profile in M3 is different. This is due to an obstruction in the M3 module, near the interconnection M3-M4. The obstruction created eddies at the interconnection upstream that locally increased the heat exchange. Note that the obstruction effect is not visible when the modules are tested with the 2 Direction configuration as the water flow direction in the channel is reversed (see Figure 7.27).

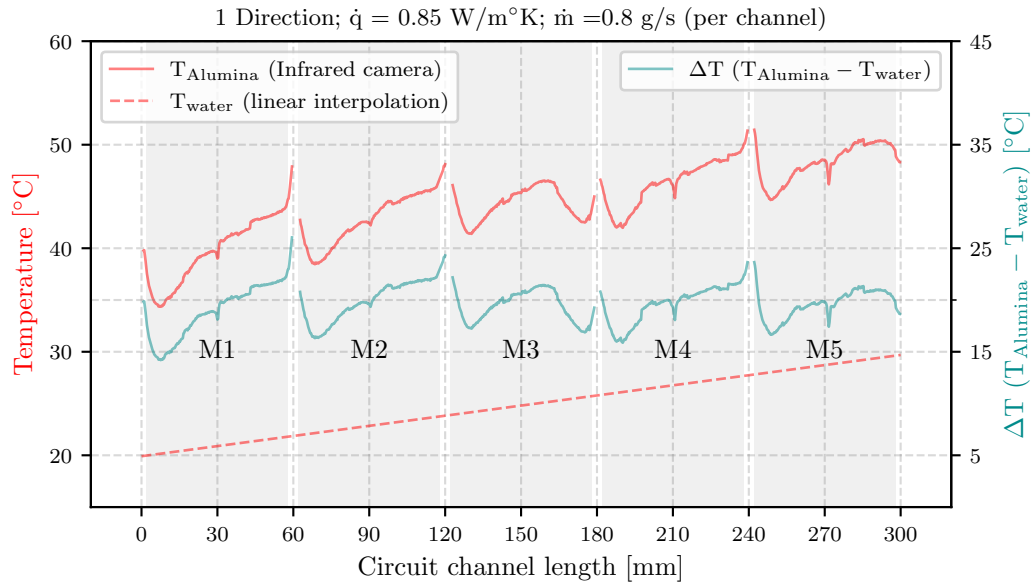


Figure 7.25: Temperature increase along the channel circuit length. An array of five alumina modules (M1-M5) are tested with 1 Direction configuration (see Figure 7.19). The dissipated heat flux (\dot{q}) and the mass flow rate per channel (\dot{m}) are 0.85 W/cm^2 and 0.8 g/s , respectively. The water flows from left to right. The values refer to the thermal image in Figure 7.26. The temperature values are taken on the top surface of the heaters, glued to the alumina prototypes, in correspondence with the channel (red dashed line in the plot and white dashed line in Figure 7.26). The temperature of the water is linearly interpolated from the temperature values taken at the inlet and outlet of the circuit. The blue line corresponds to the estimate temperature difference along the circuit.

To conclude, the interconnection downstream, with a venturi tube diffuser shape, contributes to the detaching of the flow boundary layer, causing turbulent (eddies) flow. In addition, when the flow in the throat of sealing is close to the transitional regime ($Re_1 \sim 2100$), the turbulence is magnified, improving fluid mixing. Both effects are then translated into an enhancement of the heat transfer coefficient at the downstream interconnection according to the flow direction. On the other hand, the seal is also responsible for a decrease of the h_c at the module end. Both effects must be considered and accurately studied during the design of a circuit.

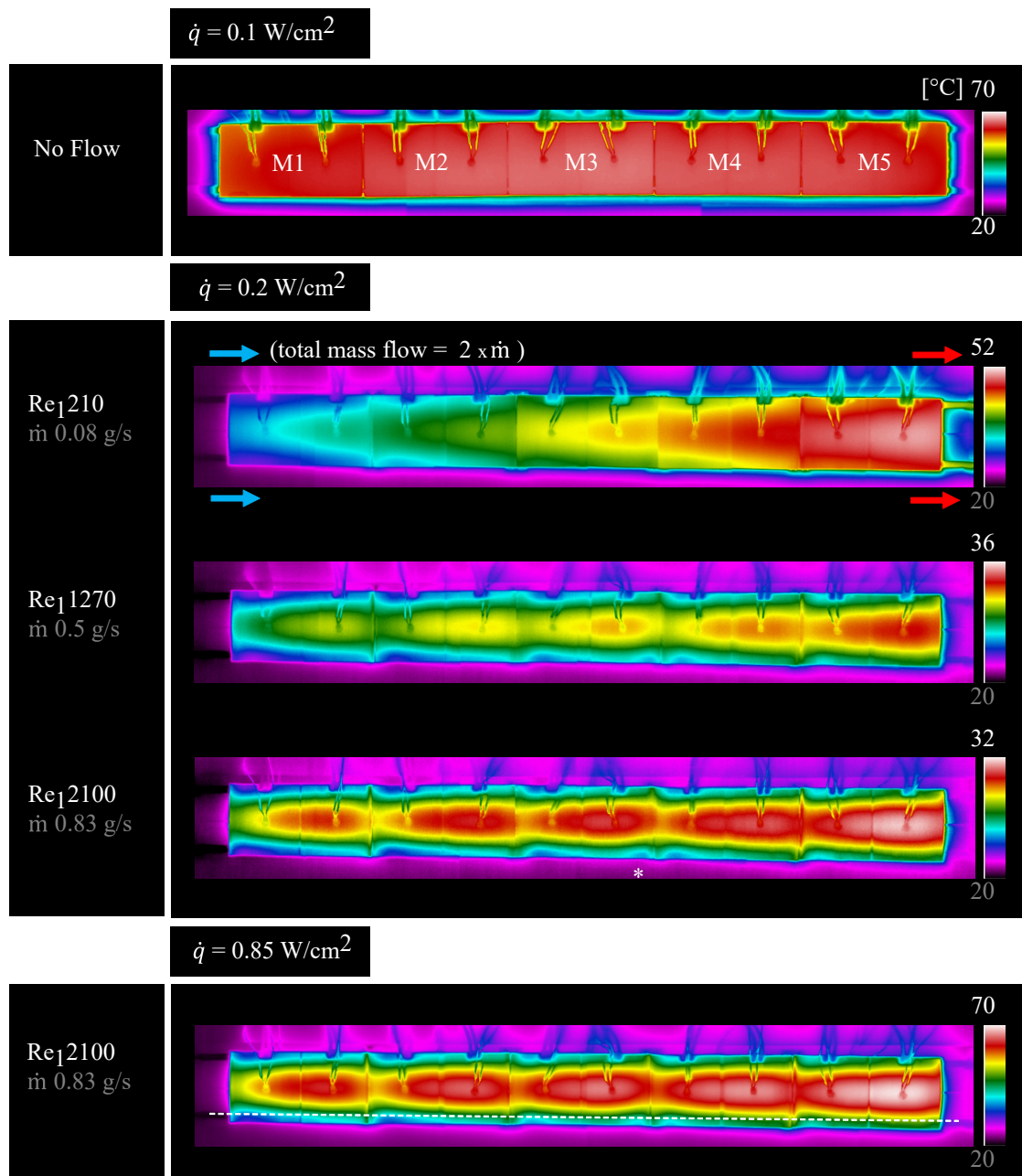


Figure 7.26: Interconnection effect for the configuration "1 Direction". An array of five modules (M1-M5) was tested with 1 Direction configuration (see Figure 7.19), different dissipated heat fluxes ($0.1 - 0.85 \text{ W/cm}^2$) and mass flow rates in the channel ($0.08 - 0.83 \text{ g/s}$). The water flows from left to right for the two channels embedded in the modules. The total mass flow rate is two times the mass flow rate of each channel (\dot{m}). Thermal images were taken for each interconnection, stitched together, forming the picture of the entire assembly. The dashed line in the bottom picture refers to the same analysis in Figure 7.25. An obstruction was noticed in the channel restriction highlighted with (*), corresponding to the interconnection between M3 and M4. This obstruction influenced the temperature profile of the modules' top surface.

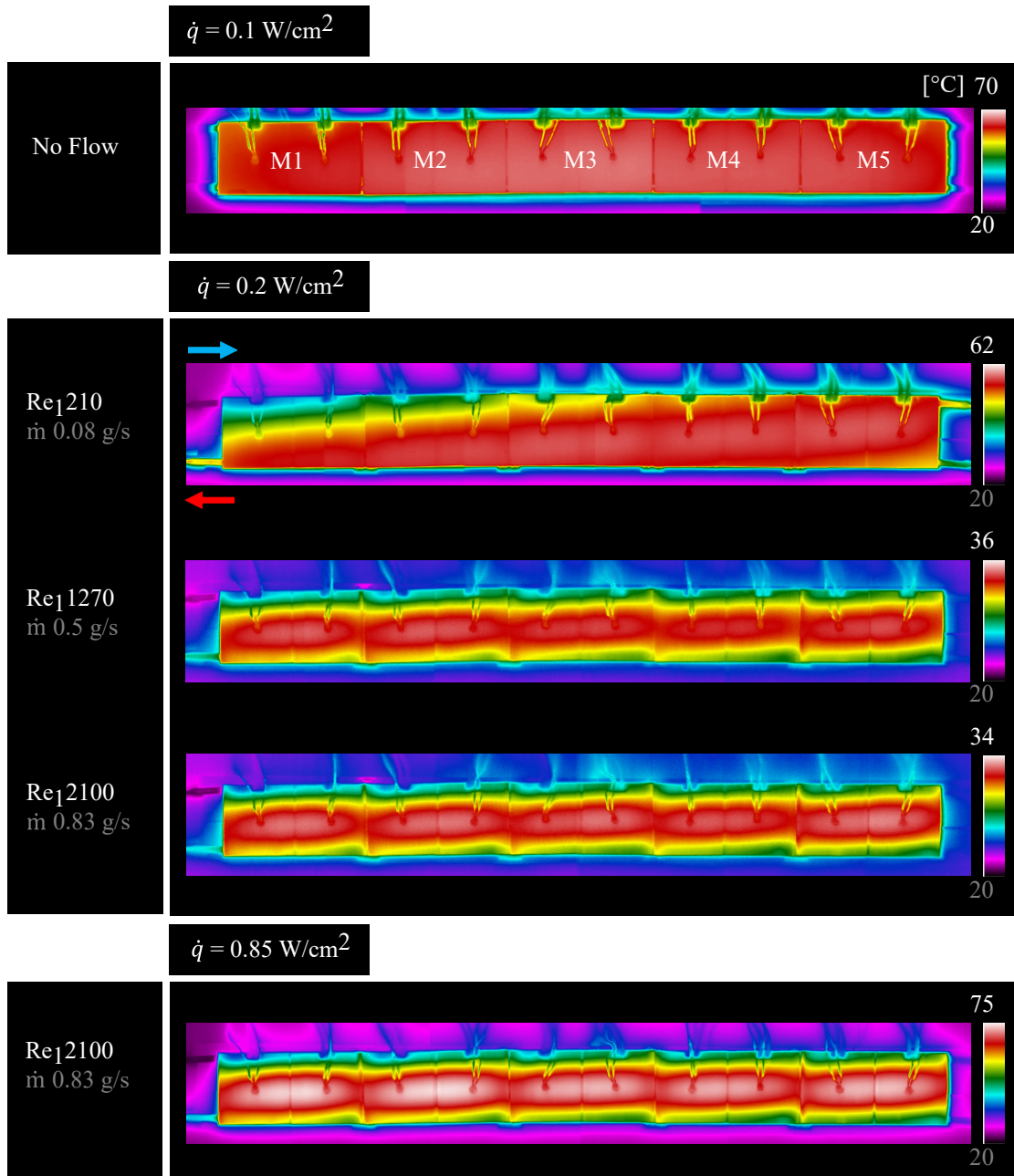


Figure 7.27: Interconnection effect for the configuration "2 Directions". An array of five modules (M1-M5) was tested with 2 Directions configuration (see Figure 7.19), different dissipated heat fluxes ($0.1 - 0.85 \text{ W/cm}^2$) and mass flow rates in the channel ($0.08 - 0.83 \text{ g/s}$). The flow inlet and outlet are on the left side of the module array. Thermal images were taken for each interconnection, stitched together, forming the picture of the entire assembly. Note that the obstruction effect on the temperature, noticed in Figure 7.25 and Figure 7.26, is not visible. In this case, the flow direction in the channel is reserved compared to the 1 Direction case.

Thermal performance

The thermal figure of merit, described in Section 2.4, was used to evaluate the thermal performances and to compare them with the analytical estimate. The experimental values of the TFM and the analytical estimate were calculated by the equation 2.3 and equation 2.5, respectively.

The conductive heat transfer resistance of the cooling substrate (R_s) was evaluated through a 2D finite element analysis (linear thermal steady state). The 2D geometry of the cross-section, under investigation, and its final thermal mapping are reported in Figure 7.28. The thermal conductivities of the alumina prototypes [214] (substrate) and the bi-adhesive [208] (thermal interface) are 32 and 0.19 W/mK, respectively. The heat transfer coefficient (h_s), between the channel wall (T_{wall}) and the hotter substrate point (T_s), at the middle of the cross-section, is 245 W/m²K ($R_s = 40.81$ cm²K/W). The h_c is conservatively assumed to be 2611 W/m² K (fully developed laminar flow regime, see Figure 7.24) and R_c corresponds to 3.83 cm² K/W. The estimated TFM for our prototype, sum of R_c and R_s , is therefore 44.64 cm²K/W.

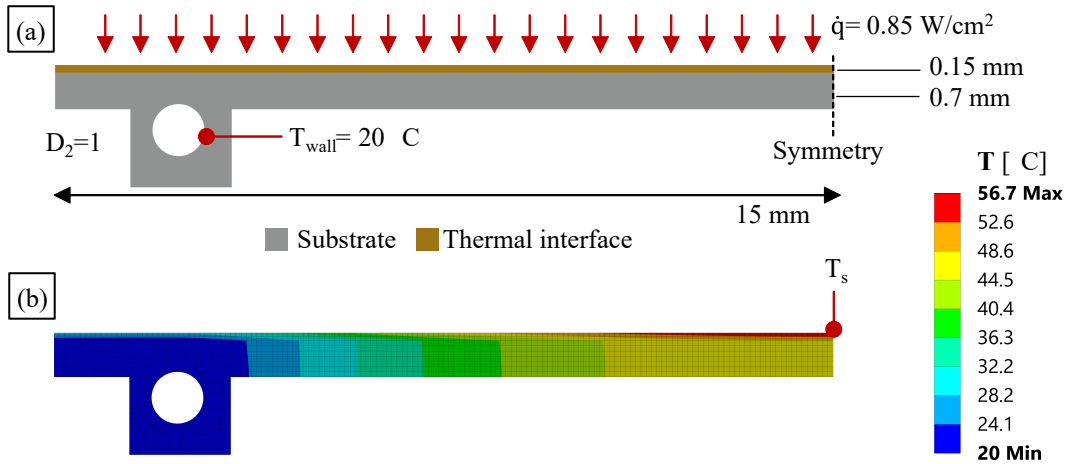


Figure 7.28: Thermal analysis of the alumina cooling substrate. The geometry and boundary conditions are reported in (a), while the temperature profile of the cross-section is in (b). Half of the module cross-section was analysed, and symmetry condition was applied. A uniform heat flux (\dot{q}) of 0.85 W/cm² was imposed at the substrate's top surface. The temperature of the channel wall (T_{wall}) was imposed at 20 °C. The resulting temperature of the substrate hotter point (T_s) was used to evaluate the substrate thermal resistance ($R_s = (T_{wall} - T_s) / \dot{q}$). Different \dot{q} gives same R_s . ANSYS Workbench 2021 [175] software was used for the analysis.

Figure 7.29 shows the TFM values for the array of five alumina modules tested with the two configurations, different mass flow rates and dissipated heat fluxes. The temperature sensors, glued on the top surface of the heaters (10 temperature sensors) and the temperature sensors at the inlet and outlet of the fluid circuit were used to calculate the temperature difference (ΔT_{sub} , See Equation 2.4). During the tests, the percentage of heat exchanged with the environment (natural convection, $T_{air} \sim 20$ -21 °C) with respect to the total heat of the heaters, was less than 10% for mass flow rates greater than 0.5g/s and 30-40% for a mass flow rate of

0.1 g/s. Information on the test error analysis is reported in Appendix C.5.1.

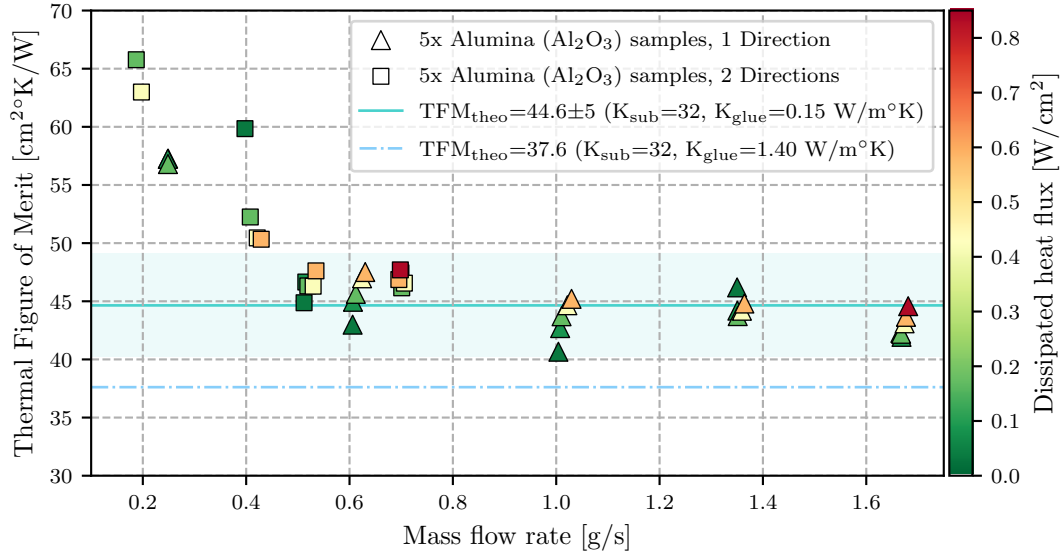


Figure 7.29: Experimental evaluation of the TFM for the alumina samples. The TFM obtained for each test is plotted as a function of the mass flow rate (ranges from 0.1 to 1.7 g/s). An array of five alumina samples was tested with the two configurations (see Figure 7.19), 1 Direction and 2 Directions. The value of the dissipated heat flux during the test ranges from 0.033 to 0.833 W/cm². The corresponding dissipated heat flux colours each marker (see the colour bar on the right). The analytical estimate (TFM = 44.64 cm²K/W) is plotted as a turquoise line for comparison. The light-turquoise area corresponds to the error of the analytical estimate ($\pm 10\%$, ± 5 cm²K/W). The dashed light-blue line corresponds to the estimated TFM if a thermally conductive glue is considered ($k_{glue} = 1.4$ W/mK). The data (temperatures and mass flow rate) were taken once they reached a steady state condition. The data were averaged over 1 minute of the test.

The experimental TFMs range from 40 to 50 cm²K/W for mass flow rates greater than 0.5 g/s. They matched with the estimate (44.64 cm²K/W). While for mass flow rates lower than 0.5 g/s, the experimental TFMs was greater than the estimate, probably due to the set-up limitation and the non-negligible thermal gradient in the water, due to the non-optimum mass flow rate, which also brought uneven thermal conditions in the modules.

Table 7.1: Estimate of the thermal figure of merit with different materials. "Th." means thickness.

Substrate	k [W/mK]	Thermal interface	k [W/mK]	Th. [mm]	TFM [cm ² K/W]
Al ₂ O ₃ [214]	32 (T = 30 °C)	Bi-adhesive [208]	0.19	0.15	44.6
Al ₂ O ₃ [214]	32 (T = 30 °C)	Thermal glue [207]	1.4	0.15	37.6
AlN [199]	160 (T < 50 °C)	Thermal glue [207]	1.4	0.15	11

Assuming a thermally conductive glue ($k=1.4$ W/m²K), like Masterbond EP37-3FLFAO [207], and the possibility in the future of producing cooling substrates in 3D printed aluminium nitride ($k = 160$ W/m²K conservative [199]), the theoretical figure of merits drop down to 11 cm² K/W (Table 7.1) which is in line with low-mass vascular CCS solutions (see Section 2.2.2

and Section 2.4).

In the tested module design, the channels are confined to the surface side, increasing the temperature at the centre of the cooling substrate. In addition, the dissipated power was uniform along the surface of the modules, while in a real application, the cooling circuit must deal with non-uniform power dissipation.

The circuit channels placed closer to the region with higher dissipated power bring higher thermal performances. At the same time, avoiding coolant at the active sensing areas minimises the material budget contribution. A good approach for circuit design is to find the best compromise between the two aspects, thermal performance and material budget contribution (Section 2.4).

7.5 Outcomes

Microfluidic modular cooling substrates can be produced with different materials and production processes, such as silicon with FS engraved channels, CFRP cold plates with embedded polyimide/stainless steel pipes, polymers and ceramics cooling substrates. They all merit further investigation.

Taking as reference the future tracker of the next ALICE 3 experiment [204], real-scale prototypes with integrated modular microfluidic cooling substrates were produced. 3D printed i-M μ CS, both ceramics and polymeric, were integrated into the mechanical support structure.

The assembly of these prototypes give us the opportunity to focus on aspects of the ceramics i-M μ CS that are key for their implementation into a real detector layout, i.e. flatness, glueing interface with thin MAPS sensors and hydraulic and thermal performances.

The flatness of large ceramic substrates, with dimensions ranging from 30x30 up to 30x210 mm², were out of the design requirements (± 50 μ m). The geometrical distortion of the substrate surface, mainly due to the sintering process, required an additional machining step at the end of the production process. The flatness of re-machined thicker LCM ceramic substrates (30x30 mm²) was < 50 μ m, and 0.2 mm was achieved as the final wall thickness. Procedures and tools for this machining step must be further optimised. In parallel, further investigation on alternative solutions, i.e. tuning the sintering parameters or holding the samples during sintering, to achieve the flatness requirement can be carried out.

An ALICE ITS2 electrical module composed of 2x7 MAPS sensors (ALPIDE sensors), 100 μ m thin, and a flexible printed circuit bus was successfully glued, following the glueing procedure of the i-M μ CS detector, on a 30x210 mm² ceramic module having a minimum wall thickness of 0.2 mm.

The assembled i-M μ CS was cooled down to -10 °C, and subsequently, an electronic check was performed on all the ALPIDE sensors as a demonstration of the integrity and proper working

after the glueing procedure and thermal cycle. However, voids at the glueing interface between the substrate and the sensors were noticed, provoked by the substrate flatness out of tolerance (0.787 mm).

The hydraulic and thermal behaviours of ceramic i-M μ CSs were studied on 30x60 mm² substrates (with 1 mm diameter channels) interconnected by the radial seal solution and the pin-based mechanical interface. Deionised water in a laminar flow regime (100-2000 *Re*) was used as a coolant.

The accuracy of the channel features, i.e. restriction at the interconnection, affects the total pressure drop significantly. Particular attention to the channel micro-features, which means inspection, re-machining or cleaning of the channel features, must be then pursued. In this manner, standard correlations are reliable in predicting the pressure drop.

The radial seal interconnection is responsible for a fluid mixing and eddy's flow at the interconnection downstream that causes an increase in the local heat transfer coefficient, which can be of the order of +40% with respect to the laminar expected value. This effect can be positively utilised to optimise the microfluidic circuit design where higher heat fluxes need to be evacuated.

The observed thermal performances were in line with the analytic prediction. However, the tested samples were based on module substrates in aluminium oxide with a limited thermal conductivity of 32 W/mK. The possible use of aluminium nitride (>160 W/mK) instead, whose use is under investigation for 3D printing, will allow reaching thermal performance comparable to or even better than that of a carbon vascular cooling substrate solution with/without re-workable TIM.

8 Conclusions

This research laid the foundation of a novel type of cooling substrate denoted as *interlocking Modular microfluidic Cooling Substrate* (i-M μ CS). The proposed modular microfluidic concept, which relies on an in-plane hydraulic interconnection, fulfils two fundamental objectives of the cooling and mechanics for future silicon tracking detectors:

- To access industrialised and distributed series production.
- To provide a high thermal performance which is predictable and reliable.

Different interlocking hydraulic and mechanical interconnections were designed and their functionality was validated by analysis, prototyping and experimental test. The production of modular microfluidic cooling substrates with ceramic additive manufacturing, as a new material and technology for HEP applications, was accomplished, and its integration and operation with a functional electrical module was achieved.

8.1 Summary

(Etched silicon μ CS) The research started with looking into the microfluidic cooling substrates currently implemented in HEP experiments, which are mainly based on microchannels etched into a silicon wafer, closed by a bonded silicon top cover. Limits for this technology were identified in dimensional constraints, in its complexity and high cost, when a large cooling substrate is required. In order to address these limits, the research activity started with the investigation of possible alternative production processes.

(FS laser engraving of silicon) A laser technology used to engrave the channels in the silicon substrate was considered, and its feasibility was evaluated (Chapter 4). It was demonstrated that microchannels can be engraved inside silicon substrates (380 μ m thin) with femtosecond laser technology (ultrashort pulse, 250 ps) and can be anodic bonded to a glass cover. Channels (200 μ m deep) with a width down to 100 μ m and an inter-distance between channels down to 100 μ m were successfully produced. In addition, an adhesive-based solution to close

the channels was identified as an alternative to the high temperature bonding. Silicon dies ($15 \times 15 \text{ mm}^2$, $380 \text{ }\mu\text{m}$ thick) with FS engraved channels were successfully closed with a carbon veil (carbon fleece) cover impregnated with epoxy resin.

Regardless of the successful production and qualification of microchannels using femtosecond laser technology, no clear advantages were identified in terms of process simplification and cost saving with respect to the more standard etching process. It was, therefore, decided to refrain from investing additional time in analysing the other design key aspect of the silicon cooling substrates, i.e. the interconnection between Si substrates, and to move instead to other technologies, i.e. Additive Manufacturing.

(Interlocking interconnection) A novel re-workable interlocking microfluidic interconnection, the sum of mechanical and hydraulic interfaces, was developed (Section 5.2). The substrate interconnection relies on a mechanical fixation based on a LEGO[®]-like concept (pin-based), and on hydraulic in-plane sealing, across microfluidic modules, guaranteed by micro O-rings (face-seal). The new broad range of possibilities opened up by 3D printing gave an immediate solution for sample production. It became clear that the advantage offered by 3D printing would have been paid with the need to tune the design for each selected material and production technology since the interconnection geometry and the mechanical properties of the substrate are intimately linked to the manufacturing process and material. Therefore, while targeting AM processes that use materials more suitable for HEP application (such as ceramics), several tests were performed with polymer samples. Since the micro-dimensions of the substrate features are close to the printing tolerance, the development had to be supported by experimental verification. The research finally demonstrated the feasibility of the LEGO[®]-like concept, fulfilling the design requirements of future detectors.

Based on the experimental observations, alternative solutions to the LEGO[®]-like baseline, less dependent on substrate accuracy, were designed and tested, for both the mechanical and the hydraulic interfaces.

(Alternative hydraulic interface) An alternative solution for the hydraulic interface, based on a radial seal concept, was developed (Section 5.4). The face seal was replaced by a cylindrical micro-fitting that engages two adjacent substrates. The fitting is equipped with a number of micro O-rings that are radially compressed once inside the substrates, such to provide the required sealing. The performance achieved with this new design was demonstrated to be independent of the mechanical coupling across substrates, i.e. from the manufacturing tolerances of the parts. This solution represents a good candidate to cope with highly demanding cooling performance and fluids, e.g. evaporative CO₂.

(Alternative mechanical interface) For the mechanical interface, alternative solutions that rely on different ways to hold and keep in position the modules were investigated (Section 5.5), namely clip-based, spring-based and rail-based. Each of these solutions can be considered an evolution of the previous one. While the first two rely on a direct interconnection between two adjacent modules using either a clip or a spring mechanism, the rail-based option counts

on two side rails that simultaneously keep an array of modules. The rail-based solution with radial seal results in being an attractive alternative to the pin-based one for its simplicity.

Among the different 3D printing processes, used for the development of the interconnection design, the ceramic AM was identified as the more appealing for HEP application based on the good matching with the design requirements.

(Ceramic 3D printed substrate) Following a preliminary screening, two promising ceramic AM technologies, i.e. NPJ and LCM, were identified (Chapter 6). The development focused on printed aluminium oxide, as a well-known and consolidated printed ceramic option, even if the final target is aluminium nitride for its better thermal and thermo-elastic properties. The use of aluminium nitride for 3D printing processes is not yet commercialised, and it requires future R&D. It was demonstrated that both technologies are suitable for microchannel cooling substrates production. It was also observed that some geometrical deformations occur due to anisotropy phenomena. This affects the micro features and the overall substrate flatness. Indeed, a key aspect specific to ceramics is the high temperature sintering process (1500-1800 °C) of the "green part"; this impacts the final accuracy of the part due to non-balanced thermoplastic expansion/contraction. As an alternative, the use of the "green part" without sintering as the final material was also considered. However, the green samples appeared to be brittle due to the improper mixture of the alumina powder and type of binder. Further R&D is required for the correct binder choice and the optimum mixture. At this moment, the baseline is a sintered ceramic cold plate with a post-machining step to achieve the required flatness. The obtained tolerances of the micro features and the ceramic hardness imposed a design optimisation for the mechanical and hydraulic interface to avoid wearing and guarantee leak-tightness.

(Modular microfluidic implementation in Si tracking systems) Taking as reference the future tracker of the next ALICE3 experiment [204], 3D printed ceramic and polymeric modular microfluidic substrates were integrated into the detector layout as an example of possible modular microfluidic implementation (Chapter 7). An electrical module, composed of 2x7 real MAPS sensors (15x30 mm², 100 µm thin), was glued on a 30x210 mm² ceramic substrate. The assembled module was cooled down to -10 °C; after that, all the sensors were read out by the electronic test bench to verify the sensors' integrity after gluing and thermal cycle. This exercise was the first demonstration of the possibility of integrating the new modular microfluidic concept at a system level.

8.2 Future work

Within the research scope of this work, an alternative process for the fabrication of a silicon microchannel cooling substrate, based on femtosecond laser engraving, was investigated. Even if the solution did not show clear advantages with respect to the more standard etching process for the series production of large cooling substrates, it is worth performing further R&D on microchannel engraving at the back side of the diced chips. The possibility of closing the

Chapter 8. Conclusions

microchannels and connecting them to the feed-line connector with adhesive-based carbon fleece shall also be investigated in depth. The scope of this R&D line should be to develop a reliable process flow for a working chip that allows engraving of a microchannel circuit on its back, avoiding any complex and high-temperature steps (e.g. etching and bonding) that could compromise the sensor integrity.

The research then focused on microfluidic cooling substrates with a new hydraulic and mechanical interlocking concept that was characterized and, finally, integrated into a HEP detector module with sensors and electronics components. Several areas of possible future development have been identified in these studies. They can be divided into component and system level developments.

At the component level:

- The i-M μ CS production shall be extended to manufacturing processes alternative to 3D printing, such as composite material or injection moulding.
- The improvement of the flatness of the ceramic cooling substrate shall be further assessed either by tuning a process that does not require high-temperature sintering, i.e. direct use of the "green part", or by optimising and standardising a machining post-processing phase.
- The i-M μ CS based on 3D printing provides the possibility to extend the standard planar substrate concept to a 3 Dimensional shape. This is well aligned with the sensor trend to move from flat to cylindrical or to more complex 3D shapes.
- The circuit of a i-M μ CS and its interlocking interconnection shall be finally validated for different cooling system strategies in terms of low operative temperature (-40 C), fluid compatibility (e.g. with evaporative CO₂) and pressure resistance. Radiation resistance and thermal-cycling behaviour shall also be assessed with accelerated ageing tests.

At the system level:

- The integration performed on one functional sensing module shall be extended to a larger scale integration exercise such to better assess assembly procedures and electrical services interfaces and interconnections.
- The large scale dimension will push the production of the detector integrated modules towards an industrialised process. This will probably require moving the substrate production from 3D printing to injection molding to rely on a more effective and homogeneous process.
- The repeatability and reliability of the assembly procedure of the sensing module and the modular microfluidic cooling substrate must be demonstrated. It will be key to entrust to the industry the entire process.

- A suitable quality control method has to be developed for the acceptance of the produced modules and for the next assembly and interconnection phases, required to build the entire detector.

To conclude, the new tracker for ALICE 3 [\[204\]](#), to be installed in LS4 (2035), represents a unique opportunity to push the interlocking microchannel design from the present R&D phase to a construction phase.

Bibliography

- [1] CERN Collaboration, “Strategic R&D Programme on Technologies for Future Experiments,” CERN, Tech. Rep., Dec. 2018. DOI: [10.17181/CERN.5PQI.KDL2](https://doi.org/10.17181/CERN.5PQI.KDL2).
- [2] CERN Collaboration, “Strategic R&D Programme on Technologies for Future Experiments - Annual report 2020,” CERN, Tech. Rep., 2020. DOI: [10.17181/CERN-EP-RDET-2021-001](https://doi.org/10.17181/CERN-EP-RDET-2021-001).
- [3] CERN Collaboration, “Strategic R&D Programme on Technologies for Future Experiments - Annual report 2021,” CERN, Tech. Rep., 2021. DOI: [10.17181/CERN-EP-RDET-2022-006](https://doi.org/10.17181/CERN-EP-RDET-2022-006).
- [4] ECFA Collaboration, “The 2021 ECFA Detector Research and Development Roadmap Prepared by the Detector R&D Roadmap Process Group of the European Committee for Future Accelerators,” Tech. Rep., 2021. DOI: [10.17181/CERN.XDPL.W2EX](https://doi.org/10.17181/CERN.XDPL.W2EX).
- [5] L. Evans and P. Bryant, “LHC Machine,” *Journal of Instrumentation*, vol. 3, no. 08, S08001, Aug. 2008, ISSN: 1748-0221. DOI: [10.1088/1748-0221/3/08/S08001](https://doi.org/10.1088/1748-0221/3/08/S08001).
- [6] ALICE Collaboration, “The ALICE experiment at the CERN LHC,” *Journal of Instrumentation*, vol. 3, no. 08, S08002, Aug. 2008, ISSN: 1748-0221. DOI: [10.1088/1748-0221/3/08/S08002](https://doi.org/10.1088/1748-0221/3/08/S08002).
- [7] ATLAS Collaboration, “The ATLAS Experiment at the CERN Large Hadron Collider,” *Journal of Instrumentation*, vol. 3, no. 08, S08003, Aug. 2008, ISSN: 1748-0221. DOI: [10.1088/1748-0221/3/08/S08003](https://doi.org/10.1088/1748-0221/3/08/S08003).
- [8] CMS Collaboration, “The CMS experiment at the CERN LHC,” *Journal of Instrumentation*, vol. 3, no. 08, S08004, Aug. 2008, ISSN: 1748-0221. DOI: [10.1088/1748-0221/3/08/S08004](https://doi.org/10.1088/1748-0221/3/08/S08004).
- [9] LHCb Collaboration, “The LHCb Detector at the LHC,” *Journal of Instrumentation*, vol. 3, no. 08, S08005, Aug. 2008, ISSN: 1748-0221. DOI: [10.1088/1748-0221/3/08/S08005](https://doi.org/10.1088/1748-0221/3/08/S08005).
- [10] D. Bortoletto, “How and why silicon sensors are becoming more and more intelligent?” *Journal of Instrumentation*, vol. 10, no. 8, Aug. 2015, ISSN: 17480221. DOI: [10.1088/1748-0221/10/08/C08016](https://doi.org/10.1088/1748-0221/10/08/C08016).
- [11] S. Seidel, “Silicon strip and pixel detectors for particle physics experiments,” *Physics Reports*, vol. 828, pp. 1–34, Oct. 2019, ISSN: 0370-1573. DOI: [10.1016/J.PHYSREP.2019.09.003](https://doi.org/10.1016/J.PHYSREP.2019.09.003).

Bibliography

- [12] P. Riedler, “Monolithic Pixel Detectors for LHC,” PSI seminar, Tech. Rep., 2018. [Online]. Available: <https://www.readkong.com/page/the-alice-its-inner-tracking-system-upgrade-monolithic-7050494>.
- [13] W. Snoeys, “CMOS monolithic active pixel sensors for high energy physics,” *Nuclear Instruments and Methods in Physics Research Section A: Accelerators, Spectrometers, Detectors and Associated Equipment*, vol. 765, pp. 167–171, Nov. 2014, ISSN: 0168-9002. DOI: [10.1016/J.NIMA.2014.07.017](https://doi.org/10.1016/J.NIMA.2014.07.017).
- [14] S. Meroli, D. Passeri, and L. Servoli, “Measurement of charge collection efficiency profiles of CMOS active pixel sensors,” *Journal of Instrumentation*, vol. 7, no. 09, P09011, Sep. 2012, ISSN: 1748-0221. DOI: [10.1088/1748-0221/7/09/P09011](https://doi.org/10.1088/1748-0221/7/09/P09011).
- [15] L. Servoli, D. Biagetti, S. Meroli, P. Placidi, D. Passeri, and P. Tucceri, “Use of a standard CMOS imager as position detector for charged particles,” *Nuclear Physics B - Proceedings Supplements*, vol. 215, no. 1, pp. 228–231, Jun. 2011, ISSN: 0920-5632. DOI: [10.1016/J.NUCLPHYSBPS.2011.04.016](https://doi.org/10.1016/J.NUCLPHYSBPS.2011.04.016).
- [16] A. Dorokhov *et al.*, “High resistivity CMOS pixel sensors and their application to the STAR PXL detector,” *Nuclear Instruments and Methods in Physics Research Section A: Accelerators, Spectrometers, Detectors and Associated Equipment*, vol. 650, no. 1, pp. 174–177, Sep. 2011, ISSN: 0168-9002. DOI: [10.1016/J.NIMA.2010.12.112](https://doi.org/10.1016/J.NIMA.2010.12.112).
- [17] L. Greiner *et al.*, “A MAPS based vertex detector for the STAR experiment at RHIC,” *Nuclear Instruments and Methods in Physics Research Section A: Accelerators, Spectrometers, Detectors and Associated Equipment*, vol. 650, no. 1, pp. 68–72, Sep. 2011, ISSN: 0168-9002. DOI: [10.1016/J.NIMA.2010.12.006](https://doi.org/10.1016/J.NIMA.2010.12.006).
- [18] J. Schambach *et al.*, “A MAPS Based Micro-Vertex Detector for the STAR Experiment,” *Physics Procedia*, vol. 66, pp. 514–519, Jan. 2015, ISSN: 1875-3892. DOI: [10.1016/J.PHPRO.2015.05.067](https://doi.org/10.1016/J.PHPRO.2015.05.067).
- [19] M. Mager, “ALPIDE, the Monolithic Active Pixel Sensor for the ALICE ITS upgrade,” *Nuclear Instruments and Methods in Physics Research Section A: Accelerators, Spectrometers, Detectors and Associated Equipment*, vol. 824, pp. 434–438, Jul. 2016, ISSN: 0168-9002. DOI: [10.1016/J.NIMA.2015.09.057](https://doi.org/10.1016/J.NIMA.2015.09.057).
- [20] CMS Collaboration, *The Phase-2 Upgrade of the CMS Tracker*, CERN-LHCC-2017-009. CMS-TDR-014, Jun. 2017. DOI: [10.17181/CERN.QZ28.FLHW](https://doi.org/10.17181/CERN.QZ28.FLHW).
- [21] ATLAS Collaboration, “ATLAS detector and physics performance - CERN Document Server,” CERN, Geneva, Tech. Rep., 1999. [Online]. Available: <http://cds.cern.ch/record/391177>.
- [22] LHCb Collaboration, “LHCb VELO Upgrade Technical Design Report,” CERN-LHCC-2013-021, Tech. Rep., 2013. [Online]. Available: <https://cds.cern.ch/record/1624070>.

- [23] N. Wermes, "Pixel detectors ... where do we stand?" *Nuclear Instruments and Methods in Physics Research Section A: Accelerators, Spectrometers, Detectors and Associated Equipment*, vol. 924, pp. 44–50, Apr. 2019, ISSN: 0168-9002. DOI: [10.1016/J.NIMA.2018.07.003](https://doi.org/10.1016/J.NIMA.2018.07.003).
- [24] CMS Collaboration, *CMS tracker layout repository*, 2016. [Online]. Available: <https://cms-tklayout.web.cern.ch/cms-tklayout/layouts-work/cmssw-models/>.
- [25] M. Moll, "Radiation damage in silicon particle detectors: Microscopic defects and macroscopic properties - INSPIRE," Ph.D. dissertation, Hamburg university, Hamburg, 1999. [Online]. Available: <https://inspirehep.net/literature/513308>.
- [26] G. Knoll, A. Arbor, and J. Wiley, *Radiation Detection and Measurement - 4th Edition*. 2010, ISBN: 978-0-470-13148-0.
- [27] R. Alia *et al.*, "Single event effects in high-energy accelerators," *Semiconductor Science and Technology*, vol. 32, no. 3, p. 034 003, Feb. 2017, ISSN: 0268-1242. DOI: [10.1088/1361-6641/AA5695](https://doi.org/10.1088/1361-6641/AA5695).
- [28] I. Dawson, F. Faccio, M. Moll, A. Weidberg, and A. Wei-Dberg, "Overview of radiation effects on detector systems," Tech. Rep., Apr. 2021, pp. 3–3. DOI: [10.23731/CYRM-2021-001.3](https://doi.org/10.23731/CYRM-2021-001.3).
- [29] S. Terzo *et al.*, "Novel 3D Pixel Sensors for the Upgrade of the ATLAS Inner Tracker," *Frontiers in Physics*, vol. 9, p. 2, Apr. 2021, ISSN: 2296424X. DOI: [10.3389/FPHY.2021.624668/BIBTEX](https://doi.org/10.3389/FPHY.2021.624668/BIBTEX).
- [30] M. Van Rijnbach *et al.*, "Radiation hardness and timing performance in MALTA monolithic pixel sensors in TowerJazz 180 nm," *Journal of Instrumentation*, vol. 17, no. 04, p. C04034, Apr. 2022, ISSN: 1748-0221. DOI: [10.1088/1748-0221/17/04/C04034](https://doi.org/10.1088/1748-0221/17/04/C04034).
- [31] G. Gustavino *et al.*, "Timing performance of radiation hard MALTA monolithic Pixel sensors," Sep. 2022. DOI: [10.48550/arxiv.2209.14676](https://doi.org/10.48550/arxiv.2209.14676).
- [32] R. L. Clough, "High-energy radiation and polymers: A review of commercial processes and emerging applications," *Nuclear Instruments and Methods in Physics Research, Section B: Beam Interactions with Materials and Atoms*, vol. 185, no. 1-4, pp. 8–33, 2001, ISSN: 0168583X. DOI: [10.1016/S0168-583X\(01\)00966-1](https://doi.org/10.1016/S0168-583X(01)00966-1).
- [33] B. Kumar, R. Singh, and T. Nakamura, "Degradation of Carbon Fiber-Reinforced Epoxy Composites by Ultraviolet Radiation and Condensation," *Journal of Composite Materials*, vol. 36, no. 24, pp. 2713–2733, Jul. 2016. DOI: [10.1177/002199802761675511](https://doi.org/10.1177/002199802761675511).
- [34] F. Guarino, C. Hauviller, and M. Tavlet, "Compilation of radiation damage test data, part IV: adhesives," Tech. Rep., 2001, p. 127. DOI: [10.5170/CERN-2001-006](https://doi.org/10.5170/CERN-2001-006).
- [35] S. Ilie, M. Tavlet, S. Ilie, and M. Tavlet, "Qualification of coolants and cooling pipes for future high-energy-particle detectors," *NIMPB*, vol. 185, no. 1-4, pp. 318–322, Dec. 2001, ISSN: 0168-583X. DOI: [10.1016/S0168-583X\(01\)00806-0](https://doi.org/10.1016/S0168-583X(01)00806-0).
- [36] H. Schonbacher and A. Stolarz-Izycka, "Compilation of radiation damage test data. Part I: Cable insulating materials.," Tech. Rep., 1979. DOI: [10.5170/CERN-1979-004](https://doi.org/10.5170/CERN-1979-004).

Bibliography

- [37] H. Schönbacher, M. Tavlet, and A. Fontaine, “Compilation of radiation damage test data, part I, 2nd edition: Halogen-free cable-insulating materials.,” Tech. Rep., 1989. DOI: [10.5170/CERN-1989-012](https://doi.org/10.5170/CERN-1989-012).
- [38] H. Schönbacher and A. Stolarz-Izycka, “Compilation of radiation damage test data, part II: thermosetting and thermoplastic resins.,” Tech. Rep., 1979. DOI: [10.5170/CERN-1979-008](https://doi.org/10.5170/CERN-1979-008).
- [39] M. Tavlet, H. Schönbacher, and A. Fontaine, “Compilation of radiation damage test data, part II, 2nd edition: thermoset and thermoplastic resins, composite materials.,” Tech. Rep. May, 1998, May. DOI: [10.5170/CERN-1998-001](https://doi.org/10.5170/CERN-1998-001).
- [40] P. Beynel, H. Schönbacher, and P. Maier, “Compilation of radiation damage test data , part III: materials used around high-energy accelerators.,” Tech. Rep., 1982. DOI: [10.5170/CERN-1982-010](https://doi.org/10.5170/CERN-1982-010).
- [41] CERN Collaboration, “The Use of Plastic and other Non-Metallic Materials at CERN with respect to Fire Safety and Radiation Resistance Contents,” CERN, Geneva, Tech. Rep., 2005. [Online]. Available: <https://cds.cern.ch/record/910404>.
- [42] M. Gupta, “Calculation of radiation length in materials - CERN PH-EP-Tech-Note-2010-013,” Tech. Rep. [Online]. Available: <https://cds.cern.ch/record/1279627?ln=it>.
- [43] Particle Data Group (PDG), *Atomic and Nuclear Properties of Materials*. [Online]. Available: <https://pdg.lbl.gov/2019/AtomicNuclearProperties/>.
- [44] H. H. Wieman *et al.*, “STAR PIXEL detector mechanical design,” *Journal of Instrumentation*, vol. 4, no. 05, P05015, May 2009, ISSN: 1748-0221. DOI: [10.1088/1748-0221/4/05/P05015](https://doi.org/10.1088/1748-0221/4/05/P05015).
- [45] G. Contin *et al.*, “The STAR MAPS-based PiXeL detector,” *Nuclear Instruments and Methods in Physics Research Section A: Accelerators, Spectrometers, Detectors and Associated Equipment*, vol. 907, pp. 60–80, Nov. 2018, ISSN: 0168-9002. DOI: [10.1016/J.NIMA.2018.03.003](https://doi.org/10.1016/j.nima.2018.03.003).
- [46] H. Wieman, *STAR HFT PXL Vertex Detector Mechanics - Forum on Tracking Detector Mechanics (FTDM) 2014*, (Hamburg DESY), Germany, 2014. [Online]. Available: <https://indico.cern.ch/event/287285/contributions/1640694/>.
- [47] A. Collaboration, “Letter of Intent for an ALICE ITS Upgrade in LS3,” CERN, CERN-LHCC-2019-018 ; LHCC-I-034, Tech. Rep., 2019. DOI: [10.17181/CERN-LHCC-2019-018](https://doi.org/10.17181/CERN-LHCC-2019-018).
- [48] B. Abelev *et al.*, “Technical Design Report for the Upgrade of the ALICE Inner Tracking System,” *Journal of Physics G: Nuclear and Particle Physics*, vol. 41, no. 8, p. 087 002, 2014, ISSN: 0954-3899. DOI: [10.1088/0954-3899/41/8/087002](https://doi.org/10.1088/0954-3899/41/8/087002).
- [49] A. Mapelli *et al.*, “Low material budget microfabricated cooling devices for particle detectors and front-end electronics,” *Nuclear Physics B - Proceedings Supplements*, vol. 215, no. 1, pp. 349–352, Jun. 2011, ISSN: 0920-5632. DOI: [10.1016/J.NUCLPHYSBPS.2011.04.050](https://doi.org/10.1016/j.nuclphysbps.2011.04.050).

-
- [50] 3M™ technology, “Novec™ 649 Engineered Fluid - Technical datasheet,” Tech. Rep. [Online]. Available: https://www.3m.com/3M/en_US/p/d/b5005005025/.
- [51] D. Attree *et al.*, “The evaporative cooling system for the ATLAS inner detector,” *Journal of Instrumentation*, vol. 3, no. 07, P07003, Jul. 2008, ISSN: 1748-0221. DOI: [10.1088/1748-0221/3/07/P07003](https://doi.org/10.1088/1748-0221/3/07/P07003).
- [52] A. Francescon *et al.*, “Performance of the ALICE SPD cooling system,” *Journal of Physics: Conference Series*, vol. 395, no. 1, p. 012 063, Nov. 2012, ISSN: 1742-6596. DOI: [10.1088/1742-6596/395/1/012063](https://doi.org/10.1088/1742-6596/395/1/012063).
- [53] P. Tropea, J. Daguin, P. Petagna, H. Postema, B. Verlaat, and L. Zwalinski, “CO₂ evaporative cooling: The future for tracking detector thermal management,” *Nuclear Instruments and Methods in Physics Research Section A: Accelerators, Spectrometers, Detectors and Associated Equipment*, vol. 824, pp. 473–475, Jul. 2016, ISSN: 0168-9002. DOI: [10.1016/J.NIMA.2015.08.052](https://doi.org/10.1016/J.NIMA.2015.08.052).
- [54] B. Verlaat *et al.*, “CO₂ cooling challenges at CERN for the future phase 2 upgrade program,” *25th IIR International Congress of Refrigeration*, vol. 2019-Augus, pp. 351–359, Aug. 2019, ISSN: 01511637. [Online]. Available: <https://cds.cern.ch/record/2723848>.
- [55] V. Bhanot, P. Petagna, A. Cioncolini, and H. Iacovides, “Development and validation of a simulation tool for next generation detector cooling systems,” *Nuclear Instruments and Methods in Physics Research Section A: Accelerators, Spectrometers, Detectors and Associated Equipment*, vol. 955, p. 163 264, Mar. 2020, ISSN: 0168-9002. DOI: [10.1016/J.NIMA.2019.163264](https://doi.org/10.1016/J.NIMA.2019.163264).
- [56] G. Alberti *et al.*, “Development of a Thermal Control System with Mechanically Pumped CO₂ Two-Phase Loops for the AMS-02 Tracker on the ISS,” Tech. Rep., Feb. 2013. DOI: [10.48550/arxiv.1302.4294](https://doi.org/10.48550/arxiv.1302.4294).
- [57] W. Adam *et al.*, “The CMS Phase-1 pixel detector upgrade,” *Journal of Instrumentation*, vol. 16, no. 02, P02027, Feb. 2021, ISSN: 1748-0221. DOI: [10.1088/1748-0221/16/02/P02027](https://doi.org/10.1088/1748-0221/16/02/P02027).
- [58] A. Collaboration, “ATLAS Insertable B-Layer Technical Design Report,” CERN-LHCC-2010-013 ; ATLAS-TDR-19, Tech. Rep., 2010. [Online]. Available: <https://cds.cern.ch/record/1291633?ln=it>.
- [59] ATLAS Collaboration, “Technical Design Report for the ATLAS Inner Tracker Pixel Detector,” CERN-LHCC-2017-005 , ATLAS-TDR-025, Tech. Rep., 2017. DOI: [10.17181/CERN.FOZZ.ZP3Q](https://doi.org/10.17181/CERN.FOZZ.ZP3Q).
- [60] ATLAS Collaboration, “Technical Design Report for the ATLAS Inner Tracker Strip Detector,” CERN-LHCC-2017-005 ; ATLAS-TDR-025, Tech. Rep., 2017. [Online]. Available: <https://cds.cern.ch/record/2257755>.

Bibliography

- [61] G. Calderini, “The ATLAS ITk detector for High Luminosity LHC upgrade,” *Nuclear Instruments and Methods in Physics Research Section A: Accelerators, Spectrometers, Detectors and Associated Equipment*, p. 167 048, Jun. 2022, ISSN: 0168-9002. DOI: [10.1016/J.NIMA.2022.167048](https://doi.org/10.1016/J.NIMA.2022.167048).
- [62] S. Chowdhury, “The Phase-2 Upgrade of the CMS Outer Tracker,” *Nuclear Instruments and Methods in Physics Research Section A: Accelerators, Spectrometers, Detectors and Associated Equipment*, vol. 979, p. 164 432, Nov. 2020, ISSN: 0168-9002. DOI: [10.1016/J.NIMA.2020.164432](https://doi.org/10.1016/J.NIMA.2020.164432).
- [63] S. Orfanelli, “The Phase 2 Upgrade of the CMS Inner Tracker,” *Nuclear Instruments and Methods in Physics Research, Section A: Accelerators, Spectrometers, Detectors and Associated Equipment*, vol. 980, Nov. 2020, ISSN: 01689002. DOI: [10.1016/J.NIMA.2020.164396](https://doi.org/10.1016/J.NIMA.2020.164396).
- [64] L. Contiero and P. Barroca, *Hybrid cycle with Krypton for cooling of future silicon detectors in HEP, Forum on Tracking Detector Mechanics (FTDM) 2022*, Frascati (RM), Italy, 2022. [Online]. Available: <https://indico.cern.ch/event/853861/contributions/4841295/>.
- [65] L. Contiero, P. Barroca, A. Hafner, B. Verlaat, P. Petagna, and K. Banasiak, “Krypton, applied as refrigerant for cooling of silicon detector trackers,” in *Krypton, applied as refrigerant for cooling of silicon detector trackers*, Trondheim, Norway: IIR-Gustav Lorentzen Conference on Natural Refrigerants (GL2022)., 2022. DOI: [10.18462/IIR.GL2022.0203](https://doi.org/10.18462/IIR.GL2022.0203).
- [66] Huntsman company, “Araldite ® 2011 Structural Adhesive - Technical datasheet,” Tech. Rep. [Online]. Available: www.araldite2000plus.com.
- [67] Henkel Adhesives, “LOCTITE STYCAST 2850FT - Technical datasheet,” Tech. Rep. [Online]. Available: https://www.henkel-adhesives.com/ch/de/produkt/potting-compounds/loctite_stycast_2850ft.html.
- [68] M. Gomez Marzoa, “Innovative low-mass cooling systems for the ALICE ITS Upgrade detector at CERN,” Ph.D. dissertation, CERN-THESIS-2016-160, 2016. [Online]. Available: <http://cds.cern.ch/record/2231119?ln=it>.
- [69] V. Zherebchevsky *et al.*, “Experimental investigation of new ultra-lightweight support and cooling structures for the new Inner Tracking System of the ALICE Detector,” *Journal of Instrumentation*, vol. 13, no. 08, T08003–T08003, Aug. 2018, ISSN: 1748-0221. DOI: [10.1088/1748-0221/13/08/T08003](https://doi.org/10.1088/1748-0221/13/08/T08003).
- [70] M. Angeletti, *Study of the mechanical support and positioning of the sensors for the new tracker of the ALICE experiment at CERN (MSc thesis)*. Polytechnic University of Turin, CERN-THESIS-2016-300, 2016. [Online]. Available: <http://cds.cern.ch/record/2265692>.
- [71] MPD Collaboration, “Multipurpose Detector Inner Tracking System Technical Design Report,” Tech. Rep., 2022. DOI: [10.13140/RG.2.2.19857.51046](https://doi.org/10.13140/RG.2.2.19857.51046).

- [72] M. X. Liu, G. Odyniec, and R. Redwine, "A Monolithic-Active-Pixel-Sensor-based Vertex Detector (MVTX) for the 2 sPHENIX Experiment at RHIC," Los Alamos National Laboratory, Tech. Rep., 2017. [Online]. Available: <https://www.phenix.bnl.gov/WWW/publish/barish/publish/mxliu/sPHENIX/MVTX-Project/MVTX-Preproposal-v1.5-02012017.pdf>.
- [73] M. Angeletti and C. Gargiulo, *Production, quality assurance and integration of staves mechanics for the new ALICE Inner Tracking System. Forum on Tracking Detector Mechanics (FTDM) 2019*, Cornell University, Ithaca (NY), USA, 2019. [Online]. Available: <https://indico.cern.ch/event/775863/contributions/3413647/>.
- [74] Arctic, *Arctic Alumina, Premium Ceramic Thermal Compound -Datasheet*. [Online]. Available: http://www.arcticsilver.com/arctic_alumina.htm.
- [75] Arctic, *Arctic Silver Incorporated - Ceramique2 - Datasheet*. [Online]. Available: <http://www.arcticsilver.com/cm2.html>.
- [76] ARCTIC, *MX-4 - High performance thermal paste -Datasheet*. [Online]. Available: <https://www.arctic.de/MX-4/ACTCP00008B>.
- [77] ARCTIC, *MX-5 - Premium thermal compound - Datasheet*. [Online]. Available: <https://www.arctic.de/MX-5/ACTCP00043A>.
- [78] Henkel, "BERGQUIST GAP FILLER TGF 3500LVO - Technical datasheet," Tech. Rep. [Online]. Available: https://www.henkel-adhesives.com/ch/de/produkt/thermal-gap-fillers/bergquist_gap_fillertgf3500lvo.html.
- [79] Panasonic Industrial Devices, *EYG-S Graphite-TIM (Compressible Type) PGS -Datasheet*. [Online]. Available: <https://na.industrial.panasonic.com/products/thermal-management/thermal-management/lineup/thermal-management-products/series/70488>.
- [80] A. Rizzi, *Mounting dummy TBPS modules*, Pisa (ita), 2022. [Online]. Available: <https://indico.cern.ch/event/1132736/>.
- [81] P. Rose, "Tilted TBPS Ring Mechanics for CMS Phase 2 Upgradeack - Indico," FTDM 2022, Frascati (ita), Tech. Rep., 2022. [Online]. Available: <https://indico.cern.ch/event/853861/contributions/4841278/>.
- [82] D. Alvarez and et al., "Design Overview of the Bare Local Supports for the ITk Pixel Outer Barrel," Geneva, Tech. Rep., 2021. [Online]. Available: <https://edms.cern.ch/document/2632352>.
- [83] D. B. Tuckerman and R. F. Pease, "High-Performance Heat Sinking for VLSI," *IEEE Electron Device Letters*, vol. EDL-2, no. 5, pp. 126–129, 1981, ISSN: 15580563. DOI: [10.1109/EDL.1981.25367](https://doi.org/10.1109/EDL.1981.25367).
- [84] Y. Joshi and P. Kumar, *Energy efficient thermal management of data centers*. Springer US, Aug. 2013, vol. 9781441971, pp. 1–625, ISBN: 9781441971241. DOI: [10.1007/978-1-4419-7124-1/COVER](https://doi.org/10.1007/978-1-4419-7124-1/COVER).

- [85] N. Lamaison, "Dynamic Modeling and Experimental Evaluation of a Controlled Two-Phase On-Chip Cooling System Designed for High Efficiency Datacenters," Ph.D. dissertation, 2014. DOI: [10.5075/EPFL-THESIS-6301](https://doi.org/10.5075/EPFL-THESIS-6301).
- [86] R. V. Erp, G. Kampitsis, and E. Matioli, "A manifold microchannel heat sink for ultra-high power density liquid-cooled converters," *Conference Proceedings - IEEE Applied Power Electronics Conference and Exposition - APEC*, vol. 2019-March, pp. 1383–1389, May 2019. DOI: [10.1109/APEC.2019.8722308](https://doi.org/10.1109/APEC.2019.8722308).
- [87] R. Van Erp, G. Kampitsis, and E. Matioli, "Efficient Microchannel Cooling of Multiple Power Devices with Compact Flow Distribution for High Power-Density Converters," *IEEE Transactions on Power Electronics*, vol. 35, no. 7, pp. 7235–7245, Jul. 2020, ISSN: 19410107. DOI: [10.1109/TPEL.2019.2959736](https://doi.org/10.1109/TPEL.2019.2959736).
- [88] A. Y. Ali, E. M. Abo-Zahhad, M. F. Elkady, S. Ookawara, A. H. El-Shazly, and A. Radwan, "Temperature uniformity enhancement of densely packed high concentrator photovoltaic module using four quadrants microchannel heat sink," *Solar Energy*, vol. 202, pp. 446–464, May 2020, ISSN: 0038-092X. DOI: [10.1016/j.solener.2020.03.106](https://doi.org/10.1016/j.solener.2020.03.106).
- [89] S. J. Pety, M. H. Y. Tan, A. R. Najafi, P. R. Barnett, P. H. Geubelle, and S. R. White, "Carbon fiber composites with 2D microvascular networks for battery cooling," *International Journal of Heat and Mass Transfer*, vol. 115, pp. 513–522, Dec. 2017, ISSN: 0017-9310. DOI: [10.1016/j.ijheatmasstransfer.2017.07.047](https://doi.org/10.1016/j.ijheatmasstransfer.2017.07.047).
- [90] J. A. Khan, A. K. Monjur Morshed, and R. Fang, "Towards Ultra-compact High Heat Flux Microchannel Heat Sink," *Procedia Engineering*, vol. 90, pp. 11–24, Jan. 2014, ISSN: 1877-7058. DOI: [10.1016/j.proeng.2014.11.798](https://doi.org/10.1016/j.proeng.2014.11.798).
- [91] P. Smakulski and S. Pietrowicz, "A review of the capabilities of high heat flux removal by porous materials, microchannels and spray cooling techniques," *Applied Thermal Engineering*, vol. 104, pp. 636–646, Jul. 2016, ISSN: 1359-4311. DOI: [10.1016/j.applthermaleng.2016.05.096](https://doi.org/10.1016/j.applthermaleng.2016.05.096).
- [92] M. A. Ebadian and C. X. Lin, "A review of high-heat-flux heat removal technologies," *Journal of Heat Transfer*, vol. 133, no. 11, Nov. 2011, ISSN: 00221481. DOI: [10.1115/1.4004340/467288](https://doi.org/10.1115/1.4004340/467288).
- [93] J. B. Marcinichen, J. A. Olivier, N. Lamaison, and J. R. Thome, "Advances in Electronics Cooling," *Heat Transfer Engineering*, vol. 34, no. 5-6, pp. 434–446, Jan. 2012, ISSN: 01457632. DOI: [10.1080/01457632.2012.721316](https://doi.org/10.1080/01457632.2012.721316).
- [94] M. Asadi, G. Xie, and B. Sunden, "A review of heat transfer and pressure drop characteristics of single and two-phase microchannels," *International Journal of Heat and Mass Transfer*, vol. 79, pp. 34–53, Dec. 2014, ISSN: 0017-9310. DOI: [10.1016/j.ijheatmasstransfer.2014.07.090](https://doi.org/10.1016/j.ijheatmasstransfer.2014.07.090).
- [95] T. Frei, "Thermal management of components for high energy physics experiments and space applications," Ph.D. dissertation, EPFL, Lausanne, 2021. DOI: [10.5075/EPFL-THESIS-8776](https://doi.org/10.5075/EPFL-THESIS-8776). [Online]. Available: <https://infoscience.epfl.ch/record/288397>.

- [96] C. W. Chan, E. Siqueiros, J. Ling-Chin, M. Royapoor, and A. P. Roskilly, "Heat utilisation technologies: A critical review of heat pipes," *Renewable and Sustainable Energy Reviews*, vol. 50, pp. 615–627, Oct. 2015, ISSN: 1364-0321. DOI: [10.1016/J.RSER.2015.05.028](https://doi.org/10.1016/J.RSER.2015.05.028).
- [97] N. H. Naquiuddin, L. H. Saw, M. C. Yew, F. Yusof, T. C. Ng, and M. K. Yew, "Overview of micro-channel design for high heat flux application," *Renewable and Sustainable Energy Reviews*, vol. 82, pp. 901–914, Feb. 2018, ISSN: 1364-0321. DOI: [10.1016/J.RSER.2017.09.110](https://doi.org/10.1016/J.RSER.2017.09.110).
- [98] Y. L. Zhai, G. D. Xia, X. F. Liu, and Y. F. Li, "Exergy analysis and performance evaluation of flow and heat transfer in different micro heat sinks with complex structure," *International Journal of Heat and Mass Transfer*, vol. 84, pp. 293–303, May 2015, ISSN: 0017-9310. DOI: [10.1016/J.IJHEATMASSTRANSFER.2015.01.039](https://doi.org/10.1016/J.IJHEATMASSTRANSFER.2015.01.039).
- [99] Y. Fan, P. S. Lee, L. W. Jin, B. W. Chua, and D. C. Zhang, "A parametric investigation of heat transfer and friction characteristics in cylindrical oblique fin minichannel heat sink," *International Journal of Heat and Mass Transfer*, vol. 68, pp. 567–584, Jan. 2014, ISSN: 0017-9310. DOI: [10.1016/J.IJHEATMASSTRANSFER.2013.09.027](https://doi.org/10.1016/J.IJHEATMASSTRANSFER.2013.09.027).
- [100] H. C. Chiu, J. H. Jang, H. W. Yeh, and M. S. Wu, "The heat transfer characteristics of liquid cooling heatsink containing microchannels," *International Journal of Heat and Mass Transfer*, vol. 54, no. 1-3, pp. 34–42, Jan. 2011, ISSN: 0017-9310. DOI: [10.1016/J.IJHEATMASSTRANSFER.2010.09.066](https://doi.org/10.1016/J.IJHEATMASSTRANSFER.2010.09.066).
- [101] A. Mapelli *et al.*, "Low Mass Integrated Cooling," in *Proceedings of Science*, vol. 046, 2013. [Online]. Available: <https://pos.sissa.it/198/046/pdf>.
- [102] A. Mapelli, "Microfabricated silicon substrates for pixel detectors assembly and thermal management a.k.a. Silicon Microchannel Cooling Plates," *Nuclear Instruments and Methods in Physics Research, Section A: Accelerators, Spectrometers, Detectors and Associated Equipment*, vol. 958, p. 162 142, Apr. 2020, ISSN: 01689002. DOI: [10.1016/j.nima.2019.04.096](https://doi.org/10.1016/j.nima.2019.04.096).
- [103] A. Mapelli, P. Petagna, and M. Vos, "Micro-channel cooling for collider experiments: review and recommendations," CERN, AIDA-2020-NOTE-2020-003, Tech. Rep., 2020. [Online]. Available: <https://cds.cern.ch/record/2712079>.
- [104] G. Romagnoli *et al.*, "Silicon micro-fluidic cooling for NA62 GTK pixel detectors," *Microelectronic Engineering*, vol. 145, pp. 133–137, Sep. 2015, ISSN: 0167-9317. DOI: [10.1016/J.MEE.2015.04.006](https://doi.org/10.1016/J.MEE.2015.04.006).
- [105] G. Romagnoli, "Micro-fabricated silicon devices for advanced thermal management and integration of particle tracking detectors - CERN Document Server," Ph.D. dissertation, Università degli studi di Genova, Genova, 2016. [Online]. Available: <https://cds.cern.ch/record/2230933?ln=it>.

Bibliography

- [106] O. A. D. A. Francisco *et al.*, “Microchannel cooling for the LHCb VELO Upgrade I,” *Nuclear Instruments and Methods in Physics Research Section A: Accelerators, Spectrometers, Detectors and Associated Equipment*, p. 166 874, May 2022, ISSN: 0168-9002. DOI: [10.1016/J.NIMA.2022.166874](https://doi.org/10.1016/J.NIMA.2022.166874).
- [107] A. Mapelli, “Microfabricated silicon substrates for pixel detectors assembly and thermal management,” The 15th Vienna Conference on Instrumentation, VCI2019, Vienna University, Vienna, Tech. Rep., 2019. [Online]. Available: <https://indico.cern.ch/event/716539/contributions/3246036/>.
- [108] A. Mapelli, “The NA62 GTK, from silicon microchannel cooling plates to tracking detectors · Indico,” Vertex 2017 conference, Asturias (Spain), Tech. Rep., 2017. [Online]. Available: <https://indico.cern.ch/event/627245/contributions/2665160/>.
- [109] G. A. Rinella *et al.*, “The NA62 GigaTracker: a low mass high intensity beam 4D tracker with 65 ps time resolution on tracks,” *Journal of Instrumentation*, vol. 14, no. 07, P07010, Jul. 2019, ISSN: 1748-0221. DOI: [10.1088/1748-0221/14/07/P07010](https://doi.org/10.1088/1748-0221/14/07/P07010).
- [110] G. Fiorenza, V. Manzari, C. Pastore, I. Sgura, M. Torresi, and C. Gargiulo, “An innovative polyimide microchannels cooling system for the pixel sensor of the upgraded ALICE inner tracker,” *Proceedings of the 2013 5th IEEE International Workshop on Advances in Sensors and Interfaces, IWASI 2013*, pp. 81–85, 2013. DOI: [10.1109/IWASI.2013.6576065](https://doi.org/10.1109/IWASI.2013.6576065).
- [111] A. Francescon *et al.*, “Development of interconnected silicon micro-evaporators for the on-detector electronics cooling of the future ITS detector in the ALICE experiment at LHC,” *Applied Thermal Engineering*, 2015, ISSN: 13594311. DOI: [10.1016/j.applthermaleng.2015.09.013](https://doi.org/10.1016/j.applthermaleng.2015.09.013).
- [112] L. Andricsek *et al.*, “Integrated cooling channels in position-sensitive silicon detectors,” *Journal of Instrumentation*, vol. 11, no. 06, P06018, Jun. 2016, ISSN: 1748-0221. DOI: [10.1088/1748-0221/11/06/P06018](https://doi.org/10.1088/1748-0221/11/06/P06018).
- [113] F. Sanders, *Design & Production challenges for the LHCb Velo Upgrade Modules*. [Online]. Available: <https://indico.cern.ch/event/793299/>.
- [114] J. Buytaert, *LHCb Velo microchannels experience*. [Online]. Available: <https://indico.cern.ch/event/810687/contributions/3452036/>.
- [115] O. A. De Aguiar Francisco, *Microchannel CO2 cooling for the LHCb VELO Upgrade*. [Online]. Available: <https://indico.cern.ch/event/669866/contributions/3226465/>.
- [116] A. Francescon, “Experimental investigation of flow boiling in silicon microchannel devices for electronics cooling,” Ph.D. dissertation, University of Padova, Jan. 2016. [Online]. Available: <http://paduaresearch.cab.unipd.it/9358/>.
- [117] A. Toros, *Microfluidic Silicon Devices for the Cooling of Particle Detectors (Msc thesis)*. Lausanne, Switzerland. [Online]. Available: https://edms.cern.ch/ui/file/1538000/5/2015_MSc_TOROS_Adrien.pdf.
- [118] T. Abe *et al.*, “Belle II Technical Design Report,” Tech. Rep., Nov. 2010. DOI: [10.48550/ARXIV.1011.0352](https://doi.org/10.48550/ARXIV.1011.0352).

-
- [119] O. Alonso *et al.*, “DEPFET active pixel detectors for a future linear e+e - collider,” *IEEE Transactions on Nuclear Science*, vol. 60, no. 2, pp. 1457–1465, 2013, ISSN: 00189499. DOI: [10.1109/TNS.2013.2245680](https://doi.org/10.1109/TNS.2013.2245680).
- [120] R. Cardella, “CMOS detector and system developments for LHC detector upgrades,” Ph.D. dissertation, University of Oslo, Oslo, 2019. [Online]. Available: <https://cds.cern.ch/record/2702969?ln=it>.
- [121] L. Frehner, *Buried microchannels for thermal management of silicon detectors (Msc thesis)*, Lausanne, master thesis, 2020. [Online]. Available: https://edms.cern.ch/ui/file/2430450/2/PDM_LFrehner_OK.pdf.
- [122] R. van Erp, R. Soleimanzadeh, L. Nela, G. Kampitsis, and E. Matioli, “Co-designing electronics with microfluidics for more sustainable cooling,” *Nature* 2020 585:7824, vol. 585, no. 7824, pp. 211–216, Sep. 2020, ISSN: 1476-4687. DOI: [10.1038/s41586-020-2666-1](https://doi.org/10.1038/s41586-020-2666-1).
- [123] M. Kluba, A. Arslan, R. Stoute, J. Muganda, and R. Dekker, “Single-Step CMOS Compatible Fabrication of High Aspect Ratio Microchannels Embedded in Silicon,” *Proceedings Euroensors 2017*, vol. 1, no. 4, p. 291, Aug. 2017, ISSN: 2504-3900. DOI: [10.3390/PROCEEDINGS1040291](https://doi.org/10.3390/PROCEEDINGS1040291).
- [124] Hisateru Akachi, *US4921041A - Structure of a heat pipe*, 1990. [Online]. Available: <https://patents.google.com/patent/US4921041A/en>.
- [125] H. Jouhara, A. Chauhan, T. Nannou, S. Almahmoud, B. Delpech, and L. C. Wrobel, “Heat pipe based systems - Advances and applications,” *Energy*, vol. 128, pp. 729–754, Jun. 2017, ISSN: 0360-5442. DOI: [10.1016/J.ENERGY.2017.04.028](https://doi.org/10.1016/J.ENERGY.2017.04.028).
- [126] Hisateru Akachi, *US5219020A - Structure of micro-heat pipe*, 1993. [Online]. Available: <https://patents.google.com/patent/US5219020A/en>.
- [127] M. Dias, “Pressure resistance characterisation of micro-vascular networks embedded in carbon composites for High Energy Physics applications,” FTDM2022, Frascati (ita), Tech. Rep., 2022. [Online]. Available: <https://indico.cern.ch/event/853861/contributions/4867438/>.
- [128] M. W. McElroy, A. Lawrie, and I. P. Bond, “Optimisation of an air film cooled CFRP panel with an embedded vascular network,” *International Journal of Heat and Mass Transfer*, vol. 88, pp. 284–296, Sep. 2015, ISSN: 0017-9310. DOI: [10.1016/J.IJHEATMASSTRANSFER.2015.04.071](https://doi.org/10.1016/J.IJHEATMASSTRANSFER.2015.04.071).
- [129] S. Pety, “Microvascular composites as a multifunctional material for electric vehicles,” Ph.D. dissertation, 2017. [Online]. Available: <https://www.ideals.illinois.edu/items/102426>.
- [130] M. Demiral, H. Tanabi, and B. Sabuncuoglu, “Experimental and numerical investigation of transverse shear behavior of glass-fibre composites with embedded vascular channel,” *Composite Structures*, vol. 252, p. 112 697, Nov. 2020, ISSN: 0263-8223. DOI: [10.1016/J.COMPSTRUCT.2020.112697](https://doi.org/10.1016/J.COMPSTRUCT.2020.112697).

Bibliography

- [131] A.Toros, *Catalog of fluidic connectors for the inlet/outlet of the cooling system of the ALICE ITS Inner Barrel Staves*, 2014. [Online]. Available: <https://edms.cern.ch/ui/#/master/navigator/document?D:100088426:100088426:subDocs>.
- [132] A. Mapelli and AL.(CERN), *Standard connectors for micro-channels*, 2018. [Online]. Available: <https://cds.cern.ch/record/2314041/files/AIDA-2020-MS77.pdf>.
- [133] Idex Health & Science, *Multiport Connectors for Fluidic Applications*. [Online]. Available: <https://www.idex-hs.com/store/fluidics/fluidic-connections/connectors.html>.
- [134] CEA-Leti, *LETI 3S SPECIALTY SILICON SOLUTIONS*. [Online]. Available: <https://www.leti-cea.com/cea-tech/leti/english/Pages/Industrial-Innovation/Innovate%20with%20Leti/LETI-3S.aspx>.
- [135] Y. Temiz, R. D. Lovchik, G. V. Kaigala, and E. Delamarche, “Lab-on-a-chip devices: How to close and plug the lab?” *Microelectronic Engineering*, vol. 132, pp. 156–175, Jan. 2015, ISSN: 0167-9317. DOI: [10.1016/J.MEE.2014.10.013](https://doi.org/10.1016/J.MEE.2014.10.013).
- [136] P. K. Yuen, “SmartBuild—A truly plug-n-play modular microfluidic system,” *Lab on a Chip*, vol. 8, no. 8, p. 1374, Jul. 2008, ISSN: 1473-0197. DOI: [10.1039/b805086d](https://doi.org/10.1039/b805086d).
- [137] C. Owens, *Modular LEGO brick microfluidics (Msc thesis)*. Massachusetts Institute of Technology: Massachusetts Institute of Technology, 2017. [Online]. Available: <https://dspace.mit.edu/handle/1721.1/117456>.
- [138] C. E. Owens and A. J. Hart, “High-precision modular microfluidics by micromilling of interlocking injection-molded blocks,” *Lab on a Chip*, vol. 18, no. 6, pp. 890–901, Mar. 2018, ISSN: 1473-0197. DOI: [10.1039/C7LC00951H](https://doi.org/10.1039/C7LC00951H).
- [139] K. Vittayarukskul and A. P. Lee, “A truly Lego® -like modular microfluidics platform,” *Journal of Micromechanics and Microengineering*, vol. 27, no. 3, p. 035 004, Mar. 2017, ISSN: 0960-1317. DOI: [10.1088/1361-6439/aa53ed](https://doi.org/10.1088/1361-6439/aa53ed).
- [140] A. C. Fernandes, K. V. Gernaey, and U. Krühne, ““Connecting worlds – a view on microfluidics for a wider application,”” *Biotechnology Advances*, vol. 36, no. 4, pp. 1341–1366, Jul. 2018, ISSN: 0734-9750. DOI: [10.1016/J.BIOTECHADV.2018.05.001](https://doi.org/10.1016/J.BIOTECHADV.2018.05.001).
- [141] D. G. Johnson, R. D. Frisina, and D. A. Borkholder, “In-Plane Biocompatible Microfluidic Interconnects for Implantable Microsystems,” *IEEE Transactions on Biomedical Engineering*, vol. 58, no. 4, pp. 943–948, Apr. 2011, ISSN: 0018-9294. DOI: [10.1109/TBME.2010.2098031](https://doi.org/10.1109/TBME.2010.2098031).
- [142] B. Dang, M. Bakir, and J. Meindl, “Integrated thermal-fluidic I/O interconnects for an on-chip microchannel heat sink,” *IEEE Electron Device Letters*, vol. 27, no. 2, pp. 117–119, Feb. 2006, ISSN: 0741-3106. DOI: [10.1109/LED.2005.862693](https://doi.org/10.1109/LED.2005.862693).
- [143] T. Morais, *Development of an in-plane microfluidic interconnect for the thermal management of particle detectors (Msc thesis)*, Lausanne, Switzerland, 2016. [Online]. Available: https://edms.cern.ch/ui/file/1709804/5/2016_MSc_MORAIS_Tiago.pdf.

- [144] A. Abada *et al.*, “FCC-hh: The Hadron Collider: Future Circular Collider Conceptual Design Report Volume 3,” *European Physical Journal: Special Topics*, vol. 228, no. 4, pp. 755–1107, Jul. 2019, ISSN: 19516401. DOI: [10.1140/epjst/e2019-900087-0](https://doi.org/10.1140/epjst/e2019-900087-0).
- [145] A. Abada *et al.*, “FCC-ee: The Lepton Collider,” *The European Physical Journal Special Topics* 2019 228:2, vol. 228, no. 2, pp. 261–623, Jun. 2019, ISSN: 1951-6401. DOI: [10.1140/EPJST/E2019-900045-4](https://doi.org/10.1140/EPJST/E2019-900045-4).
- [146] N. Bacchetta *et al.*, “CLD – A Detector Concept for the FCC-ee,” LCD-Note-2019-001, Tech. Rep., Nov. 2019. DOI: [10.48550/arxiv.1911.12230](https://doi.org/10.48550/arxiv.1911.12230).
- [147] B. A. Jasperson, Y. Jeon, K. T. Turner, F. E. Pfefferkorn, and W. Qu, “Comparison of micro-pin-fin and microchannel heat sinks considering thermal-hydraulic performance and manufacturability,” *IEEE Transactions on Components and Packaging Technologies*, vol. 33, no. 1, pp. 148–160, Mar. 2010, ISSN: 15213331. DOI: [10.1109/TCAPT.2009.2023980](https://doi.org/10.1109/TCAPT.2009.2023980).
- [148] F. Xu, Z. Pan, and H. Wu, “Experimental investigation on the flow transition in different pin-fin arranged microchannels,” *Microfluidics and Nanofluidics*, vol. 22, no. 1, pp. 1–13, Jan. 2018, ISSN: 16134990. DOI: [10.1007/S10404-017-2030-4/FIGURES/12](https://doi.org/10.1007/S10404-017-2030-4/FIGURES/12).
- [149] Y. Qiu, W. Hu, C. Wu, and W. Chen, “An Experimental Study of Microchannel and Micro-Pin-Fin Based On-Chip Cooling Systems with Silicon-to-Silicon Direct Bonding,” *Sensors* 2020, vol. 20, no. 19, p. 5533, Sep. 2020, ISSN: 1424-8220. DOI: [10.3390/S20195533](https://doi.org/10.3390/S20195533).
- [150] J. Wang, “Pressure drop and flow distribution in parallel-channel configurations of fuel cells: U-type arrangement,” *International Journal of Hydrogen Energy*, vol. 33, no. 21, pp. 6339–6350, Nov. 2008, ISSN: 0360-3199. DOI: [10.1016/J.IJHYDENE.2008.08.020](https://doi.org/10.1016/J.IJHYDENE.2008.08.020).
- [151] J. Wang, “Pressure drop and flow distribution in parallel-channel configurations of fuel cells: Z-type arrangement,” *International Journal of Hydrogen Energy*, vol. 35, no. 11, pp. 5498–5509, Jun. 2010, ISSN: 0360-3199. DOI: [10.1016/J.IJHYDENE.2010.02.131](https://doi.org/10.1016/J.IJHYDENE.2010.02.131).
- [152] J. Wang, “Theory of flow distribution in manifolds,” *Chemical Engineering Journal*, vol. 168, no. 3, pp. 1331–1345, Apr. 2011, ISSN: 1385-8947. DOI: [10.1016/J.CEJ.2011.02.050](https://doi.org/10.1016/J.CEJ.2011.02.050).
- [153] L. Rihakova and H. Chmelickova, “Laser micromachining of glass, silicon, and ceramics,” *Advances in Materials Science and Engineering*, vol. 2015, 2015, ISSN: 16878442. DOI: [10.1155/2015/584952](https://doi.org/10.1155/2015/584952).
- [154] C. Gaudio, P. N. Terekhin, A. Volpe, S. Nolte, B. Rethfeld, and A. Ancona, “Laser ablation of silicon with THz bursts of femtosecond pulses,” *Scientific Reports* |, vol. 11, p. 13321, 123. DOI: [10.1038/s41598-021-92645-7](https://doi.org/10.1038/s41598-021-92645-7).
- [155] M. E. Shaheen, J. E. Gagnon, and B. J. Fryer, “Femtosecond laser ablation behavior of gold, crystalline silicon, and fused silica: A comparative study,” *Laser Physics*, vol. 24, no. 10, Oct. 2014, ISSN: 15556611. DOI: [10.1088/1054-660X/24/10/106102](https://doi.org/10.1088/1054-660X/24/10/106102).
- [156] Sirris company, *Sirris Driving industry by technology*. [Online]. Available: <https://sirris.be/>.

Bibliography

- [157] Lasea, “Datasheet LASEA LS5-1 10W,” Tech. Rep. [Online]. Available: https://www.lasea.eu/wp-content/uploads/2014/07/Machine-LS5_EN.pdf.
- [158] Schott, *BOROFLOAT®*. [Online]. Available: <https://www.schott.com/en-gb/products/borofloat-p1000314>.
- [159] *Equipment – Center of MicroNanoTechnology CMi - EPFL*. [Online]. Available: <https://www.epfl.ch/research/facilities/cmi/equipment/>.
- [160] *EP-DT | Experimental Physics Department, Detector technologies group*. [Online]. Available: <https://ep-dep.web.cern.ch/organisation/dt>.
- [161] B. Tan and K. Venkatakrishnan, “A femtosecond laser-induced periodical surface structure on crystalline silicon,” *Journal of Micromechanics and Microengineering*, vol. 16, no. 5, p. 1080, Apr. 2006, ISSN: 0960-1317. DOI: [10.1088/0960-1317/16/5/029](https://doi.org/10.1088/0960-1317/16/5/029).
- [162] J. Bonse and J. Krüger, “Pulse number dependence of laser-induced periodic surface structures for femtosecond laser irradiation of silicon,” *Journal of Applied Physics*, vol. 108, no. 3, p. 034 903, Aug. 2010, ISSN: 0021-8979. DOI: [10.1063/1.3456501](https://doi.org/10.1063/1.3456501).
- [163] J. Bonse, J. Krüger, S. Höhm, and A. Rosenfeld, “Femtosecond laser-induced periodic surface structures,” *Journal of Laser Applications*, vol. 24, no. 4, p. 042 006, Jul. 2012, ISSN: 1042-346X. DOI: [10.2351/1.4712658](https://doi.org/10.2351/1.4712658).
- [164] J. Bonse, S. Hohm, S. V. Kirner, A. Rosenfeld, and J. Kruger, “Laser-Induced Periodic Surface Structures-A Scientific Evergreen,” *IEEE Journal of Selected Topics in Quantum Electronics*, vol. 23, no. 3, pp. 109–123, May 2017, ISSN: 15584542. DOI: [10.1109/JSTQE.2016.2614183](https://doi.org/10.1109/JSTQE.2016.2614183).
- [165] Keyence, *Measurement head: Violet semiconductor laser - VK-X1100 - Technical datasheet*. [Online]. Available: https://www.keyence.com/products/microscope/laser-microscope/vk-x100_x200/models/vk-x1100/.
- [166] B. Wu, A. Kumar, and S. Pamarthy, “High aspect ratio silicon etch: A review,” *Journal of Applied Physics*, vol. 108, no. 5, p. 051 101, Sep. 2010, ISSN: 0021-8979. DOI: [10.1063/1.3474652](https://doi.org/10.1063/1.3474652).
- [167] Technical fibre products Ltd, *Optiveil® Technical datasheet*. [Online]. Available: <https://shop.swiss-composite.ch/shop/resources/downloads/t-carbonvlies-e.pdf>.
- [168] “Accura ® 25 plastic for use with solid-state stereolithography (SLA ®) systems - Technical Datasheet,” Tech. Rep., 2005. [Online]. Available: <https://www.3dsystems.com/materials/accura-25-sla/tech-specs>.
- [169] Trotec, “Speedy 400 Laser engraving system,” Tech. Rep. [Online]. Available: <https://www.troteclaser.com/static/pdf/speedy-400/Datasheet-Speedy-400C-8070-en.pdf>.
- [170] M. Angeletti, P. Renaud, and C. Gargiulo, “First steps towards interlocking modular microfluidic cooling substrates (i-M μ CS) for future silicon tracking detectors in High Energy Physics (HEP),” *Microelectronic Engineering*, vol. 255, p. 111 707, Feb. 2022, ISSN: 0167-9317. DOI: [10.1016/J.MEE.2022.111707](https://doi.org/10.1016/J.MEE.2022.111707).

-
- [171] Ord 5700, "Parker O-Ring Handbook," Tech. Rep., 2021. [Online]. Available: <https://www.parker.com/Literature/O-Ring%20Division%20Literature/ORD%205700.pdf>.
- [172] *How to Select, Design, and Install O-Ring Seals – Tarkka*. [Online]. Available: <https://tarkka.co/2019/03/24/o-rings-o-yeah-how-to-select-design-and-install-o-ring-seals/>.
- [173] *What is PolyJet Technology for 3D Printing?* | Stratasys. [Online]. Available: <https://www.stratasys.com/polyjet-technology>.
- [174] *Vero: A Realistic Multi-Color 3D Printing Material* | Stratasys. [Online]. Available: <https://www.stratasys.com/materials/search/vero>.
- [175] ANSYS, *Engineering Simulation*. [Online]. Available: <https://www.ansys.com/>.
- [176] D. Huo, K. Cheng, and F. Wardle, "Design of Precision Machines," in *Machining Dynamics: Fundamentals, Applications and Practices*, K. Cheng, Ed., London: Springer London, 2009, pp. 283–321, ISBN: 978-1-84628-368-0. DOI: [10.1007/978-1-84628-368-0_10](https://doi.org/10.1007/978-1-84628-368-0_10).
- [177] T. J. Teo and A. H. Slocum, "Principle of elastic averaging for rapid precision design," *Precision Engineering*, vol. 49, pp. 146–159, Jul. 2017, ISSN: 01416359. DOI: [10.1016/j.precisioneng.2017.02.003](https://doi.org/10.1016/j.precisioneng.2017.02.003).
- [178] Mitutoyo, "CRYSTA-APEX S SERIES," Tech. Rep. [Online]. Available: https://www.mitutoyo.com/wp-content/uploads/2013/01/2097_CRYSTA_ApexS.pdf.
- [179] *U5100 High Accuracy Pressure Sensor*. [Online]. Available: <https://www.cdiweb.com/datasheets/te/us-5100.pdf>.
- [180] Isoswiss Watchparts SA, *Gaskets*. [Online]. Available: <https://www.isoswiss.ch/en/products/components/gaskets.html>.
- [181] Apple Rubber, *MicrOrings - Micro Miniature Seals*. [Online]. Available: <https://www.applerubber.com/products/microrings/>.
- [182] Mettler toledo, "Precision Balance MS4002TSDR/00," Tech. Rep. [Online]. Available: https://www.mt.com/de/en/home/products/Laboratory_Weighing_Solutions/precision-balances/MS4002TSDR.html.
- [183] Parker, "Radial Seal Design Guide Extruded and Machined Elastomeric Products Radial Seal Design Guide," Tech. Rep. [Online]. Available: https://www.parker.com/literature/O-Ring%20Division%20Literature/Parker_TechSeal_Radial%20Seal%20Design%20Guide_TSD%205440.pdf.
- [184] Nanodimension Fabricagroup, "Precision N-800, N-900 materials - Technical datasheet," Tech. Rep. [Online]. Available: https://www.nano-di.com/wp-content/uploads/2022/02/Nanofabrica_One-Page_Materials-2021.pdf.
- [185] N. Company, *AME Manufacturing Company*. [Online]. Available: <https://www.nano-di.com/product-overview/micro-am-fabrica>.

Bibliography

- [186] N. C. Menon, M. Walker, M. Anderson, and N. Colgan, "Compatibility of polymers in super-critical carbon dioxide for power generation systems: High level findings for low temperatures and pressure conditions," Nov. 2019. DOI: [10.2172/1592964](https://doi.org/10.2172/1592964).
- [187] B. J. Briscoe, T. Savvas, and C. T. Kelly, "'Explosive Decompression Failure' of Rubbers: A Review of the Origins of Pneumatic Stress Induced Rupture in Elastomers," *Rubber Chemistry and Technology*, vol. 67, no. 3, pp. 384–416, Jul. 1994, ISSN: 0035-9475. DOI: [10.5254/1.3538683](https://doi.org/10.5254/1.3538683).
- [188] B. Schrittester, G. Pinter, T. Schwarz, Z. Kadar, and T. Nagy, "Rapid Gas Decompression Performance of elastomers – A study of influencing testing parameters," *Procedia Structural Integrity*, vol. 2, pp. 1746–1754, Jan. 2016, ISSN: 2452-3216. DOI: [10.1016/J.PROSTR.2016.06.220](https://doi.org/10.1016/J.PROSTR.2016.06.220).
- [189] Dupont, "Kalrez® - Superior Seal Performance in Aggressive Environments," Tech. Rep. [Online]. Available: <https://www.dupont.com/kalrez.html>.
- [190] Parker, *KA183-85 Low temperature HNBR - Technical datasheet*, 2010. [Online]. Available: www.parkerorings.com.
- [191] NACE International, "NACE TM0297-2017," Tech. Rep., 2016. [Online]. Available: <https://www.normadoc.com/english/nace-tm0297-2017-2016.html>.
- [192] Y. Li, S. Sam Ge, K. Mo, and B. Liu, "Effect of radiation on mechanical properties and molecular structure of rubbers for nuclear robots," *Materials Express*, vol. 11, no. 9, pp. 1561–1570, Aug. 2021, ISSN: 2158-5849. DOI: [10.1166/MEX.2021.1897](https://doi.org/10.1166/MEX.2021.1897).
- [193] Ceramics Industry, *Ceramic Materials Properties Charts*. [Online]. Available: <https://www.ceramicindustry.com/ceramic-materials-properties-charts/>.
- [194] Y. Lakhdar, C. Tuck, J. Binner, A. Terry, and R. Goodridge, "Additive manufacturing of advanced ceramic materials," *Progress in Materials Science*, vol. 116, p. 100736, Feb. 2021, ISSN: 0079-6425. DOI: [10.1016/J.PMATSCI.2020.100736](https://doi.org/10.1016/J.PMATSCI.2020.100736).
- [195] H. Levi, "Additive Manufacturing in Technical Ceramics," *Interceram - International Ceramic Review* 2018 67:3, vol. 67, no. 3, pp. 12–13, May 2018, ISSN: 2523-8957. DOI: [10.1007/S42411-018-0009-0](https://doi.org/10.1007/S42411-018-0009-0).
- [196] M. Schwentenwein and J. Homa, "Additive Manufacturing of Dense Alumina Ceramics," *International Journal of Applied Ceramic Technology*, vol. 12, no. 1, pp. 1–7, Jan. 2015, ISSN: 1744-7402. DOI: [10.1111/IJAC.12319](https://doi.org/10.1111/IJAC.12319).
- [197] J. Schlacher *et al.*, "Strength of additive manufactured alumina," *Journal of the European Ceramic Society*, vol. 40, no. 14, pp. 4737–4745, Nov. 2020, ISSN: 0955-2219. DOI: [10.1016/J.JEURCERAMSOC.2020.03.073](https://doi.org/10.1016/J.JEURCERAMSOC.2020.03.073).
- [198] U. Scheithauer, E. Schwarzer, T. Moritz, and A. Michaelis, "Additive Manufacturing of Ceramic Heat Exchanger: Opportunities and Limits of the Lithography-Based Ceramic Manufacturing (LCM)," *Journal of Materials Engineering and Performance*, vol. 27, no. 1, pp. 14–20, Jan. 2018, ISSN: 15441024. DOI: [10.1007/S11665-017-2843-Z/FIGURES/10](https://doi.org/10.1007/S11665-017-2843-Z/FIGURES/10).

-
- [199] J. Rauchenecker, J. Rabitsch, M. Schwentenwein, and T. Konegger, "Additive manufacturing of aluminum nitride ceramics with high thermal conductivity via digital light processing," *Open Ceramics*, vol. 9, Mar. 2022, ISSN: 26665395. DOI: [10.1016/J.OCERAM.2021.100215](https://doi.org/10.1016/J.OCERAM.2021.100215).
- [200] AIDA Innova, *WP10: Advanced Mechanics for Tracking and Vertex Detectors*. [Online]. Available: <https://aidainnova.web.cern.ch/wp10>.
- [201] ZEISS, "ZEISS METROTOM - Specifications," Tech. Rep., 2018. [Online]. Available: https://www.msiviking.com/documents/ZEISS/CT/METROTOM_2018.pdf.
- [202] KEYENCE company, "Wide-Area 3D Measurement System Head - VR-5200 - Technical datasheet," Tech. Rep. [Online]. Available: <https://www.keyence.com/products/microscope/macroscope/vr-3000/models/vr-5200/>.
- [203] ISO, "ISO 21920-1:2021 - Geometrical product specifications (GPS) — Surface texture: Profile — Part 1: Indication of surface texture," Tech. Rep. [Online]. Available: <https://www.iso.org/standard/72196.html>.
- [204] ALICE collaboration, "Letter of intent for ALICE 3: A next generation heavy-ion experiment at the LHC - CERN Document Server," CERN, Geneva, Tech. Rep., 2022. [Online]. Available: <https://cds.cern.ch/record/2803563>.
- [205] W. Rybiński and J. Mikielwicz, "Analytical solutions of heat transfer for laminar flow in rectangular channels," *Archives of Thermodynamics*, vol. 35, no. 4, pp. 29–42, Jan. 2014, ISSN: 20836023. DOI: [10.2478/AOTER-2014-0031](https://doi.org/10.2478/AOTER-2014-0031).
- [206] *DragonFly IV - Nano Dimension - AME Manufacturing Company*. [Online]. Available: <https://www.nano-di.com/dragonfly-iv/>.
- [207] Masterbond company, "Masterbond EP37-3FLFAO - Technical datasheet," Tech. Rep. [Online]. Available: www.masterbond.com.
- [208] 3M™ technology, "3M™ Adhesive Transfer Tape 468MP - Technical datasheet," Tech. Rep., 2017. [Online]. Available: <https://multimedia.3m.com/mws/media/1581295O/3m-adhesive-transfer-tape-468mp.pdf>.
- [209] National Instruments Corp, *What is LabVIEW? Graphical Programming for Test & Measurement*. [Online]. Available: <https://www.ni.com/it-it/shop/labview.html>.
- [210] Flir, "FLIR E60 - Technical datasheet," Tech. Rep., 2014. [Online]. Available: <https://docs.rs-online.com/5098/0900766b8137184a.pdf>.
- [211] Armacell Germany, *ArmaFlex*. [Online]. Available: <https://local.armacell.com/de/armacell-deutschland/produkte/afarmaflex/>.
- [212] I. E. Idelchik, A. S. Ginevskiy, A. V. Kolesnikov, G. R. Malyavskaya, and N. K. Shveyeva, *Handbook of Hydraulic Resistance, 4th Edition Revised and Augmented*. Begell House, 2008, ISBN: 978-1-56700-251-5.
- [213] U. Grigull and H. Tratz, "Thermischer einlauf in ausgebildeter laminarer rohrströmung," *International Journal of Heat and Mass Transfer*, vol. 8, no. 5, pp. 669–678, May 1965, ISSN: 0017-9310. DOI: [10.1016/0017-9310\(65\)90016-5](https://doi.org/10.1016/0017-9310(65)90016-5).

Bibliography

- [214] Xjet Technology, “C700 - Alumina - Technical datasheet,” Tech. Rep. [Online]. Available: <https://www.xjet3d.com/wp-content/uploads/2022/04/C700-Alumina-data-sheet-04.22.pdf>.
- [215] CERN Collaboration, *CERN Accelerating science*. [Online]. Available: <https://home.cern/science>.
- [216] J. Haffner, “The CERN accelerator complex. Complexe des accélérateurs du CERN,” 2013. [Online]. Available: <https://cds.cern.ch/record/1621894>.
- [217] D. Froidevaux and P. Sphicas, “General-Purpose Detectors for the Large Hadron Collider,” *Annual Review of Nuclear and Particle Science*, vol. 56, no. 1, pp. 375–440, Nov. 2006, ISSN: 0163-8998. DOI: [10.1146/annurev.nucl.54.070103.181209](https://doi.org/10.1146/annurev.nucl.54.070103.181209).
- [218] S. Chatrchyan *et al.*, “Observation of a new boson at a mass of 125 GeV with the CMS experiment at the LHC,” *Physics Letters B*, vol. 716, no. 1, pp. 30–61, Sep. 2012, ISSN: 0370-2693. DOI: [10.1016/J.PHYSLETB.2012.08.021](https://doi.org/10.1016/J.PHYSLETB.2012.08.021).
- [219] G. Aad *et al.*, “Observation of a new particle in the search for the Standard Model Higgs boson with the ATLAS detector at the LHC,” *Physics Letters B*, vol. 716, no. 1, pp. 1–29, Sep. 2012, ISSN: 0370-2693. DOI: [10.1016/J.PHYSLETB.2012.08.020](https://doi.org/10.1016/J.PHYSLETB.2012.08.020).
- [220] G. Knoll, *Radiation Detection and Measurement (4th ed.)* Hoboken, NJ: John Wiley, 2010, ISBN: 978-0-470-13148-0.
- [221] S. R. Davis, “Interactive Slice of the CMS detector,” 2016. [Online]. Available: <https://cds.cern.ch/record/2205172>.
- [222] T. Sakuma and T. McCauley, “Detector and Event Visualization with SketchUp at the CMS Experiment,” *Journal of Physics: Conference Series*, vol. 513, no. 2, p. 22 032, Jun. 2014. DOI: [10.1088/1742-6596/513/2/022032](https://doi.org/10.1088/1742-6596/513/2/022032).
- [223] I. Neutelings, *CMS coordinate system – TikZ.net*. [Online]. Available: https://tikz.net/axis3d_cms/.
- [224] F. Gianotti, *Closing remarks and a look to the future, 10th anniversary of the Higgs boson discovery*. [Online]. Available: <https://indico.cern.ch/event/1135177/timetable/>.
- [225] CERN Collaboration, *The High Luminosity Large Hadron Collider*. [Online]. Available: <https://hilumilhc.web.cern.ch/>.
- [226] O. Brüning *et al.*, “The scientific potential and technological challenges of the High-Luminosity Large Hadron Collider program,” eng, *Reports on progress in physics. Physical Society (Great Britain)*, vol. 85, no. 4, Mar. 2022, ISSN: 1361-6633 (Electronic). DOI: [10.1088/1361-6633/ac5106](https://doi.org/10.1088/1361-6633/ac5106).
- [227] C. Rossi, *Studies for the ALICE ITS microchannel cooling system, ANSYS CFX simulations*. [Online]. Available: <https://edms.cern.ch/ui/#!/master/navigator/document?P:1245110527:1406084290:subDocs>.
- [228] NACA 23021 (*naca23021-il*). [Online]. Available: <http://airfoiltools.com/airfoil/details?airfoil=naca23021-il>.

- [229] Huntsman company, "Araldite ® 2020 (XW 396 / XW 397) - Technical datasheet," Tech. Rep., 2007. [Online]. Available: www.araldite2000plus.com.
- [230] "EKWB EK-CryoFuel Solid Premix - Safety datasheet," Tech. Rep. [Online]. Available: <https://www.ekwb.com/shop/EK-IM/EK-IM-3831109829929.pdf>.
- [231] Bronkhorst, "mini CORI-FLOW Coriolis Flow Meter and controller - Technical datasheet," Tech. Rep. [Online]. Available: <https://www.bronkhorst.com/int/products/liquid-flow/mini-cori-flow/m14/>.
- [232] Huba Control, "Pressure sensor 511 - Technical datasheet," Tech. Rep. [Online]. Available: <https://www.hubacontrol.com/en/products/pressure-transmitter/pressure-sensor-511>.
- [233] M. Bahrami, M. M. Yovanovich, and J. R. Culham, "Pressure Drop of Fully-Developed, Laminar Flow in Microchannels of Arbitrary Cross-Section," *Journal of Fluids Engineering*, vol. 128, no. 5, pp. 1036–1044, Sep. 2006, ISSN: 0098-2202. DOI: [10.1115/1.2234786](https://doi.org/10.1115/1.2234786).
- [234] M. E. Steinke and S. G. Kandlikar, "Single-phase liquid friction factors in microchannels," *International Journal of Thermal Sciences*, vol. 45, no. 11, pp. 1073–1083, Nov. 2006, ISSN: 1290-0729. DOI: [10.1016/J.IJTHEMALSCI.2006.01.016](https://doi.org/10.1016/J.IJTHEMALSCI.2006.01.016).
- [235] R. K. Shah and A. L. London, "Chapter VII - Rectangular Ducts," in *Laminar Flow Forced Convection in Ducts*, Academic Press, 1978, pp. 196–222, ISBN: 978-0-12-020051-1. DOI: [10.1016/B978-0-12-020051-1.50012-7](https://doi.org/10.1016/B978-0-12-020051-1.50012-7).
- [236] Gems Sensors, "H-28 Pressure transducer S 31IS Series and 32IS - Technical datasheet," Tech. Rep. [Online]. Available: www.GemsSensors.com.
- [237] Dino-lite, "Edge digital microscope AF4115ZT - Technical datasheet," Tech. Rep. [Online]. Available: <https://www.dino-lite.eu/en/component/eshop/af4115zt-wired?Itemid=0>.
- [238] Pfeiffer Adixen, "Compact multipurpose helium leak detectors ASM 142 series - Technical datasheet," Tech. Rep. [Online]. Available: https://uhvts.com/wp-content/uploads/2018/10/ASM142_Brochure.pdf.
- [239] Rohde & Schwarz, "R&S®HMP4000 Power supply series - Technical datasheet," Tech. Rep. [Online]. Available: https://www.rohde-schwarz.com/us/products/test-and-measurement/dc-power-supplies/rs-hmp4000-power-supply-series_63493-47360.html.

Bibliography

A Introduction to High Energy Physics experiments

The CERN website [215] provides an effective introduction to HEP experiments. Below is a summary of the concepts most relevant to this thesis work.

A.1 The goal of High Energy Physics experiments

The goal of HEP experiments is the understanding of the elementary particles that are the fundamental constituents of matter. The Standard Model (SM) has provided a framework for the interpretation of most particle interactions, but it has also created a foundation from which a deeper level of open questions can begin to be explored, such as the origin of mass, the preponderance of matter over antimatter in the Universe, the identity of "dark matter", the physics of the "Big Bang", and the microscopic structure of space-time.

HEP experiments study the formation of particles as a result of high energy collisions between either two primary particle beams ("collider machines") or between a high energy particle beam and a fixed target ("fixed target experiments"). The type, number and energy of such particles provide the distinctive signature for events of physical interest. Particle physics experiments employ a variety of detectors dedicated to the measurement of different parameters of the emitted particles. Statistical analysis is used to identify events of interest over a radiation background which is often overwhelming. In order to achieve a high statistical significance, high collision rates are required. This translates into high fluxes for fixed-target experiments or high luminosity for collider experiments.

A.2 Hadron and lepton colliders

In a collider experiment, accelerated particles, close to the speed of light, collide in an "Interaction Point" (IP). The "luminosity" at a collider experiment is defined as the number of collisions per unit area per second at a given IP. Luminosity is expressed in units of $\text{cm}^{-2}\text{s}^{-1}$. The luminosity at an IP is directly related to the collision rate seen by the experiment, and

the luminosity tends to be used as a stand-in term for the collision rate. The "integrated luminosity", in turn, is the total number of potential collisions per unit area for a given period of time, and, when multiplied by the cross-section, yields the total number of collisions seen by a given experiment in that time. Usually, it is expressed in the inverse of cross-section (1fb or 1fb^{-1} - femtobarn⁻¹).

Hadron colliders accelerate protons and/or ions, which are at least two thousand times heavier than electrons. Thus, in order to obtain colliding beams where the "centre-of-mass" (CM) energy of each particle should have a certain value E , the "Lorentz factor" E/m needed for the protons will be much less than the one needed for an electron. Therefore, using the same resources, a proton-antiproton pair can be accelerated to much higher CM energy compared to an electron-positron pair. This advantage is counterbalanced by the fact that protons, unlike electrons, are not fundamental particles. Protons are composed by quarks, and therefore the actual collisions occur at the quark level. Since the momenta of individual quarks inside the proton are unknown, when a proton-antiproton collision occurs, the collision energy is not exactly defined. This fact introduces a lot of uncertainty in interpreting the final state particles. Conversely, there is no such problem in a lepton/lepton collision (e.g. electron/antielectron), where the CM energy is uniquely determined by the energy of the colliding particles.

Hadron colliders are a fertile ground for new discoveries, since they allow the formation of heavier particles. Once a new particle is found, an electron-positron machine is usually employed to make precision measurements.

A.3 The Large Hadron Collider and its experiments

The Large Hadron Collider (LHC) [5] is the world's largest and most powerful particle accelerator, located at the European Organization for Nuclear Research (CERN). The LHC is a synchrotron with a 27 km diameter (Figure A.1). The beams inside the LHC are made to collide at four locations around the accelerator ring, corresponding to the positions of the four main LHC experiments: ALICE [6], ATLAS [7], CMS [8] and LHCb [9].

The priority benchmark for the designs of the general-purpose detectors ATLAS (A Toroidal LHC Apparatus) and CMS (Compact Muon Solenoid) was to unambiguously discover (or rule out) the Standard Model Higgs boson for all possible masses up to 1 TeV [217–219]. The challenges for the Higgs search also guaranteed the detectors' potential for many kinds of searches for physics beyond the Standard Model, which was the other driving physics motivation at this energy frontier. From the outset, the LHC was conceived as a highly versatile collider facility. With its huge production of b and c quarks, it offered the possibility to explore flavour physics, which is the main scope of the LHCb (Large Hadron Collider beauty) experiment. Furthermore, during special runs, the LHC provides heavy-ion collisions (Pb-Pb collisions) to study the Quark Gluon Plasma (QGP), the state of matter present in the early moment of the Universe. This is the field of interest of the ALICE (A Large Ion Collider Experiment) experiment.

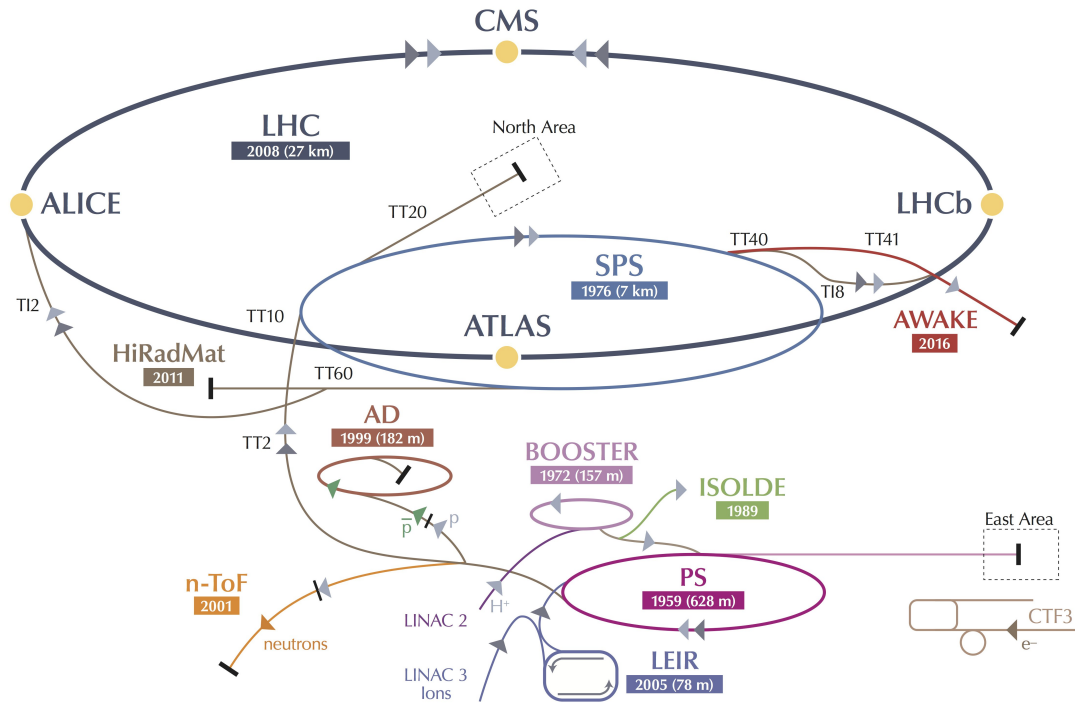


Figure A.1: The CERN accelerator complex. The complex is a succession of machines that accelerate particles to increasingly higher energies. Each accelerator boosts the energy of a beam of particles before injecting it into the next accelerator in the sequence. The LHC is the last element in this chain. The picture is taken from [216].

Particles formed in collisions usually travel in straight lines, but in the presence of a magnetic field, their pathways become curved. To take advantage of this phenomenon, electromagnets placed around particle detectors generate magnetic fields. In this way, the curvature of a particle's path can be used to compute its momentum, which is a clue to its identity: particles with high momentum travel essentially in straight lines, while those with very low momentum move forward in tight spirals inside the detector (Figure A.2).

Modern particle detectors are made out of layers of subdetectors, each of which is designed to look for specific properties or types of particles. Tracking devices reveal the path of a particle; calorimeters stop, absorb and measure a particle's energy; and particle-identification detectors employ a wide range of techniques to determine a particle's identity. As an example, Figure A.3 shows the cutout of the CMS experiment and its main subdetector systems. For a more detailed description of the different types of (sub)detectors, references are provided [220].

Appendix A. Introduction to High Energy Physics experiments

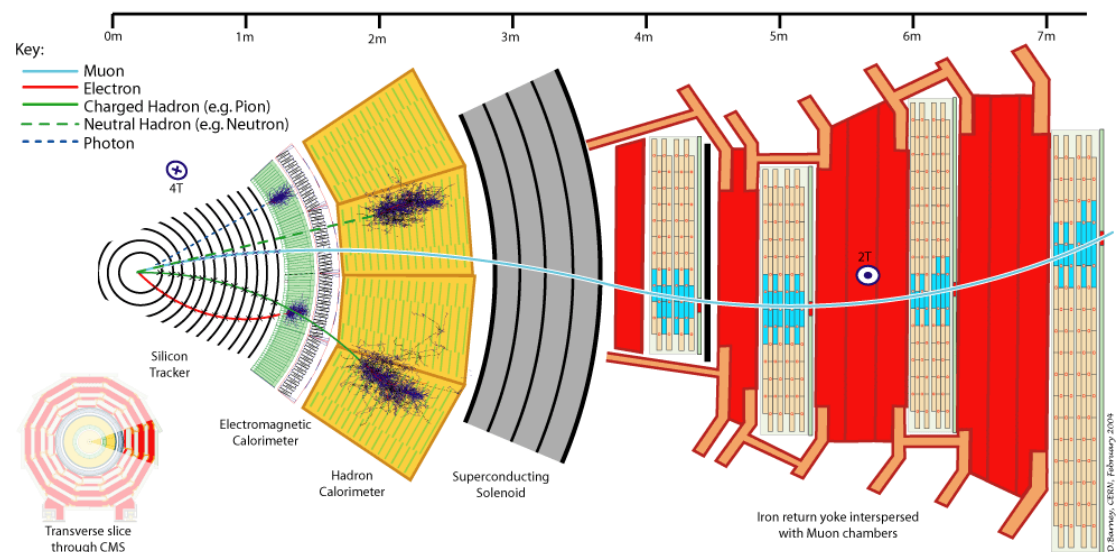


Figure A.2: Slice of the CMS experiment. This slice shows a colorful cross-section of the CMS experiment with five types of particles crossing the sub-detectors. The Picture is taken from [221].

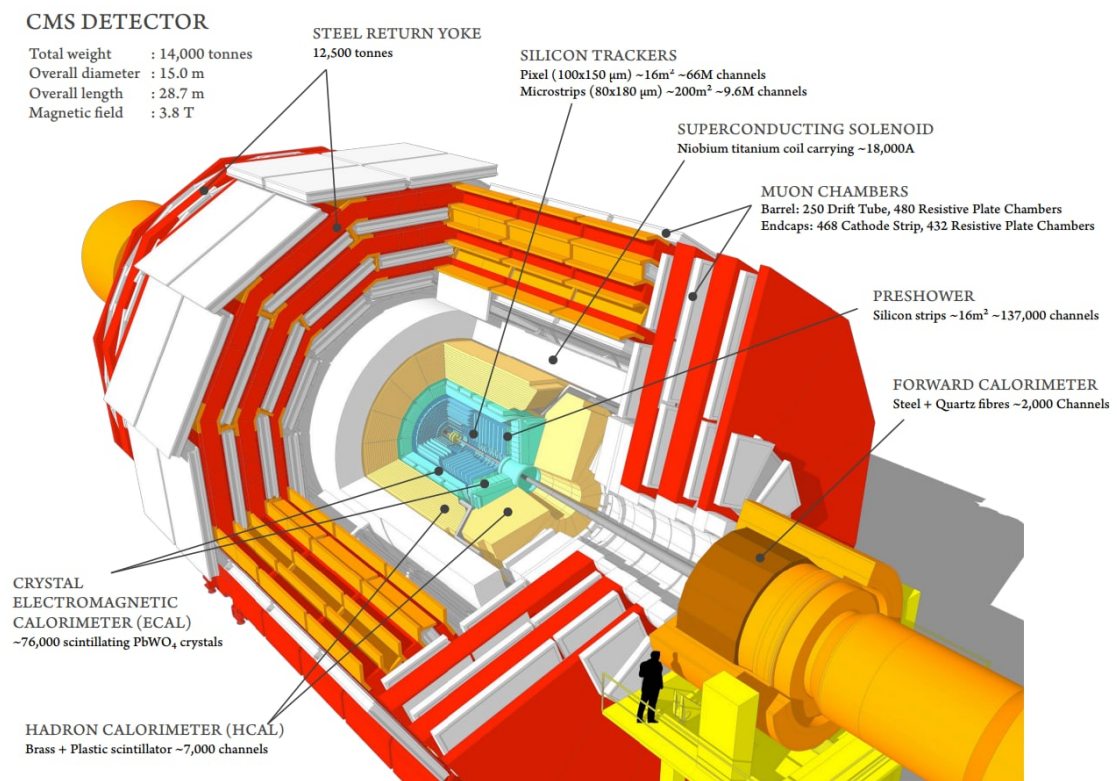


Figure A.3: A cutaway view of the CMS experiment. The CMS detector has several concentric layers of components and is shaped like a cylindrical onion. The Picture is taken from [222].

In LHC experiments, the coordinate system has the origin at the nominal IP, the x-axis pointing to the centre of the accelerator ring, the y-axis pointing up, and the z-axis along the anticlockwise-beam direction (Figure A.4). Cylindrical coordinates (ρ , ϕ) are used in the transverse plane, ϕ being the azimuthal angle around the z-axis. The polar angle θ is measured from the positive z-axis. The pseudo rapidity η is defined as $-\ln[\tan(\theta/2)]$.

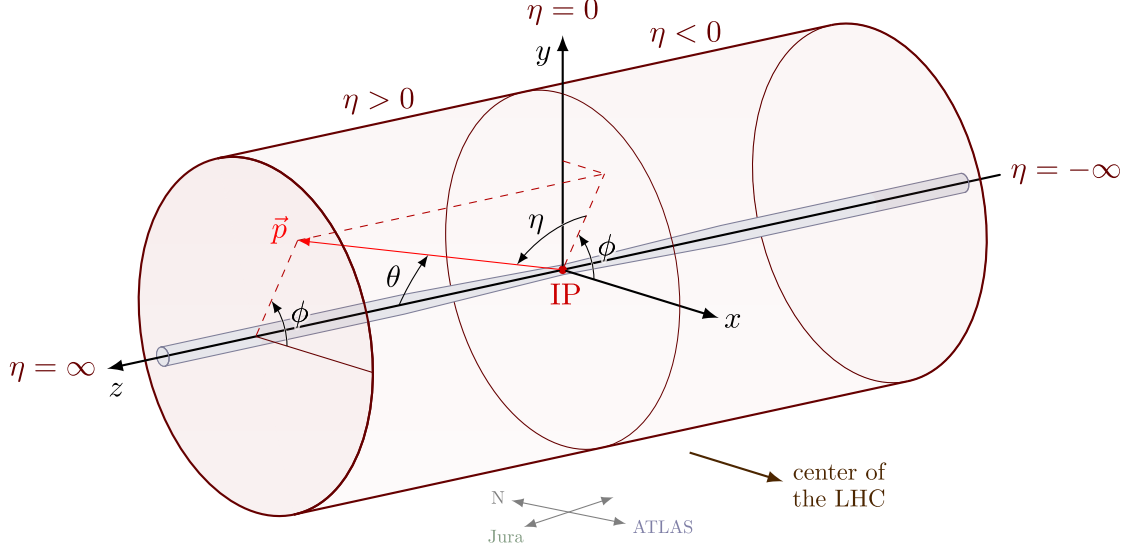


Figure A.4: The coordinate system with the CMS cylindrical detector. The Picture is taken from [223].

The LHC is planned to "run" over the next ~20 years, with several stops scheduled for upgrades and maintenance work. The main experiments' upgrades and maintenance work take place during the "Long Shutdown" (LS) periods. The schedule timeline of the LHC, updated to July 2022 [224], is shown in Figure A.5. The LHC accelerator will be fully upgraded during the LS3.

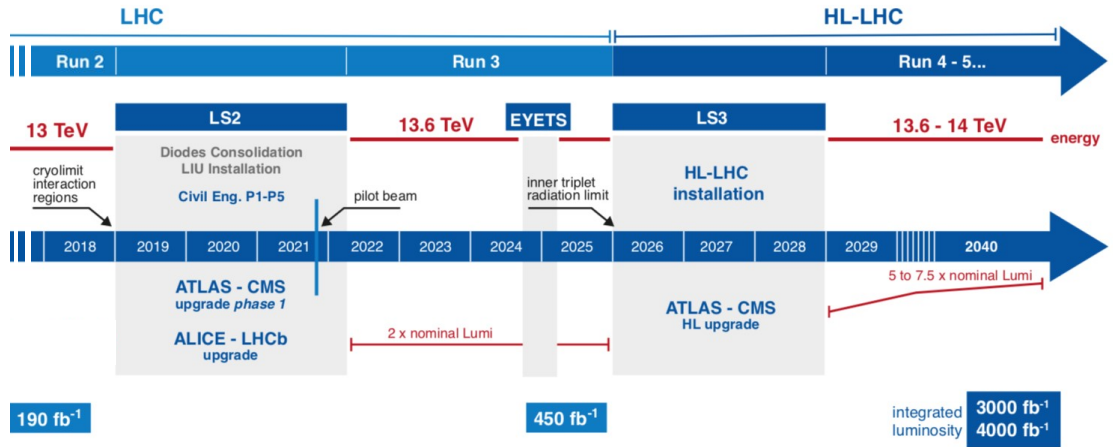


Figure A.5: Upgrade plans of the LHC and its experiments. The High Luminosity Large Hadron Collider (HL-LHC) is an upgrade of the LHC, which aims to achieve instantaneous luminosities a factor of five larger than the LHC nominal value [225, 226]. The picture is adapted from [224].

B Flow distribution optimisation on silicon frame μ CS

B.1 Boiling flow distribution in multi-microchannel configuration

The homogeneous distribution of the fluid in multi-microchannels is essential to achieve optimal performance. For boiling microchannel applications, it is crucial to guarantee that the fluid is equally distributed in the liquid phase throughout the many parallel channels and that boiling occurs only after.

For high-pressure boiling coolants, such as boiling CO_2 , very extreme configurations can be afforded. The pressure drop induced by micro-capillaries introduced at the inlet of the evaporative microchannel causes a predominant pressure drop, which ensures the correct homogeneous distribution of the sub-cooled liquid and protects the circuit from instability phenomena. For a correct triggering of the boiling phase, the dimension of the micro-capillaries (diameter of the restriction) is typically 5 times less than the microchannel dimension.

For low-pressure boiling coolants, such as C_4F_{10} , R134 or R1234yf, the total pressure drop over the entire circuit is limited, as well as the admissible micro-capillary dimensions at the multi-microchannel inlets. In this case, the distribution manifold, which often takes the form of a "*plenum*", is the main responsible for the homogeneous flow distribution to the multi-microchannels that must be guaranteed while ensuring minimum pressure drop.

B.2 Silicon microchannel frame solution for the ALICE ITS2 detector

A silicon cooling solution, based on multi-microchannels, was also proposed during the R&D phase of the present ALICE ITS2 [111, 116, 117] (Section 2.3.2).

The silicon solution was designed to operate with evaporative Perfluorobutane (C_4F_{10}) at ambient temperature. The sensing module to be cooled is composed of an array of 9 Monolithic Active Pixel Sensors (MAPS sensors), namely ALice Pixel DEtector (ALPIDE [19]) sensors, electrically interconnected through wire bonding and a Flexible Printed Circuit (PCB). The maximum power consumption of an ALPIDE sensor ($\sim 30 \times 15 \text{ mm}^2$, $50 \text{ }\mu\text{m}$ thick) is 180 mW,

which corresponds to a power density of about 40 mW cm^{-2} . Most of this power ($\sim 150 \text{ mW}$, $\sim 300 \text{ mW cm}^{-2}$) is dissipated by the digital interface circuitry and the high-speed output data links, which are located in a small area of about $30 \times 1.5 \text{ mm}^2$ close to one long edge (30 mm) of the chip. Only about a sixth of the total power is dissipated in the pixel matrix, which corresponds to a power density of about 7 mW cm^{-2} . Because most of the power is concentrated at the edge of the chip, a frame shape design was proposed for the silicon cooling substrate (see Figure 2.18). It was intended to minimise the material contribution in the detection region (sensor active area) while guaranteeing efficient thermal management. The coolant is supplied to the microchannels integrated into the silicon frame through a feed-line connector while a carbon fibre structure stiffens the assembly.

Interconnected sub-circuits and flow boiling distribution

The coverage of large detection surface ($15 \times 270 \text{ mm}^2$) with an integrated silicon microchannel cooling substrate would have required the fabrication on very large wafers (12 inches). It implies issues with the frame fabrication process and challenges of frame handling during assembly. Furthermore, only a few frames, with 270 mm length, can be produced starting from a 12-inch wafer. This drastically would have affected the unit price making the solution unaffordable.

Therefore, the entire cooling circuit was split into two "*sub-circuits*" interconnected [111]. The two silicon frames (135 mm in length) can then be fabricated on a single 6-inch silicon wafer. The fluid distribution to the different sub-circuits is obtained with the introduction of "*distribution lines*" ("*supply*" and "*return lines*") running in the frame thickness alongside each microchannel sub-circuit (Figure B.1.a). The distribution lines of the nearby frame were intended to be hydraulically interconnected through silicon "*bridge*" [111, 143].

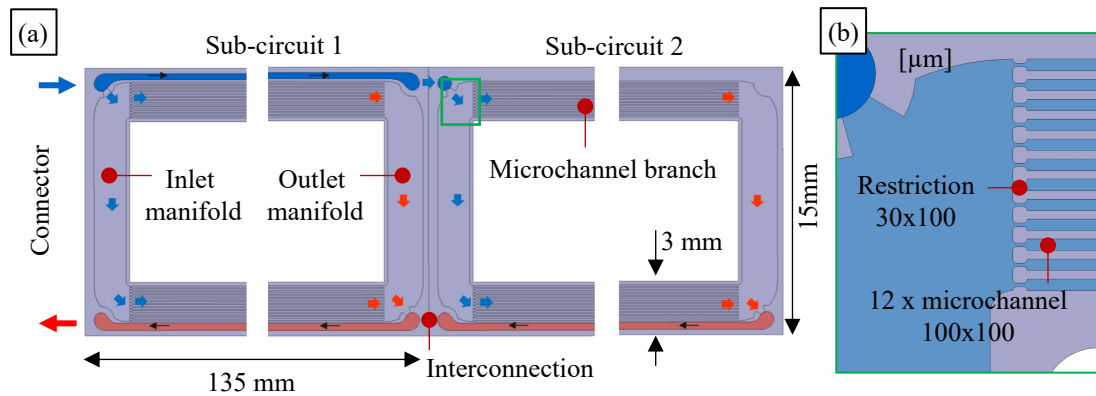


Figure B.1: Layout of the two interconnected microfluidic sub-circuits. (a) Top view of the two sub-circuits and (b) detail of a microchannel branch. The picture is adapted from [117].

The sub-circuit consists of an "*inlet manifold*" to distribute the coolant in the two branches of 12 microchannels each ($100 \times 100 \text{ μm}^2$) confined at the side (3 mm wide). At the end of

the frame, an additional manifold ("*outlet manifold*") recollects the coolant coming from the microchannels [111].

Unfortunately, the sub-circuit and the interconnection concepts introduced new serious challenges:

- Efficient distribution of the refrigerant fluid to multiple devices.
- Complexity in guaranteeing efficient operation of two-phase flow networks.
- Reliability of the hydraulic interconnection for multiple microchannel evaporators.

The solution did not achieve a sufficient level of maturity to be applied for the ALICE ITS2. Nevertheless, preliminary thermal tests demonstrated that the interconnected frame design can successfully remove heat fluxes up to 0.3 W cm^{-2} over the entire sensing module area while keeping the sensor temperature below $30 \text{ }^{\circ}\text{C}$ [116]. The silicon solution over-satisfied the thermal requirements and, therefore, remains an excellent candidate for HEP low-mass applications that operate with low-pressure boiling coolants.

B.3 Purpose of the research

Besides the success of the preliminary thermal tests conducted previously, a non-uniform fluid distribution in the microchannels was detected, which also limited the achievable thermal performances [111].

The leading cause was attributed to the non-optimised distribution manifold at the inlet of the microchannels, which created unbalanced hydraulic conditions; the evaporation in the microchannels, triggered by the restriction and sudden expansion at the inlet, resulted in different boiling flow patterns as well as no boiling or dry-out conditions. This produces flow instabilities and, at the same time, it decreases thermal and hydraulic performances.

The approximative design for the distribution manifold seemed functional but brought significant flaws. It was, therefore, decided to analyse the manifold, searching for potential design elements that caused the unbalanced flow distribution and, possibly, optimising the manifold geometry to achieve a more homogeneous flow and reduce pressure losses.

The optimisation of the manifold design was supported by inherited Computational Fluid Dynamics (CFD) simulations performed by C. Rossi [227]. The main outcomes of these CFDs (performed with ANSYS CFX [175]) are here below described (Section B.4).

My contribution to this research was to produce samples and experimentally validate the optimisation.

B.4 CFD analysis of the flow distribution inside the inlet manifold

The aim of the CFD was to investigate the localised pressure drop at the inlet of the two microchannel branches. The microbridge area, the inlet manifold area and the initial 2 mm portion of microchannels were examined for a consistent evaluation of the fluid behaviour. Single-phase C_4F_{10} at room temperature (20 °C) was considered, and different mass flow rates, varying from 0.1 g/s to 0.5 g/s with 0.1 g/s steps, were inspected. The average static relative pressure at the microchannel outlet was set to 0 Pa.

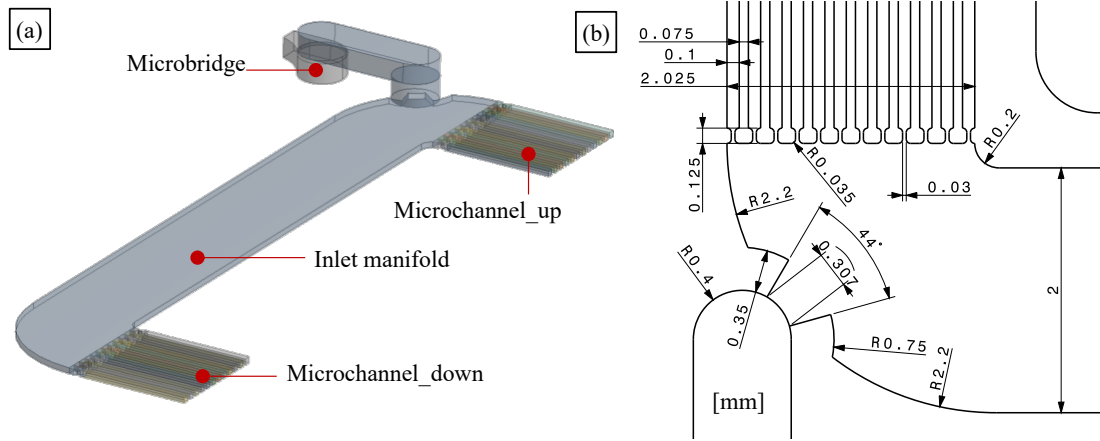


Figure B.2: The fluid domain of the CFD simulation. (a) Fluid domain and (b) detail of the dimensions at the outlet of the microbridge. The CFD simulations were performed with ANSYS CFX R15.0 software [175]

The device was designed for two-phase fluids where evaporation occurs exclusively in the microchannels. However, finite volume (or finite difference) models for two-phase flow are more complex and depend on various parameters.

For a preliminary assessment, the calculation was made in single-phase, assuming that, in first approximation, a pressure loss reduction for a single-phase fluid corresponds to a pressure loss reduction for a two-phase fluid. The analysis validated the proper working of the inlet manifold in single-phase conditions.

The extrapolation of these results to two-phase fluids requires a further assessment based on the additional process complexity that relies on the restriction to guarantee the correct evaporation triggering and to avoid back-flow.

To understand the causes of pressure loss, an investigation of the streamlines was done (Figure B.3). The simulations highlighted several problems:

- The flow was detached from the manifold wall in different regions, and several re-circulation areas were visible in the manifold.
- The velocity at the microchannel outlets was unevenly distributed in the upper section.

B.4 CFD analysis of the flow distribution inside the inlet manifold

The lower microchannel section showed a maximum velocity of 1.24 m/s, while for the upper section, the range was higher, with a maximum of 5.6 m/s.

- The average velocity at the outlet of the microbridge was evidently too high (around 10 m/s), and a jet was clearly visible.

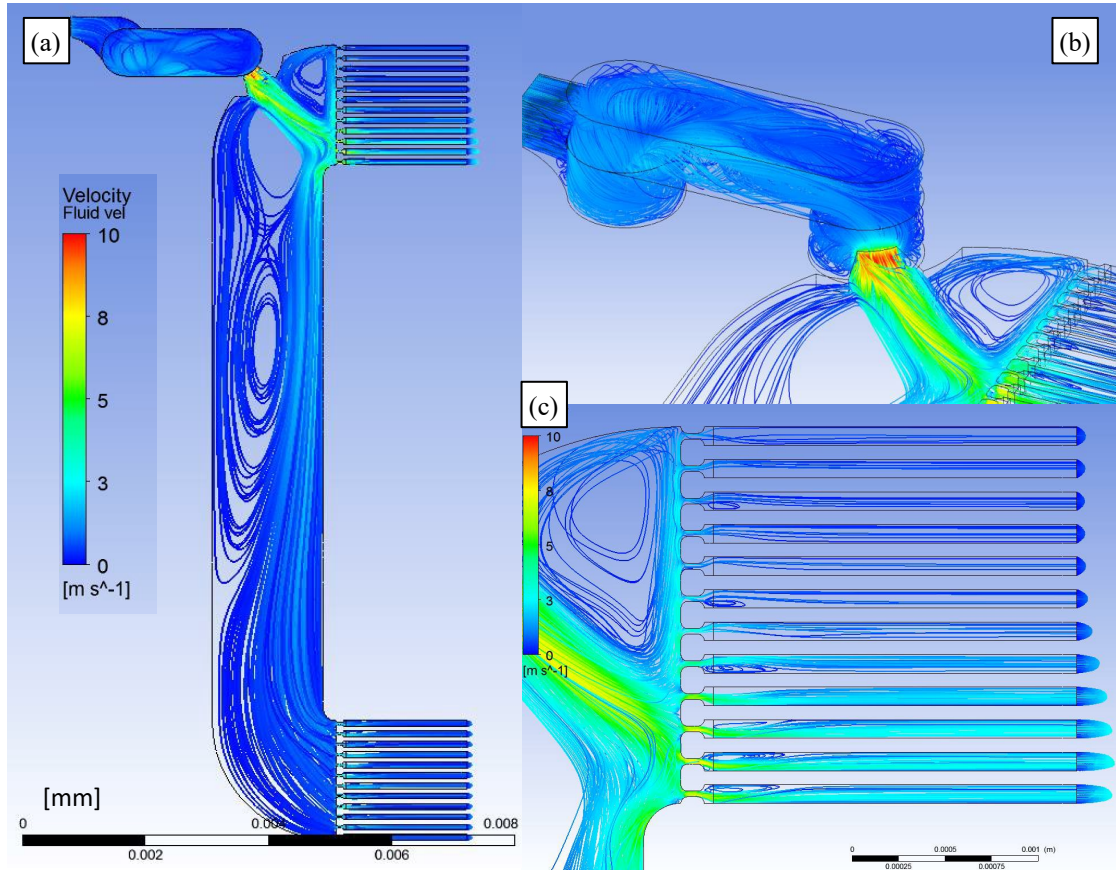


Figure B.3: CFD results of the baseline geometry. (a) Fluid velocity in the CFD volume for a 0.3g/s mass flow, (b) detail of the flow velocity at the outlet of the microbridge and (c) in the upper microchannels.

The geometry of the manifold was therefore redesigned to delay flow separation, maximise the laminar flow and keep the local flow along the wall for as long as possible. The manifold geometry was adjusted to a more aerodynamic shape according to the 23021 NACA aerofoil profile (see Figure B.4).

In addition, to better direct the flow and ensure that the transition from the microbridge to the manifold was less abrupt, the microbridge connection to the manifold was modified so as to have a larger outlet, 0.8 mm in diameter, and to avoid the bottleneck. CFD simulations were repeated for this new geometry with the same boundary conditions.

The results are shown in Figure B.5. The streamlines were also plotted again to see if the new geometry improved the flow distribution in the manifold and the microchannels. The

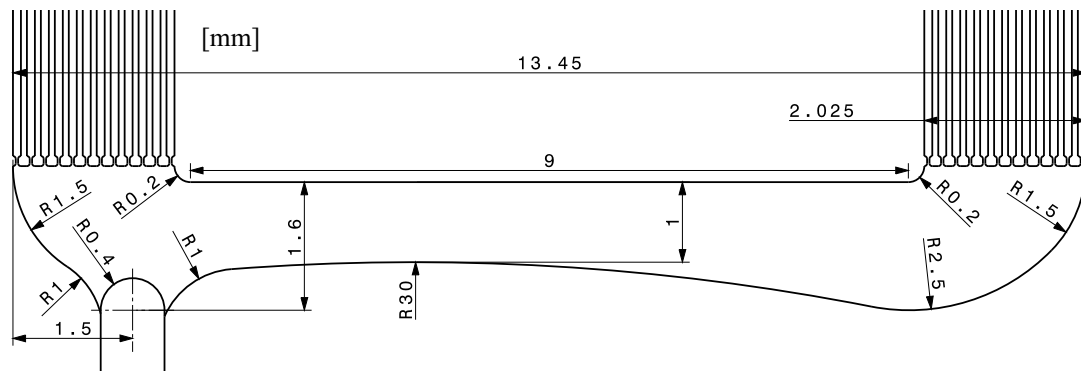


Figure B.4: Design of the new manifold according to the 23021 NACA aerofoil profile. The design, based on the low-drag five-digit symmetric NACA profile 23021 [228], was modified to ensure a less abrupt transition from the bridge to the manifold.

recirculation areas were nearly eliminated, and the average velocity was reduced (0.70 m/s for 0.3 g/s).

The flow distribution in the microchannels was also more uniform, as can be seen in Figure B.5.b and Figure B.5.c. The maximum velocity for the microchannel upper section was 1.6 m/s, while for the lower section, the maximum was 1.3 m/s.

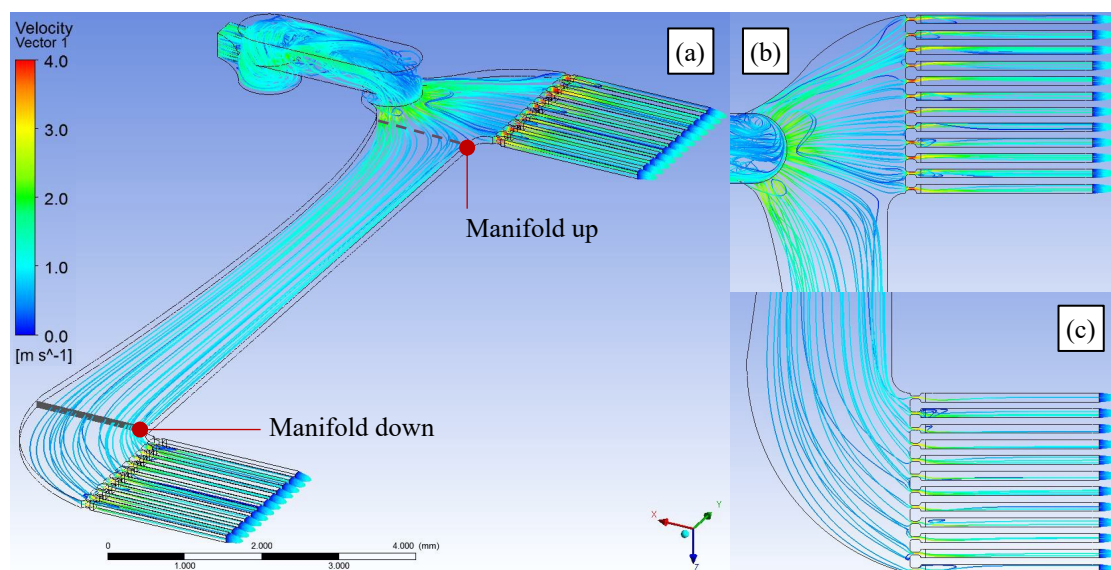


Figure B.5: CFD results of the optimised geometry. (a) Fluid velocity in the new fluidic domain of the CFD simulation for a 0.3g/s mass flow and (b-c) detail of the flow velocity at the microchannels.

Due to the absence of re-circulation areas, it was also possible to estimate the pressure drop in the manifold to evaluate the impact of the manifold pressure loss on the overall pressure drop. The total pressure and static pressure drops were thus estimated between the cross-section “ $manifold_{up}$ ” and “ $manifold_{down}$ ” (Figure B.5).

B.4 CFD analysis of the flow distribution inside the inlet manifold

The two types of pressure drops are shown in Figure B.6.a. As expected, the pressure drops increased with the mass flow rate; however, they were negligible compared to the total pressure drop in the entire inlet manifold.

In first approximation, the total pressure can be found by summing the static pressure (0 Pa) to the dynamic pressure estimated from the average fluid velocity in the steady-state condition.

Figure B.6.b shows the total pressure loss related to the two inlet manifold geometries. It was calculated by subtracting the total pressure at the outlet of the microchannel from the total pressure at the outlet of the microbridge. The total pressure loss in the manifold with the optimised geometry was between 3-7 times less than in the manifold with the baseline geometry.

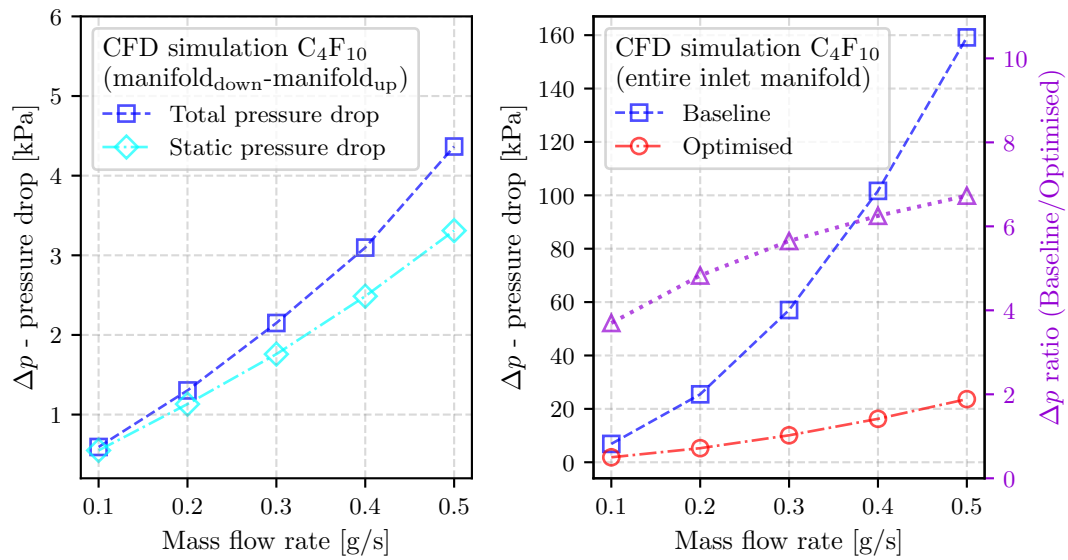


Figure B.6: Pressure losses in the inlet manifolds: (a) Pressure drop between the manifold_{up} and manifold_{down} for the optimised design. (b) Total pressure drop comparison between the baseline and the optimised designs. The violet dashed line in figure (b) refers to the ratio between the pressure drops in the two different manifolds (the baseline and the optimised inlet manifolds).

B.5 Method

The optimisation was validated by producing Si samples implementing one of the two different manifold designs in the microchannel circuit: the baseline and the optimised one. To keep the focus on the study of the manifold, the design of the validation samples does not consider the distribution to other sub-circuits; therefore, each sample has only one sub-circuit with its own connector. The Si samples were fabricated in the class 100 (ISO5) MEMS cleanroom at the EPFL (École Polytechnique Fédérale de Lausanne) Centre of MicroNanoTechnology (CMi) in Lausanne (Section B.6).

To optical inspect and highlight the flow distribution inside the two different manifolds, fluorescence fluid and demineralised water were used to feed the samples asynchronously (Section B.7).

After that, pressure drop tests with only demineralised water were conducted to quantify the design improvement in single-phase conditions. The tests were performed at CERN in the ALICE ITS2 clean room. Finally, the pressure loss reduction, due to the manifold optimisation, was analysed and compared with the CFD estimation (Section B.8).

B.6 Production and assembly of the test samples

The Si frame samples (Figure B.7), 15 mm wide and 70 mm long, were produced starting from 380 μ m thick 4-inch silicon wafers (p-type, <100>). The circuit was fabricated by photolithography and Deep Reactive Ion Etch (DRIE) techniques. The main steps of the process-flow are summarised in Figure B.8.

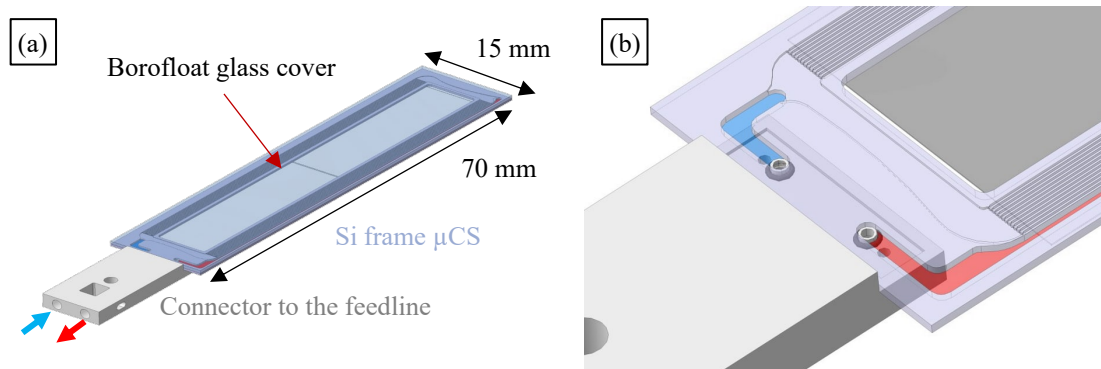


Figure B.7: CAD design of the sample for the test. (a) CAD design of the sample assembled with the connector and (b) detail of the interconnection. In Figure (b), the borofloat glass cover is not displayed.

The two different Si samples (implementing either the baseline manifold or the optimised manifold) were fabricated on the same Si wafer to minimise differences linked to the production process (Figure B.9). Additional features, called “*dummy frames*”, were inserted in the wafer layout and were used to quantify the pressure drop contribution due to the connector.

B.6 Production and assembly of the test samples

For visual inspection, the etched silicon wafer was subsequently anodic bonded to a borosilicate glass wafer cover instead of silicon (Figure B.9.a). After that, the inlet (outlet) holes were opened from the silicon side. This allowed control and inspection of the bonded interface between the connector and the Si circuit sample during the gluing. This step was performed under an optical microscope. The inner part of a Si sample was also removed during the opening of the holes (Figure B.9.b and Figure B.8 step 12). Finally, the wafer was diced, and the circuit samples were ready for assembly.

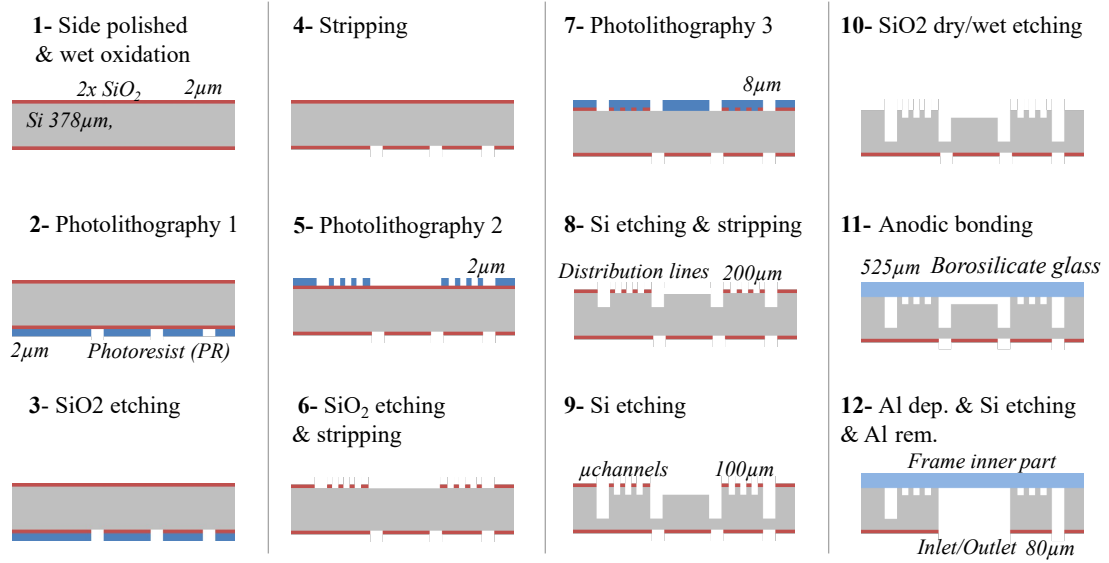


Figure B.8: Main steps of the process-flow for the production of the samples. The process flow starts from the top-left and ends at the bottom-right.

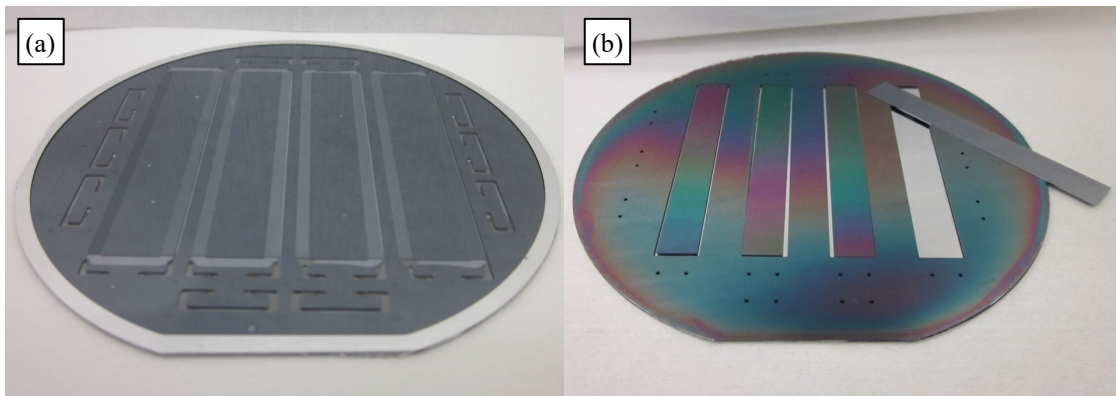


Figure B.9: Silicon wafer with embedded the microchannel circuits: (a) Si wafer anodic bonded to the borosilicate glass and (b) a second bonded wafer after etching of the inner part of the frames.

The manifolds and the microchannels are 100 μm deep, while the distribution lines are 300 μm deep. The microchannels have a width of 100 μm and an inlet restriction of 30 μm . The distribution line is 400 μm wide. Two "protrusion lines" allow the fluid to pass from the connector to the microchannel circuit and vice-versa. The shape of the outlet manifold is a

mirror image of the inlet manifold (Figure B.10). The nomenclature of each circuit element is in Figure B.11.

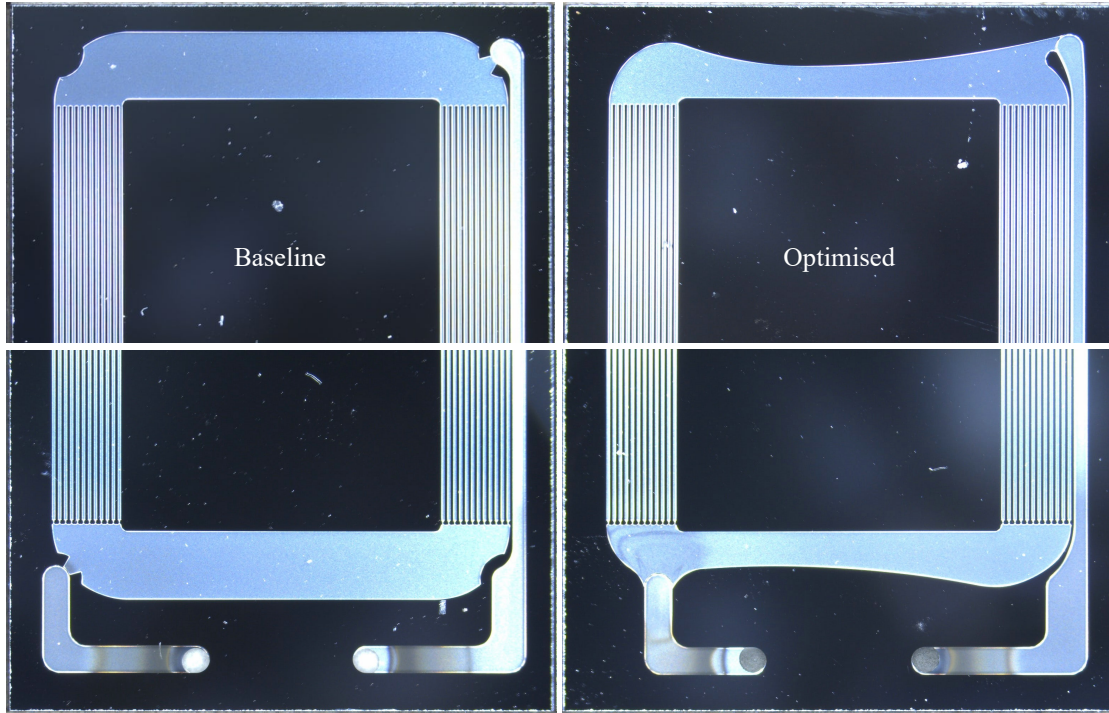


Figure B.10: Details of the samples with the two different circuits. The two circuits in the samples differ in the geometry of the inlet and the outlet manifolds.

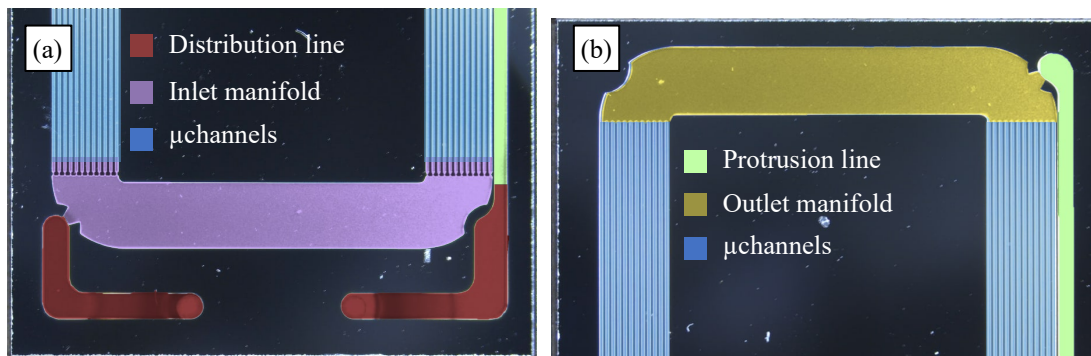


Figure B.11: Nomenclature of the circuit elements. (a) Inlet and (b) outlet elements. The two branches of microchannels are displayed in both pictures.

The samples were then glued to 3D-printed connectors. The connectors were produced by stereolithography (SLA) process, and in ACCURA25 epoxy resin [168]. Details of the interface between the connector and the silicon sample are in Figure B.12, while details of the assembly procedure are in Figure B.13. Two channel "protrusions" in the connector were designed to fit inside (with 0.1 mm of depth) the two holes present in the silicon substrate and act as a self-alignment feature during the assembly (Figure B.12.b). At the same time, a frame in the connector and two micro O-rings, engaging the two protrusions, prevent the gluing deposition

in the substrate circuit (Figure B.13.a). Unfortunately, assembly difficulties were found during the connector and the Si sample alignment, mainly due to the accuracy of the 3D printed connector ($\pm 50 \mu\text{m}$), which impacted the self-alignment features (the protrusions). Therefore, an auxiliary devoted alignment jig was used (Figure B.13.d). Reliable sealing was achieved for all the glued samples (He leak rate $< 10^{-9}$ mbar l/s, Vacuum $\sim 10^{-3}$ mbar).

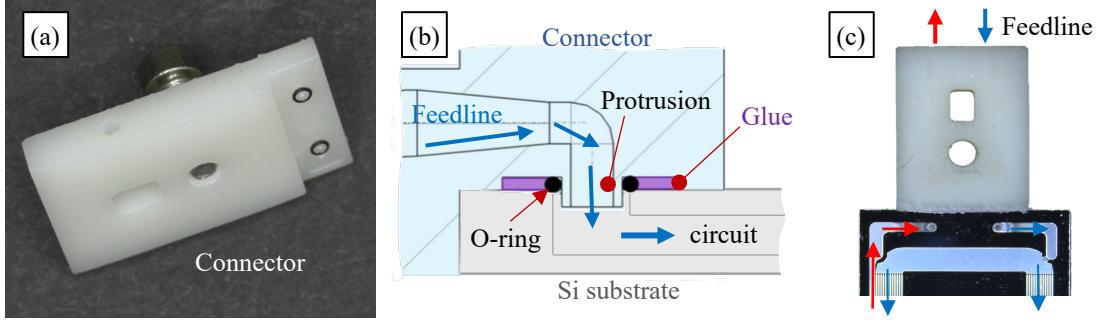


Figure B.12: Interface between the connector and the Si frame sample. (a) Detail of the connector with O-rings in position, (b) schematic view of the glued interface and (c) detail of a glued sample.

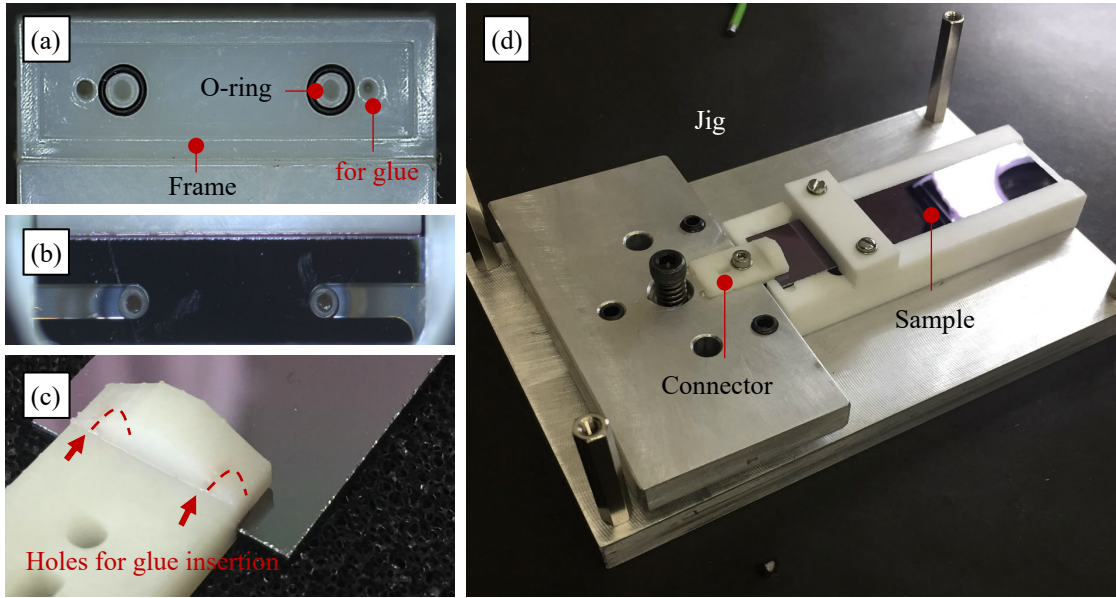


Figure B.13: Assembly details of the 3D printed connector and the Si sample. (a) Detail of the connector (hole for the glue insertion, protrusions with their O-rings engaged and connector frame) at the interface with the silicon sample, (b) detail of the interface between the connector and the silicon sample taken from the glass cover side, (c) detail of the channels for the glue insertion and (d) alignment jig. The glue used at the interface was Araldite2020 [229] because of its low viscosity (150 mPas). The glue was injected into two dedicated channels (a and d), embedded in the connector. The two dedicated channels have a diameter of 0.4 mm. The assembly and the alignment were done by using a devoted jig (c) under an optical microscope (b). The outer diameter of the protrusion is 0.7 mm, while the diameter of the holes in the silicon is 0.8 mm. The O-ring (nitrile rubber material) has a diameter of 0.4 mm, an inner diameter of 0.7 mm and a cross-section diameter of 0.2 mm. The sample shown in Figure (d) does not have the inner part removed.

B.7 Flow distribution inspection

The test set-up used to optical inspect the flow distribution inside the two samples, with the two different manifold geometries, is shown in Figure B.14 and in Appendix C. It is constituted by two supply lines with two different fluids each, a green fluorescent liquid (EKWB EK-CryoFuel Solid Premix [230]) and demineralised water. The two supply lines converge at the inlet of the connector. The two fluids were injected asynchronously, one after the other. The samples were exposed to UV lights during the inspection to highlight the liquid path.

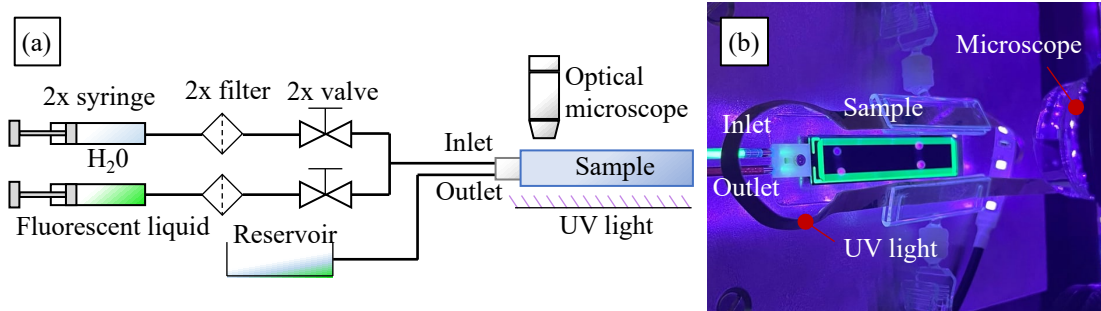


Figure B.14: Set-up for the flow distribution inspection. (a) Sketch of the set-up and (b) a sample illuminated with UV light (strip lights) during the inspection. The two fluids (fluorescent liquid and water) are pumped inside the samples by syringes. Two filters, with 30 μ m porous size, were inserted in the supply lines to minimise microchannel contamination. A return line connected to a recipient collects the mixture of the fluids. An adjustable digital microscope was used to examine the sub-circuits.

Images of the two sub-circuits are shown in Figure B.15. As already anticipated by the CFD simulation, a jet appeared at the inlet manifold based on the baseline manifold geometry (Figure B.15.a). For the optimised manifold geometry, almost evenly distributed flow lines that serve the different microchannels were detected as a demonstration of the improved uniform flow distribution (Figure B.15.b).

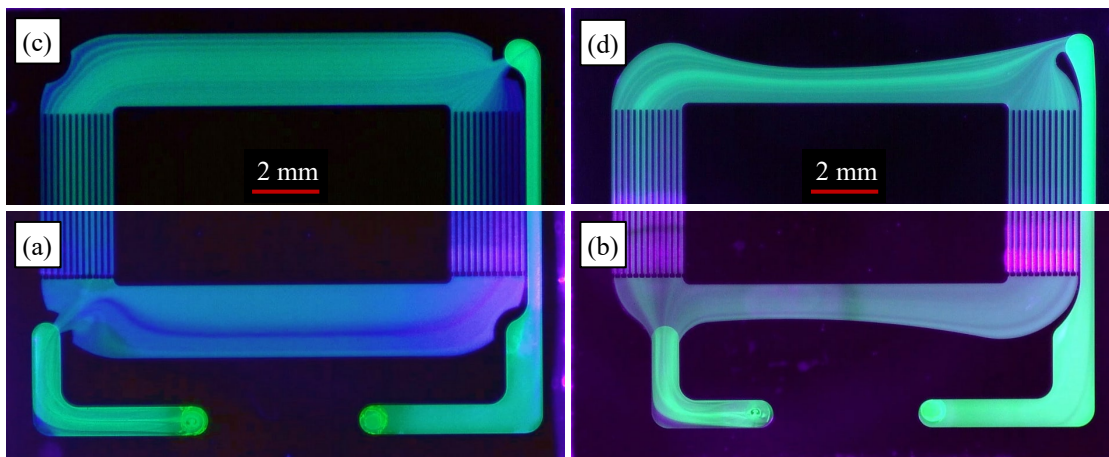


Figure B.15: Inspection of the flow distribution inside the manifolds. (a-b) Pictures of the two inlet manifolds (baseline and optimised) and (c-d) pictures of the two outlet manifolds (baseline and optimised).

B.8 Pressure test results and analysis

B.8.1 Pressure test campaign

Demineralised water ($T = 20\text{ }^{\circ}\text{C}$) was used to evaluate the single-phase pressure drops in the two circuits. The pressure drop was evaluated for different mass flow rates. Once the steady state condition was achieved for the mass flow rate under investigation, the average value of the pressure drop over 1 minute of the test was kept. This minimises the fluctuation effect of the pressure sensor. Firstly, a pressure drop test campaign for the connectors, assembled with the "dummy frames" (Figure B.16), was performed. The results are in Figure B.17.

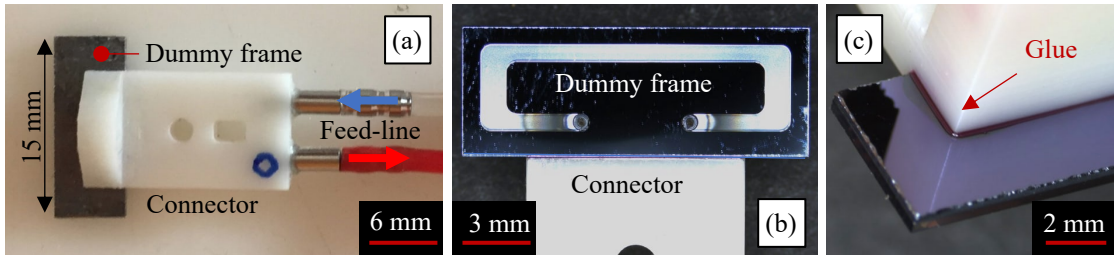


Figure B.16: Details of the connector assembled with the dummy frame. (a) glued connector, (b) view of the dummy frame circuit from the glass cover and (b) detail of the glued interface.

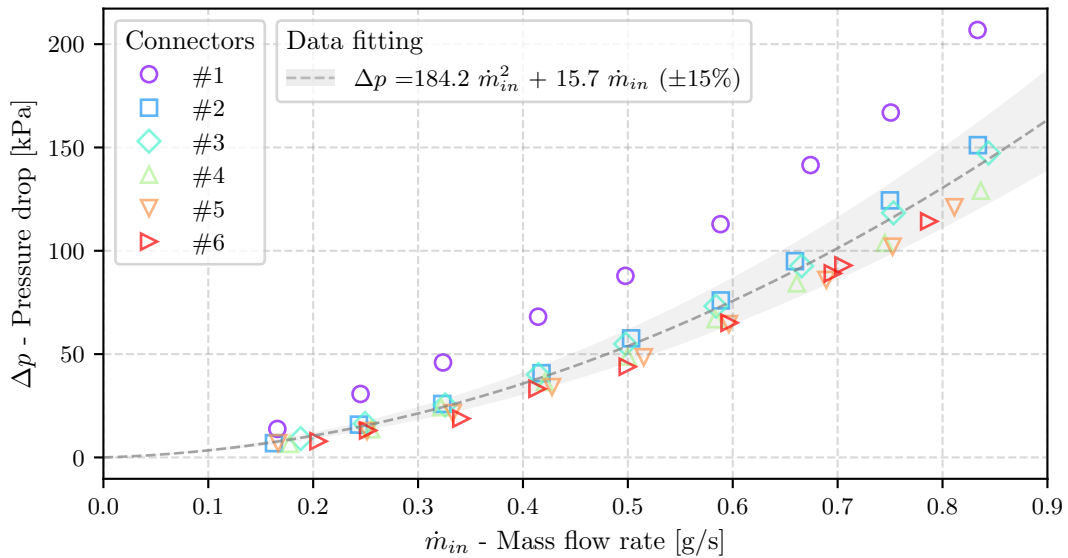


Figure B.17: Results of the pressure drop test for the connectors. The pressure drop of the connectors is plotted as a function of the mass flow rate. The connector number #1 had a visible obstruction in one of the protrusion channels (see Figure B.12). The results of the remaining connectors (from #2 to #6) were fitted. The mass flow sensor used is the Coriolis flowmeter Bronkhorst mini CORI-FLOW M14 [231], and it is positioned at the inlet line. Its flow rate ranges from 0.03 to 2.78 g/s with an accuracy of $\pm 0.2\%$ of the rate ($< \pm 0.01\text{ g/s}$). Two absolute pressure sensors (Huba Control 511-930201041w [232]) were positioned at the connector inlet and outlet. They measure the pressure drop in the range of 0-1000 kPa (0-10 bar) with an accuracy of 0.5% full scale (FS), corresponding to $\pm 5\text{ kPa}$ ($\pm 0.05\text{ bar}$).

Appendix B. Flow distribution optimisation on silicon frame μ CS

The pressure drop in the connectors (Δp) had a quadratic dependence behaviour with respect to the mass flow rate (\dot{m}_{in}) because of concentrated losses coming from the elbows present in the connectors. The dependence was modelled (Equation B.1 and Figure B.17) and was used to remove the connector pressure drop contribution to the total pressure drop in the circuits.

$$\Delta p[\text{kPa}] = 184.2 \dot{m}_{in}^2 + 15.7 \dot{m}_{in} \quad (\text{B.1})$$

In the above equation, \dot{m}_{in} is expressed in [g/s] while Δp is expressed in [kPa]. The pressure drop tests were performed on both circuits equipped with the same connectors (Figure B.18). Figure B.19 shows the pressure drop test results for the two different geometries.

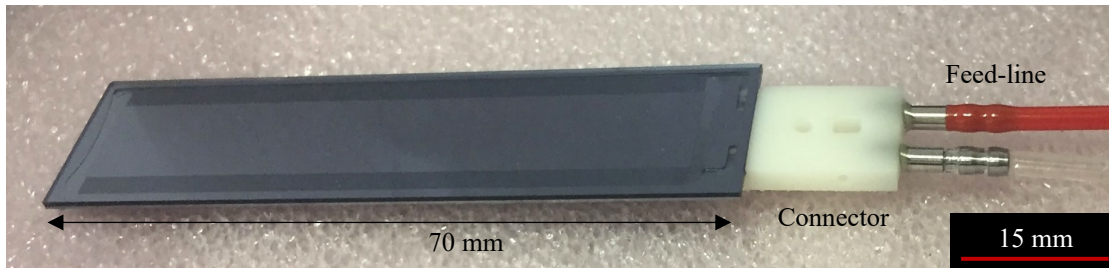


Figure B.18: Circuit sample assembled with the connector. The sample shown in the figure does not have the inner part removed (no frame shape). The circuit in the sample has the optimised geometry for both the inlet and outlet manifolds.

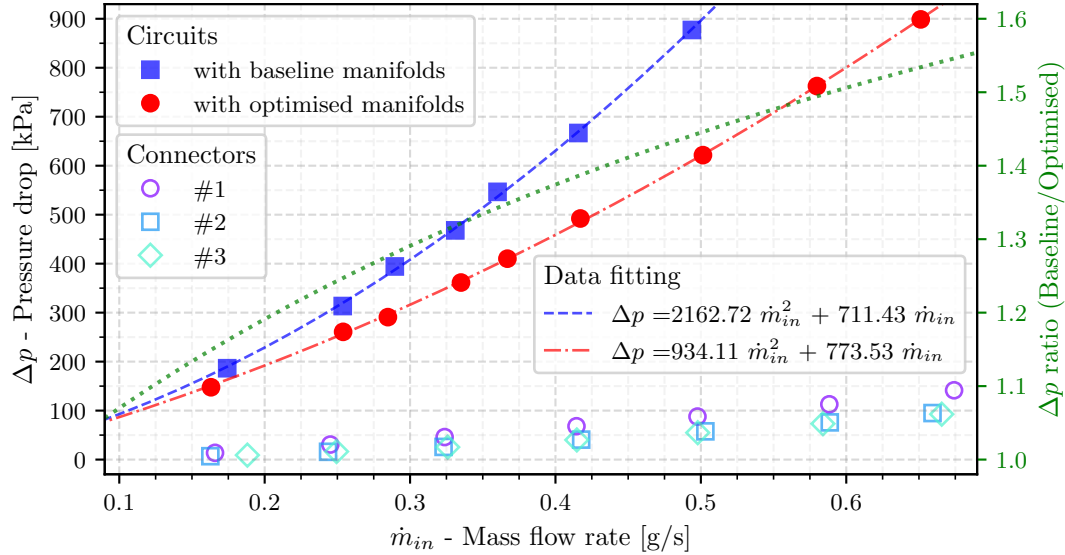


Figure B.19: Results of the pressure drop test for the two different circuits. The pressure drop in the two different circuits is plotted as a function of the mass flow rate. For comparison, the pressure drops in three connectors are also plotted. The ratio between the pressure drops in the baseline and in the optimised circuits increases with the mass flow rate increase. It varies from 1 to 1.55 (green line and Y-axis). The sensors utilised for the pressure drop measurement are the same employed in the previous pressure tests of the connectors (Figure B.17).

As expected, the optimised geometry brought to a lower pressure drop than the baseline one. The pressure drop in the connector is almost one order of magnitude less (Figure B.19). Therefore, a possible variation in the connector quality did not significantly affect the results.

The test campaign qualitatively confirmed the numerical prediction; for a mass flow rate of 0.5 g/s, the pressure drop in the new circuit geometry is 250 kPa (2.5 bar) less than in the baseline one. For a mass flow rate varied from 0.15 to 0.5 g/s, the pressure drop in the optimised circuit was in the range of 150-600 kPa (1.5 - 6 bar).

In the first approximation, the pressure drop in the manifolds only (baseline and optimised) were quantified by subtracting the pressure losses related to the different circuit elements (nomenclature in Figure B.11) from the measured pressure drops of the circuits (baseline and optimised). The distributed pressure losses related to the microchannels and the distribution line were analytically estimated while the pressure drop in the connector & protrusion line were extrapolated from the previous characterisation test (Equation B.1).

B.8.2 Analytical estimate of the microchannel and distribution line pressure drops

The flow in the two circuit elements, the 24 parallel microchannels and the distribution line, is liquid (single-phase) in developing and fully developed laminar regimes.

The influence of the wall roughness on the pressure drop for laminar, fully developed liquid flow can be neglected when the relative roughness, i.e. the ratio between the root mean square (RMS) roughness (Rq) and the hydraulic diameter (D_h) is less than 3% [233]. The Rq of typical DRIE etched channels is $\ll 1 \mu\text{m}$.

The two distributed pressure losses were, therefore, estimated with the Steinke and Kandlikar correlation [234], which takes into account the contribution of both the developing and the fully developed regions:

$$\Delta p = 2f \frac{L}{D_h} \rho \bar{v}^2 + \frac{1}{2} k(\infty) \rho \bar{v}^2 \quad (\text{B.2})$$

where $L[\text{m}]$ is the channel length, $D_h[\text{m}]$ is the hydraulic diameter, $\bar{v}[\text{m/s}]$ is the average velocity, ρ is the fluid density $[\text{kg/s}]$, f is the Fanning friction factor in fully laminar developed flow, while $k(\infty)$ is the Hagenbach factor which takes into account the contribution of the developing region to the pressure drop at the entire channel length.

The hydraulic diameter of any channel cross-section can be calculated as follow:

$$D_h = \frac{4A}{p} \quad (\text{B.3})$$

where $A [\text{m}^2]$ and $p [\text{m}]$ are the area and perimeter of the channel cross-section, respectively.

Appendix B. Flow distribution optimisation on silicon frame μ CS

The average velocity \bar{v} [m/s] in a channel is calculated by:

$$\bar{v} = \frac{\dot{m}}{\rho A} \quad (\text{B.4})$$

where \dot{m} [kg/s] is the mass flow rate at the channel. In the circuits under investigation, the total mass flow rate (\dot{m}_{in} [kg/s]) is parallel split into the two branches of 12 microchannels each. In addition, the mass flow is not equally distributed in the microchannels, especially for the baseline circuit (Figure B.15). Nevertheless, the average mass flow rate in a single microchannel ($\dot{m}_\mu = \dot{m}_{in}/24$) can be utilised for a first estimation of the microchannel pressure loss.

The Fanning friction factor, defined as the ratio of the wall shear stress to the flow kinetic energy per unit volume, can be evaluated through the dimensionless Poiseuille number, $Po = f Re$. Where Re is the dimensionless Reynolds number, corresponding to the ratio of inertia forces to viscous forces. For single-phase laminar flow and rectangular channel cross-section, the Poiseuille number is constant, and it can be determined using Equation B.5 from Shah and London [235]:

$$Po = f Re = 24 (1 - 1.3553\epsilon + 1.9467\epsilon^2 - 1.7012\epsilon^3 + 0.9564\epsilon^4 - 0.2537\epsilon^5) \quad (\text{B.5})$$

where ϵ is the channel aspect ratio, defined as the channel width, a , divided by the channel height, b . The fully developed Hagenbach factor, $k(\infty)$, for rectangular channels also depends on ϵ and it can be determined by Equation B.6:

$$k(\infty) = (0.6796 - 1.2197\epsilon + 3.3089\epsilon^2 - 9.5921\epsilon^3 + 8.9089\epsilon^4 - 2.9959\epsilon^5) \quad (\text{B.6})$$

The different parameters influencing the pressure drop in the microchannels and the distribution line are summarised in Table B.1.

Table B.1: Parameters to estimate the pressure drops of the circuit elements. The two circuit elements, the microchannel and the distribution line, are visible in Figure B.11. The pressure drop contribution of the developing region, i.e. coming from $k(\infty)$, to the entire pressure drop in the microchannel is between 0.2-1.4%. In the distribution line this contribution is between 4-22%.

Circuit element	a [mm]	b [mm]	L [mm]	D_h [mm]	ϵ	$Po = f Re$	$k(\infty)$
microchannel	0.1	0.1	57	0.1	1	14.23	1.53
protrusion line	0.4	0.3	63	0.343	0.75	14.48	1.52

Figure B.20 shows the different contributions to the total pressure drop with respect to the optimised circuit, while Figure B.21 shows the losses of the manifolds (inlet and outlet) only. The pressure drop of the manifolds was quantified by subtracting the pressure losses of the different circuit elements from the pressure drop of the entire circuits (Figure B.19).

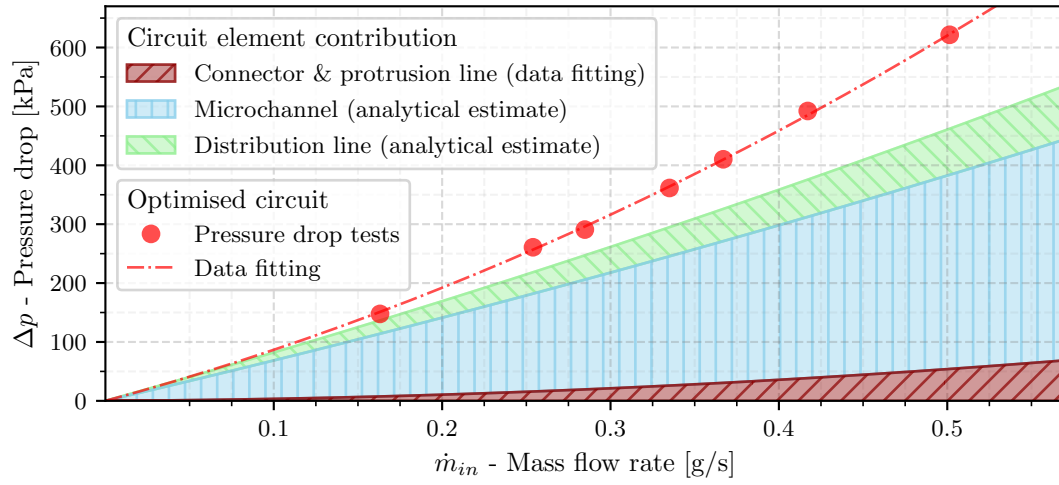


Figure B.20: Pressure drop estimation of the different circuit elements. The different circuit elements refer to Figure B.11. The pressure drop in the connector & protrusion line was estimated from Equation B.1, while the pressure drops in the microchannel and in the distribution line were analytically estimated by Equation B.2 (parameters in Table B.1).

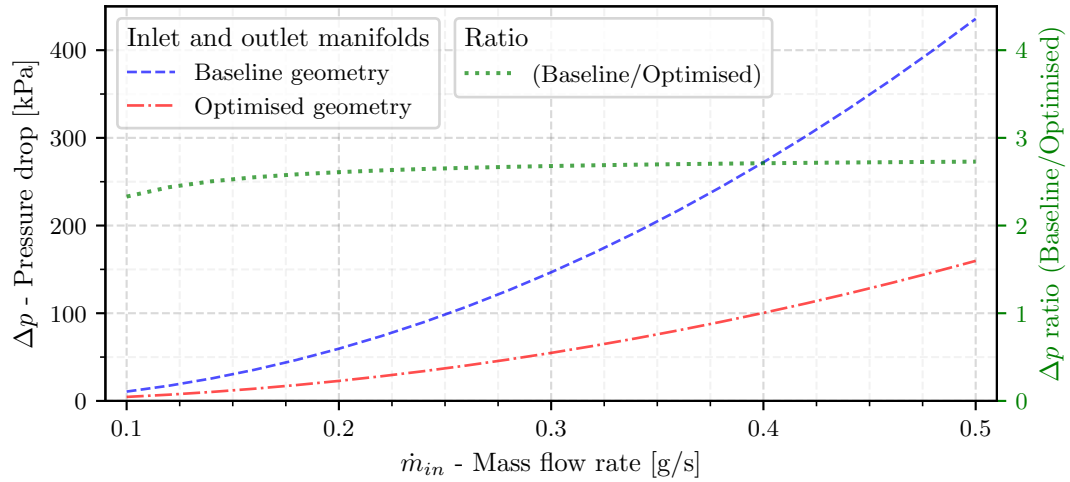


Figure B.21: Estimation of the pressure drop in the manifolds. The pressure drop in the manifolds was extrapolated by subtracting the contribution of each circuit element (Figure B.20) to the total pressure drop in the two circuits (Figure B.19). The dashed green line represents the ratio between the pressure drops in the baseline and in the optimised manifolds (inlet and outlet).

B.8.3 Comparison between the CFD and the experimental results

From the result of the tests, the ratio between the pressure drops in the baseline and in the optimised manifolds (inlet and outlet) was ± 2.8 (Figure B.21). From the CFD estimation, the ratio between the pressure drop in the two different inlet manifolds only was 4-7 (Figure B.16).

Appendix B. Flow distribution optimisation on silicon frame μ CS

Unfortunately, the CFD analyses and the test results cannot be directly compared as the experimental results refer not only to the inlet manifold but also to the outlet manifold. In addition, the fluid considered in the CFD analysis was C_4F_{10} while the tests were performed with water.

Nevertheless, additional information can be extrapolated through fluid dynamic similarity. In flowing a liquid (single-phase) through a completely filled pipe, gravity has no effect on the flow pattern. Also, capillarity is of no practical importance, while the dominant forces are inertia and fluid friction due to viscosity. Therefore, the Reynolds number can be employed as the parameter for the comparison.

The microchannel region (cross-section = $100 \times 100 \mu m^2$, $D_h = 100 \mu m$) can be considered as the reference element for the fluid dynamic comparison, and its Reynolds number Re_μ was calculated as follows:

$$Re_\mu = \frac{\rho D_h v}{\eta} = \frac{1}{\eta D_h} \frac{\dot{m}_{in}}{24} \quad (B.7)$$

where η [Pa s] is the fluid's dynamic viscosity. Figure B.22 shows the ratio between the pressure drops (baseline and optimised designs) for the CFD analysis and the experimental tests as a function of Re_μ . At Re_μ greater than 200, the ratio is ~ 4 and ~ 2.8 for the CFD and experimental results, respectively. This difference can be attributed to the restriction connecting the outlet manifold to the distribution lines (see Figure B.15), which inevitably creates a non-negligible local pressure drop for both the manifold geometries.

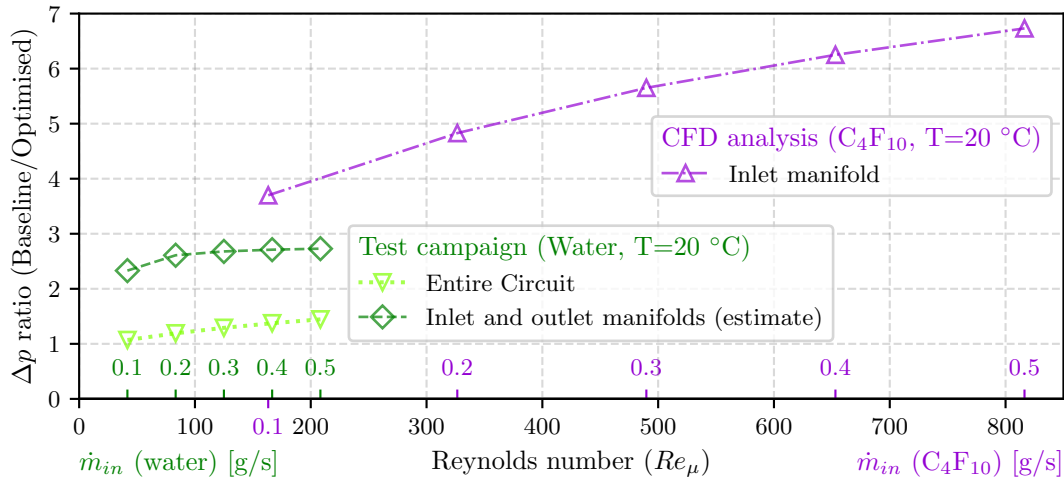


Figure B.22: Comparison between the CFD analysis and the test campaign. The pressure drop ratios, extrapolated from the CFD analysis and the test campaign, are plotted as a function of the Reynolds number at the microchannel (Re_μ). The corresponding mass flow rates are given on the additional x-axes (green and violet ticks). The dynamic viscosity of the water and the C_4F_{10} , at $T = 20^\circ C$, are 1 and 0.2552 mPa S, respectively.

B.9 Conclusion

An approximative design for a distribution manifold may seem functional, but it can bring significant flaws. Flow anomalies, such as high velocity at the inlet, flow re-circulation and stagnant zone, observed in the distribution manifold, with a careless geometry, were solved by a manifold design optimisation supported by an inherited CFD simulations.

The new inlet manifold is based on a larger inlet area and an optimised shape (derived from the low-pressure 23021 NACA profile). It provides a better flow uniformity, minimisation of re-circulation and stagnant zone. The velocity at the inlet of the manifold was reduced, and the flow was more homogeneous at the entrance of the microchannels; consequently, the local pressure drop decreased.

My contribution to this research was to produce samples and experimentally validate the CFD optimisation.

The CFD numerical prediction was then validated by experimental tests (flow inspection and pressure test). This confirmed the reliability of the CFD simulation for design optimisation of the microchannel manifold.

For a mass flow rate of 0.5 g/s, the pressure drop related to the new geometry was reduced by 250KPa (2.5 bar). Further improvement can be achieved by optimising the geometry of the outlet manifold, which was designed to operate with low-pressure boiling coolants. Therefore, further CFD analyses and tests, considering two-phase fluids, must be performed to fully characterise the silicon microchannel sub-circuit.

Pressure drop management in microchannels is key, especially in the case of large surface coverage. Indeed, for the 70 mm long microchannel sub-circuit, the pressure drop of the optimised geometry was in the range of 150 - 600 kPa (1.5 - 6 bar) for mass flow rates varied from 0.15 up to 0.5 g/s.

The design solution to overcome the significant pressure drop, when large surfaces (long distances) have to be covered, implies using distribution lines and manifolds that serve microchannel sub-circuits connected in parallel. At the same time, the limitation on the Si wafer size (Section 2.3.2) requires the investigation of a reliable hydraulic interconnection along the distribution lines as the main target to extend the use of silicon μ CS for the thermal management of large surfaces.

C Experimental set-ups

C.1 Set-up for the pressure test

The pressure test set-up can be moved and adapted for testing different types of samples. It was used to test the O-rings alone (face seal and radial seal) and the polymer and ceramic samples. In Figure C.1, the set-up is adapted to test the micro O-rings alone.

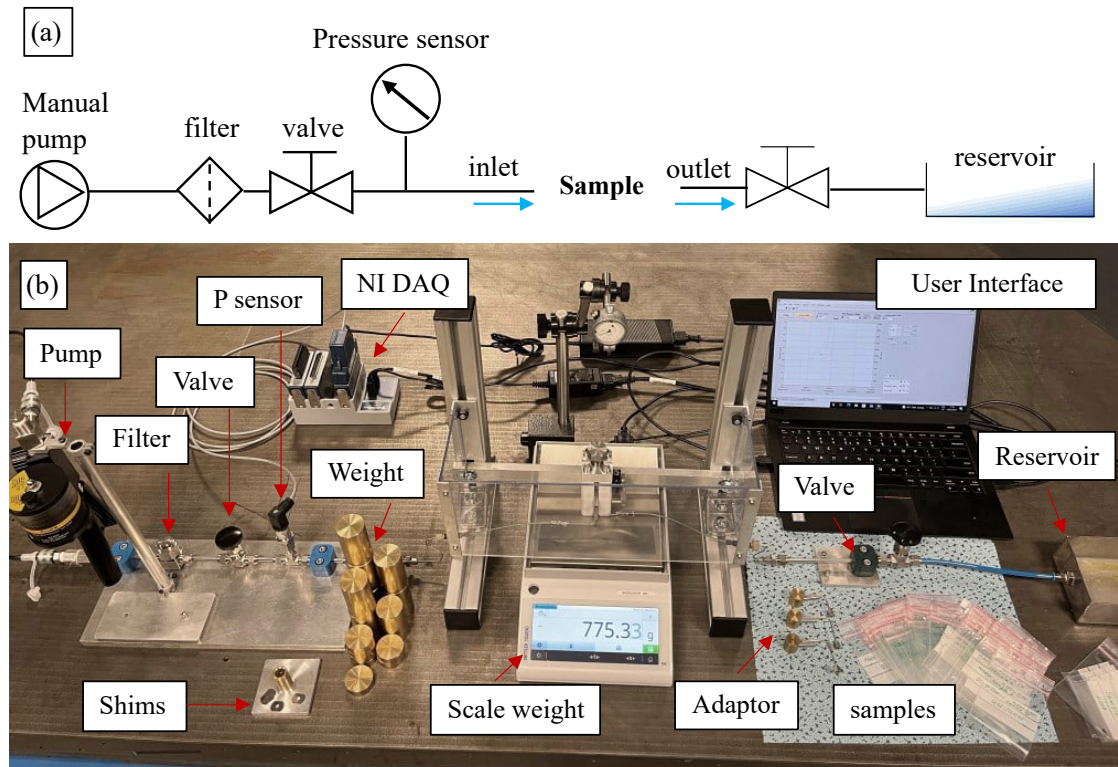


Figure C.1: Set-up for the pressure test. (a) Schematic representation of the set-up and (b-d) set-up. A relative pressure sensor (Gems sensor ATEX Series 31IS-B-0400S-01-R-0-00 [236]) is positioned at the inlet of the test section. The pressure sensors range from 0-40000 kPa (0-400 bar), with an accuracy of 0.25% full scale (FS), corresponding to ± 100 kPa (± 1 bar).

Appendix C. Experimental set-ups

Before each test, the water flows inside the samples and is collected in the reservoir. If no obstructions are noticed, the valve near the reservoir is closed, and the sample is pressurized.

C.2 CERN EP-DT set-up for the burst pressure test of silicon device

The experimental set-up is located at the CERN EP-DT department (Figure C.2) [103]; all the silicon samples are tested with this set-up and the information collected for comparison.

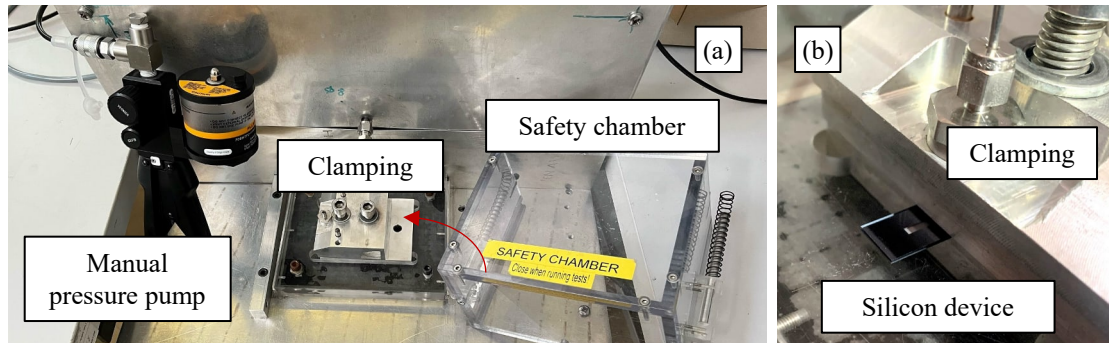


Figure C.2: CERN EP-DT set-up for the burst pressure test of silicon device. (a) Manual pressure pump and safety chamber with the dedicated clamping inside and (b) detail of a clamped sample. An O-ring provides the sealing between the sample and the clamping tool.

C.3 Set-up for the flow distribution inspection

The experimental set-up is visible in Figure C.3:

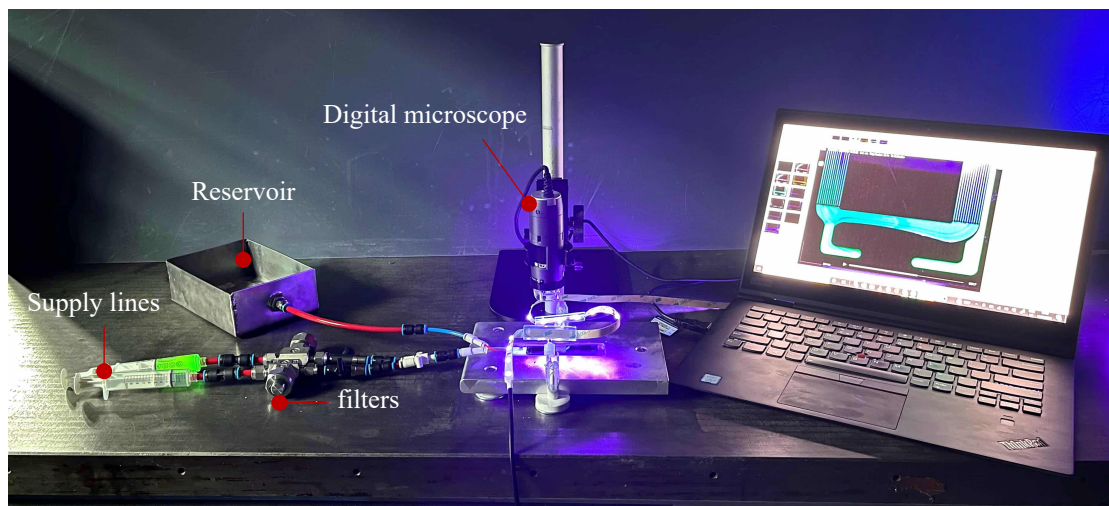


Figure C.3: Set-up for the flow distribution inspection. The magnification range and sensor resolution of the digital microscope (Dino-Lite edge digital microscopes AF4115ZT [237]) are 20-220x and 1.3 Megapixel (1280x1024).

C.4 Set-up for the He leak rate test

The experimental set-up is visible in Figure C.4.a. The sample to be tested is connected to the set-up and put under vacuum ($< 10^{-3}$ mbar), while helium is sprayed on the sample's external surface. The quantity of Helium particles that enter inside the sample is measured.

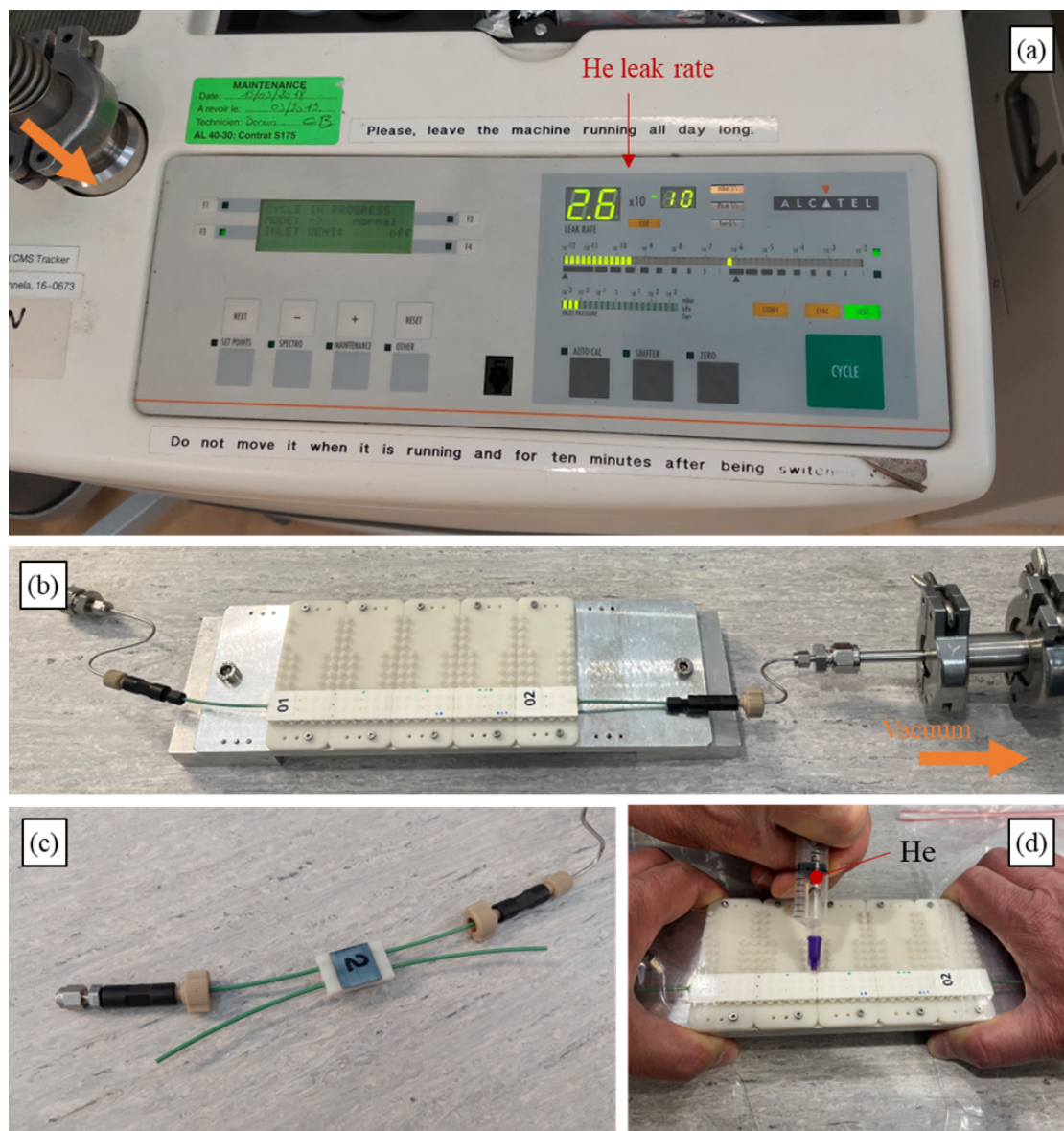


Figure C.4: Set-up for the He leak rate test. (a) set-up and (b-d) connected samples. The helium leak detector is the Pfeiffer Adixen ASM 142 [238].

C.5 Set-up for the hydraulic and thermal test

The experimental set-up is visible in Figure C.5, while the schematic representation of the hydraulic circuit, present in the clean room of the ALICE ITS Upgrade at CERN, is in Figure C.6

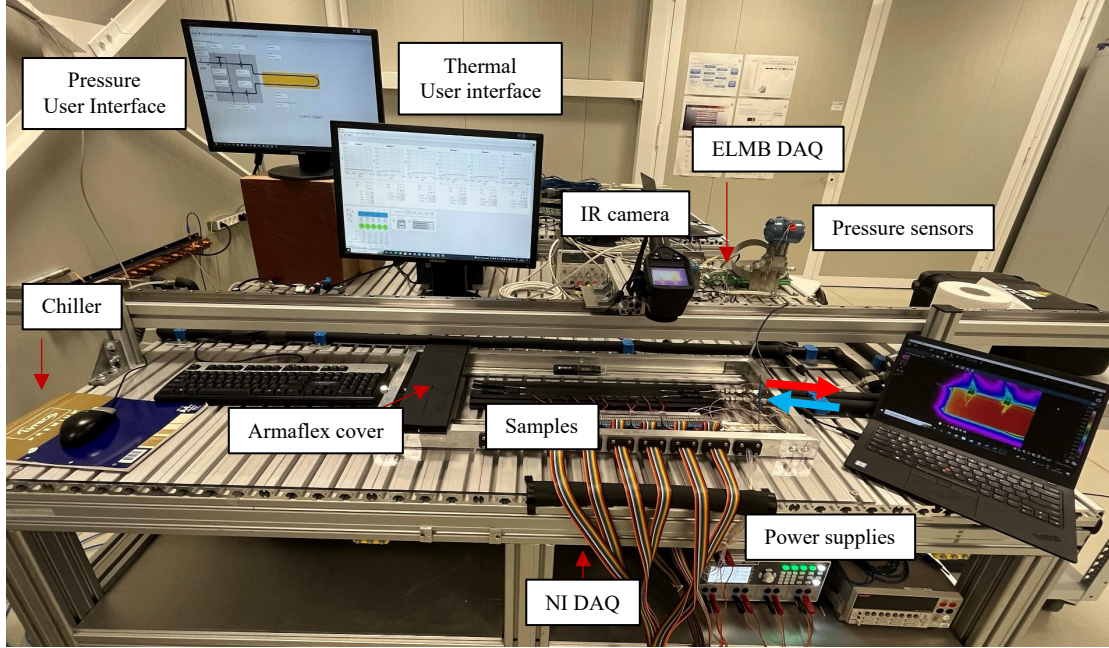


Figure C.5: Set-up for the hydraulic and thermal tests. The chiller and the NI DAQ system are not visible.

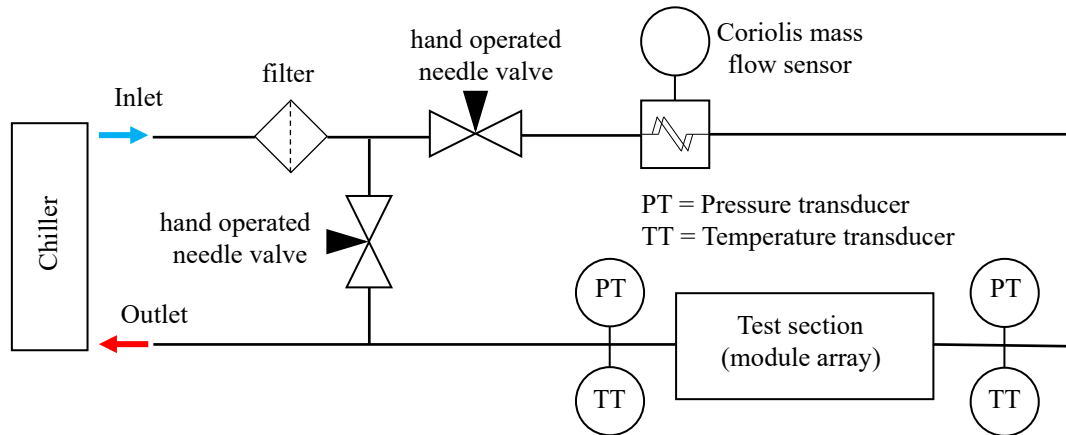


Figure C.6: Schematic representation of the hydraulic circuit. The mass flow sensor (Coriolis flowmeter Bronkhorst mini CORI-FLOW M14 [231]) is positioned at the inlet line. Its flow rate ranges from 0.03 to 2.78 g/s with an accuracy of $\pm 0.2\%$ of the rate ($< \pm 0.01$ g/s). Two temperature sensors (PT1000, class 3) and two absolute pressure sensors (Huba Control 511-930201041w [232]) are positioned at the inlet and outlet of the test section. The pressure sensors range from 0-1000 kPa (0-10 bar), with an accuracy of 0.5% full scale (FS), corresponding to ± 5 kPa (± 0.05 bar).

Power supplies (3 x R&S HMP4040 [239]), an additional DAQ system (NI cDAQ-9174, 4 x PT1000 analogue input modules NI 9226) and its acquisition program (LabView [209]) were used to control the heaters and temperature sensors. The set-up was therefore constituted by two sub-systems, one for the "hydraulic part" and another for the "thermal part". Proportional–Integral–Derivative (PID) controllers were implemented for the heaters' regulation.

C.5.1 Uncertainty analysis

The assessments of the experimental set-up's uncertainties on the TFM (Equation 2.3) and their propagation were approached as n independent variables x_i affecting the quantity TFM, which may be written as:

$$\partial TFM_{x_i} = \frac{\partial TFM}{\partial x_i} \partial x_i \quad (C.1)$$

Assuming that the uncertainties have a Gaussian distribution, the maximum uncertainty of TFM can be estimated as a euclidian norm of the uncertainties:

$$\partial TFM_{x_i} = \left(\sum_{i=1}^n \left(\frac{\partial TFM}{\partial x_i} \partial x_i \right)^2 \right)^{1/2} \quad (C.2)$$

The instrument errors correspond to C.1, and they were added in quadrature (C.2) to find the uncertainty of TFM listed in table C.1.

Table C.1: Error uncertainties of the instruments and TFM propagation. The error uncertainty of the temperatures is conservatively calculated for temperatures $\sim 20^\circ\text{C}$ (error $\sim 0.75\%$).

Instrument	Quantity	Error	Quantity
PT1000 (class 3)	T sensor	0.15°C	12 (5 modules x2 + 2 water)
R&S HMP4040 [239]	Voltage	$<0.05\%$	10 (5 modules x2)
R&S HMP4040 [239]	Current	$<0.1\%$	10 (5 modules x2)
Kapton Heater	Resist.	2%	5 (5 modules 2 in parallel)
Exper.			
	Power [W]	4.48%	
	$\Delta T [^\circ\text{C}]$	2.6%	
	TFM [$\text{cm}^2 \text{K/W}$]	5.18%	

D Additional parts on the i-M μ CS implementation

D.1 ALICE 3 Inner tracking system

Hybrid Integrated Circuit (HIC): CMOS Monolithic Active Pixel Sensor (MAPS) is considered the baseline sensor technology for the ALICE3 tracking detector, and variants of MAPS sensors will be investigated.

For the vertex detector, wafer-sized sensors with excellent position resolution will be the target. For the tracker, wafer-sized or reticle-size sensors of a few cm^2 with a more relaxed position resolution are planned. These developments will be a continuation of the ITS2 and ITS3 activities, which constitute the first large-scale application of MAPS ($10m^2$) at the LHC. The developments for ITS3 are now pioneering the 65 nm TowerJazz technology and stitching techniques for large silicon sensor production (up to $95 \times 280 mm^2$ and 20-40 μm thin).

As a baseline, only the MAPS sensor will constitute the HIC for the vertex and, if possible, also for the tracker. This aspect will be strictly connected to the ongoing R&D on large MAPS silicon sensor (for ALICE ITS3). Several challenges, such as long-distance data and power transfer, sensor and pixel yields, still need to be addressed. Other solutions for the HIC will be investigated as well. In the worst case, the HIC will be constituted by several sensors glued and electrically connected to a thin FPC as it is now for i-M μ CS ITS2.

To summarise, a single thin large sensor or reticle-size sensor connected by an FPC will constitute the HIC for the vertex and outer tracker. Independently from the final HIC, the modules assembly will target to be industrialised as the numbers of HIC production will exceed the capability of research centres production. Based on this, the final modules must be qualified in all possible aspects before being integrated.

HIC to HIC electrical connection: Different sensing module-to-sensing module electrical connections exist depending on several requirements (e.g. sensing module design, electrical power distribution, signal-to-noise ratio and read-out frequency).

As it was done for the ALICE ITS2, the adjacent sensing modules of the new tracker can be

interconnected using flex bridges soldered to pads present on the edges of the sensing modules. For the ALICE ITS2, the bridge was made of a single-layer polyimide flex circuit hosting a certain number of lines which connect pairs of pads of adjacent modules. These bridges were double-sided circuits. Lines running on the top and bottom layers were connected by through-vias. After an accurate alignment, the bridges were tin welded to the solder pads on the FPCs. Melted tin flows through vias and gets the bridge soldered to the FPC.

D.2 Flatness of large 3D printed ceramic substrates

The 3D scan of all the large ceramic substrates is in table [D.1](#).

For 3D printed samples printed in Alumina with NPJ technology, the surfaces of the modules having 0.7 mm thickness exhibit a deflection in the centre for both lateral and longitudinal directions caused by the firing process. The deflection on the longitudinal direction, corresponding to the greater dimension, is more pronounced as evidence of the deformation dependence on the dimension. The flatness of 30x60 mm² samples was in the range of 0.159-0.338mm (Figure [7.9.a](#)), while the flatness of the 30x210 mm² samples was 0.865mm (Figure [7.9.c](#)).

Similar distortion effects were noticed for the LCM samples with reduced thickness (0.2mm for the plate and 0.5mm for the frame areas). The flatness of the 30x60 mm² samples ranges from 0.472 to 1.377 mm (Figure [7.9.b](#)). For the reduced thickness, higher distortion was noticed along the 30 mm edge direction as the long side is stiffer by the channels and slots for the rails. The flatness of the 30x210 mm² sample was 0.787mm (Figure [7.9.d](#)).

For the frame configuration, the flatness for the 30x30 mm² samples printed with both the technology (NPJ and LCM) was in the range 0.176-0.367mm (Figure [7.10.b](#)). Furthermore, the 30x30 mm² samples produced with the LCM technology showed an additional warping effect on the 0.2mm plate. This warping effect is often noticed in ceramic tape casting where large plates with small thicknesses, in our case 0.2mm, easily go under buckling of the wall induced by the firing step.

Table D.1: Summary of large ceramic substrate flatness. "IF" means InterFace.

Mech. IF	Hydraulic IF	Technology	Material	substrate	Width[mm]	Length[mm]	Flatness[mm]	minimum	center	maximum
Rails-based	Radial-seal	NPJ	Alumina	frame(0.5mm)	30	30	0.256	-0.209	-0.081	0.047
Rails-based	Radial-seal	NPJ	Alumina	frame(0.5mm)	30	30	0.267	-0.132	0.002	0.135
Rails-based	Radial-seal	NPJ	Alumina	frame(0.5mm)	30	30	0.176	-0.091	-0.003	0.085
Rails-based	Radial-seal	NPJ	Alumina	frame(0.5mm)	30	30	0.244	-0.207	-0.084	0.038
Rails-based	Face-seal	NPJ	Zirconia	frame(2.2mm)	30	30	0.046	-0.024	-0.001	0.022
Rails-based	Radial-seal	Lithoz	Alumina	frame(0.5mm)	30	30	0.277	-0.18	-0.042	0.096
Rails-based	Radial-seal	Lithoz	Alumina	frame(0.5mm)	30	30	0.227	-0.097	0.017	0.13
Rails-based	Face-seal	Lithoz	Alumina	frame(0.5mm)	30	30	0.367	-0.274	-0.09	0.094
Rails-based	Radial-seal	Lithoz	Alumina	plate (0.2mm) frame(0.4mm)	30	30	0.406	-0.279	-0.76	0.127
Rails-based	Radial-seal	Lithoz	Alumina	plate (0.2mm) frame(0.5mm)	30	30	0.933	-0.45	0.016	0.483
Rails-based	Face-seal	Lithoz	Alumina	plate (0.2mm) frame(0.5mm)	30	30	0.704	-0.466	-0.114	0.238
Rails-based	Face-seal grinded	Lithoz	Alumina	plate (0.2mm) frame(0.5mm)	30	30	0.068	-0.034	0	0.034
Rails-based	Radial-seal grinded	Lithoz	Alumina	plate (0.2mm) frame(0.5mm)	30	30	0.034	-0.019	-0.002	0.015
Rails-based	Face-seal grinded	Lithoz	Alumina	frame(0.5mm)	30	30	0.055	-0.043	-0.016	0.012
Pin-based	Face-seal	NPJ	Alumina	plate(0.7mm)	30	60	0.159	-0.103	-0.024	0.056
Pin-based	Face-seal	NPJ	Alumina	plate(0.7mm)	30	60	0.259	-0.176	-0.046	0.084
Pin-based	Face-seal	NPJ	Alumina	plate(0.7mm)	30	60	0.286	-0.157	-0.014	0.129
Pin-based	Face-seal	NPJ	Alumina	plate(0.7mm)	30	60	0.169	-0.105	-0.021	0.063
Pin-based	Face-seal	NPJ	Alumina	plate(0.7mm)	30	60	0.197	-0.133	-0.035	0.064
Pin-based	Radial-seal	NPJ	Alumina	plate(0.7mm)	30	60	0.216	-0.137	-0.029	0.079
Pin-based	Radial-seal	NPJ	Alumina	plate(0.7mm)	30	60	0.323	-0.192	-0.031	0.13
Pin-based	Radial-seal	NPJ	Alumina	plate(0.7mm)	30	60	0.363	-0.201	-0.019	0.163
Pin-based	Radial-seal	NPJ	Alumina	plate(0.7mm)	30	60	0.288	-0.172	-0.028	0.116
Pin-based	Radial-seal	NPJ	Alumina	plate(0.7mm)	30	60	0.338	-0.169	0	0.17
Rails-based	Face-seal	NPJ	Alumina	plate (0.2mm) frame(0.5mm)	30	60	1.134	-0.755	-0.188	0.379
Rails-based	Face-seal	NPJ	Alumina	plate (0.2mm) frame(0.5mm)	30	60	0.638	-0.469	-0.15	0.169
Rails-based	Face-seal	NPJ	Alumina	plate (0.2mm) frame(0.5mm)	30	60	1.377	-0.829	-0.141	0.548
Rails-based	Face-seal	NPJ	Alumina	plate (0.2mm) frame(0.5mm)	30	60	1.58	-0.974	-0.184	0.607
Rails-based	Radial-seal	NPJ	Alumina	plate (0.2mm) frame(0.5mm)	30	60	0.472	-0.355	-0.119	0.116
Rails-based	Radial-seal	NPJ	Alumina	plate (0.2mm) frame(0.5mm)	30	60	0.791	-0.586	-0.19	0.205
Pin-based	Face-seal	NPJ	Alumina	plate(0.7mm)	30	210	0.865	-0.431	0.002	0.435
Rails-based	Radial-seal	NPJ	Alumina	plate (0.2mm) frame(0.5mm)	30	210	0.787	-0.448	-0.055	0.339

E CAD drawing

Appendix E. CAD drawing

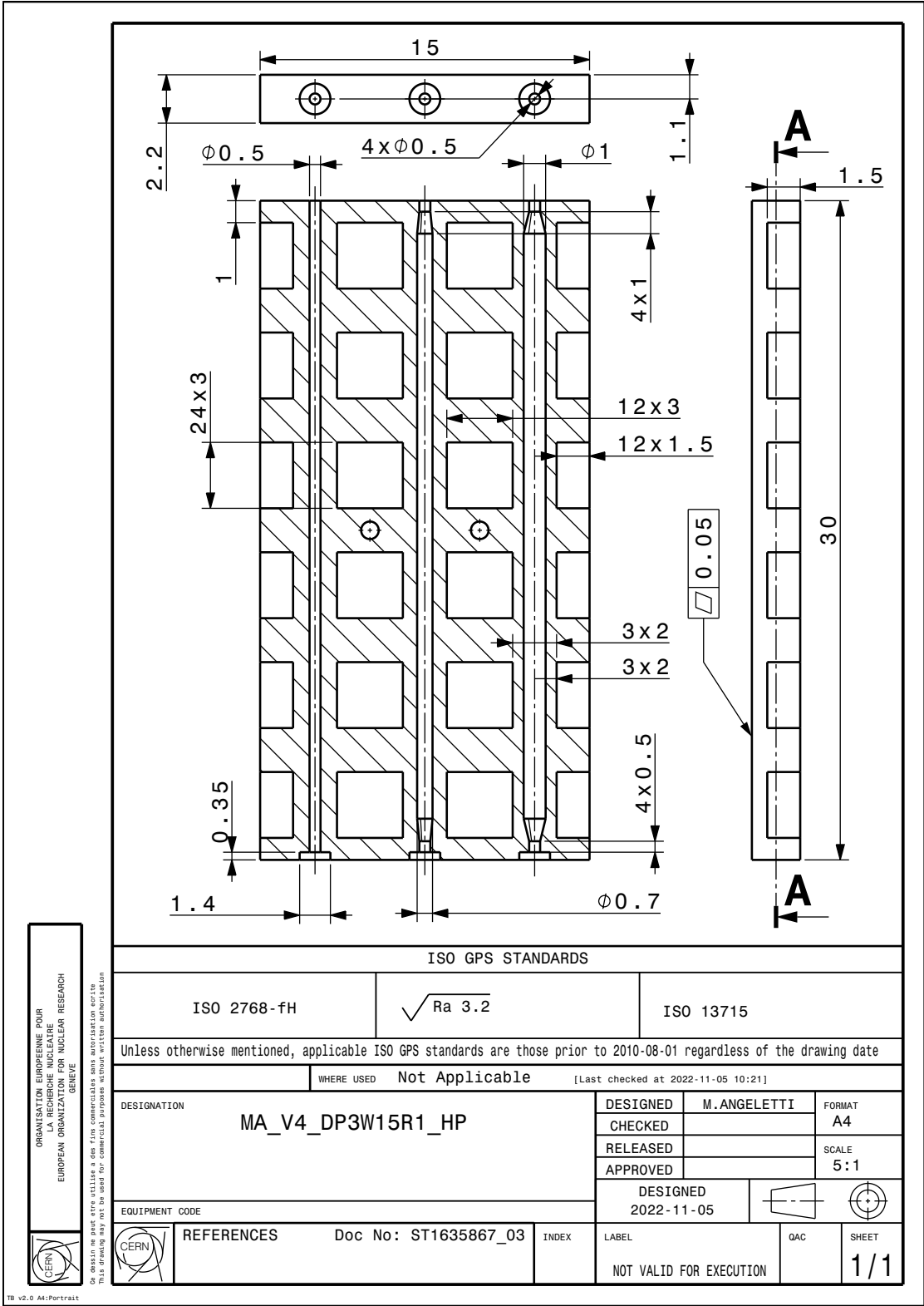


Figure E.1: Drawing of the polymeric pin-based samples.

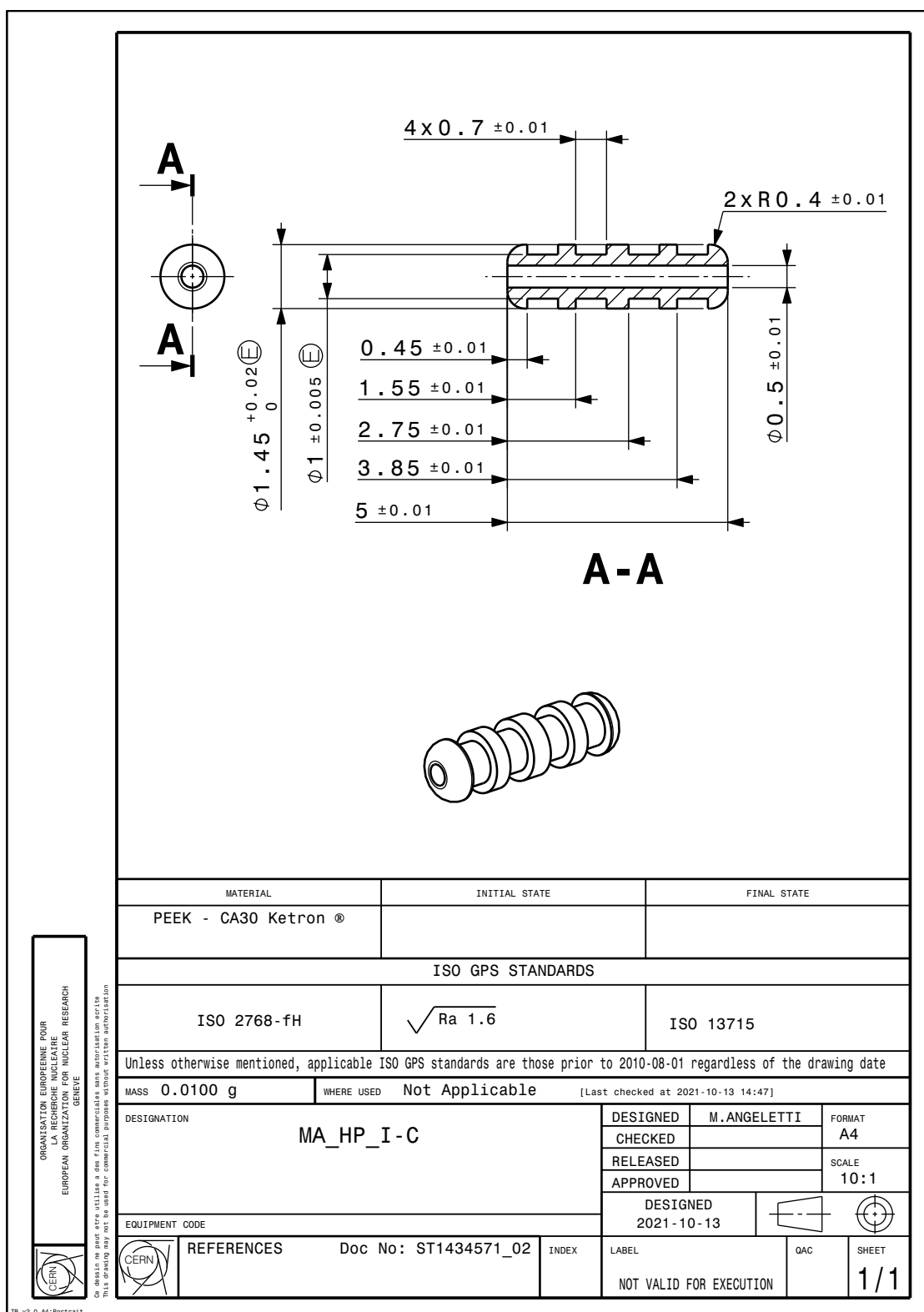


Figure E.2: Drawing of the seal fitting.

Appendix E. CAD drawing

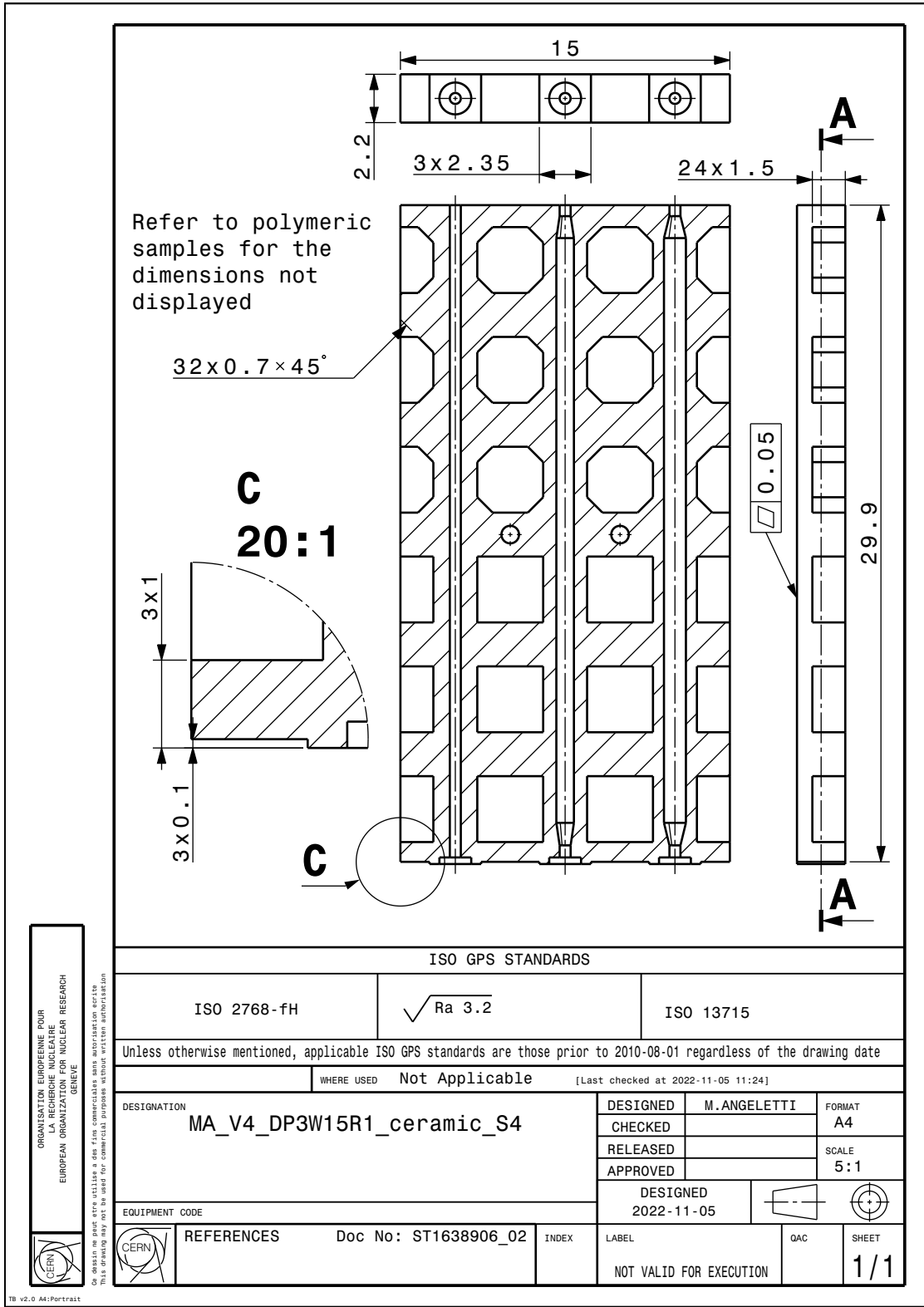


Figure E.3: Drawing of the pin-based ceramic sample type 4.

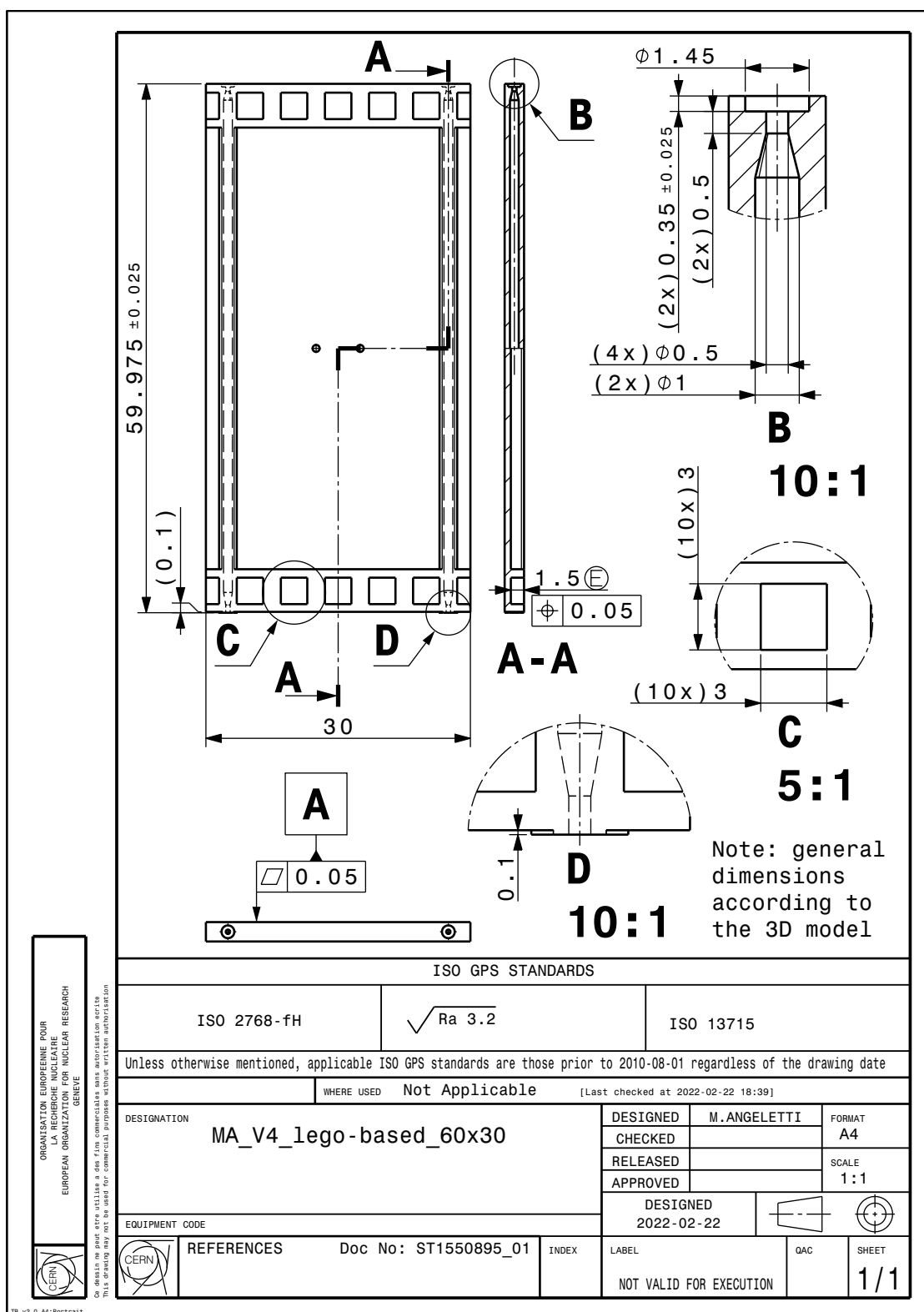


Figure E.4: Drawing of the 30x60 mm² pin-based ceramic module

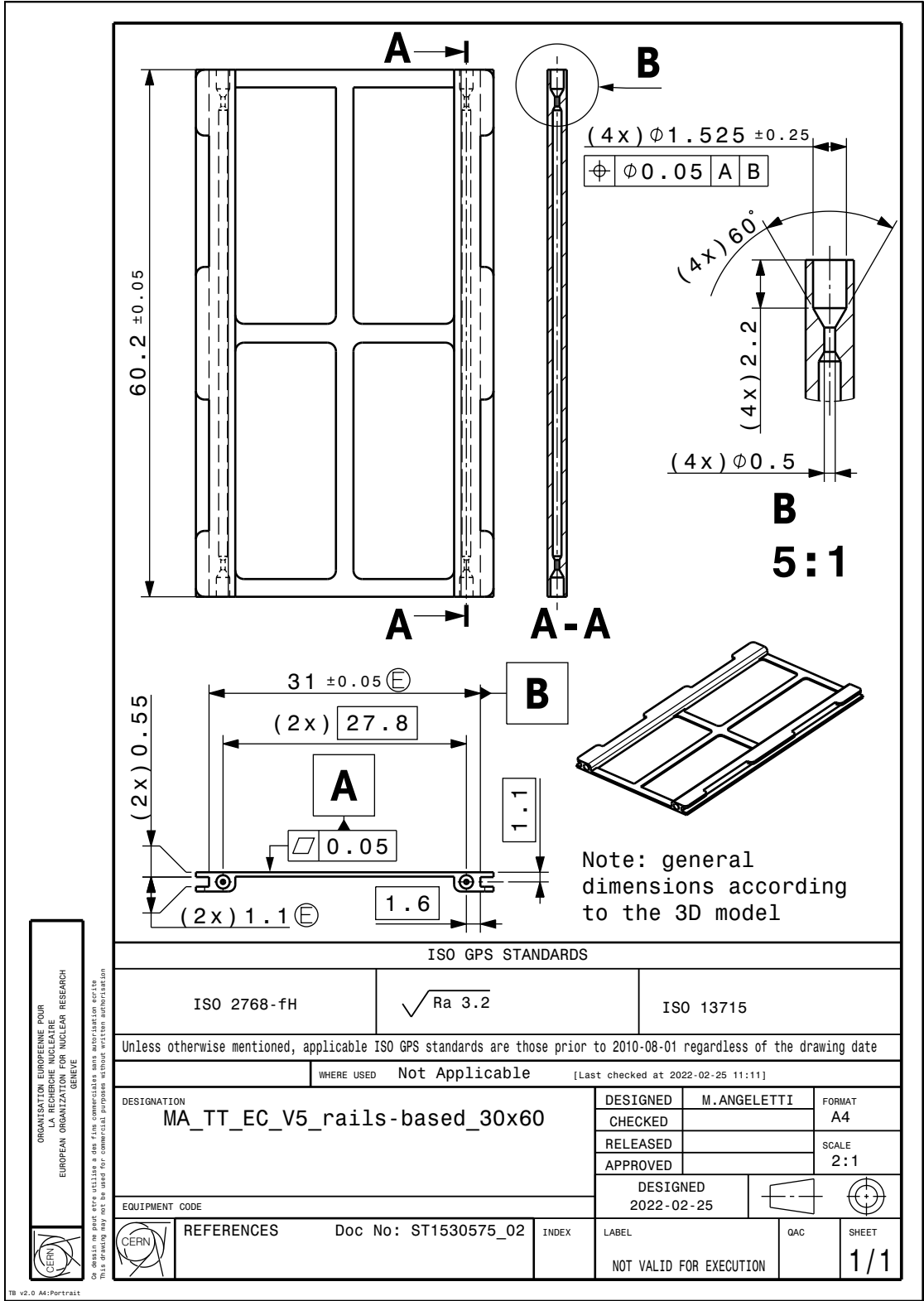


Figure E.5: Drawing of the 30x60 mm² rail-based ceramic module

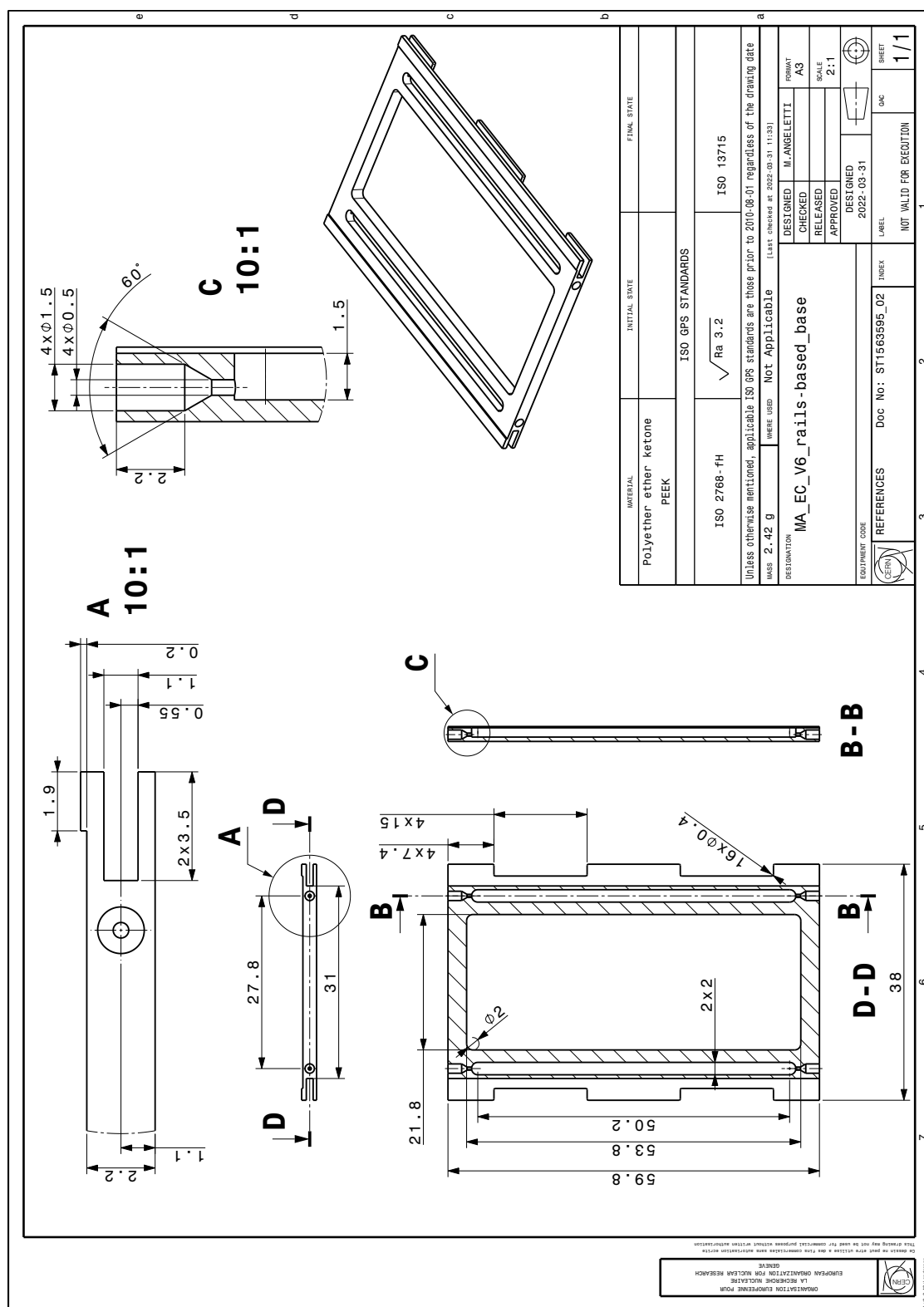


Figure E.6: Drawing of the auxiliary PEEK substrate for the CFRP i-M μ CS solution.

Massimo Angeletti

GENERAL INFORMATION

Born on March 13, 1991 –Turin (ITALY)
Nationality Italian

Email massimoangeletti13@gmail.com

EDUCATIONAL BACKGROUND

PhD candidate in Micromechanical Engineering.

Period 01/11/2017 – Today

University EPFL - ÉCOLE POLYTECHNIQUE FÉDÉRALE DE LAUSANNE

Department EDMI - Microsystems and Microelectronics.

Subject Interlocking modular microfluidic cooling substrate for future HEP experiments

MSc in Energy and Nuclear Engineering, 110 cum Laude /110 (Top Grade).

Period 21/10/2013 – 25/10/ 2016

University POLITO - Polytechnic University of Turin

Thesis Study of the mechanical support and positioning of the sensors for the new tracker of the ALICE Experiment at CERN.

PROFESSIONAL & STUDENT EXPERIENCE

01/11/2017 - Doctoral Student - Senior Fellow at CERN

EPFL PhD Candidate: cooling and microfluidic interconnection.

Mechanical Engineer: Integration and installation of the ALICE ITS2. (01/02/2020-20/05/2021)

01/02/2017-01/11/2017 User at CERN

Mechanical Engineer: Characterisation tests and database management. (01/02/2017-Today)

01/02/2016-01/02/2017 Technical Student at CERN

Mechanical Engineer: Detector design and FEA of ultra-light composite structures (CFRP, Sandwiches). (01/02/2016-Today)

01/10/2015-31/01/2016 **Collaboration at INFN of Turin**

CMM programmer: Mitutoyo CMM developer (01/10/2015-Today)

PROJECTS AT CERN:

- ALICE experiment: ALICE 3, ITS3, ITS2.
- CERN EP R&D WP4:
 - Low mass structure
 - Ultra-light cryostat
 - Robotics (Interface and services)
- AIDAInnova: WP10 Task10.2
 - Cooling substrates
 - 3D printed
 - CFRP
- CFRP for CSES-02 satellite
 - CFRP cooling plate & supporting structure

LANGUAGE SKILLS

Mother tongue Italian

Other languages

English French

Listening

C1 A2

Reading

C1 A2

Speaking

B2 A2

Writing

B2 A2

Certificate

IELTS EDUQUA

PROFESSIONAL COMPETENCES

- Design and building of new ultralight carbon composite structures. Deep knowledge and experience of mechanical systems and advanced methods and tools for structural analyses (Structural, Buckling, Modal, and Random Vibration analyses).
- Specific experience in metrology (CMM), mechanical tests (bending, torsional, random vibration, sine sweep), thermo-mechanical, burst pressure and pressure drop tests
- Production of low-mass carbon vascular cooling substrates with embedded polyimide/metal pipes.
- Quality assurance control, information storage and management of Database.
- Microfabrication technology with specific experience in silicon microfluidic substrate production at the EPFL CMi cleanroom: photolithography, silicon etching (DRIE, WET), and anodic bonding.
- Laser technology. Specific experience with femtosecond laser engraving of silicon and CO2 laser cut.
- Additive Manufacturing technology (photosensitive polymers, multi-materials, ceramics, metals). Specific experience with Stereolithography (SLA): Lithography-based Ceramic Manufacturing (LCM), Direct Metal Laser Sintering (DMLS) and Material Jetting (MJ) technology: Polyjet for acrylic resins and NanoParticle Jetting (NPJ) for ceramics.
- Microcontroller development systems for thermal and mechanical test set-ups.